DISS. ETH NO. 28918

Engineering living immunotherapeutic agents for magnetically enhanced tumour targeting

A thesis submitted to attain the degree of

DOCTOR OF SCIENCES of ETH ZURICH

(Dr. sc. ETH Zurich)

presented by

Tinotenda Gwisai

M.Sc. *Biomedical Engineering, Imperial College London*

born on 06.11.1992

accepted on the recommendation of

Prof. Simone Schürle-Finke, examiner

Prof. Selman Sakar, co-examiner

Dr. Karina Silina, co-examiner

2022

Acknowledgements

Over the last four years, I have been incredibly fortunate to have received support from many people, without whom successful completion of this project would not have been possible.

Firstly, I would like to thank my PhD supervisor Prof. Dr. Simone Schürle-Finke for her valuable guidance, her immense dedication and her mentorship over the last four years. My PhD journey started with an interview over a relatively unpredictable internet connection, after which I was delighted to receive an offer to join the team at RBSL. Simone, thank you so much for putting your trust in me to pursue this project in your lab. Thank you for sharing your enthusiasm and passion for science with me and always providing the encouragement I needed keep pushing to make progress with my experiments. I was very appreciative of the fact that, no matter the circumstances, you were always available to provide ongoing support and give constructive and helpful feedback. Under your supervision, I have grown and developed as a researcher and the skills I have learnt at RBSL will serve me well in the future.

Special thanks to Dr. Karina Silina for agreeing to come on board as my co-supervisor and as a committee member. Your support and feedback were incredibly valuable and helped to make this work better. I would also like to extend my gratitude to Prof. Selman Sakar for his willingness to co-examine this thesis.

Many thanks to Dr. Michael G. Christiansen for his support and guidance. I have appreciated your encouragement and admired your willingness to always lend a helping hand. In our many discussions I learnt a lot about several things ranging from dinosaurs and camping to chemistry and magnetism, and I typically left with a different perspective that I could apply to improving my experiments. I would also like to thank Dr. Matej Vizovisek for sharing his wealth of knowledge about molecular biology and, of course, proteases with me. Your sense of humour made the time in the lab with you especially memorable and enjoyable.

This project would have not been possible without the contributions and help of students who chose to work on this project for their master's theses. Thuy Trinh Nguyen, Mira Jacobs, Simone Hersberger, Jonathas Enders and Sina Günther - I am incredibly grateful that I had the opportunity to work with all of you. During my time supervising these projects I gained many important skills and I thoroughly enjoyed working on these fruitful collaborations. I wish each of you the very best in your next steps.

I was very lucky to spend my time at RBSL with an awesome cohort of fellow PhD students. Thank you to Dragana Dubey, my twin sister, who showed me around the lab on my first day and patiently answered all my questions about 'how to Switzerland', Nima Mirkhani who became my *in vivo* buddy and fiercest rival in our fantasy football league, Daphne Asgeirsson whose infectious positivity made the office a more pleasant place to work, Stefano Menghini who always went above and beyond for the team, Yimo Yan whose wit and humour kept us entertained and Ping Shu Ho who showed me the ropes in my first few months. Doing a PhD is a long journey with many ups and downs, and I am incredibly grateful to have shared this journey with all of you.

This work was also supported by contributions from collaborators and personnel outside RBSL. I would like to thank the RCHCI staff for support with animal experiments, the Flow Cytometry Core Facility and Scientific Center for Optical and Electron Microscopy (ScopeM) at ETH Zurich for access to their facilities. I would also like to thank Dr. Gabriella Éva Bodizs for providing training for the histology facility. Many thanks to Prof. Maries van den Broek, Prof. Tal Danino, Dr. Tetsuhiro Harimoto and Dr. Tobias Weiss for very helpful discussions and input for experimental design. I'd also like to thank David C. Bono for useful input for the magnetometer design, Lucas Amoudruz for helpful discussions on computational modeling of MTB, Lucien Stöcklin for his assistance with the inductive detection experiments and Chantel Spencer for input on various cell culture techniques.

I received so much support throughout this journey from many incredible friends, particularly through the more challenging times. I especially want to thank Anna Brown who listened patiently, encouraged me and provided assistance during the writing process. I would also like to thank Thanusha Rasaiah who assisted with proof-reading and who has become a dear friend after our time together at RBSL.

Last, but certainly not least, I would like to thank my family. To my big brother, Tafadzwa, you have constantly set the bar very high and I have always admired your immense work-ethic and dedication. Your constant encouragement has pushed me to achieve as much as I have. To my incredible mother, Dr. Buhle Ncube, you have always been my inspiration. Your love, patience, sacrifices and unwavering support have gotten me to this point. Words cannot begin to express my profound gratitude for everything you both have done for me. This PhD is a shared achievement.

Abstract

Due to the inherent limitations of currently available therapies, there has been increasing interest in harnessing the functionalities of biological agents that self-propel and have tumour homing properties. Unlike conventional chemotherapeutics that rely on passive diffusion, living delivery systems can overcome challenges to transport posed by pathological characteristics of the tumour environment. The ability of bacteria to colonise tumours and trigger regression was recognized centuries ago and several bacterial strains have been tested in human clinical trials. While these studies have demonstrated the immense potential of bacterial cancer therapy, translation has been hindered by incomplete clinical responses, partly due to insufficient tumour colonisation. Thus, developing strategies to enhance accumulation of intravenously administered bacteria is essential for facilitating robust colonisation and increasing therapeutic efficacy. A unique group of bacteria that biomineralize magnetic nanoparticles arranged in chains have recently been studied as drug carriers for cancer therapy. Magnetotactic bacteria (MTB) are motile, aquatic bacteria that preferentially accumulate in hypoxic tumour tissue and their magnetic properties can be leveraged for guidance using external magnetic fields. This thesis investigated the use of rotating magnetic fields to manipulate *Magnetospirillum magneticum* AMB-1 with liposomal cargo to produce a living, controllable drug delivery vehicle.

To employ MTB for cancer therapy, an understanding of the interaction between host immunity and MTB is essential. Thus, several key properties of human innate immune cells in response to stimulation with MTB were examined. MTB proliferated under physiological conditions, with increased proliferation at higher temperature, although magnetic responsiveness decreased over time. MTB remained viable in whole human blood and persisted in samples for 3 h. These findings imply that magnetic actuation should be implemented within the first 3 h after administration when viable, magnetically responsive MTB would likely be in circulation. MTB substantially increased the uptake of cancer cell material by monocyte-derived dendritic cells and induced their maturation, both of which are crucial steps for mounting an effective T cell-mediated antitumour response.

Having established the potential benefit of using MTB for immune-mediated cancer therapy, the use of MTB-liposome conjugates that combine the adaptability of traditional nanocarriers and the functionality of magnetic-based platforms was explored for targeted drug delivery. Conjugates were fabricated using a copper-free click reaction and the effective delivery of 5-fluorouracil, a

widely used antimetabolite, by the MTB-liposome complex was then investigated. MTB combined with 5-fluorouracil in solution was shown to substantially increase apoptosis, suggesting a possible complementary therapeutic effect of MTB and this payload. Cell proliferation was significantly reduced in 4T1 cells cultured with MTB-liposome conjugates compared to MTB or liposomes alone, further indicating that MTB enhances the efficacy of the chemotherapeutic.

The ability of this delivery system to cross robust biological barriers when aided by external magnetic fields was also investigated. The chain-like structure of magnetosomes enables the application of magnetic torques which can be exploited to enhance the delivery of MTB-LP. A magnetic torque-based actuation scheme that utilises rotating magnetic fields was employed to wirelessly control MTB-liposome conjugates. A 4-fold increase in translocation across a model of the vascular endothelium was observed, and increased surface exploration resulting from magnetic torque-driven motion was proposed as the chief mechanism driving increased transport. Using spheroids as a 3D tumour model, fluorescently labelled bacteria colonised their core regions with up to 21-fold higher signal in samples exposed to rotating magnetic fields. Finally, our actuation scheme was assessed *in vivo* and enhanced tumour accumulation following systemic intravenous administration was observed.

This thesis establishes that the MTB-liposome system, combined with scalable magnetic torque-driven control strategies, can be leveraged for effective delivery of living, magnetically responsive bacteria. This system could be used to improve targeting and colonisation of therapeutic bacteria in tumours. The findings presented here lay the foundation for further development of the MTB-liposome platform for cancer therapy.

Zusammenfassung

Aufgrund der Beschränkungen der derzeit verfügbaren Therapien besteht ein zunehmendes Interesse an der Nutzung der Funktionen biologischer Wirkstoffe, die sich selbst fortbewegen und über Eigenschaften verfügen, die den Tumor ansteuern. Im Gegensatz zu herkömmlichen Chemotherapeutika, die auf passiver Diffusion beruhen, können lebende Trägersysteme die durch die pathologischen Merkmale der Tumorumgebung bedingten Transportprobleme überwinden. Die Fähigkeit von Bakterien, Tumore zu besiedeln und eine Rückbildung auszulösen, wurde schon vor Jahrhunderten erkannt, und mehrere Bakterienstämme wurden in klinischen Studien am Menschen getestet. Während diese Studien das immense Potenzial der bakteriellen Krebstherapie gezeigt haben, wurde die Umsetzung durch unvollständige klinische Antworten verhindert, die teilweise auf eine unzureichende Tumorkolonisierung zurückzuführen sind. Daher ist die Entwicklung von Strategien zur Verbesserung der Akkumulation intravenös verabreichter Bakterien von entscheidender Bedeutung, um eine robuste Besiedlung zu ermöglichen und die therapeutische Wirksamkeit zu erhöhen. Eine einzigartige Gruppe von Bakterien, die in Ketten angeordnete magnetische Nanopartikel biomineralisieren, wurde kürzlich als Medikamententräger für die Krebstherapie untersucht. Magnetotaktische Bakterien (MTB) sind bewegliche, aquatische Bakterien, die sich bevorzugt in hypoxischem Tumorgewebe ansiedeln und deren magnetische Eigenschaften zur Steuerung durch externe Magnetfelder genutzt werden können. In dieser Arbeit wurde der Einsatz rotierender Magnetfelder zur Manipulation von *Magnetospirillum magneticum* AMB-1 mit liposomaler Ladung untersucht, um einen lebenden, kontrollierbaren Wirkstoffträger herzustellen.

Für den Einsatz von MTB in der Krebstherapie ist ein Verständnis der Interaktion zwischen Wirtsimmunität und MTB unerlässlich. Daher wurden mehrere Schlüsseleigenschaften menschlicher angeborener Immunzellen als Reaktion auf die Stimulation mit dem MTB untersucht. MTB vermehrte sich unter physiologischen Bedingungen, wobei die Proliferation bei höheren Temperaturen zunahm, obwohl die magnetische Reaktionsfähigkeit mit der Zeit abnahm. MTB blieben in menschlichem Vollblut lebensfähig und hielten sich 3 Stunden lang in den Proben. Diese Ergebnisse deuten darauf hin, dass die magnetische Stimulation innerhalb der ersten 3 Stunden nach der Verabreichung erfolgen sollte, wenn lebensfähige, magnetisch reagierende MTB wahrscheinlich im Umlauf sind. MTB steigerte die Aufnahme von Krebszellmaterial durch aus Monozyten stammende dendritische Zellen erheblich und induzierte ihre Reifung, beides entscheidende Schritte für eine wirksame T-Zell-vermittelte Antitumorreaktion.

Nachdem der potenzielle Nutzen des Einsatzes von MTB für die immunvermittelte Krebstherapie nachgewiesen wurde, wurde die Verwendung von MTB-Liposom-Konjugaten, die die

Anpassungsfähigkeit herkömmlicher Nanoträger und die Funktionalität von Plattformen auf Magnetbasis vereinen, für die gezielte Verabreichung von Medikamenten untersucht. Die Konjugate wurden mit Hilfe einer kupferfreien Click-Reaktion hergestellt, und anschließend wurde die wirksame Verabreichung von 5-Fluorouracil, einem weit verbreiteten Antimetabolit, durch den MTB-Liposom-Komplex untersucht. Es zeigte sich, dass MTB in Kombination mit 5-Fluorouracil in Lösung die Apoptose deutlich erhöht, was auf eine mögliche komplementäre therapeutische Wirkung von MTB und Nutzlast hindeutet. Die Zellproliferation wurde bei 4T1-Zellen, die mit MTB-Liposomenkonjugaten kultiviert wurden, im Vergleich zu MTB oder Liposomen allein deutlich reduziert, was ein weiterer Hinweis darauf ist, dass MTB die Wirksamkeit des Chemotherapeutikums verstärkt.

Es wurde auch die Fähigkeit dieses Verabreichungssystems untersucht, robuste biologische Barrieren zu überwinden, wenn es durch externe Magnetfelder unterstützt wird. Die kettenartige Struktur von Magnetosomen ermöglicht die Anwendung von magnetischen Drehmomenten, die zur Verbesserung der Abgabe von MTB-LP genutzt werden können. Ein auf magnetischen Drehmomenten basierendes Auslösesystem, das rotierende Magnetfelder nutzt, wurde zur drahtlosen Steuerung von MTB-Liposomen-Konjugaten eingesetzt. Es wurde eine 4-fache Steigerung der Translokation durch ein Modell des Gefäßendothels beobachtet, und die erhöhte Oberflächenexploration, die sich aus der durch das magnetische Drehmoment angetriebenen Bewegung ergibt, wurde als Hauptmechanismus für den erhöhten Transport vorgeschlagen. Unter Verwendung von Sphäroiden als 3D-Tumormodell kolonisierten fluoreszenzmarkierte Bakterien ihre Kernbereiche mit einem bis zu 21-fach höheren Signal in Proben, die rotierenden Magnetfeldern ausgesetzt waren. Schließlich wurde unser Aktivierungsschema in vivo untersucht, und es wurde eine verstärkte Tumorakkumulation nach systemischer intravenöser Verabreichung beobachtet.

Diese Arbeit zeigt, dass das MTB-Liposomen-System in Kombination mit skalierbaren, magnetischen, drehmomentgesteuerten Kontrollstrategien für eine effektive Verabreichung von lebenden, magnetisch reagierenden Bakterien genutzt werden kann. Dieses System könnte verwendet werden, um das Targeting und die Kolonisierung von therapeutischen Bakterien in Tumoren zu verbessern. Die hier vorgestellten Ergebnisse bilden die Grundlage für die weitere Entwicklung der MTB-Liposomen-Plattform für die Krebstherapie.

Table of contents

1. Introduction

Portions of this chapter are adapted from the manuscript "Engineering Cell-Based Systems for Smart Cancer Therapy" by Nima Mirkhani (co-first author), Tinotenda Gwisai (co-first author) and Simone Schuerle published in Advanced Intelligent Systems (2022).

1.1. Leveraging bacteria for cancer treatment

1.1.1. History of bacterial cancer therapy

Nanocarriers, such as liposomes and polymeric nanoparticles, have the ability to reduce systemic toxicity and improve tumour targeting by modifying the biodistribution and pharmacokinetics of their therapeutic payloads (*1*, *2*). However, the efficacy of systemically administered nanotherapeutics is currently limited by physiological barriers and diffusion-limited transport, which impedes their accumulation at tumour sites (*3–5*). The highly irregular architecture of the tumour microvasculature combined with diminished lymphatic drainage leads to impaired perfusion and elevated interstitial fluid pressure, hindering drug penetration (*6–9*). In addition, low vascular density, an abundance of stromal cells and the altered composition of the extracellular matrix impose further obstacles to effective transport of therapeutic molecules within the tumour interstitium (*10–12*). Viable quiescent cells in deeper parts of the tumour, which significantly contribute to drug resistance and clinical relapse, are particularly hard to reach by systemically administered therapeutics. External radiotherapy is also less effective in the poorly oxygenated tumour core (*13*, *14*).

Prompted by these limitations, there has been increasing interest in harnessing the functionalities of living agents that self-propel and actively target tumours (*15*). Bacteria are particularly appealing as an alternative therapeutic agent because of their innate, tumour-specific accumulation, their capacity to transport a wide range of payloads, and their ability to modulate intratumoural inflammatory responses (*16–19*). For centuries, the connection between spontaneous tumour regression and acute bacterial infections has been observed (*20*). The earliest recorded example of bacterial cancer therapy is found in the Ebers Papyrus, which is attributed to the ancient Egyptian physician Imhotep (ca. 2600 BC) (*21*). His recommended treatment of applying a poultice followed by incision of the tumour would inevitably result in the development of an infection that caused subsequent tumour regression. Scientific attempts to modulate the immune system for cancer therapy occurred in the 1800s spurred by observations that erysipelas, a

relatively common post-operative skin infection, had an influence on tumour progression (*22*). In 1867, Wilhelm Busch was the first physician to observe tumour regression after intentionally infecting a cancer patient with *Streptococcus pyogenes*, the causative agent of erysipelas (*23*). In 1882, similar experiments were performed by the German surgeon Friedrich Fehleisen who inoculated patients suffering from inoperable malignancies with cultures of *S. pyogenes* and remission was observed in some instances (*23*).

The next significant strides in the field were made by the American physician William Coley who administered bacteria to patients in an attempt to leverage the host immune system to target sarcoma in 1891 (*24*). Following fatalities in his first trial caused by *S. pyogenes* infection, he recognised the need to balance therapeutic efficacy with infection control. As such, he developed 'Coley's toxin', a mixture of heat-inactivated *Serratia marcescens* and *S. pyogenes* (*25*). The toxin was administered to over 1000 patients with inoperable bone and soft-tissue sarcomas, resulting in tumour regression and remission in more than 500 cases (*26*). Despite the success and commercialisation of Coley's toxin, use of this approach was met with resistance from physicians due to the lack of a known mechanism of action of the toxin, as well as inconsistent therapeutic outcomes (*27*). As a result, use of the toxins fell out of favour and their disuse was further accelerated by the discovery of x-ray in 1895 and the advent of radiotherapy in 1896 (*28*, *29*). In contrast to Coley's toxins, radiotherapy produced clear and consistent results in the majority of treated patients (*29*).

1.1.2. Renaissance of bacteria-mediated cancer therapy

Although the use of bacteria for cancer therapy declined in the decades following Coley's pioneering work, research in the field has experienced a resurgence. Several genera of bacteria, including *Mycobacterium, Clostridium*, *Listeria, Salmonella* and *Escherichia* have been investigated, with many showing promising results in experimental models and human clinical trials (*30*). In the last half of the 20th century, *Clostridium* were widely studied following evidence of robust colonisation and tumour lysis in a range of tumours using the oncolytic *C. butyricum* M-55 strain (*31–33*). While germination of this obligate anaerobe was confined to hypoxic regions, the production of exotoxins by the colonising bacteria resulted in high mortality rates. To increase safety, the attenuated *C. novyi*-NT strain was developed through the elimination of a residential phage α-toxin, and this strain has been tested in clinical trials (*34*). The first-in-human study using intratumoural injection of *C. novyi*-NT spores reported tumour regression in a patient with

advanced retroperitoneal leiomyosarcoma (*35*). Computed tomography scans showed extensive tumour destruction by the gas pockets formed by C. *novyi*-NT (Figure 1-1). Tumour biopsies revealed extensive tumour necrosis and an absence of viable tumour cells, while anaerobic cultures of the biopsied tissue contained C. *novyi*-NT, signifying the involvement of the bacteria in destruction of the tumour. More recent phase I clinical trials have reported evidence of bacterial colonisation of tumours, including pain and swelling at the tumour site, and systemic signs of infection, such as fever, in a large proportion of patients following either intravenous or intratumoural administration of C. *novyi*-NT spores (*14*). However, treatment with *Clostridium* can fail to eradicate all cancer cells, which leads to relapse (*33*). This might be due to the confinement of *Clostridium* to anaerobic regions making treatment of small tumours or metastases that lack a colonising niche unachievable.

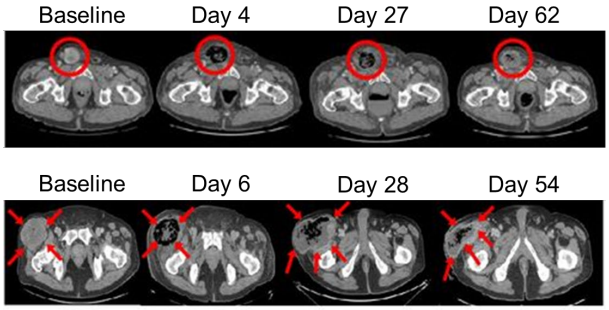

Figure 1-1: Computed tomography scans of patients treated with *C. novyi*-NT. Evidence of necrosis and gas pocket formation was observed. Reproduced from Roberts *et al.* (35).

Obligate aerobes have also been investigated for use in bacteria-mediated cancer therapy. Bacillus Calmette–Guérin (BCG) is an attenuated strain of *Mycobacterium bovis* that was developed as a tuberculosis vaccine. After observations of increased resistance to tumour transplantation in mice infected with BCG, the bacterium was investigated for the treatment of a range of cancers (*36*). Pioneering studies with patients with lymphoblastic leukaemia and malignant melanoma illustrated the potential therapeutic benefit of using BCG for cancer treatment (*37*, *38*). In 1976, an effective BCG administration schedule to treat non-muscle invasive bladder cancer was developed, and adjuvant treatment with BCG became the standard of care for many patients with bladder tumours (*39*, *40*). Treatment with BCG reduces the risk of progression to invasive disease and has been proven to be effective in preventing bladder cancer recurrences (*41*). Following approval by the Food and Drug Administration in 1990, BCG became the first and, to date, only clinically used bacteria-based cancer therapy.

More recently, facultative anaerobes that can adapt their metabolism to grow under a range of oxygen conditions, such as *E. coli* and *Salmonella*, have become the focus of bacteria cancer therapy. Since *Salmonella* can also proliferate in healthy tissues, attenuated tumour-adapted strains, such as *Salmonella enterica* serovar Typhimurium VNP20009, were developed for increased

specificity (*42*). Like BCG and oncolytic *Clostridium* strains, *Salmonella* strains and modified derivatives have been reasonably tolerated by patients in clinical trials (*43–45*). A study using TAPET-CD, a modified VNP20009 strain expressing *E. coli* cytosine deaminase, showed colonisation of target tumours following intratumoural administration (*45*). Additionally, conversion of 5-fluorocytosine to the chemotherapeutic agent 5-fluorouracil (5-FU) was achieved within colonised tumours. This resulted in a 3:1 tumour-to-plasma ratio of 5-FU and demonstrated that expression of substantial amounts of functional enzymes by bacterial colonies in human tumours can be achieved. Surprisingly, however, human trials with *Salmonella* strains have, thus far, not replicated the robust antitumour effects observed in preclinical studies. This discrepancy may be due to differences in intratumoural growth and clearance of bacteria in patients compared to murine models (*43*). Generally, pre-clinical disease models cannot fully recapitulate the heterogeneity of tumours that originate from naturally occurring mutations in patients with diverse genetic backgrounds.

Despite the small number of human trials conducted thus far, important lessons have been learnt that could enable successful translation of more bacterial strains for cancer therapy in future. Firstly, the toxicities observed in experimental animals closely resemble those seen in human patients (*14*). This observation can facilitate the selection of appropriate attenuated strains that are likely to be well tolerated in human patients. Secondly, robust colonisation of tumours is a prerequisite to achieving substantial clinical benefit. This finding has spurred interest in engineering bacteria to express proteins that target tumour cells to increase accumulation, as well as the use of bacteria that are responsive to external cues that can be guided to the tumour site. In addition, future clinical studies may employ diagnostic approaches to identify hypoxia or necrosis which can be used to select patients that are more susceptible to intratumoural bacterial colonisation (*14*).

1.2. Bacteria as living therapeutic agents

1.2.1. Intrinsic bacterial cytotoxicity

Regression resulting from localised bacterial infection can occur through a range of intrinsic antitumour mechanisms that depend on the bacterial strain and specific tumour microenvironment (TME). Intracellular *Salmonella* have been shown to induce cell death through apoptosis (*46*) and autophagy (*47*). In addition, extensive intracellular replication of *Salmonella*

can cause rupture of infected cancer cells (*48*). Infection of cancer cells by *Listeria* gives rise to the formation of highly cytotoxic reactive oxygen species mediated through nicotinamide adenine dinucleotide phosphate (NADP+) oxidase and mobilization of intracellular calcium (*49*). The toxicity of *Clostridium* is conferred by the secretion of various exotoxins by tumour colonising bacteria. Phospholipases and lipases, which are lipolytic enzymes, as well as haemolysin proteins cause damage to integral structural lipids in eukaryotic membranes (*50*, *51*). Other exotoxins, including toxin A and toxin B, are internalized and disrupt critical internal cellular structures and functions (*52*). Although early studies using bacterial therapies were reliant on natural toxicity to treat tumours, attenuated strains have been used more recently to prevent pathogenicity and improve safety.

1.2.2. Immune cell-mediated mechanisms

The intrinsic anticancer effects of bacteria are typically complemented by immune-mediated mechanisms and the dominant mechanism depends on the bacterial species and the specific nature of the tumour. Bacterial infections induce both innate and adaptive immune responses against both tumour cells and tumour-colonising bacteria.

Host immune responses are more critical for the antitumour effects of bacteria that are not sufficiently cytotoxic to tumours, like *Salmonella* (Figure 1-2A). Antigen presenting cells (APCs) are stimulated by recognition of damage-associated molecular patterns (DAMPs) released by infected and dying cancer cells or pathogen-associated molecular patterns (PAMPs), such as lipopolysaccharide (LPS) which is a major component of the outer membrane of Gram-negative bacteria. LPS-induced toll-like receptor (TLR) 4 signalling results in inflammasome activation and secretion of the pro-inflammatory cytokine interleukin (IL)-1β (*53*). Binding of LPS to the co-receptor CD14 also elicits the expression of tumour necrosis factor-alpha (TNF-α), which disrupts the vasculature within the tumour (*54*, *55*).

The bacterial flagellum subunit protein flagellin is also a potent PAMP that stimulates APCs. *Salmonella* flagellin has been found to induce the maturation of APCs by binding and activating TLR5 (*56*), and TLR5 signalling can directly inhibit cancer cell proliferation (*57*). Flagellin administration is also correlated with lower frequencies of $CD4^+$ $CD25^+$ regulatory T cells in the TME (*58*). In addition, flagellin has been found to induce natural killer (NK) cell production of interferon-gamma (IFN-γ) through a pathway involving IL-18 and MyD88 (*59*) and promotes perforin-mediated antitumour responses from NK cells (*60*). *Salmonella* infection can also induce

connexin 43 upregulation which leads to the formation of functional gap junctions between tumour cells and dendritic cells (DCs), promoting the transfer of antigenic peptides (*61*). DCs then present these peptides and activate cytotoxic T cells against tumour associated antigens. Connexin 43 upregulation in tumour cells also lowers the expression of indoleamine 2,3-dioxygenase, an immunosuppressive enzyme (*62*). Decreased indoleamine 2,3-dioxygenase expression combined with tumour antigen cross-presentation by DCs results in highly effective activation of CD8+ T cells.

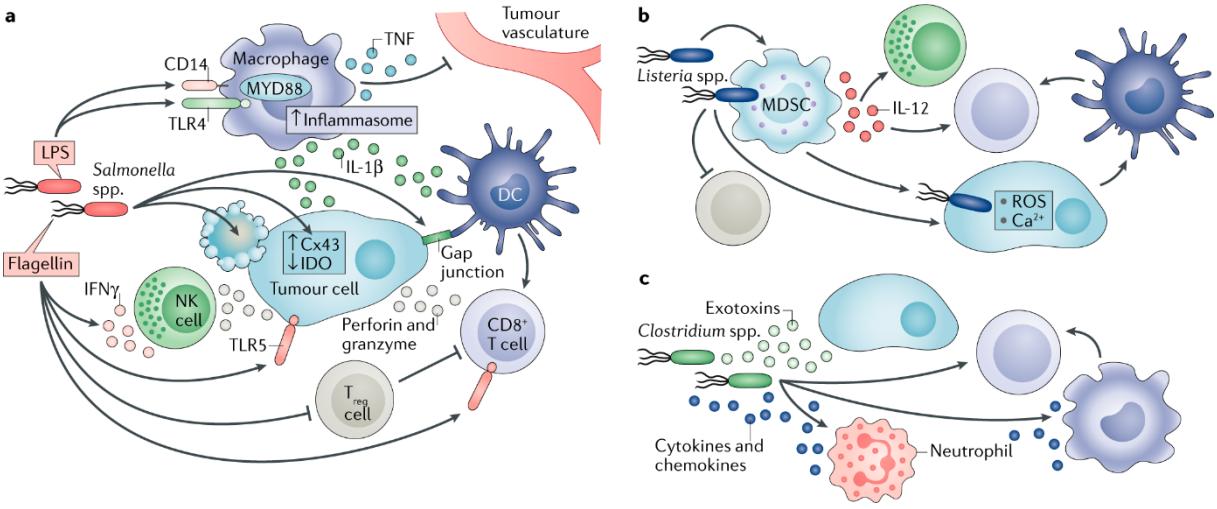

Figure 1-2: Immune cell-mediated cytotoxicity. (A) *Salmonella*, **(B)***Listeria* and **(C)** *Clostridium* have shared and distinct mechanisms to trigger the elimination of cancer. Reproduced from Zhou *et al.* (*14*).

Listeria infection of cancer cells leads to the production of reactive oxygen species, which can initiate immunogenic cell death and activate CD8+ T cells responsible for eliminating both primary tumours and metastases (Figure 1-2B) (*63*). *Listeria* can also infect immunosuppressive myeloid-derived suppressor cells causing depletion of these cells in the tumour, while also inducing phenotypic alterations in surviving cells (*64*). This immunostimulatory phenotype is characterized by elevated IL-12 production, which is associated with improved NK cell and CD8+ T cell antitumour responses.

As with other bacterial infections, expansion of *Clostridium* causes intratumoural infiltration of macrophages and granulocytes, which confines the bacteria to the site of colonisation (Figure 1-2C) (*65*). The recruited cells secrete cytokines and chemokines, including IL-6, granulocyte-colony stimulating factor (G-CSF), and macrophage inflammatory protein-2 (MIP-2) that induce a potent immune response (*66*). *Clostridium* has also been reported to trigger the production of TNF-related apoptosis-inducing ligand from neutrophils, leading to the activation

of apoptosis in cancer cells (67). Over time, secretion of chemokines and recruitment of APCs results in the recruitment of adaptive immune cells, including CD8+ T cells, that assist in eliminating cancer cells (66).

1.2.3. Engineered payload delivery

Bacteria can be engineered with functionalities that localise release of payloads and enhance therapeutic efficacy. Recently, Leventhal *et al.* developed a therapeutic platform based on non-pathogenic *E. coli* Nissle 1917 (EcN) that activated the stimulator of interferon genes (STING) pathway (68). Localized inflammation was triggered by intratumoural production of the STING-agonist cyclic diAMP and reduced tumour growth was observed in melanoma-bearing mice treated with intratumoural injections of EcN. Pioneering work by Pawelek *et al.*, explored the use of various auxotrophs of engineered *Salmonella* as anticancer vectors (69). The engineered bacteria expressed the HSV TK gene that activated the prodrug ganciclovir and suppressed tumour growth. Attenuated *S. Typhimurium* have also been genetically engineered to produce IL-2 (70). IL-2 expressing bacteria colonised tumours for at least 4 weeks *in vivo* and resulted in a significantly lower number of metastases compared to treatment with an attenuated strain without IL-2 expression.

Incorporating inducible elements sensitive to molecular cues is another attractive strategy to potentially localise antitumour effects. Camacho *et al.* engineered *Salmonella* with an inducible autolysis system triggered by anhydrotetracycline that was complemented with aspirin-dependent production of the cytotoxic Cp53 peptide and a sifA mutation that allowed the bacteria to escape vacuoles when internalized by cells (71). The engineered bacteria infected and proliferated in cancer cells, and Cp53 was shown to induce cell death. *E. coli* expressing Trz1, a glucose-sensing receptor, were shown to detect glucose gradients and express green fluorescent protein (GFP) in a microfluidic model of perfused tumour tissue (72). Based on this data, mathematical models predicted treatment of 99.2 % of cells within a tumour using Trz1-activated drug delivery compared to 70.8% with similar systemically delivered drugs.

Induction of payload release in response to local oxygen concentrations is another widely investigated strategy to confine antitumour effects. *S. typhimurium* with a gene encoding the production of the cytotoxic protein haemolysin E under the control of the hypoxia-inducible promoter FF+20* colonised hypoxic tumour regions after systemic administration leading to a reduction in tumour growth and an increase in tumour necrosis (73). In another study.

S. Typhimurium was programmed to solely survive in anaerobic conditions by placing an essential gene, asd, under the regulation of a hypoxia-conditioned promoter (74). *In vivo*, the intravenously administered engineered strain successfully colonised tumours and repressed growth, while undergoing lysis and clearance in normal tissues. Mengesha *et al.* developed a hypoxia-inducible promoter derived from the *Salmonella* pepT promoter (75). Following systemic administration of the bacteria, the reporter gene expression for GFP and RFP was restricted to hypoxic tumours and was approximately 15-fold higher compared to a constitutive promoter. In a study by Anderson *et al.*, environmental cues, including cell density, hypoxia, and inducible inputs, were used to control the internalization of *E. coli* (76). This response was achieved by placing the expression of the invasin gene from *Yersinia pseudotuberculosis* under the regulation of the quorum sensing lux operon, a hypoxia-induced fdhF promoter, or an arabinose-inducible araBAD promoter. This resulted in 8% of added bacteria being recovered following lysis of cancer cells expressing β1-integrins, while levels of bacteria without invasin expression were undetectable.

Another promising strategy is engineering therapeutic response as a function of quorum sensing to enable the bacteria to regulate gene expression in response to the density of the cell population. The bacterial quorum sensing autoinducer-2 signalling pathway of *E. coli* was utilized to enable programmed motility, sensing and payload delivery based on the density of epidermal growth factor receptor (77). *In vitro*, the engineered bacteria had the ability to survey surfaces to distinguish between diseased and healthy cells and initiated DsRed gene expression in response. EcN has also been engineered to produce and release nanobodies targeting programmed cell death–ligand 1 (PD-L1) and cytotoxic T lymphocyte–associated protein-4 (CTLA-4) intratumourally once a quorum was reached (Figure 1-3A) (78). Compared to clinically relevant antibodies, a single dose of intratumourally injected engineered bacteria resulted in an increase in activated T cells, tumour regression, as well as an abscopal effect. Using similar intratumoural quorum lysis, a non-pathogenic *E. coli* strain

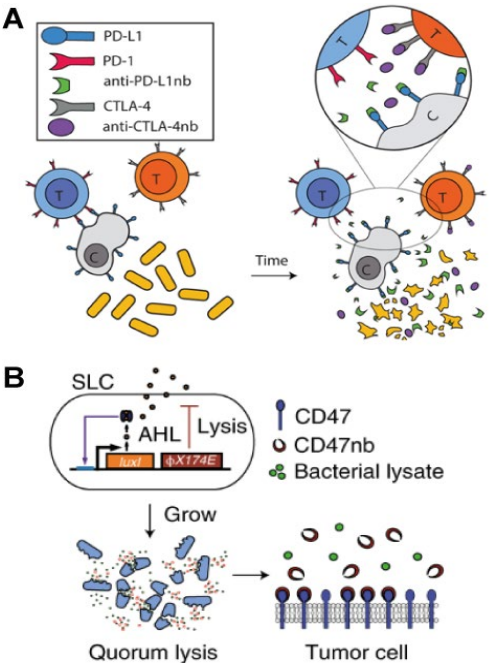

Figure 1-3: Quorum sensing-based payload release. (A) EcN engineered to release PD-L1 and CTLA-A nanobodies. Reproduced from Gurbatri *et al.* (78). **(B)** Engineered *E. coli* for controlled production and release of nanobodies through intratumoral quorum lysis. Reproduced from Chowdhury *et al.* (79).

was engineered to lyse and release a nanobody antagonist of CD47, a frequently overexpressed anti-phagocytic receptor, within the tumour (Figure 1-3B) (*79*). Delivery of the nanobody by intratumoural and intravenous administered bacteria increased tumour-infiltrating T cell activation and induced tumour regression. Harimoto *et al.* presented a bacteria-in-spheroid co-culture platform to screen *S. typhimurium* strains engineered with a variety of synthetic gene circuits for the expression of a range of antitumour therapeutics triggered once a critical density of bacteria was reached (*80*). Candidates displaying significant therapeutic efficacy in the bacteria-in-spheroid co-culture platform, such as azurin, theta-toxin, and haemolysin E, were shown to have similar efficacy *in vivo*.

1.2.4. Bacteria as cargo-carriers

The innate ability of bacteria to accumulate in the uniquely hypoxic regions of tumours can be leveraged for the localised delivery of therapeutics by cargo-carrying bacteria. The high-affinity interaction between biotin and streptavidin has been widely used to attach nanocarriers onto bacterial membranes for targeted drug delivery. Nguyen *et al.* developed a cargo-carrying system using *S.* Typhimurium and paclitaxel-loaded micro-liposomes. The bacteria-liposome complexes were shown to selectively reduce the viability of cancer cells *in vitro* (*81*). Park *et al.* attached polystyrene carboxylated microbeads onto attenuated *S.* typhimurium and investigated the potential use of this system as a theranostic tool (*82*). Chemotaxis-driven migration speeds of ~30 μm/min were observed for the complexes when exposed to cancer cell lysates or in co-culture with spheroids, while their velocity only reached ~5 μm/min in the presence of non-cancerous cells. Suh *et al.* developed a biohybrid autonomous drug delivery platform composed of polylactic-co-glycolic acid nanoparticles conjugated to an attenuated auxotrophic mutant of *S.* Typhimurium (*83*). Intercellular transmigration was determined to be the dominant mode of transport through tumour masses and the conjugates achieved significantly higher tumour penetration *in vivo* compared to nanoparticles alone.

An alternative conjugation approach was investigated by Quispe-Tintaya *et al.* (*84*). The radioisotope ^{188}Rhenium was conjugated to live attenuated *L. monocytogenes* via strain-specific antibodies. Mice with metastatic pancreatic tumours were injected intraperitoneally and bacterial proliferation was restricted to metastatic sites. Daily low dose injections for sustained delivery of radiotherapy resulted in a 90% reduction of the number of metastases compared to 50% for

L. monocytogenes alone. The measured radioactivity level in the liver and kidneys was below the limit of detection by day 7.

Therapeutic cargos have also been integrated with bacteria that are innately responsive to external cues for enhanced delivery. Taherkhani *et al.* investigated the potential of the magnetotactic bacteria (MTB) strain *Magnetococcus marinus* MC-1, as a drug carrier (Figure 1-4A) (*85*). MTB-liposome conjugates were synthesized via carbodiimide coupling by utilizing the primary amine groups on the cell membrane of the Gram-negative bacteria. The same system was employed *in vivo* to target the hypoxic core of tumours under directing magnetic fields (DMF) (*86*). Another strain of MTB, *Magnetospirillum magneticum* AMB-1, was also employed as a magnetically controllable motile carrier. Here, integrated indocyanine green nanoparticles rendered this bacteria-based platform capable of both imaging and photothermal therapy (Figure 1-4B) (*87*). Peritumoural injection of the bacteria was followed by guidance using magnetic field gradients. Photothermal therapy using near infrared (NIR) irradiation inhibited tumour growth and no significant changes in biochemical parameters associated with liver and kidney function were observed, implying acceptable safety levels. In addition to chemically conjugated payloads, doxorubicin-internalized MTB have also been investigated (*88*). Internalisation was facilitated by chelation of doxorubicin with Fe^{3+} and drug-loaded *Magnetosopirillum gryphiswalense* MSR-1 maintained their motility for 3 hr. *In vivo*, this motile platform was characterized with better targeting and improved suppression of tumour growth compared to inactivated bacteria and free doxorubicin.

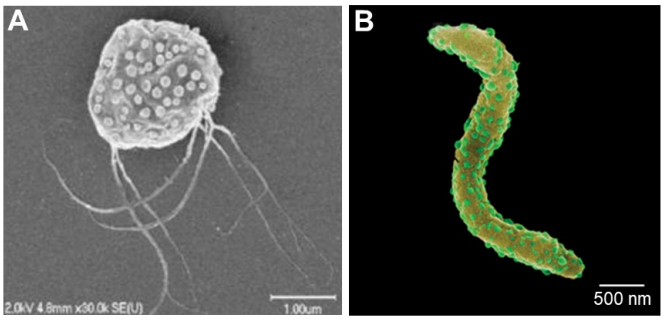

Figure 1-4: MTB with covalently coupled therapeutic cargo. **(A)** Scanning electron microscope image of nanoliposomes conjugated to MC-1. Reproduced from Taherkhani *et al.* (*85*). **(B)** Scanning electron microscope image of indocyanine green nanoparticles coupled to AMB-1. Reproduced from Xing *et al.* (*87*).

1.3. Bacterial tumour homing mechanisms

1.3.1. Bacterial navigation

Bacteria are equipped with onboard sensing and motility, allowing them to serve as intelligent anticancer agents that are capable of migrating to and infiltrating tumours. Targeted swimming

towards environments that favour bacterial growth, known as taxis, requires highly organized coordination between the sensory system and flagellar motor (*89*, *90*). This is achieved through a two-component regulatory system composed of sensors and response regulators (*91*, *92*). Signal transduction linking these two components only leads to a beneficial behavioural response when it is able to sense spatial variations of relevant compounds. Due to the small size of a single bacterium (on the order of 1 μm), random swimming over large distances is necessary for sampling the surrounding environment and detecting gradients (*89*, *92*). This continuous explorative cycle of sense and move is manifested in different forms, such as the run and tumble motion in *E. coli* (*93*), or the forward, reverse, and flick pattern in *Vibrio alginolyticus* (*94*, *95*).

The taxis behaviour of bacteria can be grouped into two categories: classical chemotaxis, where response is only dependent on the presence of chemical stimuli, and energy-taxis, such as aerotaxis and phototaxis, where cellular metabolism of the stimuli combined with the energy level regulate swimming behaviour (*96*). While membrane-spanning chemoreceptors, known as methyl-accepting chemotaxis proteins, bind to specific attractant or repellent chemoeffectors, energy transducer proteins interact with the electron transport system to sense energy levels. The transduction pathways of bacterial taxes converge further down the signalling network where, for example, in *E. coli* the phosphorylated CheY protein interacts with the flagellar motor to switch the direction of rotation of the motor (*92*, *96*). Although a general understanding of the signal transduction pathway has been elucidated from studying *E. coli* and *Salmonella*, sensory systems with higher complexity featuring more diverse receptors have been identified in other genera (*89*, *90*).

Due to the viscous-dominated low Reynolds flow regime experienced by these microorganisms, they have evolved to rely on molecularly-driven rotation of helical flagella for propulsion (*97*, *98*). These slender organelles are efficient at converting rotational motion into translational displacement by generating drag-induced thrust (*99*, *100*). Molecular motors are powered by electrochemical gradients of protons or sodium ions to rotate the flagella at frequencies of up to 300 Hz (for H^+) and 1300 Hz (for Na^+) (*101*), leading to swimming velocities in the range of tens and hundreds of microns per second respectively. Depending on the species and configuration of flagella, different strategies have been observed for changing direction in fluids and more complex media such as mucus and biofilms (*89*, *102*).

1.3.2. Taxis-guided mechanisms for tumour homing

Despite decades of experimental use of bacteria for cancer therapy, the first study of bacterial tumour homing was only conducted in 1955 by Malmgren and Flanigan (*103*). Their study showed that *Clostridium* was exclusively localised to tumours following intravenous injection. Tumour colonisation of this anaerobe was also observed in rat models, with healthy tissues only containing bacterial ungerminated spores (*104*). Similarly, *Bifidobacterium*, another anaerobic bacterium, demonstrated selective tumour localization following systemic administration into mouse tumour models (*105*).

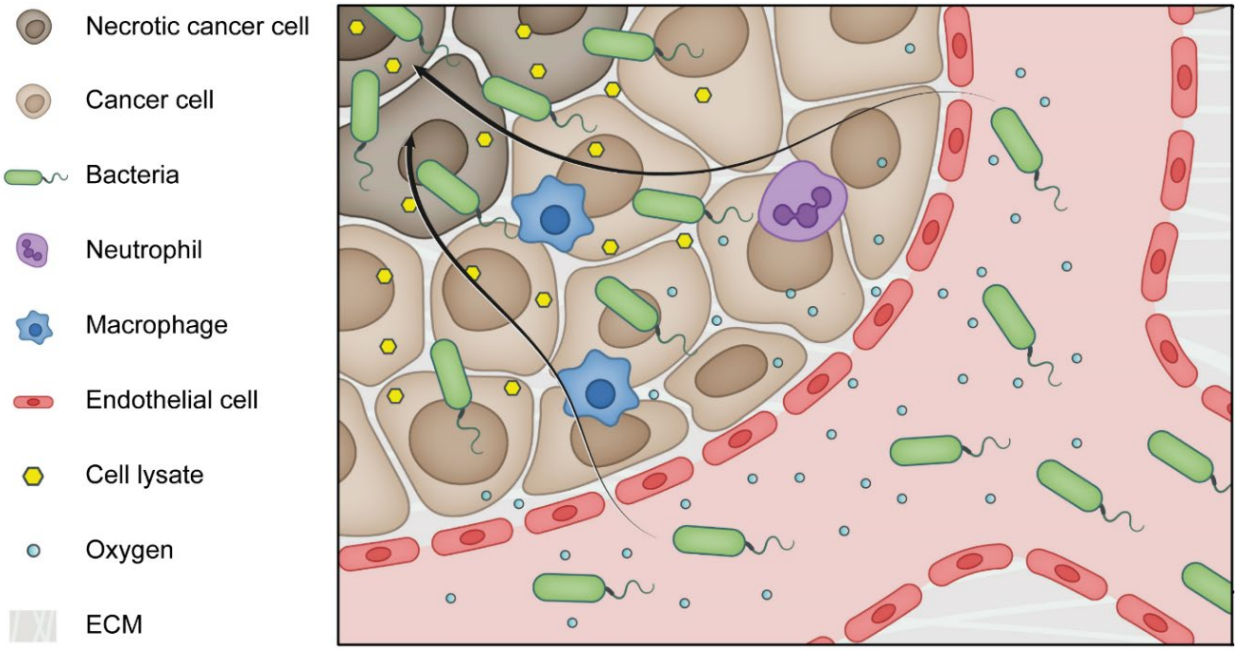

Figure 1-5: Bacterial tumour homing. Low oxygen levels, the presence of nutrients and low immune cell density are factors that contribute to preferential accumulation in tumours.

Many solid tumours are characterized by the presence of a necrotic core and hypoxia in distant regions from immature blood vessels (*106*, *107*). Therefore, low oxygen levels are considered the main driver for aerotactic migration, followed by sustained germination and colonisation of obligate anaerobes (*108*). Interestingly, when the obligate anaerobe *C. novyi-NT* was injected into mice bearing poorly vascularized, hypoxic, non-neoplastic tissues, no bacterial colonisation was observed. This was consistent with a later finding in a rat ischemic brain model (*109*). These studies highlight the role of the unique biochemical composition of the TME in the infiltration and proliferation of obligate anaerobes in solid tumours (*110*).

Other mechanisms have been proposed for tumour homing of facultative anaerobes that can survive and grow under the normal oxygen concentrations present in healthy tissues (*111*). Aspartate receptors have been shown to play a key role in the chemotaxis-driven tumour targeting of *S. typhimurium* (*112*). Serine receptors are involved at the start of infiltration, while directed penetration towards a necrotic core is achieved through ribose/galactose receptors. Although Salmonella can grow in both hypoxic and oxygenated environments, they have been shown to preferentially proliferate in tumours at a ratio of 10,000:1, compared to healthy tissue (*113*). Moreover, the correlation between both homing and intratumoural growth of bacteria with the size of the tumour highlights the key role of hypoxic, viable cells in chemotaxis (*114*).

While the above-mentioned anaerobes display a range of responses to oxygen levels, other unique features of the TME facilitate tumour homing and colonisation of all classes of bacteria (Figure 1-5). The development of hypoxia, the release of bacterial nutrients and the immune-suppressive environment in solid tumours are all a result of irregular, leaky tumour vasculature (*115*). Passive entrapment of bacteria in tumour vasculature and infiltration through endothelial gaps, which could be accelerated by TNF-α (*116*), is thought to contribute to the tumour tropism of bacteria (*117*, *118*). The role of the immune system in the homing of both obligate and facultative anaerobic strains is multifaceted. For instance, *Listeria* are trafficked to tumour sites by infecting myeloid-derived suppressor cells that infiltrate the tumour and inhibit the effector function of various leukocytes (*64*). Tumour targeting bacteria take advantage of the immunosuppressed nature of the TME, particularly in the necrotic core, to evade clearance (*119*). The targeting and preferential replication of aerobic strains in tumours underpins the critical role of defective immunosurveillance, compared to the influence of hypoxia (*119*, *120*). While immune cells limit the presence of bacteria to necrotic regions, the well perfused rim of colonised tumours were shown to still be eliminated through immune-mediated responses in immunocompetent mice (*121*).

Targeted colonisation of the tumour is the basis of almost all bacterial cancer therapies, but this process is contingent upon the homing and achievement of adequate accumulation. Accumulation is reliant on administration of a minimum amount of bacteria and the presence of a necrotic core, which is correlated with the developmental stage of the tumour (*122*). Both Gram-negative and Gram-positive bacteria, regardless of their oxygen requirements and pathogenicity, have been shown to colonise syngeneic and xenograft tumours in immunocompromised and immunocompetent mice (*119*). A further, comprehensive

understanding of the necessary conditions for tumour colonisation has been the subject of various studies (*119*, *120*, *122*).

1.4. Enhanced tumour targeting

1.4.1. Targeting moieties for enhanced tumour accumulation

Tumour-targeting bacteria are appealing living therapeutics because of their capacity to autonomously navigate through the body, transport a wide range of payloads, and modulate intratumoural inflammatory responses (*16–19*). Nevertheless, translation of this approach has been hindered by incomplete clinical responses, in part due to insufficient tumour colonisation (*14*). Developing strategies to enhance accumulation of bacteria within tumours is essential to facilitate robust colonisation and increase therapeutic efficacy.

Synthetic biology has been exploited to improve the targeting of bacteria to tumours. The expression of tumour homing peptides on the cell membrane of bacteria has been shown to be effective in enhancing tumour localization. Piñero-Lambea *et al.* programmed *E. coli* to express synthetic adhesins composed of a high affinity, surface-exposed immunoglobulin domain and a stable β-domain embedded in the outer membrane (*123*). Systemically administered bacteria more efficiently colonised solid tumours expressing the target molecule compared with wild-type *E. coli*, with lower retention in healthy organs such as the liver and spleen. In addition, the immunoglobin domains can be selected from large repertoires, enabling the rational design of the adhesion properties of *E. coli* for targeted delivery in a variety of tumours.

Massa *et al.* also demonstrated significantly improved tumour homing of systemically injected *Salmonella* with a surface-expressed antibody directed to CD20 (*124*). A 5.2-fold higher infection rate of CD20+ lymphoma cells was achieved through antibody-dependent bacterial targeting *in vivo*, with significantly diminished nonspecific cell invasion in organs such as the liver and spleen. Preferential homing to αvβ3-overexpressing tumour xenografts using an engineered Arg-Gly-Asp (RGD)-displaying *Salmonella* strain has also been demonstrated in *in vivo* studies. This resulted in significant inhibition of tumour growth and prolonged survival of mice, with 80% surviving up to 160 days after tumour inoculation. Bereta *et al.* engineered an attenuated *Salmonella* derivative expressing carcinoembryonic antigen-specific antibody fragments on the cell surface (*125*). Treatment with a single dose of systemically injected engineered bacteria resulted

in accumulation of bacteria in carcinoembryonic antigen-expressing tumours, inhibition of tumour growth, as well as local accumulation of CD3+ T cells and CD11b+ macrophages.

1.4.2. External control of bacteria for increased tumour targeting

External stimuli can also serve to improve selective targeting of cell-based therapeutics (Figure 1-6) (*126*, *127*). Responsiveness to internal stimuli, mainly in the form of chemotaxis and aerotaxis, enables bacteria to act autonomously, but at the cost of a relatively slow response time (*128*, *129*). Conversely, external control confers dual-targeting functionality to cellular agents that are already equipped with intrinsic homing mechanisms. This added specificity can lead to higher safety levels because the same efficacy could possibly be achieved at lower dosages.

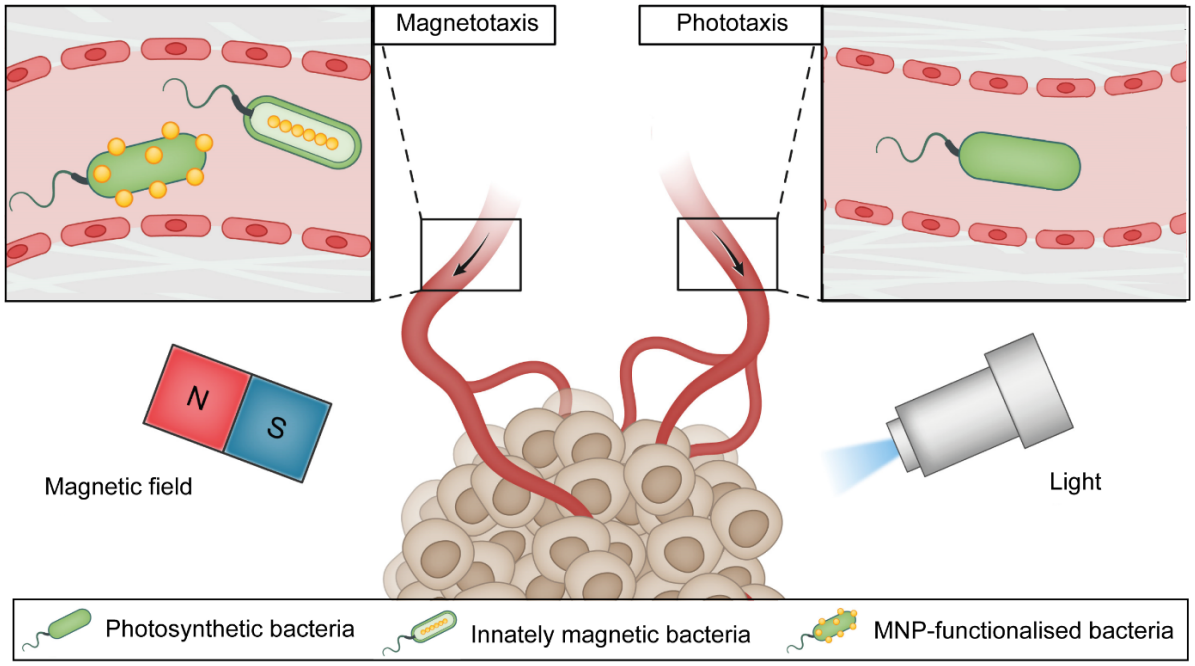

Figure 1-6: External targeting of bacteria. Enhanced tumour homing in response to external physical cues.

Phototaxis has been used to control active migration of bacteria in response to varied light intensity (*130*). Enhanced infiltration of NIR irradiated multicellular spheroids was shown using the photosynthetic bacterium *Rhodobacter johrii* (*131*). In addition, increased accumulation in hypoxic regions was observed in NIR irradiated tumours following peritumoural injection of the bacteria. Although spatial control was achieved by light-induced migration, the application of this approach is restricted to superficial tumours given the limited penetration depth of light in the body (*132*).

Among all physical stimuli, the use of magnetic energy has gained the most interest. The human body is fully penetrable to magnetic fields, which allows magnetically responsive agents to target deep-seated organs. Non-magnetic strains can be rendered magnetic through the integration of magnetic nano/microparticles with the bacteria. Magnetic particles conjugated onto the surface of bacteria like *E. coli* (*133*, *134*) and *S. marcescens* (*135*) enabled them to align with magnetic fields, although with lower swimming velocities than unmodified bacteria. Microswimmers generated by attaching several *E. coli* to multilayer microparticles loaded with doxorubicin and magnetite were demonstrated to have mean swimming speeds of up to 22.5 μm/s and to deliver doxorubicin in 4T1 breast cancer cells *in vitro* under a chemoattractant gradient and a magnetic field (*133*). Similar microswimmers composed of multiple *S. marcescens* bacteria attached to a superparamagnetic bead were shown to have mean swim speeds of up to 7.3 μm/s and were able to be steered along 2D trajectories using low magnetic field amplitudes (≤10 mT) (*135*). Additionally, through genetically engineered expression of the iron-storage protein ferritin, *E. coli* has been rendered responsive to magnetic fields (*136*, *137*).

Magnetotactic bacteria (MTB), a group of bacteria that biomineralize membrane-bound iron-rich nanocrystals called magnetosomes, have strongly contributed to the interest of using externally applied magnetic field for control of bacteria (*138*, *139*). Chains of magnetosomes serve as compass needles for MTB, helping them to navigate along the Earth's magnetic field while swimming toward the oxic–anoxic interface, a behaviour known as magnetoaerotaxis (*140–142*). The idea of using MTB as trackable medical microrobots was proposed over a decade ago (*143–145*) and since then different strains of MTB, such as *M. marinus* MC-1 (*86*), *M. magneticum* AMB-1 (*87*), and *M. gryphiswaldense* MSR-1 (*88*) have been studied *in vivo* for drug delivery into tumours. Following peritumoural injection in mice bearing flank tumours, approximately 55% of the MC-1 exposed to DMF accumulated in hypoxic regions of the tumour (*86*), and almost two-fold higher tumour infiltration was shown for magnetically assisted AMB-1 (*87*).

In terms of navigation strategies, most studies have utilized force-based field gradients (*87*, *88*) or DMF (*86*, *145*, *146*). Static fields alone are unable to focus magnetic agents at an interior point to create stable traps, as demonstrated by Earnshaw's theorem (*147*). This, together with the rapid decay of magnetic forces resulting from field gradients, limit the application of static fields to shallow targets. While promising outcomes have been demonstrated in small animal models, very

high fields are required to achieve the same forces at larger scales. The issue of scalability can partly be circumvented by using relatively low amplitude DMF to align the bacteria in the specified direction. However, success of this guiding strategy is bounded by self-propulsion forces which may not be sufficient to overcome robust physiological barriers. In addition, DMF inherently relies on positional information with respect to the target site. Hence, this control strategy is unsuitable for systemic injection because this would result in dispersed distributions of the bacteria within the body. Instead, peritumoural administration is required for DMF control, which limits the use of DMF to easily accessible tumours. Although more sophisticated control schemes, such as point-to-point closed-loop control (*148*, *149*) or the use of a virtual magnetic monopole (*150*, *151*) have been proposed for MTB guidance, none have been implemented *in vivo* to date.

The use of rotating magnetic fields (RMF) has recently emerged as an attractive actuation strategy. RMF can be generated at clinically relevant scales to control systemically dispersed bacteria, independent of position feedback. MTB exposed to RMF have been used to generate volumetric flows for local fluid convection to enhance the transport of nonmagnetic nanoparticles across collagen matrices (*152*, *153*). The time-varying character of RMF also presents the opportunity for simultaneous control and detection, enabling the adjustment of actuation parameters during operation for improved localization and infiltration. In addition, inspired by the superimposed magnetostatic fields employed in magnetic particle imaging, spatially selective actuation of MTB using RMF has also been proposed (149). These unique advantages make RMF a promising actuation strategy for wirelessly controlled transport of magnetically responsive bacteria.

1.5. Structure of the thesis

This chapter has covered the history and recent developments in bacteria-mediated cancer therapy and presented some of the current challenges in the field. Subsequent chapters explore the use of MTB for targeted cancer therapy, first by assessing the response from immune cells and then by studying their use as a therapeutic agent that can effectively traverse cellular barriers when aided by external rotating magnetic fields (Figure 1-7).

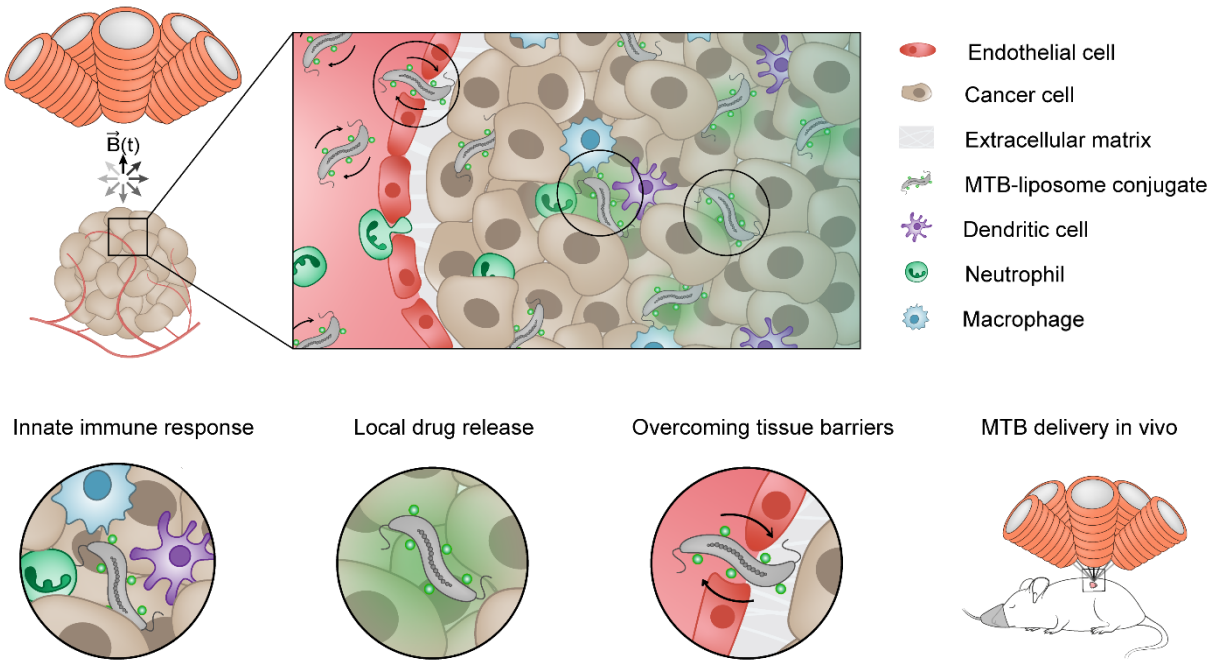

Figure 1-7: Thesis overview. This thesis explores the ability of MTB to act as a living immunotherapeutic agent that effectively crosses robust cellular barriers when aided by external rotating magnetic fields.

Chapter 2 assesses the response of human innate immune cells following stimulation with MTB. The proliferation of MTB under physiological conditions and clearance from whole human blood are first investigated. Neutrophil migration and cytokine production by macrophages in response to stimulation with MTB are then characterised. Lastly, the ability of MTB to induce maturation in monocyte-derived dendritic cells and increase the uptake of cancer cell material are assessed in a co-culture system.

Having investigated the suitability of the MTB strain AMB-1 for use in physiological environments, **Chapter 3** investigates the use of MTB-LP as drug delivery agents. Two coupling reactions to generate MTB-LP using liposomes functionalised with either carboxyl or azide groups are compared. The use of MTB-LP for effective delivery of 5-fluorouracil, a widely used

antimetabolite, is investigated by assessing the effect of MTB-LP on cell proliferation and the induction of apoptosis.

Chapter 4 establishes a hybrid control strategy that harnesses magnetic torque-driven motion followed by autonomous taxis-based locomotion for enhanced infiltration of MTB-LP across robust cellular barriers. The actuation strategy employed in these studies utilizes RMFs that can be generated at clinical scales and further advantages of this control scheme, such as simultaneous inductive detection and spatially localised actuation, are presented. Translocation of MTB-LP across endothelial monolayers is examined and increased cell surface exploration resulting from translational motion is explored as a possible transport mechanism. The spatiotemporal characteristics of magnetically driven MTB-LP infiltration in a 3D tumour model are evaluated. Finally, the accumulation of systemically administered MTB following exposure to RMF is studied *in vivo*.

Chapter 5 provides a summary of the key results of this thesis, highlighting findings that may support efforts to further characterise the MTB-LP platform for cancer therapy. It also discusses some of the challenges and considerations for successful clinical translation of bacteria-based cancer therapeutics.

2. Immunostimulatory Properties of Magnetotactic Bacteria

Portions of the introduction of this chapter are adapted from the manuscript "Engineering Cell-Based Systems for Smart Cancer Therapy" by Nima Mirkhani (co-first author), Tinotenda Gwisai (co-first author) and Simone Schuerle published in Advanced Intelligent Systems (2022).

2.1. Introduction

Disease outcomes are heavily influenced by the complex interplay between cancer cells, soluble factors within the TME and the presence of various immune cells. A variety of innate and adaptive immune subpopulations are known to migrate toward the tumour niche to mount a protumour or antitumour response. Neutrophils are among the first cells recruited to sites of inflammation, where they phagocytose pathogens and release cytokines to recruit other leukocytes (*154*, *155*). While high levels of tumour-associated neutrophils have been associated with protumoural effects and a poor prognosis, they have also been shown to display functional heterogeneity which can support antitumoural responses (*156*). Neutrophils have been shown to form barriers around *E. coli* colonies in necrotic regions of tumours, which inhibits colonization of viable tumour tissue and can result in incomplete tumour eradication (*157*). Conversely, *C. butyricum* MIYAIRI 588 was shown to induce the secretion of TRAIL from neutrophils, which resulted in the induction of cancer cell apoptosis (*158*).

Unlike neutrophils, macrophages are largely tissue resident. They differentiate from circulating monocytes after extravasation and patrol peripheral tissues for invading pathogens, cell debris, and cancer cells. Monocytes migrate towards tumours in response to a variety of chemoattractant signals, including colony-stimulating factor 1 (CSF1) (*159*), chemokine ligand (CCL) 5 (*160*), and possibly CCL2, although its role in cancer is under debate (*161–163*). Macrophages are often categorized as either proinflammatory (M1 polarization), playing a role in the elimination of immunogenic cancer cells during carcinogenesis, or anti-inflammatory (M2 polarization) where their secretion of immunosuppressive cytokines, promotion of cancer cell proliferation and stimulation of angiogenesis is protumourigenic (*164*, *165*). While the M1/M2 model has proved useful, transcriptomic analysis indicates that this paradigm is oversimplified and instead suggests that a spectrum of tumour associated macrophages exist (*166*).

DCs, like macrophages, are located in almost every tissue in the body and survey peripheral tissue for pathogens (*167*). DCs are specialized APCs that play a crucial role in the priming and

establishment of the antitumour adaptive immune response. DCs phagocytose and process tumour-derived material stemming from damaged and dying cancer cells. DAMPs released from the cells are identified by pattern-recognition receptors and can induce DC maturation. Mature DCs migrate to lymph nodes where they prime CD8+ and CD4+ T cells through antigen presentation on major histocompatibility complex class I and II molecules with appropriate co-stimulation. Activated T cells enter circulation from the lymphatic system, extravasate and migrate to the tumour site where they exert an antitumoural response. CD8+ T cells eliminate cancer cells through the production of granules containing perforin and granzyme B (*168*, *169*). CD4+ T helper 1 cells orchestrate an antitumoural response through the secretion of proinflammatory cytokines, such as IL-2 and IFN-γ, which promote CD8+ T cell cytotoxicity and antitumour responses in macrophages (*170*).

Many tumours develop methods to avoid immune recognition, including decreased expression of MHC class I molecules and the production of cytokines that inhibit DC activation, such as IL-10 (*171*). Bacteria can be used to overcome some of these immunosuppressive mechanisms. PAMPs, such as LPS, are recognized by DCs and other innate immune cells and this can induce the production of various proinflammatory cytokines (*172*). Although bacteria-mediated cancer therapy has proven to be effective in triggering tumour elimination, translation of this approach has been stalled by incomplete clinical responses, due in part to insufficient tumour colonisation. Recently, it has been suggested that MTB could be leveraged as a therapeutic agent that can be aided by external magnetic guidance to form robust colonies in tumours (*87*, *173*).

To employ MTB for cancer therapy, it is imperative to characterize their behaviour in physiological environments, as well as their immunostimulatory properties. The survival and magnetic properties of the MTB strain *Magnetospirillum magneticum* AMB-1 were studied under mammalian culture conditions. Next, some key properties of human innate immune cells in response to stimulation with MTB were assessed. MTB clearance from whole blood, neutrophil migration towards MTB and cytokine production by THP-1 derived macrophages were studied. The ability of MTB to induce maturation of monocyte-derived dendritic cells (moDCs) and increase the uptake of cancer cell material in a co-culture assay was then investigated. Lastly, a microfluidic platform to study interactions between immune cells and bacteria was established. This study lays the foundation for further characterisation of the efficacy of MTB for immune-mediated cancer therapy.

2.2. Results

Experiments were designed and executed by Tinotenda Gwisai, unless otherwise specified. Experiments presented in Figure 2-1 were performed with assistance from Mira Jacobs, and experiments in 2.2.6 were performed with assistance from Mira Jacobs and Simone Hersberger. Dr. Matej Vizovisek provided support for the design and execution of experiments in section 2.2.3. Experiments in sections 2.2.2, 2.2.4 and 2.2.5 were performed with assistance from Sina Günther. Nima Mirkhani designed and fabricated masters for the microfluidic devices.

2.2.1. MTB proliferate under physiological conditions and remain viable in blood

Since MTB are aquatic bacteria, their ability to proliferate under physiological conditions was first studied. In addition to standard MTB culture conditions of 30 °C in magnetic spirillum growth medium (MSGM), five other conditions were investigated where the type of media, the temperature, or the oxygen concentration was modified. Optical density (OD) was measured over 10 days of incubation and the corresponding bacterial concentrations were computed.

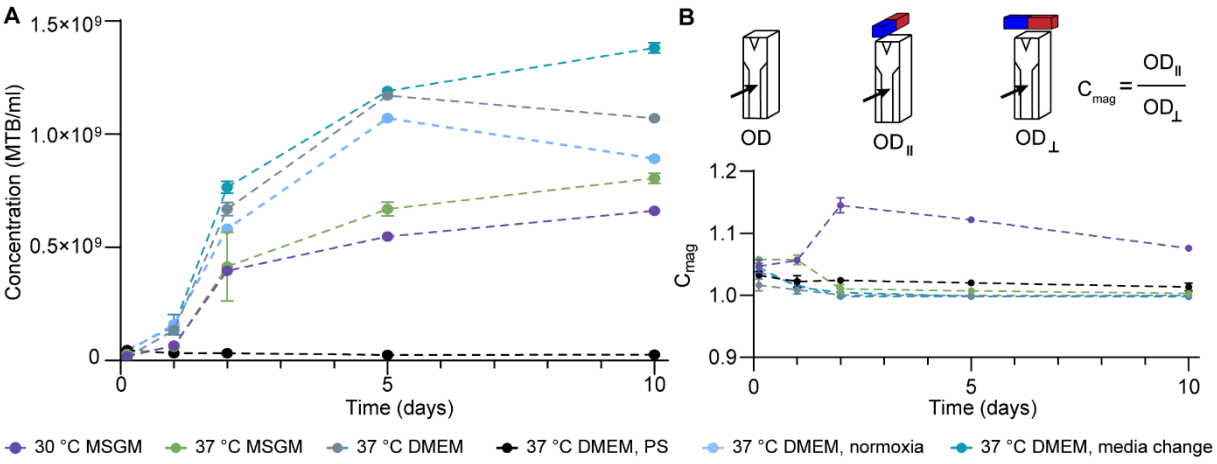

Figure 2-1: MTB proliferation and magnetic responsiveness under varying culture conditions. **(A)** Bacterial proliferation under different culture conditions over 10 days. OD was measured after 0.125, 1, 2, 5 and 10 days of incubation and used to compute bacterial concentrations (n = 3; mean ± SD). **(B)** Schematic illustrating OD and C_{mag} measurements. Magnetic responsiveness of bacterial populations, as indicated by C_{mag} values, cultured under different conditions over 10 days (n = 3; mean ± SD).

After 10 days of culture, differences in the colour of the media, as well as the colour and size of the bacterial pellets were observed (Figure S2-1). The pellets of samples cultured in the mammalian culture media Dulbecco's Modified Eagle Medium (DMEM) were paler and larger than those cultured in MSGM. Bacterial proliferation was observed in all conditions, except for

samples cultured in media supplemented with penicillin-streptomycin (37 °C DMEM, PS) (Figure 2-1A). Samples exhibited the typical characteristics of MTB proliferation, where exponential growth in the first 2 days was followed by a stationary phase. Samples cultured at 37 °C had higher MTB concentrations than cultures at 30 °C, and samples cultured in DMEM had consistently higher concentrations than cultures in MSGM. The highest concentration of 1.4×10^9 MTB/mL was observed in DMEM with a media change, where nutrients were replenished after 5 days.

A unique characteristic of MTB is their ability to biomineralize iron oxide nanoparticles that render them magnetically responsive. C_{mag} values were used to assess the magnetic properties of bacteria cultured under different conditions (Figure 2-1B). C_{mag} is the ratio of light absorbance measurements when a magnet is placed parallel and then perpendicular to the light path, with values above 1 indicating the presence of magnetic material with geometric anisotropy in the suspension. MTB cultured under standard conditions (30 °C MSGM) consistently had C_{mag} values above 1 with a peak after 2 days in culture, indicating a magnetically responsive population. All other samples, which were cultured at 37 °C, had C_{mag} values of approximately 1 by day 2, indicating that the bacterial suspensions were no longer magnetically responsive. Overall, these findings suggest that while MTB have higher rates of proliferation at 37 °C, biomineralization is impaired at this temperature.

To work towards the use of MTB for cancer therapy applications *in vivo*, a whole blood assay was performed to track bacterial viability over time following exposure to functional host bactericidal factors (Figure 2-2). This study can be used to gain insights into the amount of time that MTB might remain in circulation, which will facilitate

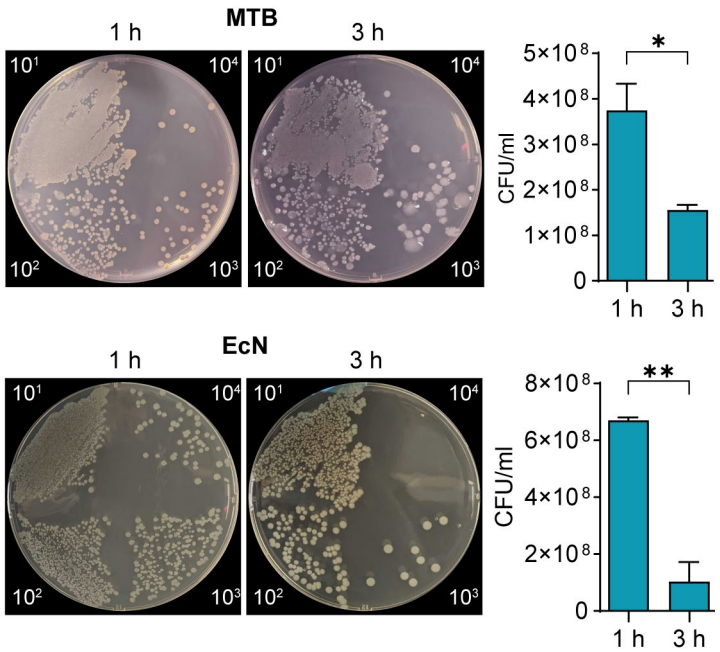

Figure 2-2: Assessing MTB viability in blood. Representative images of MTB and EcN grown on agar plates following 1 h and 3 h exposure to human whole blood. Samples were serially diluted and the number of viable bacteria was quantified. ($n \geq 2$ donors; mean ± SD; $^*P < 0.05$ and $^{**}P < 0.01$, Student's t-test).

the selection of an appropriate duration for magnetic actuation. Live *E. coli* Nissle 1917 (EcN), a gram-negative strain frequently utilised for bacteria cancer therapy, was used for comparison. After 1 h incubation, high amounts of bacteria were present in all samples, while decreased concentrations were observed after 3 hours of incubation. The amount of viable MTB decreased 2.4-fold, while EcN levels dropped sharply by over 6.5-fold. These findings suggest that an actuation window of up to 3 h can be used for *in vivo* experiments, as viable MTB may still be in circulation.

2.2.2. MTB induce moderate neutrophil migration

Having established that MTB remain viable in whole blood and proliferate under physiological conditions, responses from relevant immune cells were investigated. Neutrophils are among the first cells recruited to sites of bacterial infection where they assist in modulating an immune response. However, extensive neutrophil recruitment and expansion may inhibit tumour colonization (*157*). To assess the potential extent of neutrophil recruitment in response to MTB, neutrophil migration was investigated using a Transwell assay. Migration towards EcN, a well-characterised, probiotic strain that is widely studied for bacterial cancer therapy, was used for comparison (*174*) (Figure 2-3A).

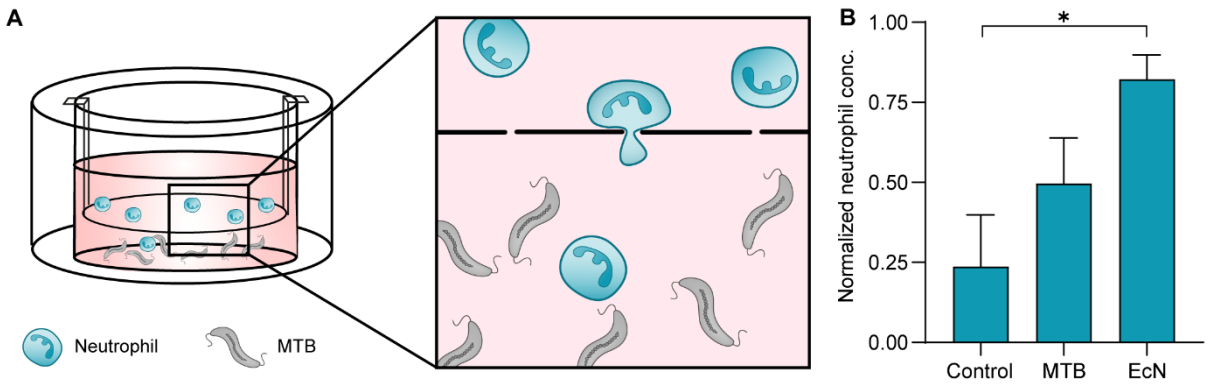

Figure 2-3: Assessing primary human neutrophil migration towards MTB. (A) Schematic representation of Transwell assay used to study neutrophil migration towards bacteria. **(B)** Comparison of normalized basolateral neutrophil concentrations following 2 h incubation in media only (control), MTB or EcN. Neutrophil concentration was normalized to concentrations resulting from directed migration along an fMLP gradient for each donor ($n \geq 2$ donors; mean ± SD; $^*P < 0.05$, ANOVA).

Transwell membranes were coated with fibronectin to facilitate cell adhesion. After 2 h incubation, neutrophils in the basolateral compartment were collected and quantified. To account for variations in donor-specific neutrophil migration capacity, directed migration along a formyl-methionyl-leucyl-phenylalanine (fMLP) gradient was used for normalisation. The

chemotactic tripeptide fMLP is present in proteins produced by bacteria and has been used extensively in neutrophil chemotaxis assays (*175*). A 4-fold increase in migration towards fMLP compared to a media only control was observed, which is in line with previous studies (*176*) (Figure S2-2). A 2-fold increase in migration towards live MTB and a 3.5-fold increase in migration towards EcN was observed, compared to the control (Figure 2-3B). These findings suggest that MTB may induce neutrophil recruitment, but less so than EcN.

2.2.3. Assessing cytokine expression from macrophages

Like neutrophils, macrophages play a central role in detecting and tackling bacterial infections. The inflammatory response of human macrophages to MTB was assessed by measuring the level of various cytokines produced by THP-1-derived macrophages co-cultured with bacteria. THP-1 is a human monocytic cell line extensively used as a model system to study monocyte-macrophage differentiation as well as macrophage-related physiological processes and functions (*177*). *In vitro* differentiation of THP-1 monocytes is most often achieved using phorbol 12-myristate-13-acetate (PMA) to produce cells with similar phenotype, cell morphology, surface marker expression and cytokine production as primary human macrophages (*178*, *179*).

To determine the optimal co-culture duration, levels of IL-1β production were assessed over 24 h using Western blotting. This cytokine is produced by macrophages in response to damage or pathogen recognition and is a key mediator of innate immune responses (*180*). Stimulation with live EcN was used for comparison and stimulation with LPS was used as a positive control. IL-1β production following co-culture with MTB and EcN peaked at 6 h while production peaked at 24 h for LPS stimulation (Figure 2-4A, Figure S2-3). To avoid bacterial overgrowth that occurs at longer co-culture durations, an intermediate period of 9 h was selected and sufficiently high levels of cytokine production were captured for all three conditions compared to the media only control (Figure 2-4B).

A human cytokine array was used to measure the levels of several cytokines produced following 9 h of co-culture (Figure 2-4C, Figure S2-4). Cytokines with 4-fold higher expression than the control were plotted and compared (Figure 2-4D). Stimulation with LPS, EcN and MTB produced similar levels of IL-8 and MIP-1α expression. Both induce migration of polymorphonuclear cells (PMNs), while MIP-1α also induces chemotaxis of monocytes, DCs, NK cells, T cells, and platelets (*181*, *182*). MTB and EcN stimulation resulted in comparable levels of

IL-1α and IL-6 production. IL-1α is an important mediator of proinflammatory responses and IL-6 supports the growth of B cells and is antagonistic to regulatory T cells (*180*, *183*, *184*).

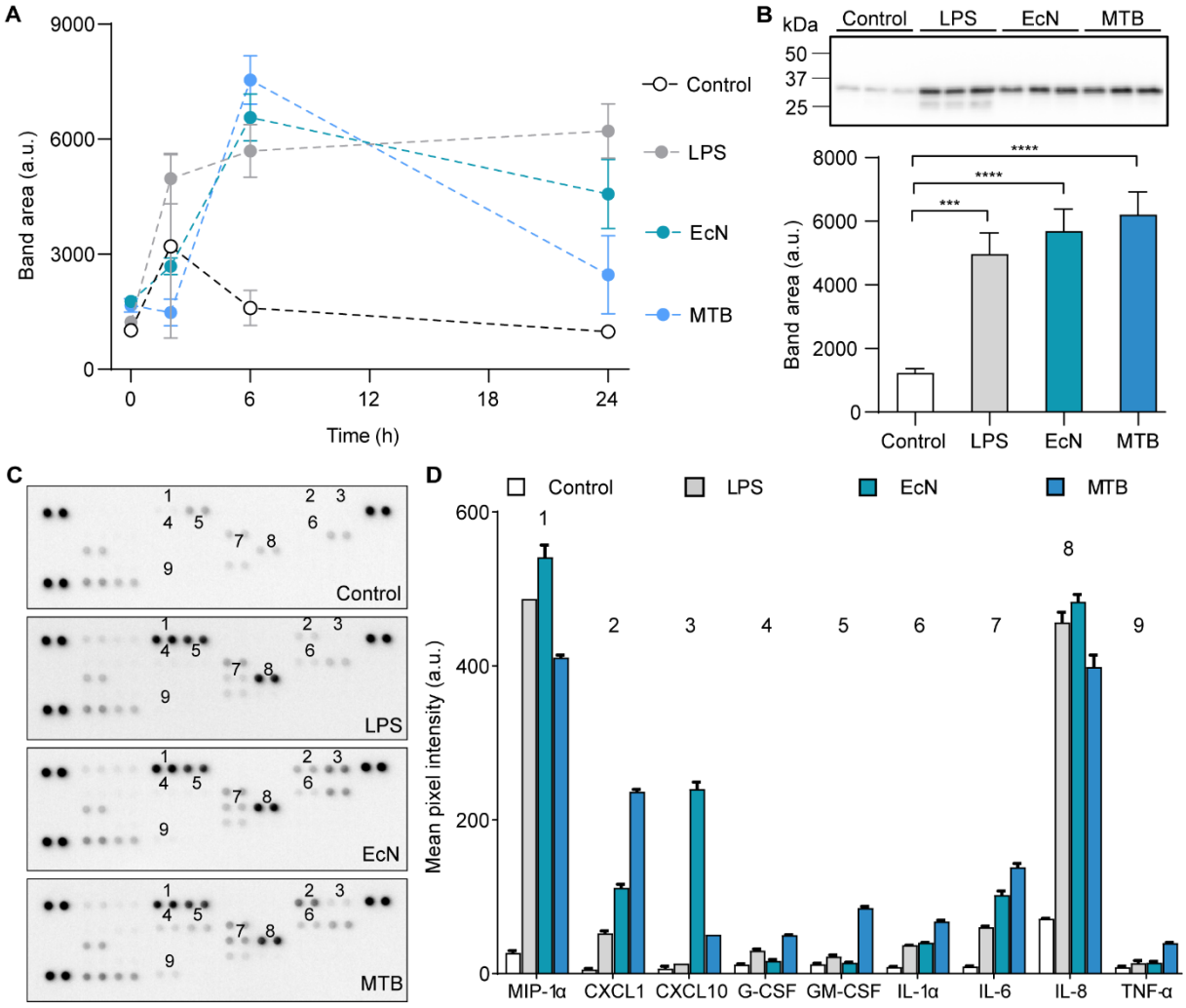

Figure 2-4: Assessing cytokine expression from THP-1 derived macrophages. **(A)** Quantification of pro-IL-1β levels in THP-1 cell lysates following incubation with media only (control), LPS, EcN or MTB over 24 h assessed using Western blotting (n = 3; mean ± SD). **(B)** Pro-IL-1β levels assessed using Western blotting after 9 h of culture with media only, LPS, EcN or MTB (n = 3; mean ± SD). **(C)** Human cytokine array performed after 9 h of culture with media only, LPS, EcN or MTB. **(D)** Quantification of cytokine levels in THP-1 cell lysates using a human cytokine array. Cytokines with 4-fold higher expression than the control are plotted (mean ± SD of duplicates on array).

MTB stimulation resulted in higher levels of TNF-α, CXCL1, G-CSF, and granulocyte-macrophage colony-stimulating factor (GM-CSF) expression than LPS and EcN. TNF-α has wide ranging effects, including causing necrotic regression of certain tumours (*185*). G-CSF and GM-CSF initiate the proliferation and differentiation of neutrophil progenitor cells, while CXCL1 induces neutrophil chemotaxis (*186–188*). In addition, GM-CSF stimulates the production of monocytes, which migrate into tissue and mature into macrophages and dendritic

cells (*189*). Although MTB did not induce substantial neutrophil migration (Figure 2-3), these findings suggest that higher levels of neutrophil recruitment are likely to occur.

EcN stimulation resulted in substantially higher levels of CXCL10 expression than MTB. CXCL10 is a chemoattractant for APCs, NK cells and T cells, and is associated with antitumour activity, although protumour effects have also been observed (*190*). Interestingly, it has been found to have direct antimicrobial functions, likely mediated through the cationic domain on the molecule causing disruption to the negatively charged bacterial cell wall (*191*). Thus, low levels of CXCL10 may be beneficial for bacteria-mediated therapies.

Overall, the proinflammatory cytokines expressed in response to stimulation with MTB were in line with those typically produced in response to other bacterial infections (*192*). Moreover, MTB stimulation generally did not result in substantially higher cytokine expression compared to EcN, which is notable since excess cytokine production can have detrimental effects, including capillary leakage, dysregulation of immune responses and tissue damage (*193*).

2.2.4. MTB induce maturation of moDCs

DCs are also of interest in the context of bacteria-mediated cancer therapy since they participate in responses to bacterial infections and also play a pivotal role in mounting an adaptive immune response against cancer. Since circulating DCs are scarce and difficult to isolate, many *in vitro* experiments are conducted using moDCs (*194*). MoDCs originate from monocytes that have been recruited to sites of injury or inflammation and differentiate into cells with a DC phenotype in response to cytokines in the surrounding environment (*195*). CD14+ monocytes are more abundant in circulation than DCs and can be differentiated into CD14– immature moDCs when cultured with the cytokines IL-4 and GM-CSF (*194*). Naïve moDCs undergo maturation upon encountering various inflammatory mediators, such as LPS, after which the maturation marker CD83 is upregulated. Mature moDCs have decreased phagocytic capacity and an increased ability to migrate towards lymphoid tissues and prime T cells (*195*) .

Monocytes were isolated from human peripheral blood and cultured with GM-CSF and IL-4 for 5 days and then stimulated with LPS for 24 h to induce maturation. Morphological changes were observed in images captured during the culture period (Figure S2-5). Validation of differentiation and maturation of moDCs was performed by assessing CD14 and CD83 expression in isolated monocytes, immature moDCs and activated moDCs using flow cytometry (Figure S2-6).

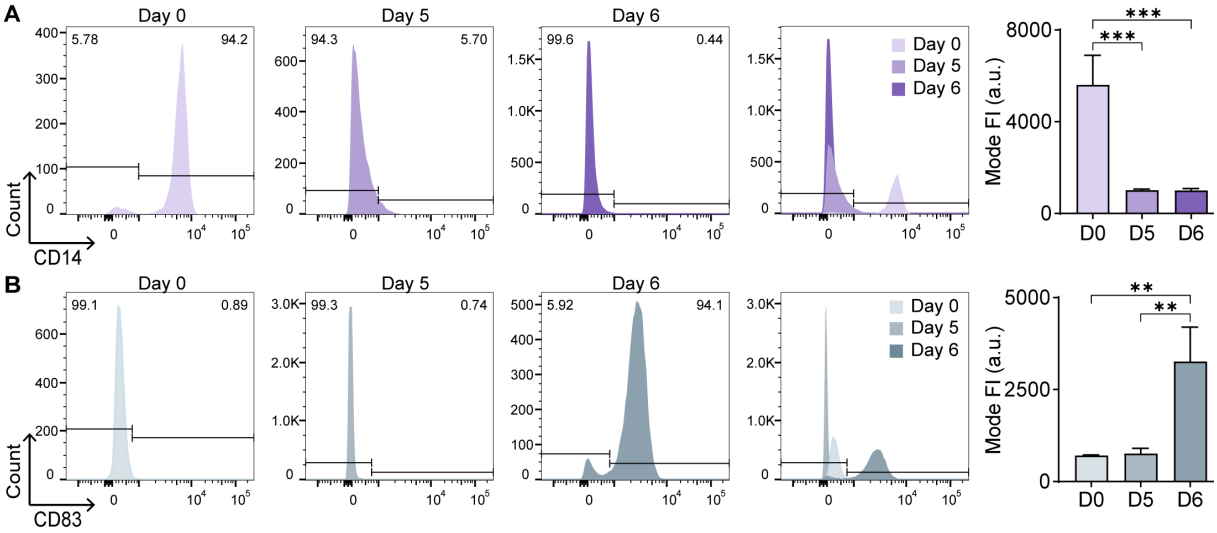

Figure 2-5: Validation of differentiation and maturation of primary human monocyte-derived DCs. **(A)** Representative flow cytometry histograms and quantification of CD14 expression in isolated monocytes (day 0), immature moDCs (day 5), and LPS-stimulated moDCs (day 6). FI= fluorescence intensity (n = 3 donors; mean ± SD; ***P < 0.001, ANOVA). **(B)** CD83 expression after isolation (day 0) and during differentiation (day 5) and maturation (day 6) ($n \geq 2$ donors; mean ± SD; **P < 0.01, ANOVA).

Downregulation of the monocyte marker CD14 was observed, as indicated by a 5.6-fold decrease in fluorescence intensity values after day 5 compared to day 0 (Figure 2-5A). Expression of the moDC maturation marker CD83 significantly increased on day 6 after 24 h stimulation with LPS (Figure 2-5B). These findings indicate that isolated monocytes differentiated into immature moDCs with the ability to develop into mature moDCs upon stimulation.

Having validated the differentiation protocol, the ability of live MTB to induce maturation of moDCs was investigated. Stimulation with EcN was used for comparison and LPS stimulation served as a positive control. To identify the optimal duration of stimulation with live bacteria, CD83 expression was measured after 6, 19, and 24 h of co-culture. Approximately 90% of the cell population was CD83+ at all timepoints in samples stimulated with LPS (Figure 2-6A). In contrast, stimulation with live EcN resulted in CD83 upregulation in over 90% of moDCs after 6 h but less than 70% of cells were CD83+ at later time points (Figure 2-6B). MTB also induced moDC maturation in 89% of cells after 6 h of co-culture. Like EcN-stimulated samples, CD83 downregulation occurred after 6 h, where CD83+ cell populations decreased to 42 % after 19 h and 50 % after 24 h (Figure 2-6C). As such, subsequent co-culture experiments were performed for less than 6 h.

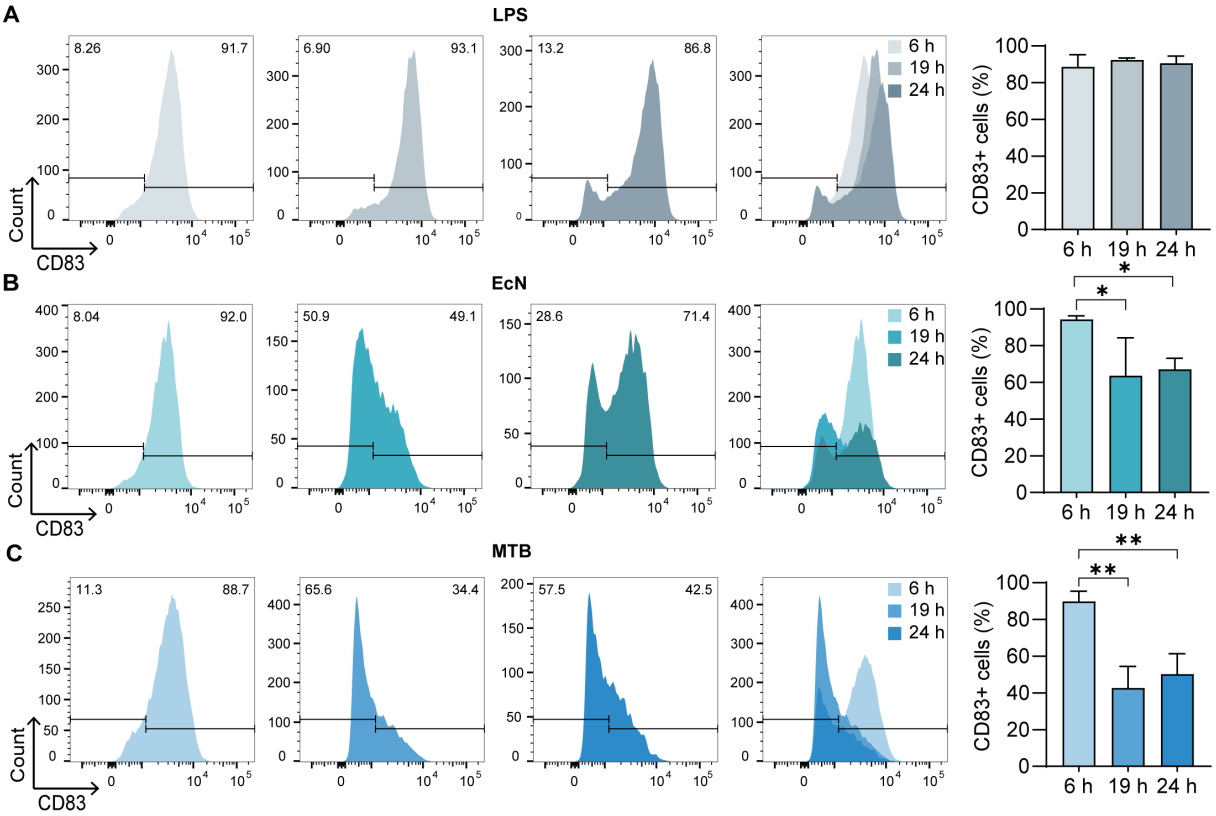

Figure 2-6: Assessment of primary human moDC maturation in the presence of MTB. **(A)** Representative flow cytometry histograms and quantification of the percentage of CD83+ moDCs following stimulation with LPS for 6, 19, and 24 h ($n \geq 2$ donors; mean ± SD). **(B)** CD83 expression and quantification of CD83+ moDCs after co-culture with EcN for up to 24 h ($n \geq 2$ donors; mean ± SD; $^{*}P < 0.05$, ANOVA). **(C)** Assessment of expression and quantification of CD83+ moDCs after co-culture with MTB over 24 h ($n \geq 2$ donors; mean ± SD; $^{**}P < 0.01$, ANOVA).

2.2.5. MTB promote cancer cell material uptake by moDCs

The uptake, processing and subsequent presentation of cancer antigens by DCs is a critical step in mounting an immune-mediated anticancer response. Zuo et al. studied the uptake of cancer cell material by immature moDCs using flow cytometry by staining both cell types and quantifying uptake as the percentage of double stained cells (*196*). The ability of MTB to increase the uptake of cancer cell material was investigated using CFSE-stained moDCs co-cultured with far-red-stained HCT116 cancer cells in the presence of MTB. Two co-culture conditions were investigated (Figure 2-7A). The first condition, where MTB and moDCs were added simultaneously, was designed to represent a TME where DCs are already present. The second condition, where cancer cells are co-cultured with MTB prior to the addition of moDCs was designed to represent a TME where moDCs are recruited after bacterial colonization has occurred.

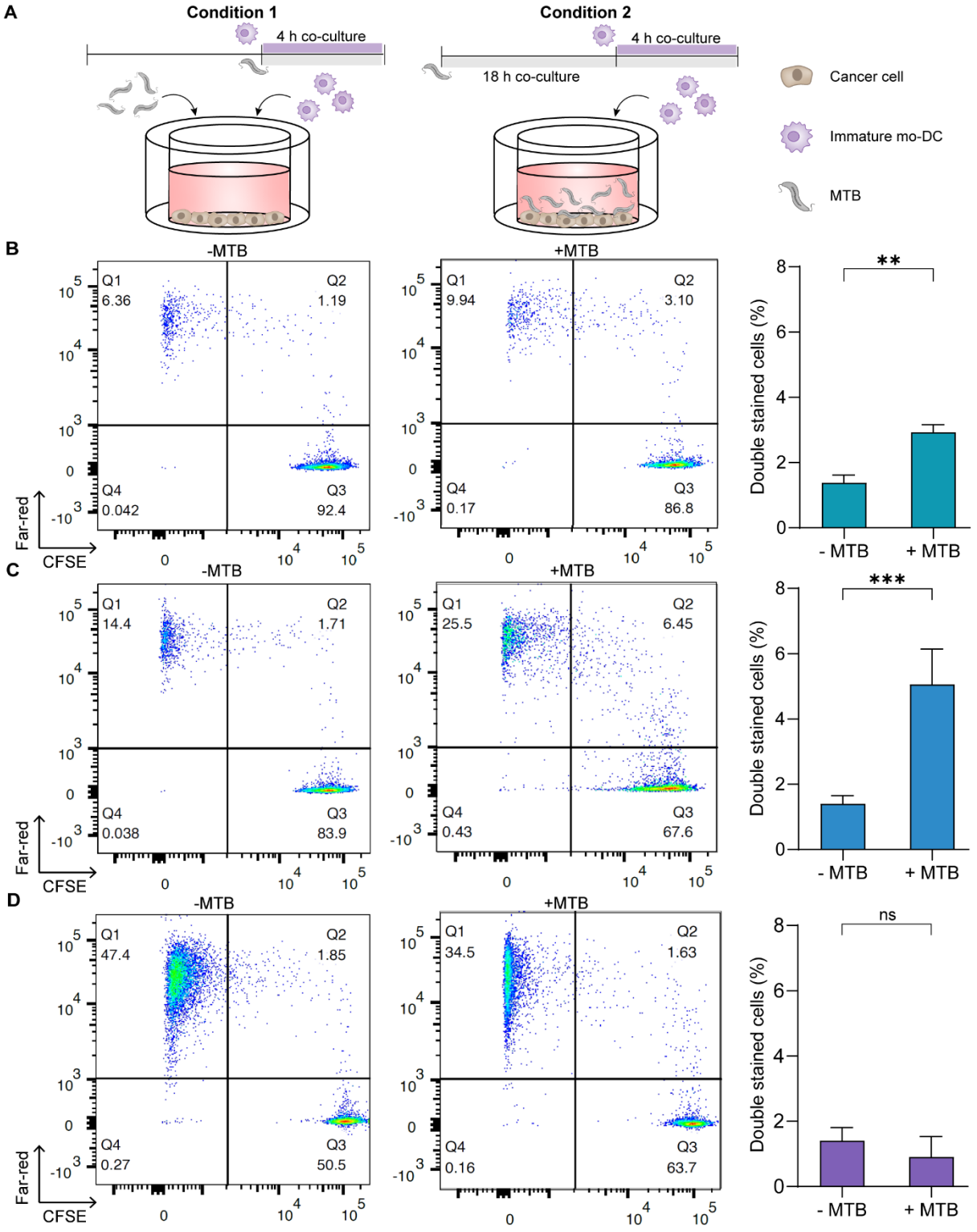

Figure 2-7: Cancer cell material uptake by primary human moDCs in co-culture with MTB. **(A)** Schematic illustrating two experimental conditions where CFSE-stained moDCs and far-red stained HCT116 cancer cells were used to assess enhanced uptake of cell material in the presence of MTB. **(B)** Representative flow cytometry plots and quantification of cell material uptake for experimental condition 1, where MTB and moDCs were added simultaneously (n = 2 donors; mean ± SD; **P < 0.01, Student's t-test). **(C)** Representative plots and quantification of material uptake for experimental condition 2 with prior MTB co-culture (n =3 donors; mean ± SD; ***P < 0.001, Student's t-test). **D)** Representative plots and quantification of material uptake for experimental condition 2 at 4 °C (n =2 donors; mean ± SD; no significance, Student's t-test).

Since mature moDCs have reduced phagocytic capacity and MTB was found to induce moDC maturation within 6 h (Figure 2-6C), a duration of 4 h was selected for moDC co-culture in both conditions (*195*). In the first condition, a 2-fold increase in the percentage of double stained cells was observed in the presence of MTB, indicating significantly increased uptake of cancer cell material (Figure 2-7B). The effect was even more pronounced in the second condition, with an almost 4-fold increase in double-stained cells, suggesting that longer exposure of cancer cells to MTB promotes the uptake of cancer cell material (Figure 2-7C). To verify that active uptake of cancer cell material was responsible for the observed increase in double-stained cells, co-culture under the second experimental condition was also performed at 4 °C where the lower temperature inhibits phagocytosis (Figure 2-7D) (*197*). At 4°C, decreased uptake in the presence of MTB was observed, supporting the notion that MTB promotes active material uptake in moDCs.

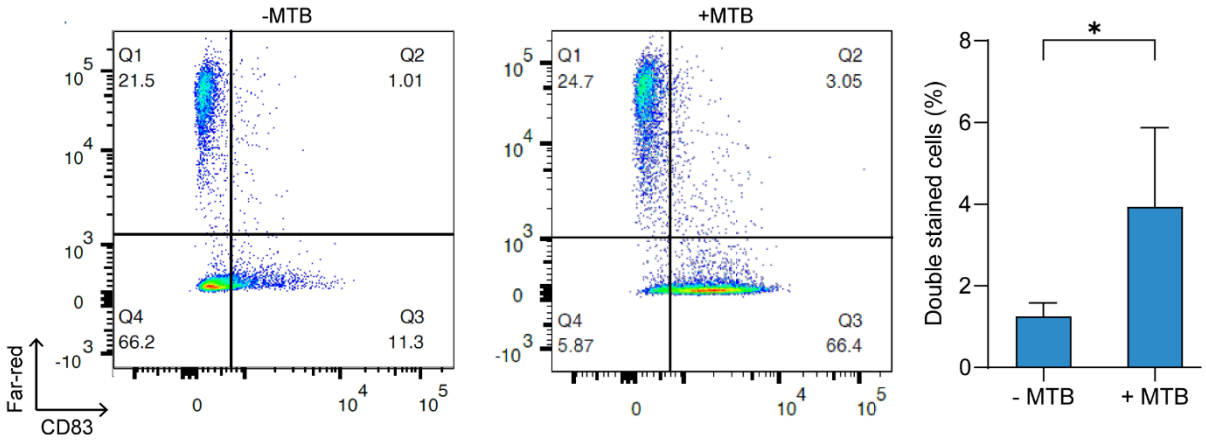

Figure 2-8: Maturation of moDCs following cancer cell material uptake in the presence of MTB. Representative plots and quantification of cell material uptake for experimental condition 2 with prior MTB co-culture (n =3 donors; mean ± SD; *P < 0.05, Student's t-test).

In addition, CD83 expression was studied to assess whether maturation was induced in moDCs that phagocytosed cancer cell material. Approximately 90% of moDCs were CD83+ when MTB was present during co-culture, while the majority of moDCs did not upregulate CD83 in the absence of MTB. Furthermore, 3-fold higher cancer cell material uptake by CD83+ moDCs was observed in cultures where MTB was present (Figure 2-8). These results show that functional maturation of moDCs occurs, in addition to increased uptake of cancer cell material in the presence of MTB.

2.2.6. Establishment of a microfluidic platform to study immune cell migration

While important information can be obtained from studying immune responses in 2D assays, using tools that more closely recapitulate the complex interplay between immune cells, cancer cells, bacteria and the surrounding tumour environment may yield further insights. Thus, having established that MTB can elicit responses from immune cells, including cell migration, developing a more complex system to examine these interactions was explored. Microfluidic devices have emerged as a versatile tool for studying cell migration using real-time imaging with high spatiotemporal resolution. Tissue architecture and function can be reconstructed in devices through the incorporation of multiple cell types and extracellular matrix components, such as collagen and hyaluronic acid (*198*, *199*). Compared to 2D assays, the ability to establish 3D tissue models in microfluidic devices offers a more physiologically relevant system to assess cell interactions in a highly controlled microenvironment (*199*).

A microfluidic platform to study interactions between immune cells, MTB and cancer cells was established using a device consisting of five parallel, interconnected chambers (Figure 2-9A). Immune cells were injected into the central channel and extracellular matrix-mimicking collagen hydrogels containing MTB were seeded into the two adjacent channels that are connected to the central channel through microchannels. The dimensions of the microchannels were selected to mimic the constrictive spaces traversed by immune cells as they cross endothelial barriers to enter tissue. Media supply to the system was provided by the peripheral channels that are separated from the collagen chambers by polydimethylsiloxane (PDMS) posts.

Proof of concept experiments to establish a workflow and image processing pipeline were performed using J774A.1 murine macrophages. Time-lapse imaging was performed at 30 min intervals to track the migration of individual cells into the MTB-collagen channel (Figure 2-9B). An incubation chamber at 37 °C was installed on a confocal microscope, enabling long-term imaging of up to 3 devices in parallel over 10 h. An image processing pipeline was developed to enable reproducible and efficient analysis of captured image stacks (Figure 2-9C). Image registration was performed to account for slight deviations in image frames between consecutive time points, and the aligned timeseries was used to track the migration of individual cells. To add even more complexity to the platform, the feasibility of incorporating spheroids seeded with MTB embedded within the collagen matrix was demonstrated (Figure 2-9D). Such a system works towards achieving more physiological relevance where interactions between cancer cells and

MTB, which may lead to the release of DAMPs and, thus, cell recruitment, can be captured and studied in real time.

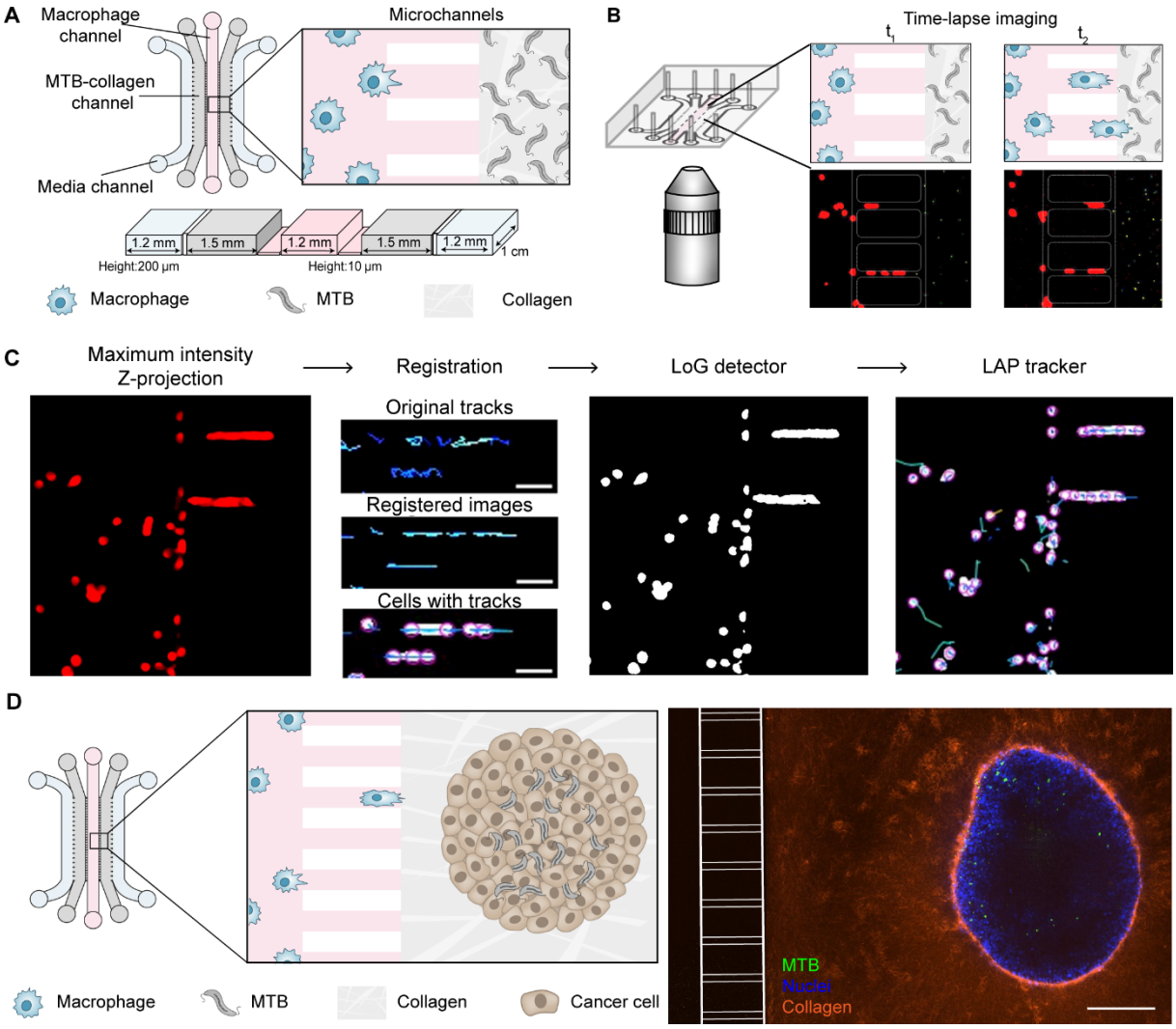

Figure 2-9: Establishment of a microfluidic platform to study immune cell migration. **(A)** Schematic representation of five-channel microfluidic device consisting of a central channel for immune cells, two adjacent MTB channels and two side channels for media supply. **(B)** Schematic representation of image acquisition for timelapse imaging. **(C)** Workflow for image processing. Z-projections are binarized, registered and individual J774A.1 cells are tracked. Scale bar = 20 µm. **(D)** Representative images of MCF-7 spheroid seeded with MTB embedded in TAMRA-stained collagen. Scale bar = 100 µm.

As neutrophils are key mediators of immune response against bacterial infection, assessing migration of these cells is of interest. However, primary neutrophils are readily activated by physical and chemical stressors which drastically reduces their viability. Proof of concept experiments were performed to ascertain the suitability of the proposed platform for the study of neutrophil migration. The previously established imaging duration of 10 h was used to maintain high levels of viability during the experimental window (Figure S2-7A). No morphological changes were observed, suggesting that activation and rapid apoptosis were not induced by the handling

and injection of the cells in the device (Figure S2-6B). These pilot experiments served to demonstrate the potential utility of microfluidic platforms to investigate neutrophil migration under more physiologically relevant conditions.

2.3. Discussion

In this study, we aimed to analyse key functional properties of human innate immune cells in response to stimulation with the MTB. We first investigated the ability of MTB to proliferate and maintain their magnetic properties under physiological conditions, as well as their viability in whole blood. The MTB strain AMB-1 is typically cultured between 25 °C and 30 °C in iron rich media under microaerophilic conditions, which contrasts with physiological conditions of 37 °C and normoxia (*200*). While MTB proliferation was highest at 37 °C in DMEM, the magnetic responsiveness of the bacterial suspensions decreased over time. Calugay *et al.* found that MTB proliferation increased and magnetosome formation decreased in low iron media (*201*), such as DMEM. Since magnetic cells biosynthesize highly organized magnetite, their growth rate is slower than that of non-magnetic cells. However, temperature appears to play a major role in the inhibition of magnetosome formation, as cultures at 37 °C in MSGM also had reduced magnetic responsiveness and higher rates of proliferation. The elevated temperature may induce stress and shift focus from the production of proteins for magnetosome synthesis to maintaining vital functions and preserving cell integrity (*202*). These findings support the use of MTB for bacteria-based cancer therapy as increased proliferation at 37 °C could enable them to form robust colonies in the tumour niche, a prerequisite for effective treatment. MTB persisted in blood samples for 3 h, with a less pronounced decrease in viable bacteria compared to EcN. These findings also suggest that magnetic intervention should be implemented within the first 3 h when the MTB population is still magnetically responsive and viable bacteria may still be in circulation.

Neutrophil migration and cytokine production by macrophages stimulated with MTB was studied. While both cytokine production and neutrophil recruitment are essential for pathogen clearance, excessive recruitment and cytokine release can also lead to tissue damage, immune cell dysregulation and the development of sepsis (*203*). In a Transwell migration assay, MTB was found to induce less directed migration of neutrophils compared to EcN. While the Transwell system is a valuable and convenient system that can be used to gain important insights into cell migration, further studies using more complex and physiologically relevant tools, such as microfluidic devices with endothelialised channels, can be used to support these findings. The

cytokines expressed by macrophages cultured with MTB were largely comparable to EcN stimulation. Characterisation of human cytokine expression in response to stimulation with MTB had yet to be performed. The established profile of cytokines could assist future efforts to determine the safety and efficacy of MTB and may also aid in identifying suitable candidates for effective combinational therapy.

Lastly, we investigated the ability of MTB to induce maturation and increase cancer cell material uptake by moDCs. MTB induced moDC maturation after 6 h of co-culture to a comparable extent as EcN and LPS. The significant decrease in CD83+ cells after 18 and 24 h in the presence of both MTB and EcN may be the result of stress caused by the proliferating bacteria, which could induce apoptosis of activated moDCs. Cell stress, characterised by ATP release, and cell death have been observed in moDCs cultured with live probiotic bacteria for 18 h (*204*). As a result, subsequent co-culture experiments with live MTB were performed for less than 6 hours.

While moDC maturation is a crucial step in mounting an efficient antitumour response, we also investigated whether the presence of MTB could promote the uptake of cancer cell material. The most substantial uptake was observed when cancer cells were cultured with MTB prior to co-culture with moDCs, suggesting the MTB had an effect on the cancer cells, possibly the induction of apoptosis. Apoptotic cells display various peptides and phospholipids, such as phosphatidylserine, which bind to receptors on phagocytic cells and induce active uptake (*205*). Mature DCs that have phagocytosed apoptotic cancer cells have been shown to mount highly efficient antitumour immunity (*206*). A further experiment could co-culture murine moDCs with MTB and murine cancer cells that express a well characterised antigen, like ovalbumin. Effective cross-presentation and stimulation of ovalbumin-specific murine T cells by the moDCs can then be assessed. In addition, *in vivo* studies can be performed to establish whether treatment with MTB results in increased T cell recruitment.

Stimulation of the immune system is an essential component for achieving tumour regression in bacterial cancer therapy. An understanding of the immunostimulatory properties of MTB is crucial for their potential clinical use and will enable the safety and efficacy of this species to be determined. The findings of this work suggest a potential beneficial effect of MTB in mounting an immune-mediated antitumour response. This work has established that the MTB strain AMB-1 stimulates various innate immune cells in a comparable way to the widely used EcN strain. This supports observations that MTB are generally well tolerated *in vivo* (*87*, *173*). Overall, this

study establishes that MTB is a viable candidate for bacteria-mediated cancer therapy and lays the groundwork for future characterisation of the immunostimulatory effects of this strain.

2.4. Materials and methods

2.4.1. Materials

MCF-7 (human breast adenocarcinoma, ATCC HTB-22), HCT116 (human colorectal carcinoma, ATCC CCL-247), J774A.1 (mouse reticulum cell sarcoma, ATCC TIB-67), THP-1 (monocytic leukemia, ATCC TIB-202), Magnetospirillum magneticum (ATCC 700264), Wolfe's Vitamin Solution and Wolfe's Mineral Solution were purchased from American Type Culture Collection (Manassas, VA). Penicillin/Streptomycin (P/S) was purchased from Corning (Corning, NY), fetal bovine serum (FBS) was purchased from BioWest (Nuaillé, France) and 4% formaldehyde (HistoFix 4%) was purchased from Carl Roth (Karlsruhe, Germany). The EasySepTM human monocyte isolation kit was purchased from Stemcell (Vancouver, Canada) and transparent PET Transwell inserts and rat-tail collagen-I were both purchased from Corning. Recombinant human anti-CD83 primary antibody, recombinant human anti-CD14 primary antibody, and goat anti-rabbit IgG (Alexa Fluor 488) secondary antibody were purchased from abcam (Cambridge, UK). Dulbecco's Modified Eagle's Medium (DMEM), McCoy's 5A medium, Minimal Essential Medium with alpha modifications (alpha-MEM), RPMI-1640, lipopolysaccharide from E. coli (O111:B4) (LPS), 0.5 M EDTA, annexin V-FITC and PI apoptosis kit, Pierce BCA Protein Assay Kit, CellTrace Far-Red cell proliferation kit and CellTrace CFSE cell proliferation kit were acquired from Thermo Fisher Scientific (Waltham, MA). The human IL-1β antibody, goat IgG HRP-conjugated antibody and the Human Cytokine Array Kit were purchased from R&D Systems. Potassium phosphate, succinic acid, tartaric acid, sodium nitrate, ascorbic acid, sodium acetate, resazurin sodium salt, Luria-Bertani (LB) broth, LB agar, Histopaque-1077, Histopaque-1119, human recombinant granulocyte-macrophage colony-stimulating factor (GM-CSF), human recombinant IL-4, N-Formyl-Met-Leu-Phe (fMLP), human serum albumin (HSA), sodium deoxycholate, IGEPAL CO-520, Tris(hydroxymethyl)aminomethane (Tris), sodium chloride (NaCl), sodium dodecyl sulfate (SDS), Hank's Based enzyme-free cell dissociation buffer, SYLGARDTM 184 Silicone Elastomer kit, agar, bovine serum albumin (BSA), phorbol 12-myristate-13-acetate (PMA), phosphate-buffered saline (PBS), Triton X-100 and N-hydroxysulfosuccinimide (sulfo-NHS) were all acquired

from Sigma-Aldrich (St. Louis, MO). Precision Plus Protein All Blue Standards, Laemmli sample buffer, 2-mercaptoethanol, Mini-PROTEAN TGX Stain-Free Precast Gels 4-20%, Immun-Blot PVDF, EveryBlot Blocking Buffer, luminol-enhancer solution and substrate peroxide solution were purchased from Bio-Rad (Hercules, CA).

2.4.2. Mammalian cell culture

THP-1 cells were cultured in RPMI-1640 supplemented with 10% FBS and 1% P/S. HCT116 cells were cultured in modified McCoy's 5A medium supplemented with 10% FBS and 1% P/S. MCF-7 cells were cultured in DMEM supplemented with 10% FBS and 1% P/S. J774A.1 cells were cultured with alpha-MEM supplemented with 10 % FBS. Cells were cultured at 37 °C and 5% CO_2 in a humidified atmosphere. One day before experiments, media was replaced with antibiotic-free media. Cell density was determined using a haemocytometer and the required number of cells was seeded for each experiment as specified.

2.4.3. Bacteria culture

M. magneticum strain AMB-1 was cultured in revised magnetic spirillum growth medium (MSGM) which contained 5.0 mL of Wolfe's Mineral Solution, 0.45 mL of 0.1 % resazurin, 0.68 g potassium phosphate, 0.37 g succinic acid, 0.37 g tartaric acid, 0.12 g sodium nitrate, 0.035 g ascorbic acid and 0.05 g sodium acetate per litre of distilled water. The final pH was adjusted to 6.9 with 1 M NaOH before autoclaving. Prior to use, Wolfe's Vitamin Solution (1000x) and 10 mM ferric quinate (200x) were added to the media. MSGM agar plates (0.7% agar) were prepared by adding 10x MSGM to an autoclaved solution of agar in DI water. MTB was grown under microaerophilic conditions at 30 °C and suspensions grown for 5 to 7 days were used for all experiments. *E. coli* Nissle 1917 cultures were grown overnight in LB media at 37°C with agitation at 225 rpm or on LB agar plates (1.5% agar) at 37°C.

2.4.4. MTB proliferation in mammalian culture conditions

MTB was grown in varying media, temperature and oxygen conditions, as indicated in Table 2-1. Bacterial proliferation was assessed by performing optical density measurements at 600 nm (OD_{600}) (Spark multimode microplate reader, Tecan). C_{mag} measurements were performed to quantify the magnetic responsiveness of the samples by placing a magnet parallel ($OD_{||}$) and then perpendicular ($OD_{\perp}$) to the light path. The C_{mag} value was calculated as $OD_{||}/OD_{\perp}$.

Table 2-1: List of MTB different culture conditions

Media	Supplements	Temperature	Oxygen condition	Media change
MSGM	2 mM Wolfe's vitamin solution 10 mM ferric quinate	30 °C	Microaerophilic	No
MSGM	2 mM Wolfe's vitamin solution 10 mM ferric quinate	37 °C	Microaerophilic	No
DMEM	10% FBS	37 °C	Microaerophilic	No
DMEM	10% FBS, 1% P/S	37 °C	Microaerophilic	No
DMEM	10% FBS	37 °C	Microaerophilic	Yes
DMEM	10% FBS	37 °C	Normoxia	No

2.4.5. In vitro whole blood bactericidal assays

Collection of human peripheral blood samples was approved by the Kantonale Ethikkommission Zürich (KEK-ZH-Nr. 2021-00413) and signed informed consent was obtained from each donor. MTB and EcN suspensions were centrifuged at 10 000 × g and 5 000 × g respectively and the pellets were resuspended in PBS at OD_{600} = 1. Next, 1 µl of either MTB or EcN was added to 100 µl of whole blood in a 96-well plate and incubated at 37 °C for 1 h or 3 h. Each sample was serially diluted and plated on agar plates. Colony counting was performed after overnight incubation at 37 °C for EcN samples or after 5 to 7 days incubation at 30 °C for MTB samples.

2.4.6. Isolation primary human neutrophils

Neutrophils were isolated by layering 20 mL of diluted blood on a double gradient of 10 mL Histopaque-1077 and 10 mL of Histopaque-1119. Tubes were centrifuged for 30 min at 700 × g (brake off). The neutrophil layer was collected and washed in PBS with centrifugation for 10 min at 280 × g (brake off). Isotonic lysis of RBCs was performed twice by adding 9 mL of sterile DI water to 1 mL of the neutrophil suspension. The tube was agitated for 20 s before 1 mL of 10x PBS was added to restore isotonicity and the suspension was washed with PBS. The final pellet was resuspended in the media required for respective experiments. To assess viability after isolation over 24 h, neutrophils were stained with CellTrace CFSE. A stock solution was prepared according to the manufacturers protocol and 2 µL was added to the MTB suspension. Cells were incubated at room temperature for 20 min, protected from light with gentle agitation. After incubation, 10 µL of 1% BSA was added to the cell suspension for 5 min to remove free dye.

Cells were pelleted, resuspended in RPMI with 10% FBS and seeded in a 96-well plate. Prior to analysis, cells were stained with 20 µg/mL PI and imaged using a confocal microscope (Nikon Eclipse Ti2 with Yokogawa CSU-W1 unit and Hamamatsu C13440-20CU Digital CMOS camera). Viability was quantified using Fiji/Image J (version 1.53s).

2.4.7. Investigation of neutrophil migration in a Transwell assay

Transwell inserts (pore size = 3.0 µm; pore density = $6 \pm 2 \times 10^5/cm^2$) were incubated at 37 °C for 1 h in wells containing 2.5 µg/mL fibronectin in PBS, which was isolated from human plasma. The fibronectin-coated inserts were washed twice with PBS and left to dry overnight. Bacteria suspensions at a concentration of 7×10^8 bacteria/mL and a 0.01 mM fMLP solution were prepared in RPMI with 0.5% HSA. To each well of a 12-well plate, 600 µl of each suspension and a media only control were added in duplicates. The plate was left for 1 h to allow the bacteria to settle. The coated Transwell inserts were then placed in the wells and 200 µl of neutrophil suspension at a concentration of 2×10^6 cells/mL in 0.5% HSA in RPMI were added to the apical compartment of each insert. The plate was placed in an incubator at 37 °C and 5% CO_2 for 2 h. The suspension from the basolateral chamber was collected and adhered cells were detached using 0.25% Trypsin-EDTA. The number of migrated cells in each sample was determined using a haemocytometer.

2.4.8. Cytokine expression in THP-1 macrophages

THP-1 monocytes were seeded at a density of 5×10^5 cells/mL in 6-well plates and differentiated into macrophages by adding 100 ng/mL PMA into the culture for two days. Differentiated macrophages were then cultured in the absence of PMA for 24 h prior to stimulation with 10 ng/mL LPS, 2.5×10^7 EcN or 2.5×10^7 MTB for up to 24 h. Cells were lysed with RIPA buffer (pH 8.0) containing 50 mM Tris, 100 mM NaCl, 0.1 % SDS, 1 % IGEPAL CO-520, 0.5% sodium deoxycholate, and 1 mM EDTA. Lysates were loaded in pre-cast gels for gel electrophoresis and transferred to PVDF membranes. Membranes were incubated in EveryBlot blocking buffer for 1 h and subsequently incubated overnight with an IL-1β primary antibody. Membranes were washed, incubated with a goat IgG HRP-conjugated secondary antibody for 1 h, developed with ECL Substrate and captured with a Biomolecular Imager (Azure Biosystems). Cytokine production was assessed using a Human Cytokine Array Kit according to manufacturer instructions.

2.4.9. Differentiation and maturation of monocyte derived dendritic cells

Peripheral blood mononuclear cells (PBMCs) were isolated by layering 16 mL of diluted blood on top of 10 mL of Histopaque-1077. Tubes were for centrifuged for 30 min at 400 × g (brake off). The PBMC layer was collected, washed with PBS twice and centrifuged for 10 min at 280 × g (brake off). The PBMC pellet was resuspended in PBS supplemented with 2% FBS and 1 mM EDTA and monocyte isolation was performed using the EasySep™ Human Monocyte Isolation Kit according to manufacturer instructions. Isolated monocytes were cultured in RPMI supplemented with 10% FBS, 1% P/S, 25 ng/mL rhGM-CSF and 20 ng/mL rhIL-4 at a density of 5×10^5 cells/mL in 12-well plates. Half of the media was replenished after 2 days. Validation of moDC differentiation and maturation was assessed by staining for CD14 and CD83 on isolated monocytes, differentiated immature moDCs cultured for 5 days, and mature moDCs stimulated for up to 24 h with MTB or EcN at a ratio of 10:1 relative to the number of seeded monocytes or 100 ng/mL LPS. Cells were blocked with 1% BSA in PBS for 1 h, followed by incubation for 45 min at 4 °C with one primary antibody at a final concentration of 1 µg/mL. Cells were fixed with 4% formaldehyde and washed with PBS prior to incubation with an Alexa Fluor 488-conjugated anti-rabbit IgG secondary antibody (diluted 1:250). Flow cytometry was performed with a 488 nm excitation laser and 530/30 filter and 20 000 events were recorded per tube (LSRFortessa, BD Biosciences). Data was analysed using FlowJo (version.10.4.2, Tree Star).

2.4.10. Cancer cell material uptake by moDCs in co-culture with MTB

HCT116 cells were cultured for 20 h at a seeding density of 5×10^4 cells/well and subsequently stained with CellTrace far-red. Uptake of cancer cell material by primary human moDCs was investigated under two different co-culture conditions. In the first condition, MTB at a ratio of 100:1 with respect to the number of seeded cancer cells was added simultaneously with stained moDCs to the wells. In the second condition, MTB at a ratio of 100:1 was co-cultured with cancer cells for 18 h at 37 °C prior to adding immature moDCs. Immature moDCs were harvested after 5 days in culture and stained with CellTrace CFSE according to manufacturer instructions. For both conditions, moDCs were added to the wells at a ratio of 2:1 with respect to the number of seeded cancer cells and the plates were incubated for 4 h at 4 °C or 37 °C.

MoDC maturation was assessed after co-culture under the second experimental condition with unstained immature moDCs and MTB at a ratio of 200:1. After co-culture, CD83 antibody

staining was performed as previously described. Analysis was performed by flow cytometry with a 488 nm excitation laser and 530/30 filter and with a 640 nm excitation laser and 670/30 filter to detect CFSE/far red or CD83/far red stained cells. At least 20 000 events were recorded for each sample and analysis was performed using FlowJo.

2.4.11. Fabrication of microfluidic chips

Microfluidic chips were fabricated using soft lithography. A master was produced by patterning an epoxy-based negative photoresist onto a silicon wafer using a photomask with the desired chip design. The surface was passivated using chemical silanization prior to the first use. Subsequently, sylgard 184 silicone polydimethylsiloxane (PDMS) was mixed with its corresponding curing agent at a 10:1 ratio poured onto the master and degassed. The PDMS was cured by placing the master in an oven for at least 3 h at 70 °C. Once cured, devices were cut out of the PDMS and 1 mm inlets were punched on both ends of each channel. The devices were and covalently bonded to glass slides using oxygen plasma treatment for 40 s. The channels were flushed with 70% ethanol and sterilized by exposure to ultraviolet light for 1 h.

2.4.12. Assessing migration in microfluidic devices

Stained MTB was mixed with 0.5 M NaOH collagen to obtain a final concentration of 5×10^8 bacteria/mL in 2.5 mg/mL collagen. MTB-collagen suspensions were in injected into relevant channels of microfluidic devices and incubated at 37 °C for 45 min to gel. Immune cell suspensions at a concentration of 1×10^6 cells/mL were injected into adjacent channels and remaining side channels were filled with media. Devices were placed in petri dishes with a humidified atmosphere and placed in an incubation chamber at 37 °C mounted onto the confocal microscope enabling time-lapse imaging over 10 h. For each device, a region of interest with both the immune and MTB channels was imaged. Stacks from each imaging time point were converted into maximum intensity Z-projections, concatenated and image registration was performed for consecutive images using the StackReg plugin in ImageJ. The time-lapse series was binarized and temporally calibrated by defining intervals between consecutive frames. The TrackMate plugin was implemented with the downsample LoG detector, a diameter of 18 µm with a threshold of 2 µm, the simple LAP tracker, a maximal bridging distance between two consecutive image frames of 40 µm. Resulting track mean speeds were extracted.

2.5. Supporting Information

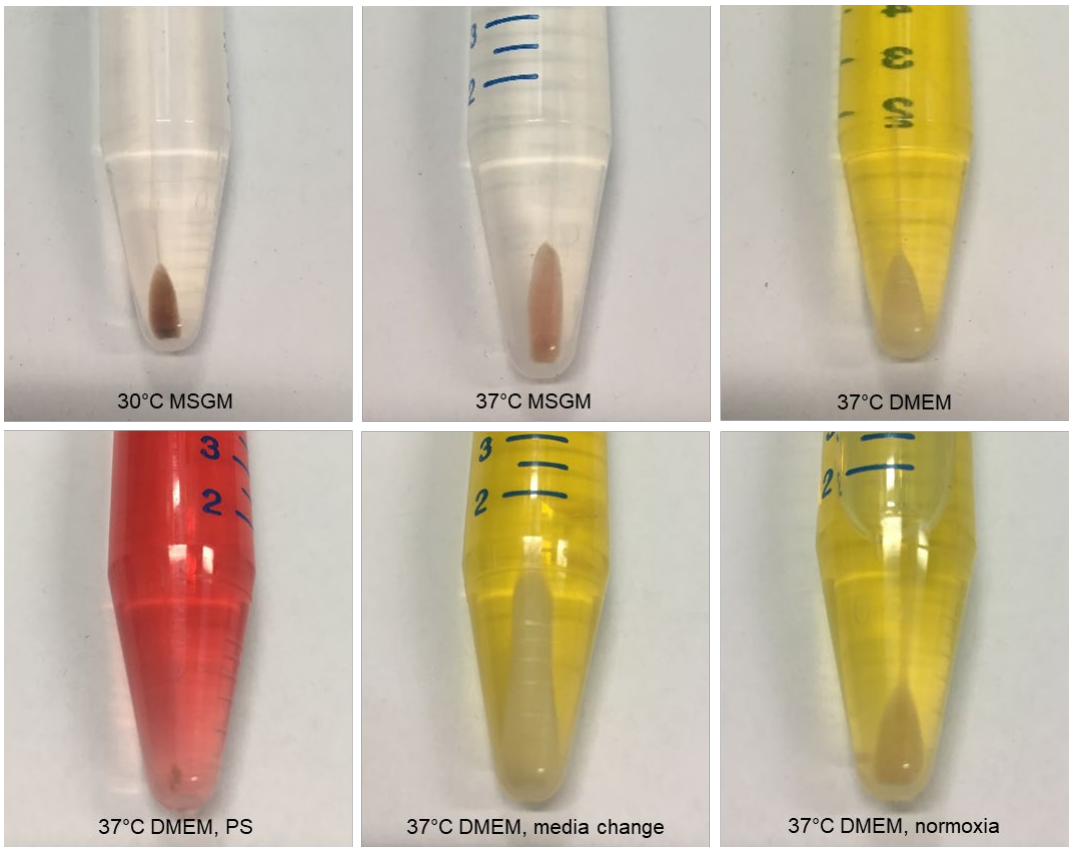

Figure S 2-1: MTB suspensions for OD and C_{mag} measurements. Representative images of MTB cultured over 10 days under different conditions (indicated in image).

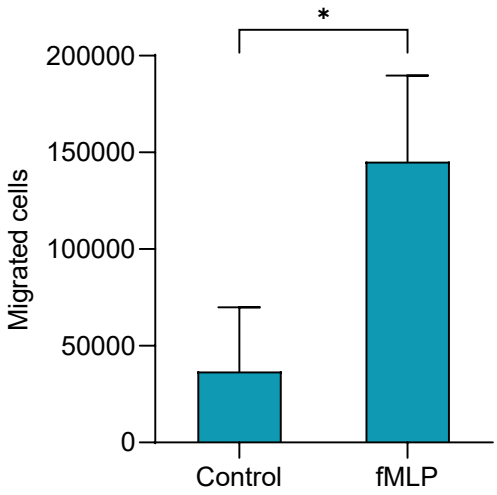

Figure S 2-2: Comparison of neutrophil migration. Number of neutrophils in basolateral compartment following 2 h incubation in the media only control or along an fMLP gradient (n = 3 donors; mean ± SD; *P < 0.05, Paired Student's t-test).

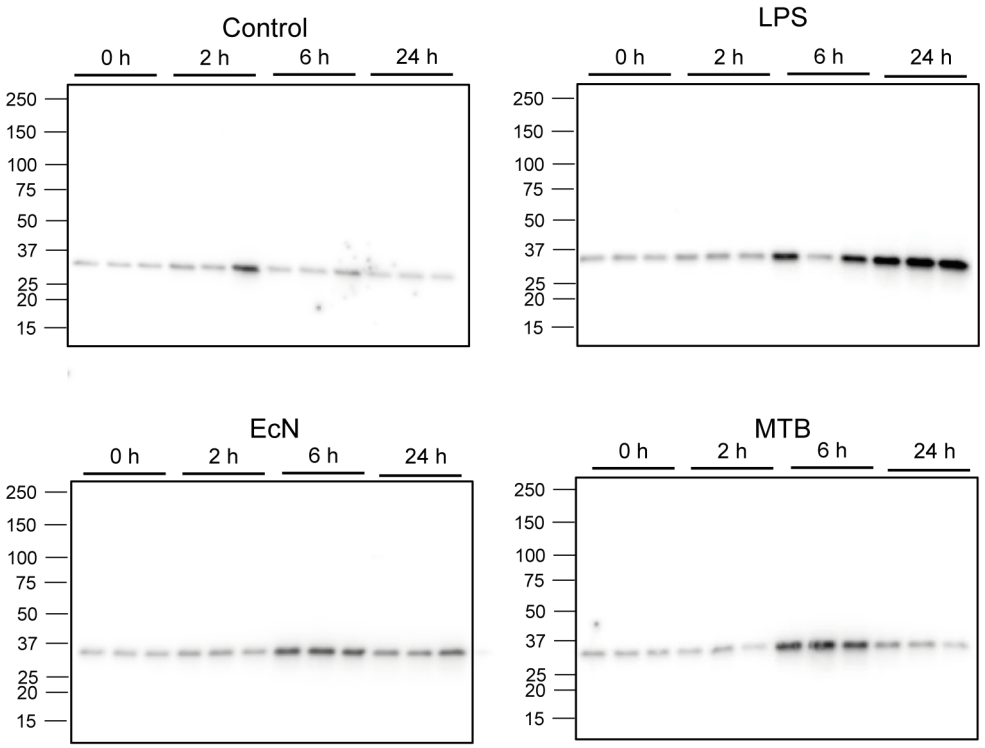

Figure S 2-3: IL-1β expression in THP-1 cells. Cytokine levels were assessed using Western blotting following incubation with media only (control), LPS, EcN or MTB over 24 h (n = 3; mean ± SD).

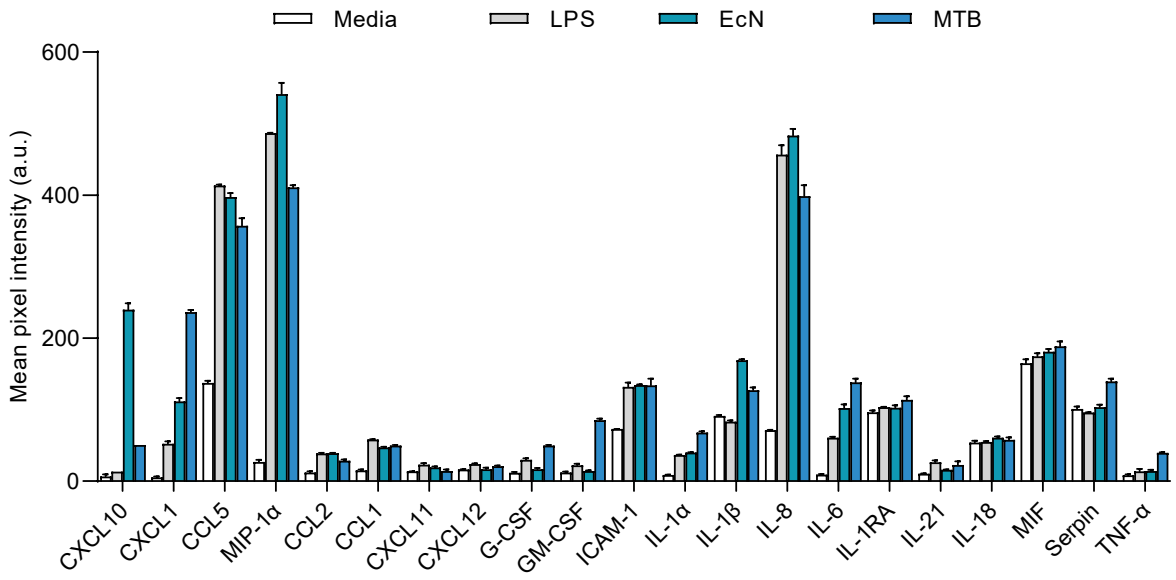

Figure S 2-4: Cytokine expression in THP-1 derived macrophages. Quantification of cytokine levels in THP-1 cell lysates using a human cytokine array after 9 h of culture with media only, LPS, EcN or MTB (mean ± SD of duplicates on array).

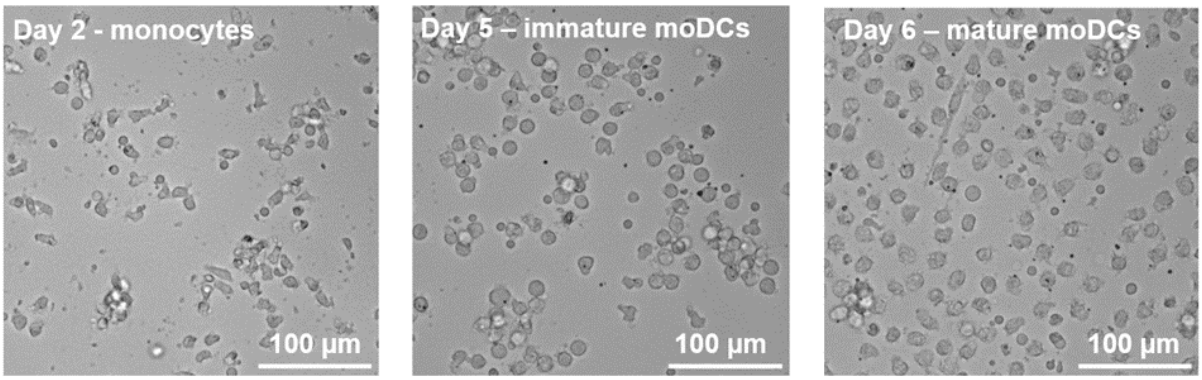

Figure S 2-5: Morphological changes in differentiating monocytes and mature moDCs. Loosely adherent monocytes observed 2 days after isolation from human whole blood. After 5 days in culture with GM-CSF and IL-4, circular immature moDCs were observed. After 24 h stimulation with LPS, mature moDCs exhibited cell protrusions.

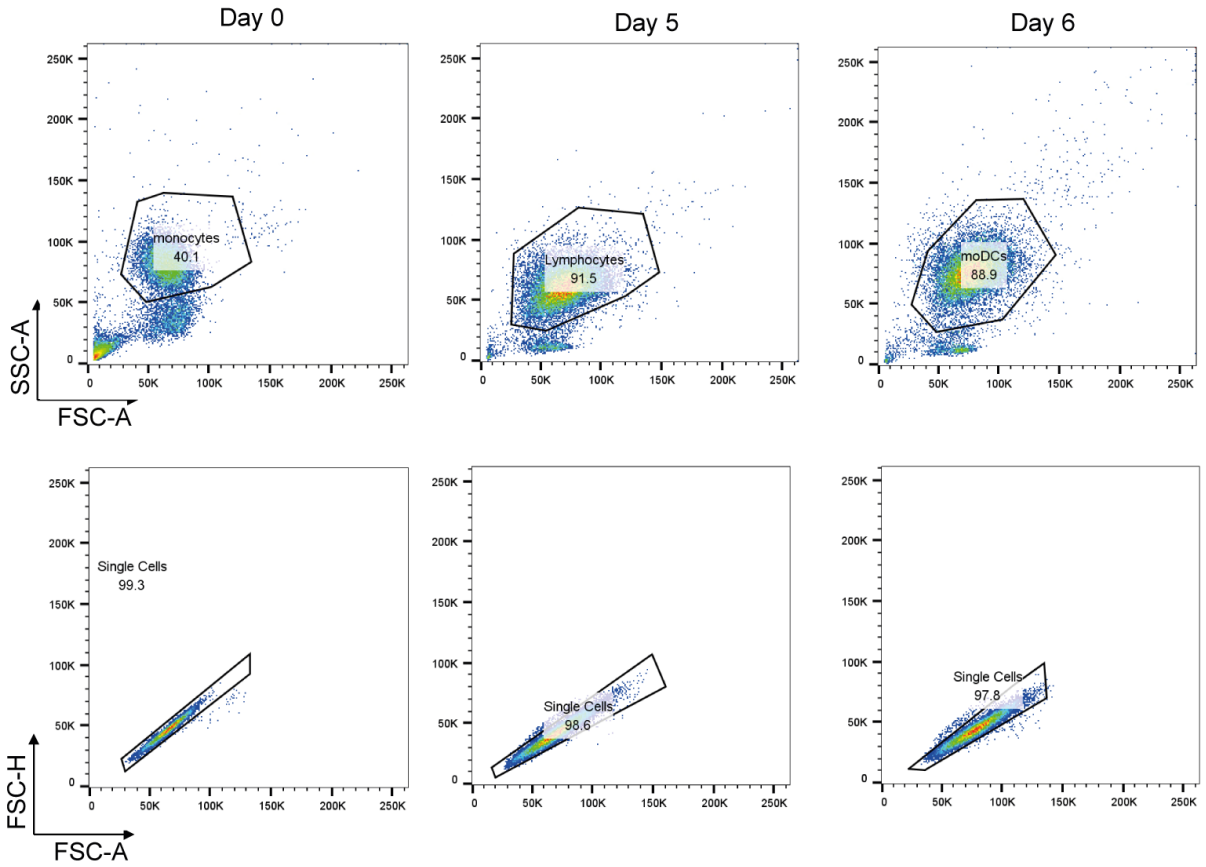

Figure S 2-6: Gating for moDC differentiation and maturation experiments. Representative plots showing gates used for analysis of isolated monocytes, differentiated moDCs and moDCs stimulated for 24 h with LPS.

Establishment of a microfluidic platform to study immune cell migration

Neutrophil viability was studied to assess the suitability of the proposed protocols and to identify a suitable imaging window for subsequent experiments. Live neutrophils were stained with CFSE and dead cells were stained with propidium iodide. Quantitative analysis of acquired images showed that neutrophil viability decreased to 78% after 18 h and substantially decreases to 23 % after 24 h (Figure S2-7A). To maintain high levels of viability during the experimental window, the previously established imaging duration of 10 h was used.

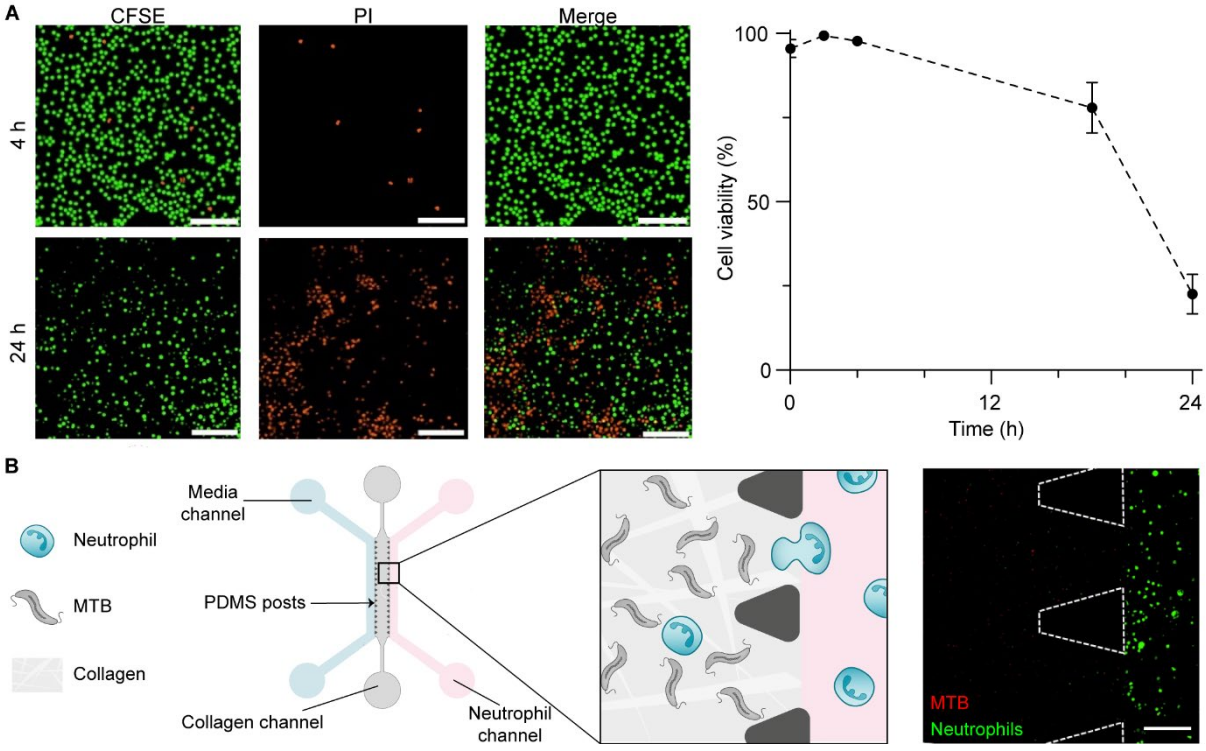

Figure S 2-7: Assessment of neutrophil viability and seeding of neutrophils in microfluidic device. (A) Representative images and quantification of neutrophil viability over 24 h (n= 3 replicates from 1 donor; mean ± SD; scale bar = 100 µm). **(B)** Schematic representation of three-channel device consisting of a central MTB-collagen channel and two media-filled side channels. Representative images of neutrophils and MTB embedded in collagen 10 h after after seeding and imaging. Scale bar = 100 µm.

Neutrophil migration was studied in a three-channel microfluidic device (Figure S2-7B). This design consisted of a central channel seeded with MTB suspended in collagen that is separated from two adjacent channels by PDMS posts. Primary neutrophils were injected into one of the side channels and media was injected into the other channel ensure nutrient supply and maintain hydration in the device. Although migration was not observed in pilot experiments these experiments still served to demonstrate the potential utility of the device for investigating neutrophil migration. MTB remained confined and well dispersed within the collagen hydrogel,

which is crucial for the establishment of a chemoattractant gradient. Additionally, morphological changes in the neutrophils were not observed, suggesting that activation and rapid apoptosis were not induced by the handling and injection of the cells in the device.

Future experiments could incorporate an endothelial cell monolayer seeded in the neutrophil channel. This would provide cell-cell contacts that facilitate migration of neutrophils into collagen (*207*). In addition, a sufficiently strong chemotactic gradient could be established by adapting the filling of the device. Other three-channel systems used to study neutrophil migration typically consist of a channel containing a chemoattractant, a matrix-filled central channel and a sink channel filled with media to facilitate the establishment of a gradient (*208*, *209*). The Kamm design can accommodate such an approach by filling one of the side channels with MTB or MTB-conditioned media and establish a chemoattractant gradient through the central collagen hydrogel. As a positive control, fMLP could be used to validate the establishment of sufficient chemoattractant gradients in the device and to adjust the dimensions of the device, if necessary.

3. MTB-liposome conjugates as effective drug delivery agents

3.1. Introduction

Nanoparticle drug carriers have the potential to improve tumour targeting and reduce systemic toxicity by modifying the biodistribution and pharmacokinetics of their therapeutic payloads (1, 2). A range of nanocarrier systems, including liposomes, micelles and polymeric nanoparticles, have been designed to increase the efficacy and safety of systemically delivered therapies (*210*). Liposome-based systems, consisting of amphiphilic phospholipids assembled in spherical bilayers, are of particular interest because of their versatility and adaptability. The amphiphilic nature of phospholipids enables encapsulation of hydrophilic drugs in the aqueous core of the liposome, while hydrophobic drugs can be embedded within the lipid bilayer. Furthermore, the physicochemical properties of liposomes can be tuned for controlled payload release, increased blood circulation half-life and enhanced accumulation in tumours (*211*). Doxil, the first approved liposomal nanodrug, has selective tumour localization and produces improved clinical outcomes compared to free doxorubicin (*212*).

Although nanoparticle delivery systems provide a range of possibilities for improving treatment outcomes, limited delivery efficiency has resulted in a translational gap between preclinical models and human patients. A meta-analysis on the delivery efficiency of nanoparticles discovered only 0.7% of the injected dose reaches solid tumours (6). This is attributed to the heterogeneity the enhanced permeability and retention (EPR) effect, the presence of larger gaps in the endothelial lining of capillaries in tumours, being higher than previously assumed. Additionally, tumours that grow rapidly frequently develop avascular regions that require long-range diffusion of drugs for effective

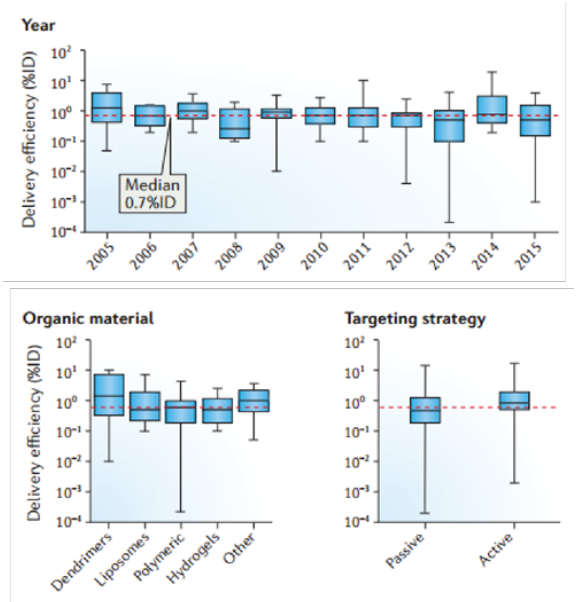

Figure 3-1: Analysis of delivery efficiency of nanoparticle delivery systems. Low delivery efficiency in solid tumours observed in publications from 2005-2015 irrespective of nanoparticle formulation. Reproduced from Wilhelm *et al.* (6).

delivery. However, nanoparticle diffusion is limited by the dense extracellular matrix and elevated interstitial pressure in tumours, which impairs convective fluid flow (*10–12*).

For these reasons, interest has grown in using agents with targeting capabilities and self-propulsion that enable them to navigate through dense tissue and overcome elevated interstitial pressures. Flagellated bacteria that are innately responsive to external cues have been integrated with liposomal cargo for enhanced delivery to distal tumour regions. Taherkhani *et al.* conjugated liposomes to the MTB strain MC-1 via an amidation reaction by utilizing the primary amine groups on the cell membrane (*85*). *In vivo,* 55% of MTB-liposome conjugates (MTB-LP) accumulated in hypoxic tumour regions following peritumoural injection and guidance using externally applied DMF (*86*). The MTB strain AMB-1 has also been used as a magnetically controllable motile carrier of indocyanine green nanoparticles for photothermal therapy (*87*). MTB-LP were delivered via peritumoural injection and magnetic field gradients were used to promote tumour accumulation. NIR irradiation at the tumour site resulted in the inhibition of tumour growth.

Having established the suitability of the MTB strain AMB-1 for use in physiological environments in Chapter 2, here, the use of MTB-LP as drug delivery agents is investigated. The MTB–LP complex combines the adaptability of liposomes with the functionality of magnetic-based platforms to produce a self-propelling, guidable agent for targeted drug delivery. Liposomes functionalised with either carboxyl or azide groups were fabricated using thin film hydration and the reaction efficiency of two coupling approaches to generate MTB-LP were compared. The use of MTB-LP for effective delivery of 5-fluorouracil (5-FU), a widely used antimetabolite, was investigated. The therapeutic effect of MTB-LP on apoptosis and cell proliferation for two cell lines was assessed. This study established the potential of the MTB-LP system as a versatile, complementary drug delivery platform.

3.2. Results

Experiments were designed and executed by Tinotenda Gwisai, unless otherwise specified. Experiments in section 3.2.1 were performed with assistance from Simone Hersberger and experiments presented in Figure 3-6C were performed with assistance from Sina Günther.

3.2.1. Effective payload release from different liposome formulations

The well-established thin film hydration method was used to fabricate liposomes functionalised with either carboxyl or azide groups (Figure 3-2A). Lipids were dissolved in chloroform and a thin film was generated by vacuum drying. The lipid film was rehydrated in an aqueous suspension containing a model payload. Sequential extrusion of multilamellar vesicles through polycarbonate membranes of decreasing pore size resulted in the reproducible formation of monodisperse liposomes with a diameter close to the pore size of 200 nm. This was reflected in the size distribution and polydispersity indices of both liposome formulations which were 198.4 nm and 212.5 nm for carboxyl and azide-functionalised liposomes respectively (Figure 3-2B). Liposomes can also be fabricated using sonication, where cavitation resulting from acoustic pressure generates high local forces that disrupt multilamellar vesicles and form small unilamellar vesicles. However, sonication is less reproducible and typically resulted in more polydisperse liposomes (Figure S3-1).

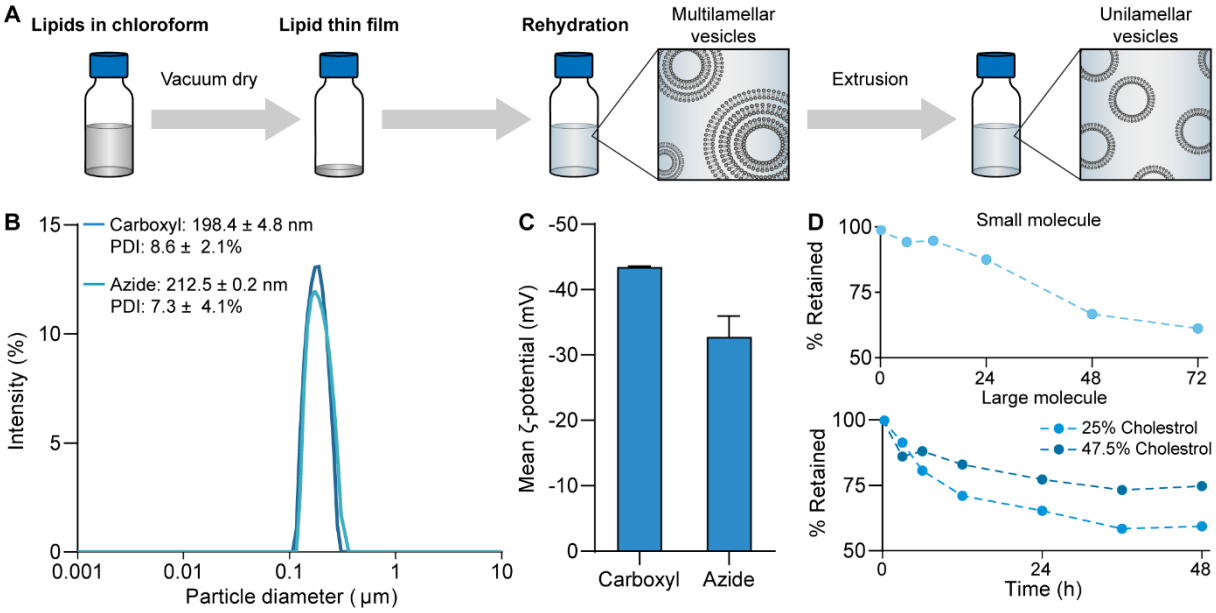

Figure 3-2: Liposome fabrication and characterisation. **(A)** Illustration of liposome fabrication using thin film hydration. **(B)** Average size distribution of liposomes functionalised with either carboxyl or azide groups. **(C)** Zeta potential measurements for both liposome formulations (n = 3 replicates; mean ± SD). **(D)** Release profile for a small molecule (calcein; 623 Da) and large molecule (FITC-dextran; 70 kDa).

Zeta potential measurements were performed to evaluate the surface charge of the liposomes (Figure 3-2C). The mean zeta potential for carboxyl-functionalised liposomes was -43.5 mV, confirming successful incorporation of negatively charged carboxyl groups on the outer membrane of the liposomes. Azide-functionalised liposomes have neutral end groups and, thus, a less negative zeta potential of -32.8 mV. A zeta potential magnitude above 30 mV indicates formation of a stable liposome suspension (*213–216*).

The release kinetics from liposomes for molecules of different sizes was also assessed (Figure 3-2D). Calcein, a self-quenching fluorescent dye with a molecular weight of 623 Da, was used as a model small molecule, while FITC-dextran with a molecular weight of 70 kDa was used as a model large molecule. Sustained and gradual release of calcein from carboxyl-functionalised liposomes was observed, with 61% payload retention after 72 h. Next, the release of FITC-dextran from azide-functionalised liposomes containing varying amounts of cholesterol were compared. Cholesterol has been shown to increase the encapsulation efficiency of payloads, which is of particular concern with larger molecules (*217*, *218*). Thus, a formulation containing cholesterol near the saturation limit of 50 mol% was assessed. In addition, liposomes containing 25 mol% cholesterol were fabricated to match reported formulations with favourable release properties (*218*). The rate of payload release was high in the initial 12 h for both formulations, after which gradual and sustained release was observed. Payload retentions of 59% for the 25 mol% cholesterol formulation and 74% for the formulation containing 47.5 mol% cholesterol were measured. Given the higher payload release and encapsulation efficiency (Figure S3-2) of the 25 mol% cholesterol formulation, this was identified as the more suitable formulation for effective payload delivery.

3.2.2. Covalent coupling of liposomes to MTB

Two covalent coupling approaches were investigated for the fabrication of MTB-LP conjugates. In comparison to widely-used affinity-based conjugation, covalent crosslinking is a robust technique which produces a stable chemical bond for *in vitro* and *in vivo* applications (*219*, *220*). The first approach investigated the covalent coupling of carboxyl-fuctionalised liposomes to the surface of MTB using carbodiimide-mediated amidation (Figure 3-3A). Carboxyl groups on the liposomes react with EDC to form an active O-acylisourea intermediate. Because the intermediate is readily hydrolysed, leading to regeneration of carboxyl groups, sulfo-NHS is added to the

reaction to form a more stable sulfo-NHS ester intermediate that reacts with primary amines on the MTB cell membrane to form a stable amide bond.

The second approach employed a copper-free click reaction to covalently couple liposomes to MTB (Figure 3-3B). Click reactions offer highly selective reactivity and this reaction was selected over copper-catalysed alternatives to preserve bacterial viability. In the first step of the reaction, MTB are functionalized with reactive dibenzocyclooctyne (DBCO) groups through an NHS reaction. Next, a fast, copper-free click reaction between DBCO-functionalized bacteria and azide-functionalized liposomes occurs, driven by the release of steric strain in the cycloalkyne molecule (*221*).

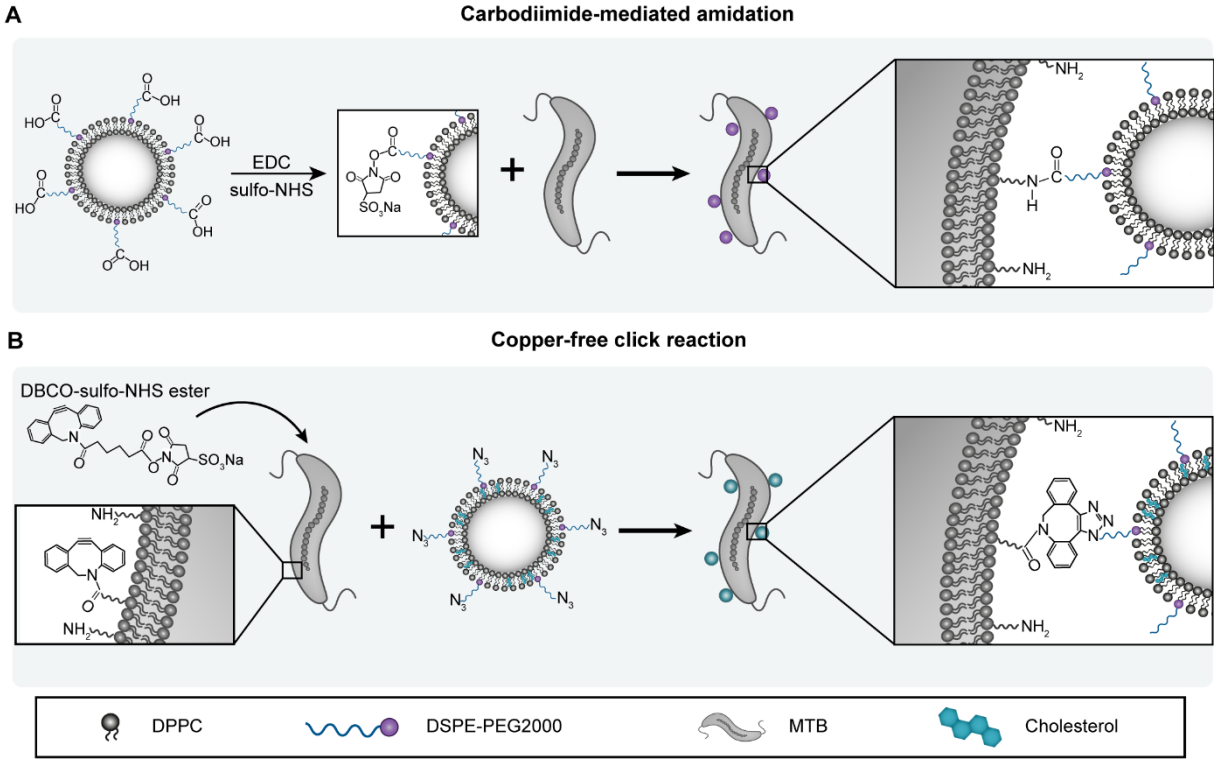

Figure 3-3: Covalent coupling approaches to fabricate MTB-LP conjugates. (A) Schematic showing coupling of carboxylated liposomes to MTB using carbodiimide-mediated amidation. **(B)** Illustration of copper-free click reaction to couple azide-functionalised liposomes to DBCO-functionalised MTB.

Both approaches utilise terminal amine groups present in phospholipids, LPS and various surface protein assemblies on the bacterial cell membrane (*222*). To develop protocols for the reactions, an estimate of the number of primary amine groups on the surface of MTB was determined using a reaction between primary amines with fluorescamine. The reaction produces a detectable fluorescent product and is extensively used to quantify amino acids and proteins (Figure 3-4A) (*223*). The estimated number of amines decreased with increasing bacterial concentrations (Figure 3-4B). Since there was an insufficient amount of fluorescamine present to react with the

excess amine groups in MTB suspensions at higher concentrations, these values represent an underestimation of the number of amines per bacterium. Therefore, lower MTB concentrations were used to provide an estimate of the number of amines per bacterium, which was found to be approximately 2.8 × 10^9 amines/MTB.

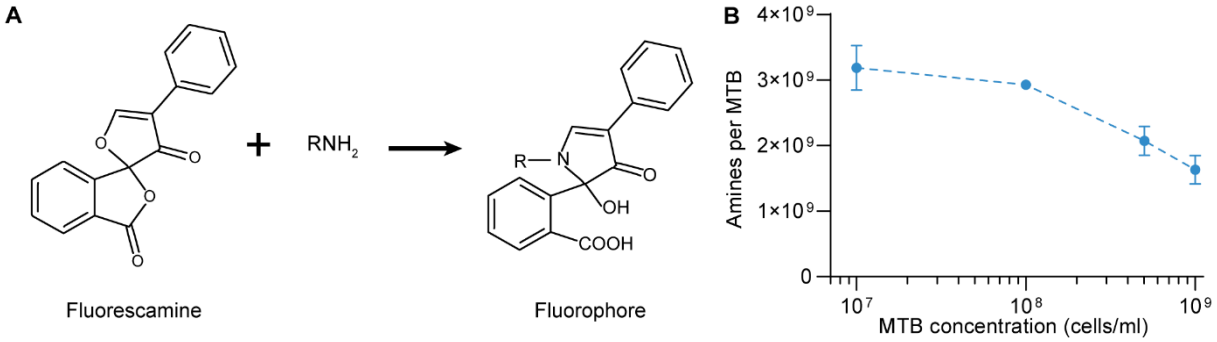

Figure 3-4: Quantification of amines on MTB cell membrane. **(A)** Reaction of fluorescamine with primary amines to produce a detectable fluorescent product. **(B)** Estimated number of primary amines per MTB at various bacterial concentrations (n = 2; mean ± SD).

Based on these estimates, conjugation with either carbodiimide crosslinking or a click reaction was performed and compared. In these experiments, DiO, a green fluorescent, lipophilic carbocyanine dye, was incorporated into the lipid bilayer. This enabled imaging and quantification of MTB-liposome conjugation.

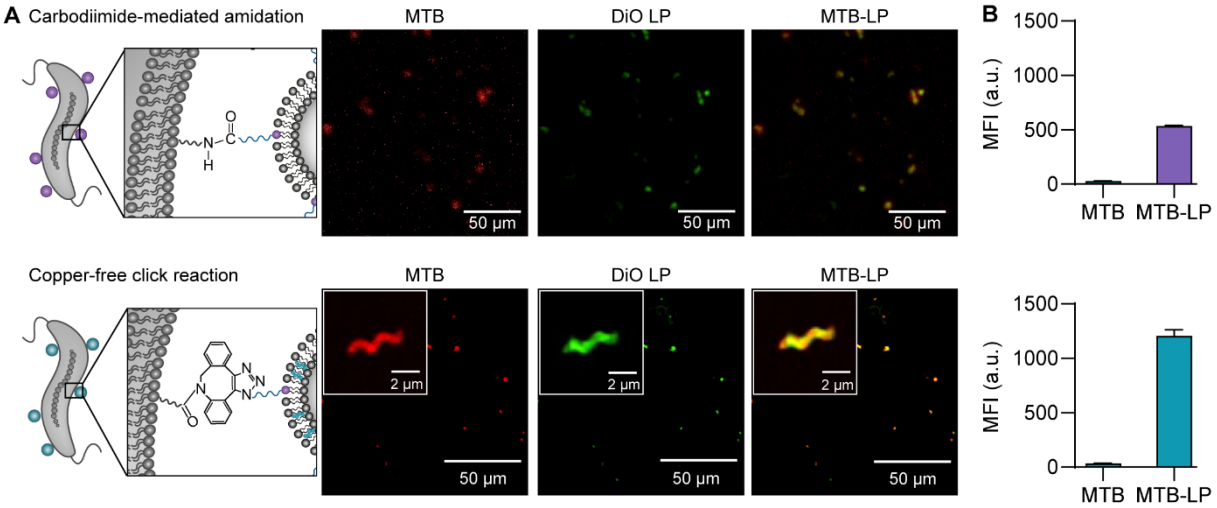

Figure 3-5: Comparison of reaction efficiency. **(A)** Confocal images of conjugates fabricated using either carbodiimide-mediated amidation or a copper-free click reaction. MTB were stained with far-red and liposomes were tagged with DiO (DiO-LP; green). **(B)** Quantification of fluorescence intensity for MTB-LP with FITC-dextran-loaded liposomes fabricated using carbodiimide crosslinking and MTB-LP with DiO-labelled liposomes fabricated using copper-free click chemistry. Values normalised to fluorescence intensity of respective liposomes (n = 3; mean ± SD; MFI = mean fluorescence intensity).

Images showed co-localisation of fluorescence signal from MTB and liposomes, confirming successful conjugation with both reactions (Figure 3-5A). Carbodiimide crosslinking resulted in

a 19-fold increase in fluorescence compared to MTB alone, while the copper-free click reaction resulted in a 35-fold increase in fluorescence (Figure 3-5B). Accordingly, the copper-free click reaction was selected as the coupling approach for fabricating MTB-LP conjugates and further characterisation to establish and improve the efficacy of the reaction was performed (Figure S3-3).

3.2.3. Complementary therapeutic effects of MTB-LP

The efficacy of MTB as a drug delivery vehicle was investigated using 5-FU, a widely used antimetabolite, as a model drug. 5-FU is an analogue of uracil, one of four nucleobases that comprise RNA, which is consumed more rapidly by cancer cells than healthy cells (*224*). The hydrogen atom in the C-5 position in uracil is substituted with a fluorine atom in 5-FU. The 5-FU metabolites fluorouridine, fluorodeoxyuridine triphosphate and fluorodeoxyuridine monophosphate disrupt RNA synthesis, DNA repair and also inhibit thymidylate synthase (*225*). Inhibition of this enzyme leads to an accumulation of metabolites that cause DNA damage and ultimately induce apoptosis via stabilization of the tumour suppressor protein p53 (*225*). 5-FU has been shown to increase survival in colorectal cancer, breast cancer and cancers of the aerodigestive tract (*226*, *227*). Although the use of 5-FU has major benefits, systemic administration often leads to major side effects, including fever, fatigue, nausea, anaemia, and neuropathy (*227*). Thus, as with other chemotherapeutics, targeted delivery is of interest to localise the effects of the treatment to tumour sites.

The use of the MTB-LP platform for localised delivery of this cytotoxic molecule was explored. Since 5-FU has been shown to have antibacterial activity (*228*, *229*), the effect of 5-FU on MTB was first investigated. 5-FU has been shown to disrupt DNA metabolism in bacteria and is particularly effective against Gram-positive bacteria (*229*). To ensure that viability of Gram-negative MTB is not compromised by 5-FU, live-dead staining was performed. Images showed comparable amounts of dead cells in samples incubated with and without 5-FU for 24 hours (Figure 3-6A). Bacterial proliferation was also assessed (Figure 3-6B). There was a significant decrease in MTB proliferation for samples incubated with 100 μM 5-FU, while the decrease in proliferation for bacteria incubated with the lower concentration of 10 μM 5-FU was less pronounced. Although MTB proliferation was reduced, 5-FU did not compromise viability or completely inhibit bacterial proliferation, validating its suitability as a model drug for further studies.

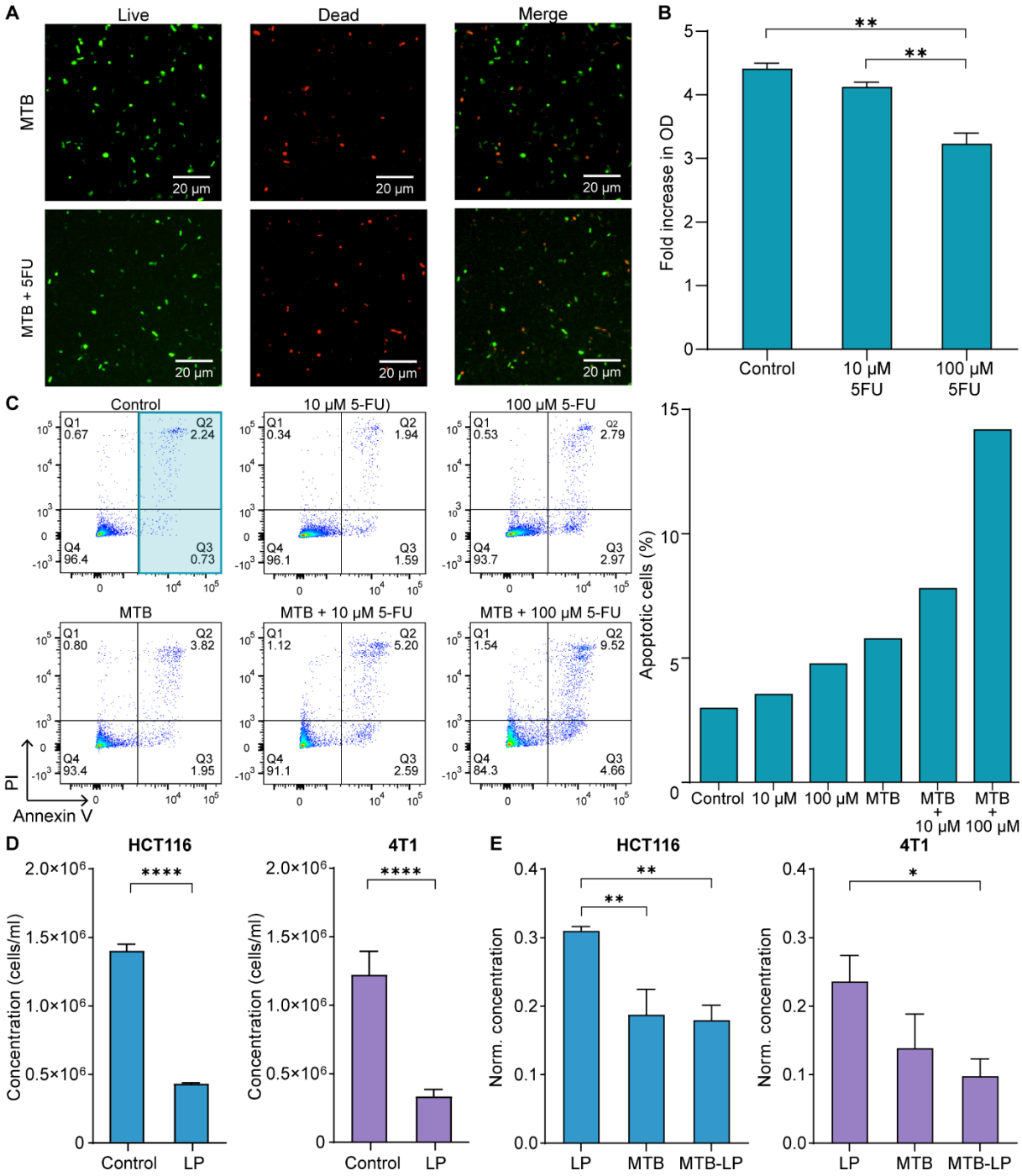

Figure 3-6: MTB-LP as delivery agents for 5-FU. **(A)** Confocal images of Syto9 and PI stained (dead) MTB following incubation with or without 10 µM 5-FU for 24 h in mammalian culture conditions. **(B)** Fold increase in OD_{600} measurements from 0 h to 24 h following incubation in media (control), 10 µM 5-FU or 100 µM 5-FU in mammalian culture conditions (n = 2; **P < 0.01 ANOVA). **(C)** Flow cytometry analysis following 24 h incubation with 10 µM and 100 µM 5-FU in the absence and presence of MTB at a ratio of 100:1 with respect to seeded cancer cells (n = 1). **(D)** Assessment of cell proliferation for HCT116 and 4T1 cells following 32 h incubation with or without 5-FU-loaded liposomes (LP) (n = 3; mean ± SD; ****P < 0.0001 ANOVA). **(E)** Cell proliferation normalised to untreated controls following 32 h incubation with LP, MTB or MTB-LP (n = 3; mean ± SD; *P < 0.05, **P < 0.01 ANOVA).

It has been shown that 5-FU is most efficient when used in combination with other therapies (*230*, *231*). Moreover, bacteria have been shown to drive cancer cells to cycle from G0/G1 to

S/G2/M, increasing their susceptibility to chemotherapy (*232*, *233*). Thus, the ability of MTB to enhance the therapeutic efficacy of the drug was investigated. Since 5-FU is the backbone of chemotherapeutic regimes for colorectal cancer (*234*), experiments were performed using the human colorectal cancer cell line HCT116. This cell line was also selected for its susceptibility to 5-FU (Figure S3-4). In an initial experiment, the combined effect of MTB and 5-FU in solution on the induction of apoptosis was investigated. After 24 h of co-culture, cells were stained with annexin V-FITC and PI and analysed using flow cytometry (Figure 3-6C). Annexin V binds to phosphatidylserine which only appears on the extracellular membrane when cells initiate apoptosis. Late apoptotic and necrotic cells have compromised membrane integrity, making them permeable to PI. There was a slight increase in the amount of early and late apoptotic cells in samples treated with 10 µM 5-FU compared to untreated controls, while the effect was more pronounced for samples treated with either 100 µM 5-FU or MTB. Notably, a substantial increase in apoptotic cells was observed for samples treated with a combination of 5-FU and MTB. A 2.6-fold and 4.8-fold increase in apoptosis was observed in samples treated with MTB combined with 10 µM and 100 µM 5-FU respectively, compared to untreated controls. This suggests that MTB may be used as a complementary therapy to potentially enhance the efficacy of cytotoxic drugs.

Having established the potential combined effect of MTB and 5-FU, the efficacy of the MTB-LP platform was investigated. In contrast to the previous experiment, only moderate effects were observed after 24 h, likely a result of gradual diffusion of 5-FU from liposomes compared to 5-FU in solution (Figure S3-5A). Pronounced cell death and cell debris were observed after 48 h of co-culture in conditions containing MTB or MTB-LP, making it difficult to resolve differences in the effect of the treatments (Figure S3-5B). Thus, subsequent experiments assessing the effect of MTB-LP on cell proliferation were performed at an intermediate timepoint of 32 h to improve the resolution of the readout.

As a basis for comparison, the effect of MTB-LP on proliferation was investigated using cell lines with different p53 statuses. HCT116 which has wildtype p53 and 4T1 cells which are p53 deficient were used (*235*, *236*). 4-T1 is a murine breast cancer cell line typically used as a syngeneic invasive cancer model. Using cell lines that require distinct pathways for 5-FU allows inferences to be made about the efficacy of the MTB-LP system for treating a wide range of cancer types. The efficacy of the nanocarrier alone was first assessed (Figure 3-6D). A significant decrease in

proliferation for both cell lines was observed compared to untreated controls. Next, the effect of the presence of MTB and MTB-LP were evaluated (Figure 3-6E). For both cell lines, co-culture with MTB resulted in a substantial reduction in cell proliferation, with a significant decrease observed in HCT116. Treatment with MTB-LP conjugates also resulted in a significant decrease in proliferation compared to liposomes only. For HCT116, the effect of MTB and MTB-LP were comparable, suggesting that most of the observed decrease in proliferation was a result of the presence of MTB. In contrast, there was a further decrease in proliferation with MTB-LP compared to MTB alone for 4T1, suggesting that MTB-LP can improve the therapeutic efficacy of a delivered payload and could potentially be used for combination therapy.

3.3. Discussion

This study investigated the use of MTB-LP as a living delivery agent with the ability to enhance the therapeutic efficacy of their payload. Liposomes were selected as drug carriers because of their versatility, which was illustrated by the ability to effectively deliver payloads with wide ranging molecular weights. Liposomes functionalised with either carboxyl or azide groups were used to fabricate MTB-LP conjugates using two reactions. A copper-free click reaction that was found to be the more efficient.

Having developed an efficient method for generating MTB-LP, the possible complementary effect of 5-FU and MTB on increasing the induction of apoptosis and inhibiting cell proliferation was assessed. Inducing apoptosis is of interest as dying cells release DAMPs which promote the uptake of cancer cell material by DCs that prime cytotoxic T cells to mount a tumour-specific immune response. In initial experiments where MTB was combined with 5-FU in solution, a substantial increase in apoptosis was observed, indicating a possible synergistic effect between MTB and 5-FU. Although the antitumour activity of 5-FU is chiefly attributed to its ability to activate p53-dependent cell growth arrest and apoptosis, other mechanisms of action have been reported (*225*). The efficacy of MTB-LP was assessed in two cell lines with different p53 statuses. Reduced cell proliferation was observed in both cell lines in response to treatment with 5-FU-loaded liposomes. Interestingly, the presence of MTB alone seemed to have a pronounced effect on arresting proliferation in HCT116 cells, since significant differences were not observed between samples cultured with MTB or MTB-LP (Figure 3-6E). MTB have been shown to compete with cancer cells for essential nutrients like iron, thus acting as a self-replicating iron-chelator, and HCT116 cells are highly susceptible to treatment with iron chelators (*237–239*). In 4T1 cells, a

notable reduction in proliferation was observed following co-culture with MTB-LP compared to MTB alone. Moreover, treatment with MTB-LP was shown to be significantly more effective than treatment with liposomes alone, indicating a possible sensitizing effect of the MTB.

Overall, these studies established the potential of the MTB-LP system as a versatile, complementary drug delivery platform. These results provide evidence for a possible synergistic effect between MTB-LP and the delivered payload, and suggest that using MTB-LP as delivery agents for chemotherapeutics might increase treatment efficacy. To ascertain the precise mechanism through which MTB enhances the efficacy of 5-FU, assessment of cell metabolic activity, caspase activation and the expression stress-related proteins could be performed. Additionally, evaluating the release of DAMPs, such as ATP and calreticulin, from cancer cells in co-culture with MTB-LP may provide further insights on the ability of the system to illicit an antitumour immune response. Future studies could also be conducted using additional cell lines, including human breast cancer cells and murine colorectal cancer cells, to further assess the use of the platform for a broad range of cancer types.

3.4. Materials and methods

3.4.1. Materials

The IVISbrite 4T1 Red F-luc Bioluminescent Tumour Cell line (Bioware Brite) was purchased from PerkinElmer (Waltham, MA). HCT116 (human colorectal cancer, ATCC® CCL-247™) *Magnetospirillum magneticum* (ATCC 700264), Wolfe's Vitamin Solution and Wolfe's Mineral Solution were purchased from American Type Culture Collection (Manassas, VA). 1,2-dipalmitoyl-sn-glycero-3-phosphocholine (DPPC) and 1,2-distearoyl-sn-glycero-3-phosphoethanolamine-N-[carboxy(polyethylene glycol)-2000] (sodium salt) (DSPE-PEG2000-COOH) were purchased from Avanti Polar Lipids, Inc. (Alabaster, AL). Calcein was purchased from Carl Roth (Karlsruhe, Germany). Penicillin/Streptomycin (P/S) was purchased from Corning (Corning, NY), fetal bovine serum (FBS) was purchased from BioWest (Nuaillé, France), 1-ethyl-3-[3-(dimethylamino)propyl]-carbodiimide (EDC) was purchased from TCI EUROPE (Eschborn, Germany) and sulfo-DBCO-NHS ester was purchased from Broadpharm (San Diego, CA). Potassium phosphate, succinic acid, tartaric acid, sodium nitrate, ascorbic acid, sodium acetate, resazurin sodium salt, sepharose CL-2B, bovine serum albumin (BSA), 3,3′-Dioctadecyloxacarbocyanine perchlorate (DiO), phosphate-buffered saline (PBS) and

N-hydroxysulfosuccinimide (sulfo-NHS), Fluorescein isothiocyanate–dextran (FITC-dextran) MW70000, puromycin, 5-fluorouracil (5-FU) and fluorescamine were all acquired from Sigma-Aldrich (St. Louis, MO). RPMI-1640, McCoy's 5A, Annexin V-FITC Apoptosis Detection kit, Baclight Bacterial Viability kit and the CellTrace Far-Red cell proliferation kits were acquired from ThermoFisher Scientific (Waltham, MA).

3.4.2. Mammalian cell culture

HCT116 cells were cultured in modified McCoy's 5A medium supplemented with 10% FBS and 1% P/S. 4T1 cells were cultured in RPMI-1640 supplemented with 10% FBS and 5 μg/mL puromycin. Cells were cultured at 37°C and 5% CO_2 in a humidified atmosphere. One day before experiments, media was replaced with antibiotic-free media. Cell concentration was determined using a haemocytometer and the required number of cells was seeded for each experiment as specified.

3.4.3. Magnetotactic bacteria culture

M. magneticum strain AMB-1 was cultured in revised magnetic spirillum growth medium (MSGM) which contained 5.0 mL of Wolfe's Mineral Solution, 0.45 ml of 0.1 % resazurin, 0.68 g potassium phosphate, 0.37 g succinic acid, 0.37 g tartaric acid, 0.12 g sodium nitrate, 0.035 g ascorbic acid and 0.05 g sodium acetate per litre of distilled water. The final pH was adjusted to 6.9 with 1 M NaOH before autoclaving. Prior to use, Wolfe's Vitamin Solution (1000x) and 10 mM ferric quinate (200x) were added to the media. MTB were grown under microaerophilic conditions at 30 °C and suspensions grown for 5 to 7 days were used for all experiments.

3.4.4. Liposome fabrication and characterization

Liposomes were prepared from a total of 14 μmol of lipids using thin-film hydration. Lipids were dissolved in chloroform at the relevant molar ratios and dried to a thin film under nitrogen with further vacuum desiccation overnight at room temperature. For imaging, 0.1 mol% DiO was combined with the lipids. The lipid film was hydrated with 1 mL payload solution and placed in a water bath for 1 h at 50 °C with continuous stirring. Liposomes were downsized using bath sonication or sequential extrusion on a heating block (Avanti) at 50 °C. For extrusion, liposomes were passed 21-times each through a 400 nm followed by a 200 nm polycarbonate membrane (Whatman). Unencapsulated payload was removed by size exclusion chromatography using a

Sepharose CL-2B column or washed 3 times with ultracentrifugation at 16,000 × g for 20 min at 4 °C. Details for each formulation can be found in Table 3-1 below:

Table 3-1: Lipid formulations and fabrication

Formulation			Functional group	Payload	Purification
DPPC	Cholesterol	DSPE-PEG2000-R			
95	0	5	R = COOH	35 mM calcein	SEC
70	25	5	R = COOH	0.49 mg/mL FITC-dextran	SEC
47.5	47.5	5	R = COOH	0.49 mg/mL FITC-dextran	SEC
70	25	5	R = azide	5 mg/mL 5-FU	Ultracentrifugation

The average diameter, size distribution and zeta potential of the liposomes were determined by dynamic light scattering (DLS) (Litesizer 500, Anton Paar).

3.4.5. Quantification of primary amines on MTB

The number of primary amine groups on the surface of MTB was evaluated using a reaction with fluorescamine. The MTB suspension was washed three times in PBS with centrifugation at 9 400 × g for 10 min. For the reaction, 100 µL of 10mM fluorescamine was added dropwise to MTB suspensions with final concentrations between 1×10^7 and 1×10^9 MTB/mL. After incubation for 5 min at RT, fluorescence measurements were performed at 430/465 nm using a Spark multimode microplate reader (Tecan).

3.4.6. MTB-liposome conjugation

MTB were stained prior to conjugation for imaging and quantification, otherwise unstained bacteria were used. MTB at a concentration of 1.5×10^8 cells/mL in PBS were stained using the CellTrace Far-Red cell proliferation kit. A stock solution was prepared according to the manufacturers protocol and 2 µL was added to the MTB suspension. Cells were incubated at room temperature for 20 min, protected from light with gentle agitation. After incubation, 10 µL of 1% BSA was added to the cell suspension for 5 min to remove free dye. Cells were pelleted and resuspended in PBS.

Bioconjugation was then achieved either through carbodiimide coupling or using a copper-free click reaction. For the carbodiimide coupling reaction, activation of carboxylated liposomes was accomplished by incubating 300 µL of liposome solution with EDC and sulfo-NHS (EDC/NHS/DSPE-PEG-COOH = 30:30:3, mol/mol) for 20 min in PBS (pH 5.5) at room temperature with gentle agitation. The activated liposomes were subsequently incubated with 1.5×10^8 MTB for 2 h at room temperature with gentle agitation. Unbound liposomes were separated from MTB-LP using a magnetic field gradient and the sample was redispersed in PBS (pH 7.4).

For the copper-free click reaction, 1.2 µmol of 150 mM sulfo-DBCO-NHS ester was added dropwise to 1×10^8 MTB in 200 µL PBS (pH 7.4) and incubated for 30 min at RT. MTB was washed three times by centrifugation at 5,000 × g for 10 min. DBCO-functionalized MTB were then incubated with azide-functionalized liposomes at a ratio of 1.75:1 azides to amines. Conjugates were washed three times by centrifugation at 5,000 × g for 10 min. Fluorescence measurements were performed at 430/465 nm using a Spark multimode microplate reader.

3.4.7. Assessment of the effect of 5-FU on MTB proliferation and viability

MTB suspensions at an optical density (OD_{600}) of 0.12 were added to a 12-well plate and 5-FU was added to the wells at a final concentration of either 10 or 100 µM. After incubation for 24 h at 37 °C, proliferation was assessed by evaluating the fold increase in OD_{600}. MTB viability was assessed using the BacLight bacterial viability kit according to manufacturer instructions.

3.4.8. Assessment of cancer cell proliferation and apoptosis

HCT116 and 4T1 cells were seeded at a density of 50 000 cells/well and incubated overnight at 37 °C and 5 % CO_2. Cells were cultured for up to 48 h with 5-FU at a final concentration of 10 µM or 100 µM, MTB or MTB-LP at a cell to MTB ratio of 1:100 or an equivalent amount of liposomes. Supernatants were collected and cells were harvested. Cell proliferation was assessed by comparing concentrations of the cell suspensions which was determined using a haemocytometer. Apoptosis was examined using an annexin V-FITC and PI staining kit according manufacturer instructions. Flow cytometry was performed and at least 10 000 events were recorded for each sample. Analysis was performed using FlowJo (version.10.4.2, Tree Star).

3.5. Supporting information

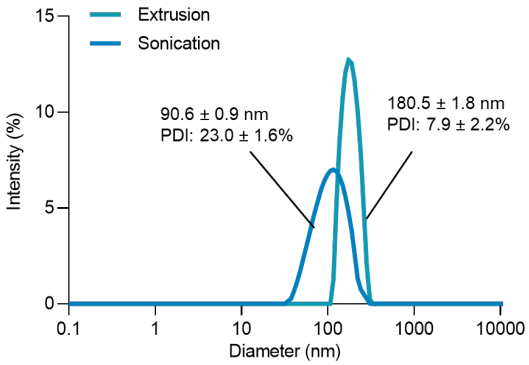

Figure S 3-1:Comparison of liposome downsizing approaches. Size distributions for liposomes fabricated using either extrusion or sonication.

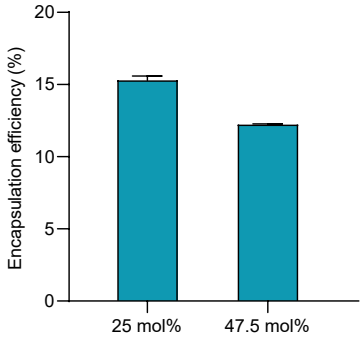

Figure S 3-2: Comparison of liposome encapsulation efficiency. Liposomes with 25 or 47.5 mol% were fabricated and loaded with FITC-dextran (70 kDa).

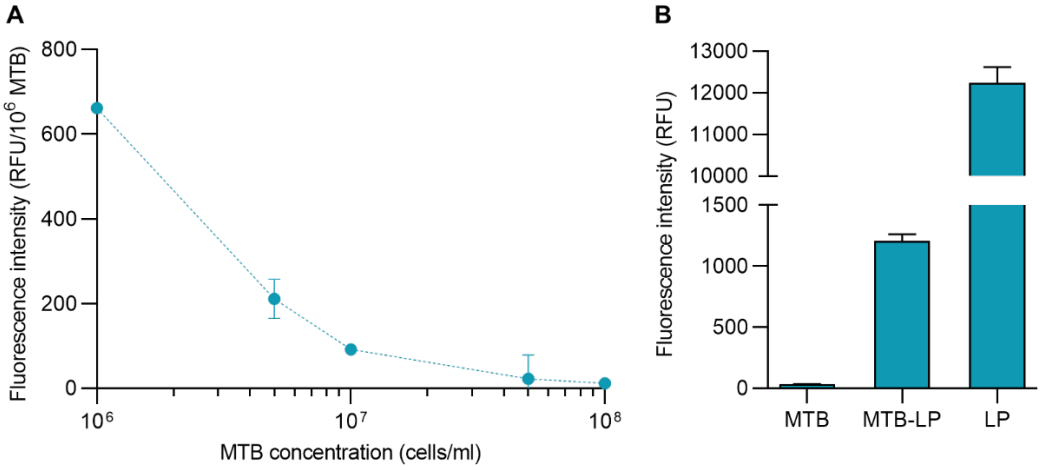

Figure S 3-3: Characterisation copper-free click reaction. (A) Conjugation was performed with MTB at different concentrations while the amount of DiO labelled liposomes was kept constant. As expected, reaction efficiency decreases with increasing MTB concentration, since there is an insufficient amount of liposomes to react with the excess amine groups in suspensions at higher concentrations. **(B)** Comparison of fluorescence intensity values for conjugates fabricated with suspensions at a concentration of 1×10^7 MTB/mL. Reaction efficiency was found to be approximately 10%.

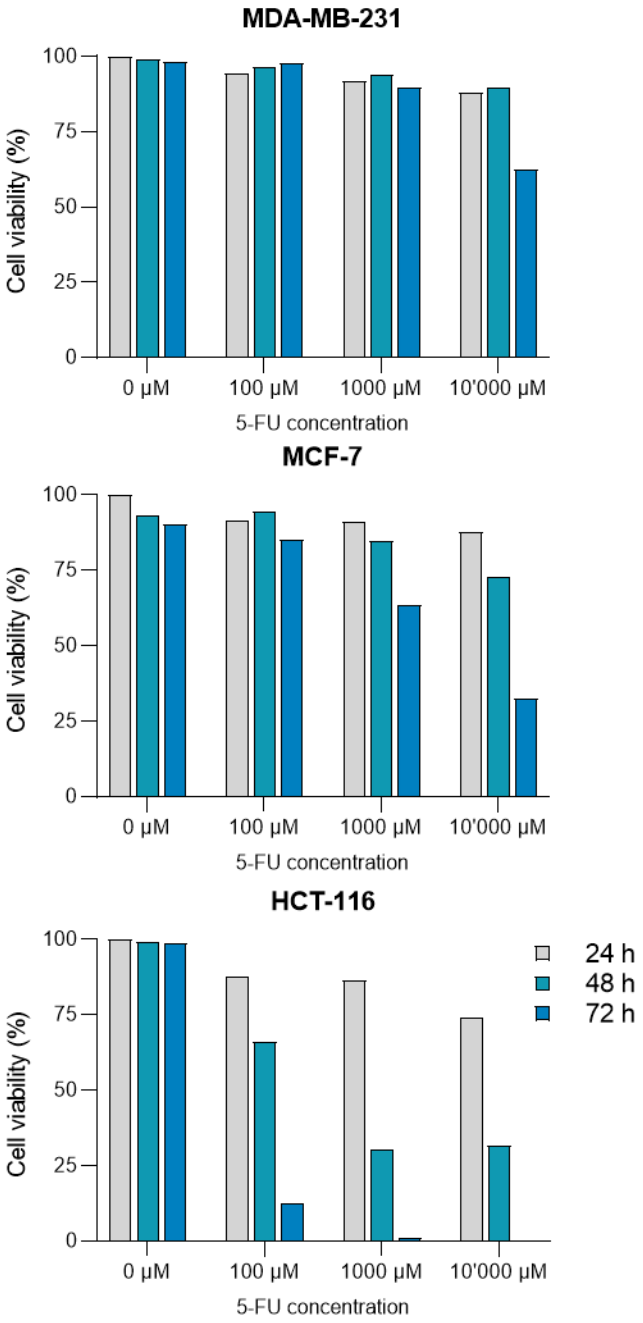

Figure S 3-4: Comparison of cell viability. MDA-MB-231 and MCF-7 and HCT116 cells were incubated with 5-FU at varying concentrations for up to 72 h. MDA-MB-231 and MCF-7 are both human breast cancer cell lines. Viability was determined using trypan blue exclusion.

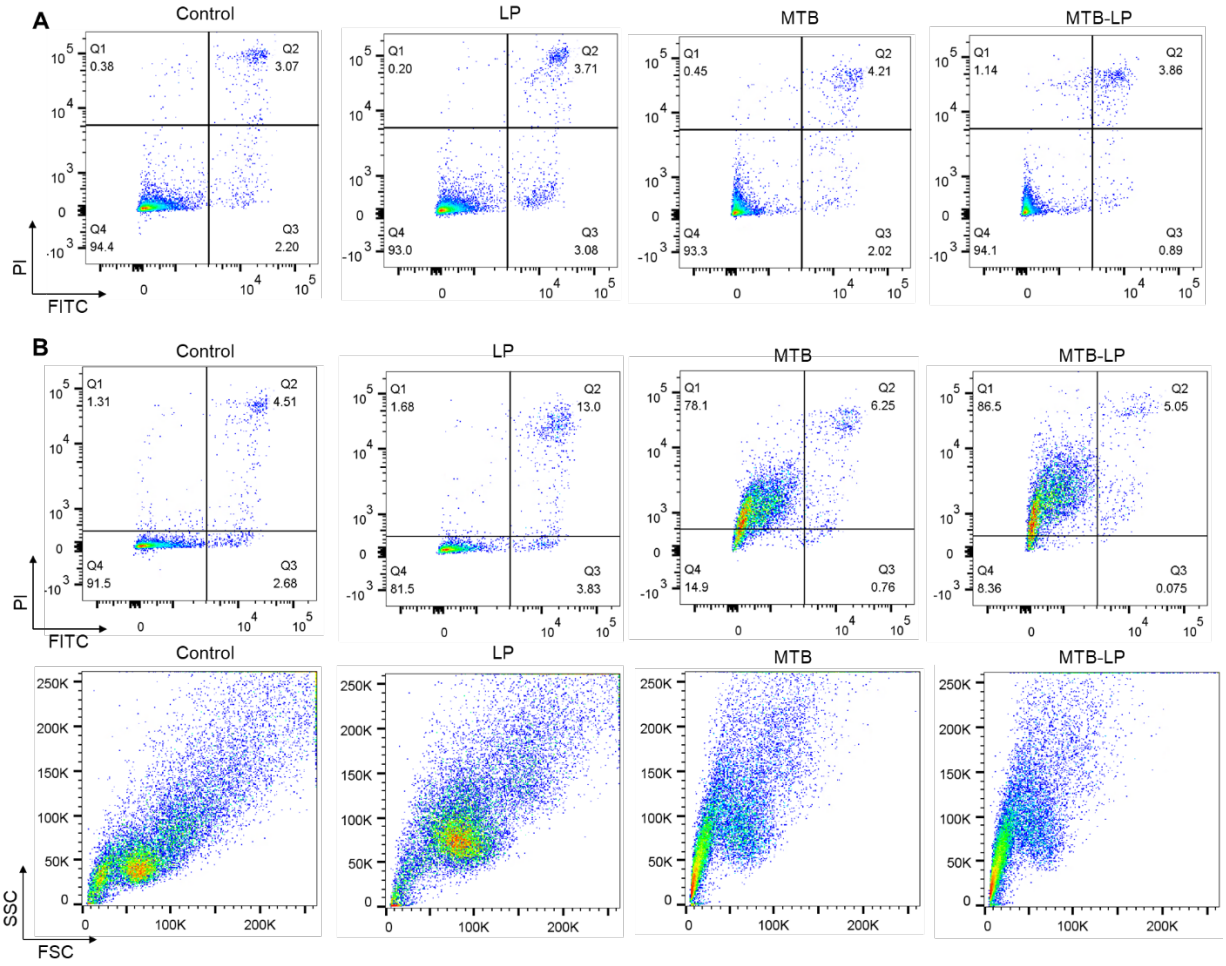

Figure S 3-5: Assessment of induction of apoptosis in HCT116 cells. **(A)** Representative flow cytometry plots of annexin-FITC and PI stained HCT116 cells following 24 h incubation in media only (control) or with liposomes, MTB or MTB-LP. **(B)** Representative scatter plots of annexin-FITC and PI stained HCT116 cells following 48 h incubation under specified conditions (top). Side and forward scatter plots showing the characteristics of cell populations after the specified treatment (bottom).

4. Magnetically enhanced tumour infiltration of MTB-liposome conjugates

Portions of this chapter are adapted from the manuscript "Magnetic torque-driven living microrobots for increased tumour infiltration", by Tinotenda Gwisai, Nima Mirkhani, Michael G. Christiansen, Thuy T. Nguyen, Vincent Ling and Simone Schuerle published in Science Robotics (2022).

4.1. Introduction

Bacteria that self-propel and preferentially colonize tumours hold promise as living microrobots for cancer treatment (*15*, *30*). Unlike conventional chemotherapeutics which are reliant on passive diffusion for transport, these living agents can actively overcome challenges posed by the pathological characteristics of the tumour environment (*4*, *6*, *9*). Tumour-targeting bacteria are particularly appealing because of their capacity to autonomously navigate through the body, transport a wide range of payloads, and modulate intratumoural inflammatory responses (*16–19*). To date, strains of *Salmonella, Mycobacterium*, and *Clostridium* have been tested in animal models and progressed to clinical trials for bacteria-based cancer therapy (*32*, *43*, *240*, *241*). Nevertheless, translation of this approach has been hindered by incomplete clinical responses, in part due to insufficient tumour colonization (*14*). Developing control strategies to enhance and accelerate accumulation of bacteria within tumours is essential to facilitate robust colonization and increase therapeutic efficacy.

Stimuli including chemical gradients, light, electric fields, and magnetic fields have been employed for wireless control of bacteria (*242–245*). Of these, magnetic fields are especially promising for medical use due to their precise spatiotemporal targeting, minimally-invasive deep tissue penetration, and well-established clinical safety (*246*). Recently, innately magnetic strains of bacteria acting as steerable therapeutic agents have been manipulated with external magnetic fields (*247*). In their native aquatic habitats, MTB biomineralize magnetite use magnetically assisted aerotaxis to migrate to regions of low oxygen concentration. *In vivo*, strains of MTB carrying payloads have been shown to preferentially proliferate in deoxygenated regions of tumours following peritumoural injection in the presence of a DMF or a magnetic field gradient (*173*, *248*). While these studies illustrate the promise of MTB as drug delivery agents, their potential for clinical translation is curbed by reliance on peritumoural administration, which is

suitable only for easily accessible tumours, in addition to limitations associated with the magnetic stimuli they employ. Using DMF inherently relies on MTB self-propulsion, which limits tissue penetration capability (*249*). Drawing MTB toward target sites with static field gradients also has fundamental shortcomings, especially in the context of deep targets, since magnetic field gradients rapidly diminish with increasing distance from their source (*250*, *251*).

This work establishes a hybrid control strategy that harnesses magnetic torque-driven motion followed by autonomous taxis-based navigation to enhance the infiltration of *Magnetospirillum magneticum* AMB-1 as a carrier for covalently-coupled liposomes (MTB-LP). Unlike some forms of magnetic stimulus, uniform RMF, like those employed here, can be generated at clinically relevant scales for deep sites within the body. MTB-LP infiltration in the presence of RMF was assessed using model tissue barriers. The Caco-2 Transwell system was used to establish that RMF increases MTB translocation across this robust cellular barrier. Extravasation was studied with computational models and in vitro, it is proposed that the main mechanism driving the enhancement of translocation is increased surface exploration resulting from torque-driven translational motion at the cell interface. Next, the spatiotemporal characteristics of magnetically driven MTB-LP infiltration is analysed and enhanced colonization in a 3D tumour model is observed. Finally, enhanced MTB tumour accumulation under RMF is demonstrated *in vivo*, while also employing more clinically relevant systemic intravenous administration. It is concluded that the MTB-LP platform combined with an RMF actuation scheme is a versatile system that could improve targeting and colonization of therapeutic bacteria in tumours. This work also lays the foundation for effective torque-based transport of other bacterial species imparted with magnetic responsiveness through genetic engineering or surface functionalization using magnetic nanoparticles.

4.2. Results

Experiments were designed and executed by Tinotenda Gwisai, unless otherwise specified. Michael G. Christiansen designed, executed and performed data analysis for experiments in section 4.2.1 with assistance from Lucien Stöcklin. Experiments in section 4.2.2 were performed with assistance from Thuy T. Nguyen. Nima Mirkhani designed and implemented the model presented in 4.2.3, and experiments in sections 4.2.7 and 4.2.8 were performed in collaboration with him.

4.2.1. RMF offers unique control advantages

Unlike DMF or gradient fields, the time-varying nature of RMF can be exploited for simultaneous actuation and monitoring of MTB, enabling the adjustment of actuation parameters during operation for improved localization and infiltration. In a proof-of-concept experiment, inductive detection of MTB during actuation was performed using a small scale, custom-built RMF magnetometer consisting of two pairs of nested Helmholtz coils (Figure 4-1A, Figure S4-1). Phase shifted sinusoidal currents were applied to each set of coils to produce a circularly rotating magnetic field. When exposed to RMF, the overall magnetic moment of the MTB varies in time by rotating, allowing the measurement of the resulting voltage induced in surrounding loops of wire. Inductive field probes for each pair of coils were placed in the central workspace along with symmetric sense and compensation coils that served to isolate inductive signal from the

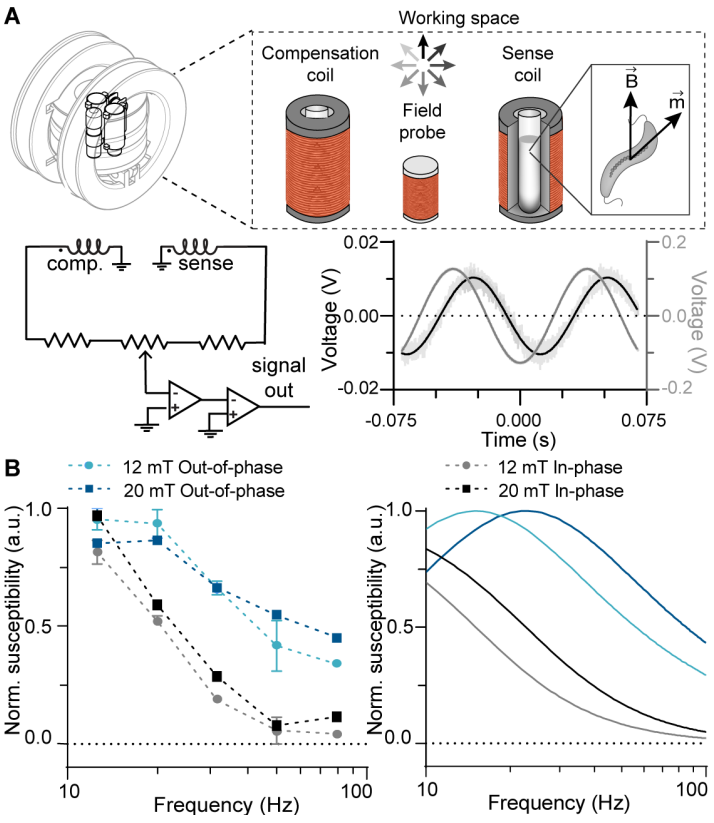

Figure 4-1: Inductive detection of MTB using an RMF magnetometer. **(A)** Cancellation and amplification scheme for RMF magnetometer. A typical signal detected from the MTB (measured at 12 mT at 12.6 Hz) and signal recorded from the in-phase field probe are shown. **(B)** Experimental in-phase and out-of-phase susceptibility (left; n = 3; mean ± SD) and analytical susceptibility data (right).

magnetization of the MTB. Following fine tuning of their cancellation via a potentiometer, the resulting signal was amplified and acquired. The magnetization of the MTB was phase shifted relative to the rotating field, reflecting the phase lag in the magnetic response of the bacteria.

Using a cosine function fitted to the in-phase field probe, integration was used to separate the acquired signal into in-phase and out-of-phase components of the susceptibility of the sample (Figure 4-1B). The experimental data was compared to analytical data to assess whether the detected signal generated by the MTB exhibited predicted characteristics (Supplementary Materials). Out-of-phase susceptibility at 12 mT and 20 mT peaked at 12.6 Hz and 20 Hz respectively, compared to 14 Hz and 24 Hz in the analytical data. The underlying trends for both the in-phase and out-of-phase susceptibility were as predicted by our models, confirming that we were able to detect MTB under actuation with rotating magnetic fields.

4.2.2. RMF enhances MTB translocation across Caco-2 monolayers

A range of strategies have previously been employed to manipulate MTB as living microrobots using external magnetic fields (Figure 4-2A). In the presence of DMF, the motion of the bacteria is dependent on the propulsive force (F_P) generated by their flagella and the fluidic drag force (F_D), which are equal and opposite when traveling at constant velocity. An estimate of the propulsive force is given by $F_P = \gamma v$, where γ is the linear drag coefficient and v is the linear velocity. For a velocity range of 19 - 49 μm/s (*252*, *253*), the propulsive force is estimated to be on the order of 0.1 pN.

In contrast to DMF, MTB self-propulsion is overridden when subjected to RMF. Viscous drag from the surrounding fluid creates a phase lag between the external field and magnetic moment of the MTB, giving rise to a magnetic torque that is exerted on the bacteria. The opposing hydrodynamic torque (τ_H) that defines the steady state lag angle between the MTB and magnetic field is governed by $\tau_H = \alpha\,\omega$, where α is the rotational drag coefficient and the angular frequency (ω) is equal to the frequency of magnetic actuation under synchronous rotation. An estimate of the force generated by this torque-based motion is given by $\frac{\tau_H}{r}$, where r is the distance from the axis of rotation, which is half the bacterial length. For angular frequencies in the range of 10 – 25 Hz at a field magnitude of 20 mT and distance r of 0.9 μm (Figure S4-2), the force generated is on the order of 1 pN. These estimates show that, on average, magnetic torque-driven motion generates forces that are an order of magnitude higher than those of MTB self-propulsion.

Static field gradients have also been employed to pull MTB towards a target site. Although this approach has shown efficacy in small animal models, an impracticable gradient of more than 1300 T/m would be required to produce a comparable force on the same magnetic moment (see Supplementary Text for detailed calculations).

We sought to examine whether the higher forces from torque-based motion produced by RMF can enhance the infiltration of MTB across biological barriers. We first characterized our magnetic control strategy under stringent conditions, employing a low field amplitude and a robust cellular barrier. Caco-2 cells cultured on Transwell membranes have been used extensively for the reconstitution of differentiated enterocyte-like monolayers to evaluate oral drug absorption and the translocation of various strains of bacteria (*254–256*).

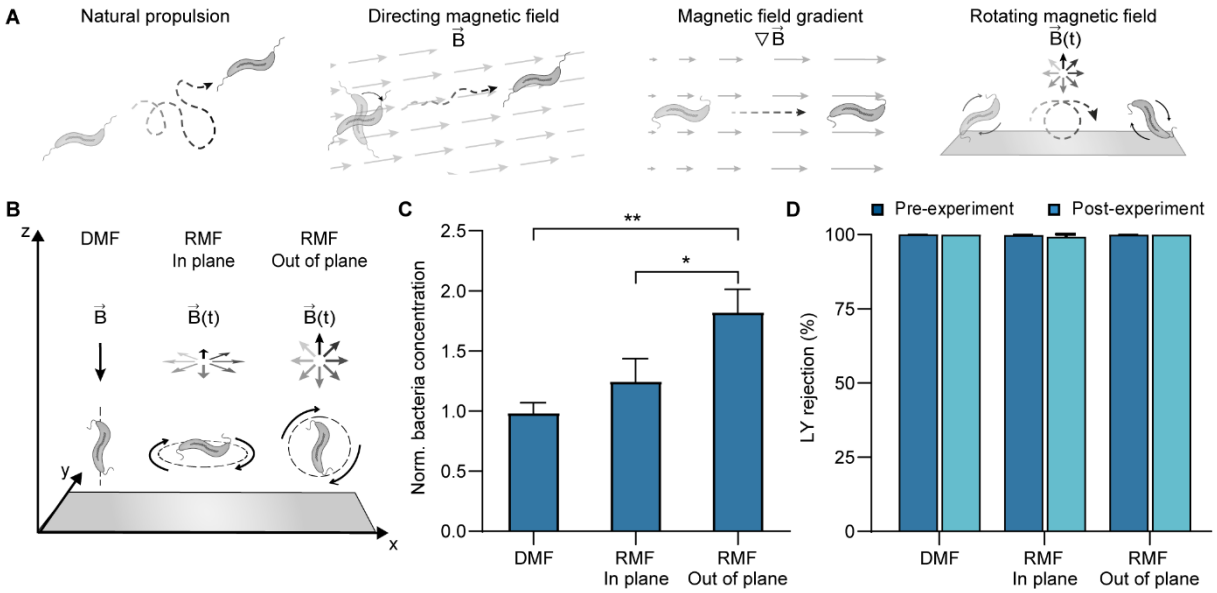

Figure 4-2: RMFs enhance translocation and enable inductive detection and spatially selective control of MTB. **(A)** Schematic illustrating various magnetic actuation strategies employed to manipulate MTB. **(B)** Schematic depicting the reference coordinate system used in all actuation experiments, and orientation of the bidirectional MTB strain (AMB-1) after exposure to directional static magnetic fields (DMF) and in-plane and out-of-plane rotating magnetic fields (RMF). **(C)** Comparison of normalized basolateral bacteria concentrations following 1 h exposure to either DMF, in-plane rotation or out-of-plane rotation, both at 14 Hz. In these experiments only, a magnetic force generated by spatial variation of the magnitude of the RMF or DMF (1 T/m) was applied along the – *z*-axis. Bacteria concentration was normalized to respective unactuated controls. (n = 3; mean ± SD; $^{*}P < 0.05$ and $^{**}P < 0.01$, ANOVA). **(D)** Pre- and post-experimental Lucifer yellow (LY) rejection values for DMF and in-plane and out-of-plane RMF (n = 3; mean ± SD).

MTB were added to the upper chamber of a Transwell insert with an established Caco-2 monolayer and placed in a PDMS well containing media. The bacterial concentration in the PDMS well was determined using a haemocytometer after one hour of magnetic actuation at 12 mT and 14 Hz using a magnetic field generator (MFG-100-i) consisting of eight electromagnets

arranged in a hemisphere. MTB were rotated in-plane (parallel) and out-of-plane (orthogonal) with respect to the cell monolayer and compared to exposure to DMF alone, which was applied along the –z-axis (Figure 4-2B). Under the stringent conditions of these initial cell monolayer experiments only, a magnetic force generated by spatial variation of the magnitude of the RMF or DMF (1 T/m) was applied along the – z-axis to support translocation. The RMF maintained its plane of rotation at all points.

Out-of-plane rotation was found to significantly increase MTB penetration compared to both in-plane RMF and DMF (Figure 4-2C). Out-of-plane actuation for frequencies between 1-20 Hz consistently resulted in higher translocation than controls without magnetic exposure (Figure S4-3). Given these findings, all subsequent experiments were performed using out-of-plane RMF.

To verify that MTB actuation does not affect monolayer integrity, the Lucifer yellow (LY) rejection assay was performed before and after each experiment. This fluorescent molecule passively diffuses through the cell monolayer by paracellular transport only and, thus, is unable to cross Caco-2 monolayers when tight junctions are well established. LY rejection values remained above 99% in all tested conditions, indicating that no damage occurred to the monolayer (Figure 4-2D and Figure S4-4).

4.2.3. Elucidating the role of torque-driven motion on translocation using computational modelling

Given the prominent effect of RMF on MTB transport across robust cell barriers, we sought to understand the main mechanism driving enhanced translocation using a computational model in COMSOL Multiphysics. Since the endothelium is the first biological barrier encountered following intravenous administration, modelling of transport across a 2D endothelial cell monolayer consisting adjacent cells forming a sealed barrier between upper and lower compartments was performed. The cells were modelled as hyperelastic materials with a shear modulus of 1 kPa (*257*, *258*) and dimensions adopted from Arefi *et al.* (*258*). Considering the relative stiffness of gram-negative bacteria compared to endothelial cells, MTB were modelled as rigid ellipsoids possessing a rigid dipole moment along the long axis. TEM images and multisizer data were used to determine the approximate size of a single bacterium, which were estimated to

be 0.45 and 1.8 μm for the short and long axis respectively (Figure S4-2) (*259*). Hydrodynamic interactions were modelled as linear and rotational viscous damping acting on the rigid body.

Modelling of the forces required for a bacterium to pass through a passive junction yielded estimated contact forces of 10s of pN (Figure 4-3A). Torque-induced contact force for a bacterium rotating at 14 Hz under 12 mT was shown to be much lower than resisting force of the cells (Figure 4-3B) as well as the forces required to break bonds formed by vascular endothelial-cadherin (VE-cadherin) (*260*), an endothelial cell-specific adhesion molecule. Buoyant forces and viscous resistance prevent the full conversion of rotational energy into a contact force, thus, the application of forces directly on an endothelial monolayer cannot be the chief mechanism responsible for enhanced translocation. As such, we sought to examine the influence of translational motion derived from torque-based actuation on bacterial translocation.

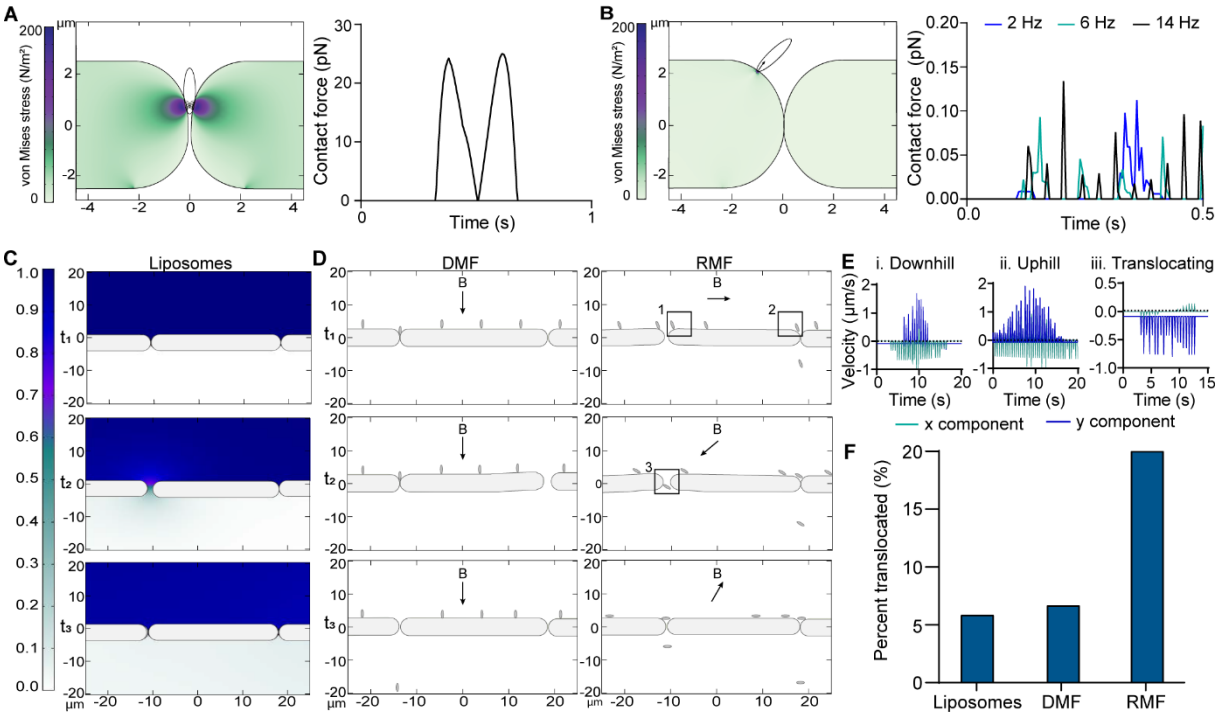

Figure 4-3: Computational modeling of MTB transport across endothelial monolayers. **(A)** Modelling of y-component contact forces resulting from a single bacterium with prescribed motion successfully transmigrating through a cell junction **(B)** Model showing discontinuous contact of a rotating bacterium with a cell monolayer. **(C)** Computational simulations of liposome diffusion across a modelled endothelial monolayer. Stochastic opening of cell-cell contacts was incorporated into the model to account for spontaneous gap formation. **(D)** Simulations of MTB transport under DMF and RMF across a modelled endothelial monolayer. **(E)** Velocity profiles showing contributions of x and y components of MTB traveling downhill (i), uphill (ii), and translocating through a cell gap (iii). **(F)** Plot of the average amount of liposome diffusion and MTB translocation under DMF and RMF for 3 simulations relative to the starting concentrations.

Recent work has shown that dynamic mechanical processes within the endothelium result in gap formations that are independent of the influence of migrating cancer or immune cells (*261*, *262*).

Using this as a basis, stochastic opening of cell-cell contacts was incorporated into the model to account for the active mechanics of the endothelium. For each simulation, the gap lifetime was set to 160 s (*258*) and a set of random parameters were generated to determine the gap size, which was within the range of 1.5 to 2.5 μm (*257*). The overall simulation time was selected to encompass opening incidences for all gaps. To characterize the permeability of our modelled monolayer, simulations of passive diffusion of liposomes with a diameter of approximately 200 nm were performed and 5.9% of the liposomes diffused into the lower compartment (Figure 4-3C). Having established the model, we proceeded to compare MTB transport under DMF and RMF (Figure 4-3D). The velocity profiles generated for the bacteria under RMF exhibited the well-studied characteristics of surface walkers under low Reynolds number flows (*263–265*) (Figure 4-3E). The higher mass density of MTB with respect to the surrounding liquid gives rise to a terminal velocity of the bacteria which results in an offset in the y-component of the velocity vector. When traveling along the monolayer, there is discontinuous contact with the surface and the contributions from the x- and y-components of the velocity vector vary depending on whether the MTB is traveling downhill, uphill or is translocating. As anticipated, the contribution from the x component is minimal as the MTB passes through an opening, reflecting the lowered contact with the cell surface.

Our model showed that only 6.6% of MTB exposed to DMF crossed the barrier, compared to 20% of MTB exposed to RMF (Figure 4-3F). Under the static conditions of DMF, the bacteria only passed through the monolayer when initially located in close proximity to a cell-cell junction. In contrast, MTB under RMF translated along the monolayer which enabled the bacteria to explore the monolayer surface and pass through any gaps that formed between the cells. Overall, these findings strongly suggest that enhanced surface exploration resulting from torque-based translational motion is the dominant mechanism facilitating increased translocation of MTB.

4.2.4. RMF increases extravasation of MTB-LP conjugates

We proceeded to investigate translocation in an *in vitro* system suited to model vascular extravasation. Human microvascular endothelial cell (HMEC-1) monolayers cultured on Transwell inserts were used to model the endothelial barriers that would be encountered following intravenous delivery. To verify that intact monolayers were formed when the cells were cultured on permeable membranes, immunostaining for VE-cadherin was performed (Figure 4-4A). Confocal imaging showed the presence of intact cell-cell contacts and the

formation of a uniform monolayer after 2 days. In an initial experiment, passive diffusion of unconjugated liposomes across the monolayer was measured (Figure S4-5). From the fluorescence intensity values, it was found that only 0.24% of the liposomes were able to cross into the basolateral chamber via passive diffusion after 1 hour (Figure 4-4B).

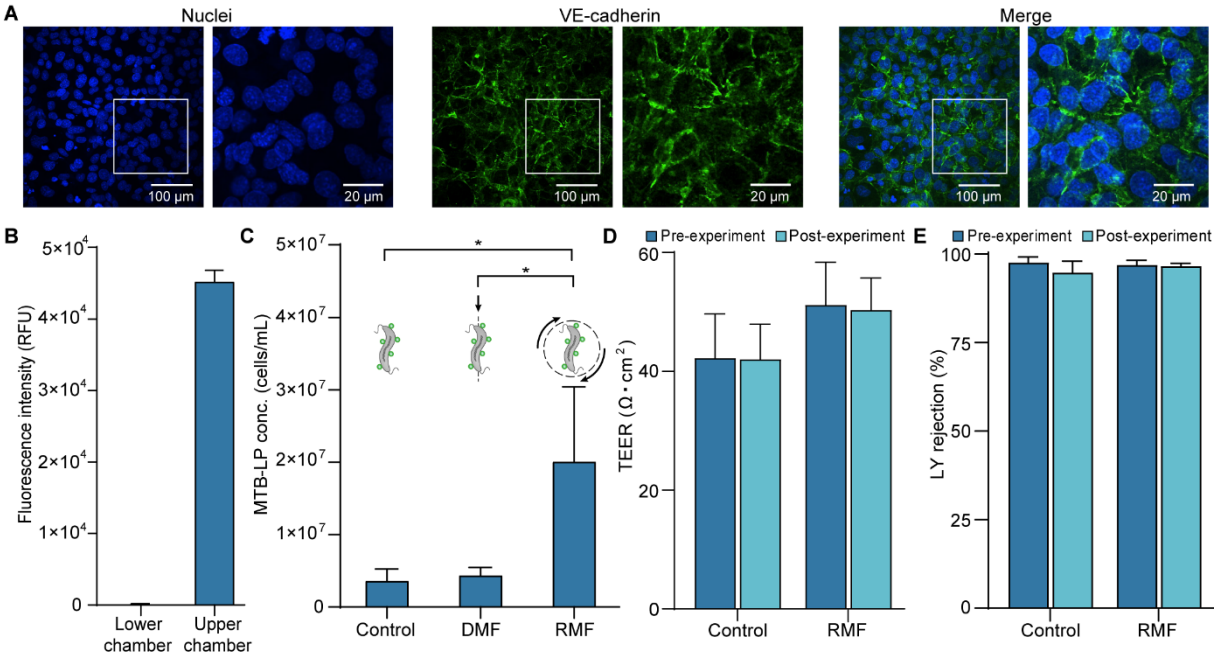

Figure 4-4: RMF-based control increases MTB translocation across endothelial monolayers. **(A)** Representative confocal images of immunostaining for VE-cadherin (green) on HMEC-1 cells cultured on a Transwell membrane. Cell nuclei were stained using Hoechst 33342 (blue). **(B)** Evaluation of the lower and upper compartment fluorescence intensity measurements following 1 h of passive diffusion of liposomes across HMEC-1 monolayers (n = 3; mean ± SD). **(C)** Comparison of lower compartment MTB-LP concentrations after 1 h for unactuated controls and exposure to either DMF (12 mT) and out-of-plane RMF (20 mT and 24 Hz) (n = 3; mean ± SD; *P < 0.05, ANOVA). No gradients were applied in these experiments. **(D)** Pre- and post-experimental transendothelial electrical resistance (TEER) measurements for unactuated controls and out-of-plane RMF (*n* = 3; mean ± SD). **(E)** Pre- and post-experimental Lucifer yellow (LY) rejection values for unactuated controls and out-of-plane RMF (*n* = 3; mean ± SD).

We then investigated the translocation of MTB-liposome conjugates across the monolayer. The MTB–LP complex combines the adaptability of traditional therapeutic nanocarriers and the functionality of magnetic-based platforms to produce a living microrobot for targeted drug delivery. Bioconjugation of fluorescently labelled liposomes to the MTB cell surface was achieved through carbodiimide mediated amidation (Figure S4-6, Table S4-1). Conjugates were added to the upper chamber of Transwell inserts and the concentration in the lower chamber was determined after one hour of actuation using an MFG-100-i. To increase the available magnetic torque, which is a function of magnetic moment and magnetic field strength, the applied field magnitude was increased to 20 mT. At this field strength, the step out frequency of our MTB

strain of interest was found to be 24 Hz (*259*), in agreement with the magnetometer data (Figure 4-1B).

MTB-LP were actuated out-of-plane relative to the monolayer for 1 hour, and this was compared to exposure to DMF, as well as unactuated controls (Figure 4-4C). Out-of-plane rotation led to 4.6-fold higher MTB-LP translocation compared to DMF. Exposure to DMF resulted in MTB-LP concentrations that were comparable to unactuated controls, as was the case in the Caco-2 monolayer experiments (Figure 4-2C). Transendothelial electrical resistance (TEER) measurements and the LY rejection assay were performed and revealed that MTB actuation does not affect monolayer integrity (Figure 4-4D & E). Both TEER and LY rejection values before and after actuation were comparable, demonstrating that disruption of the monolayer did not occur due to exposure to magnetic actuation.

4.2.5. RMF-based control improves MTB-LP transport in 3D tumour spheroids

Having demonstrated enhanced translocation across endothelial monolayers, we next sought to examine the effect of RMF-based control on MTB-LP tumour penetration in an *in vitro* tumour model using human breast adenocarcinoma (MCF-7) spheroids. Tumour spheroids can effectively recapitulate the mass transport properties and complex architecture of avascular tumour tissue and have been used to study bacteria-based cancer therapies (*8*, *266*, *267*). High levels of E-cadherin expression in MCF-7 cells facilitate the formation of strong cell-cell adhesions particularly in 3D spheroid cultures, making them an ideal model for difficult-to-penetrate tumour masses (*268*). MCF-7 cells transitioned from loose aggregates to highly compact 3D spheroids after 3 days of culture. The spheroids were transferred to PDMS wells, into which conjugates were added. MTB suspensions were stained with a proliferation dye prior to liposome conjugation to visualize daughter cells over the course of the experiment. After one hour of actuation (MFG-100-i, 20 mT and 24 Hz), spheroids were washed thoroughly and incubated for up to 120 hours (Figure 4-5A). Given that results for unactuated controls and DMF were comparable (Figure 4-2C, Figure 4-4C), as well as the lack of a clearly defined preferential direction in a spherical 3D model, RMF was compared to unactuated controls for all subsequent experiments.

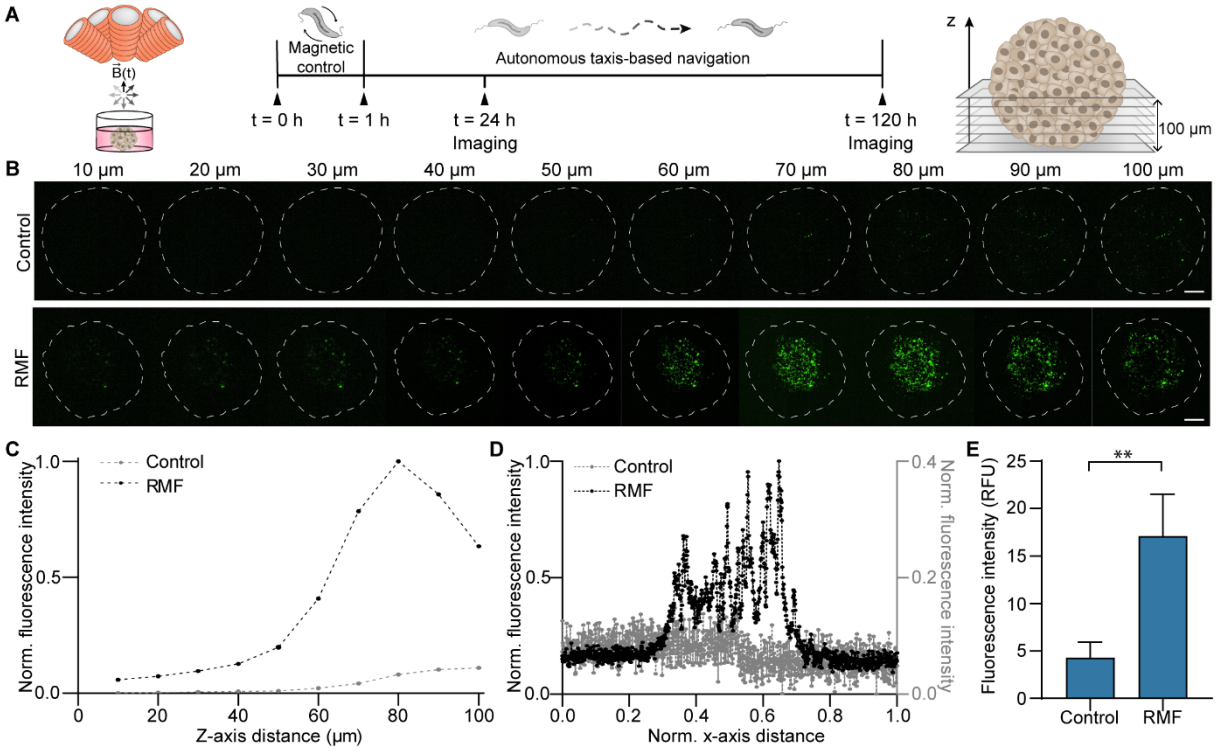

Figure 4-5: RMF-based control enhances intratumoural transport of MTB conjugates in 3D tumour spheroids. **(A)** Experimental overview of magnetic actuation followed by taxis and imaging of sequential z-slices of live tumour spheroids. **(B)** Representative confocal images of live MCF-7 spheroids following 1 h exposure to RMF (20 mT and 24 Hz), thorough washing, and 24 h incubation. Control refers to unactuated samples. Images were captured at 10 µm increments from the bottom of the spheroids and show the localization of DiO-labelled liposomes (green). Outline depicts the shape of the spheroid at its largest circumference. Scale bar = 100 µm. **(C)** Plot of mean intensity for each section at 10 µm intervals from the bottom of the spheroids along the z-axis up to a depth of 100 µm. **(D)** Representative fluorescence intensity distribution of the 80 µm section. Values were normalized to overall minimum and maximum fluorescence intensity values. Spheroid diameter was normalized along the x-axis. **(E)** Summation of mean intensity values for consecutive Z-plane images up to a depth of 100 µm (n = 3; mean ± SD; $^{**}P < 0.01$, Student's t-test).

Confocal images of live tumours were captured at increments of 10 µm from the bottom of the spheroids to visualize the distribution of DiO-labelled liposomes after 24 h of incubation (Figure 4- 5B). MTB-LP conjugates were able to propel into deep regions of avascular spheroids following exposure to RMF. The density of the conjugate clusters detected in the actuated samples increases with increasing depth. This finding was confirmed by evaluating the mean intensity of each section and compiling a fluorescence distribution for the z-plane up to a depth of 100 µm (Figure 4-5C). The fluorescence intensity values were consistently higher for actuated samples compared to controls and peak fluorescence for actuated samples occurred at 80 µm. Decreased signal after 80 µm could be caused by limitations in optical sectioning of deep tissue regions. Given that MTB-LP were mostly located in the centre of actuated samples, the high cell density in this region results in tissue opacity, light scattering, and limited light penetration which

restricts visualization of deep tissue sections by confocal microscopy (269). Nevertheless, it was still evident that a significantly higher number of conjugates penetrated the spheroids in RMF-exposed samples.

The intensity distribution profiles for the 80 µm sections show distinct differences in the distribution of MTB-LP in actuated samples compared to controls (Figure 4-5D). Control samples showed a more uniform distribution of the fluorescence signal. In contrast, the overall fluorescence intensity values were higher in actuated samples and the fluorescence signal was highest in the central region of the spheroid. A summation of mean fluorescence intensity for each section up to a depth of 100 µm showed that the overall fluorescence intensity, and thus the amount of conjugates delivered in the actuated samples is 4-fold higher than in the controls (Figure 4-5E).

4.2.6. RMF increases colonization of 3D tumour spheroids

Having characterized the efficacy of conjugate delivery using RMF, we were interested in investigating MTB tumour colonization over time. Although these experiments were performed with MTB-LP, analysis was performed only for the MTB that were stained with a proliferative stain, since subsequent generations of replicating MTB would not bear liposomes. Confocal images of live tumour spheroids were used to visualize and quantify the distribution of the replicating bacteria at 24 and 120 hours for RMF-exposed samples and unactuated controls (Figure 4-6A). The *z*-projection images revealed that MTB were still detectable within the spheroids for both actuated samples and controls after 120 hours. Fluorescence intensity profiles of the spheroids were used to study the localization of the MTB in the spheroids. MTB achieved colonization of the core regions of both actuated and unactuated samples. Additionally, there was a narrowing in the intensity profile, indicating an increased density of bacteria at the centre of the spheroid from 24 to 120 hours. This enhanced accumulation is likely attributable to autonomous taxis-based navigation. Spheroids over 400 µm in diameter can develop a hypoxic core, and preferential accumulation of MTB in this region might result from oxygen-sensing mechanisms that facilitate their navigation towards hypoxic environments (270–272).

A summation of mean fluorescence intensity for each section up to a depth of 100 µm was used to assess the relative amount of MTB present in the spheroids at various time points. The fluorescence intensity values in spheroids exposed to RMF were 9.9-fold and 21.3-fold higher

than in the controls at 24 and 120 hours, respectively. The ability of RMF to enhance transport and colonization of MTB was also investigated using HCT116 spheroids (Figure S4-7). As with MCF-7 spheroids, higher MTB colonization in the core regions of the spheroids was achieved in actuated samples after 120 hours.

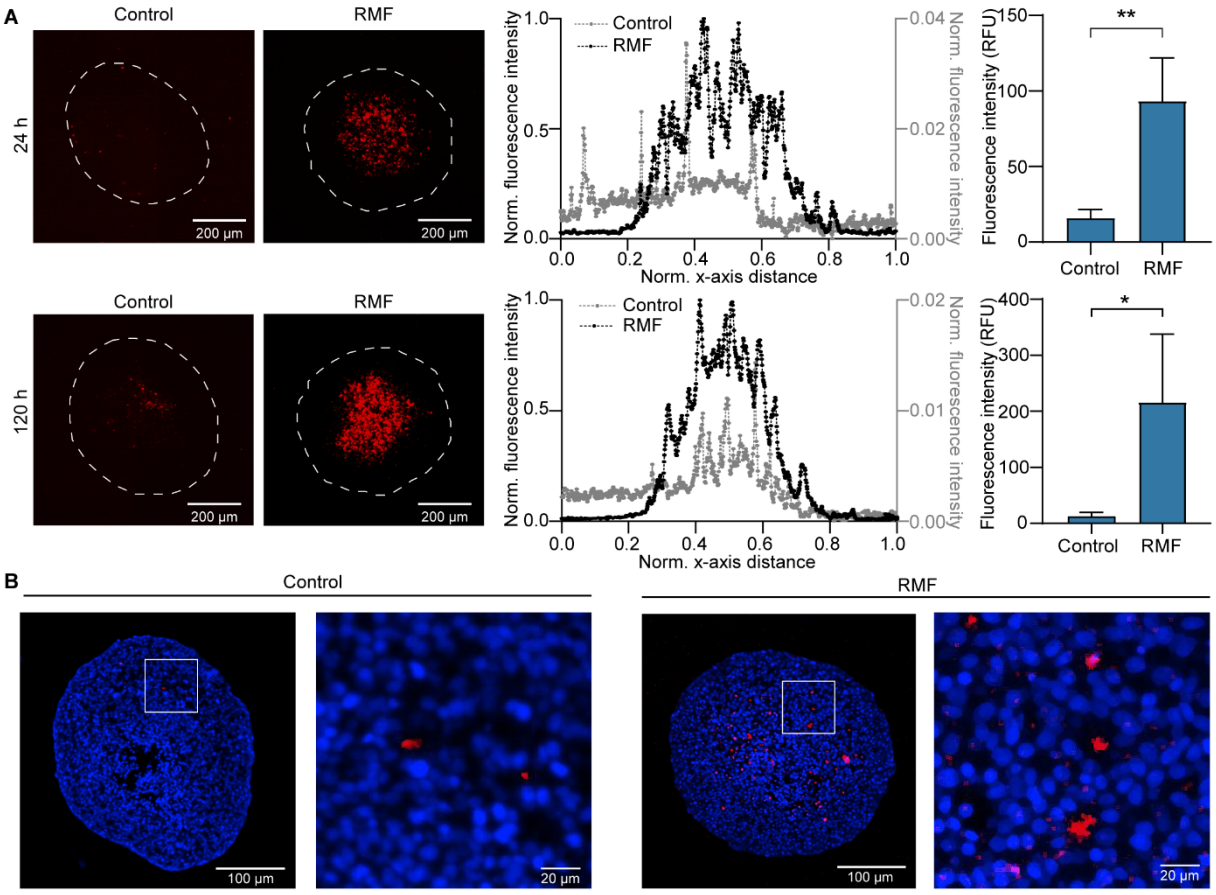

Figure 4-6: Assessment of MTB colonization in 3D tumour spheroids. (A) Representative z-projections of conjugates where MTB was stained with a far-red proliferative dye in live MCF-7 spheroids following 1 h exposure to RMF (20 mT and 24 Hz), thorough washing, and incubation for up to 120 h without actuation. Control refers to unactuated samples. Images were captured at 24 and 120 h. Outline depicts the shape of the spheroid at its largest circumference. Representative normalized fluorescence intensity distribution of actuated samples and controls at 24 and 120 h. Values were normalized to overall minimum and maximum fluorescence intensity values. Spheroid diameter was normalized along x-axis. Image-based quantification of fluorescence intensity values from z-projections at 24 and 120 h (right; $n = 3$; mean ± SD; $^{*}P < 0.05$, $^{**}P < 0.01$, Student's t-test). **(B)** Representative images of 5 µm histology sections for MCF-7 spheroids 144 h after actuation.

Importantly, over the course of the experiments the bacteria did not replicate uncontrollably, which is likely a result of the relatively low doubling time of MTB compared to other strains of bacteria. This suggests that some of the risks of infectious complications that have hampered the use of some bacterial strains could be of lower concern (240). To overcome the challenges associated with imaging whole spheroids, histological sectioning of MCF-7 spheroids was performed (Figure 4-6B). Sections from the centre of the spheroids showed that MTB formed

clusters between the cells and that there was higher signal from the MTB in spheroids exposed to RMF compared to controls. Overall, these findings indicate that the combination of magnetic torque-driven motion with taxis-based navigation results in robust tumour colonization.

4.2.7. Spatially localized actuation enhances MTB infiltration in target spheroids

Inspired by the gating fields employed in magnetic particle imaging, superimposed magnetostatic fields have recently been demonstrated as a control strategy capable of spatially confining hysteresis heating driven by high frequency alternating fields (*273*, *274*).

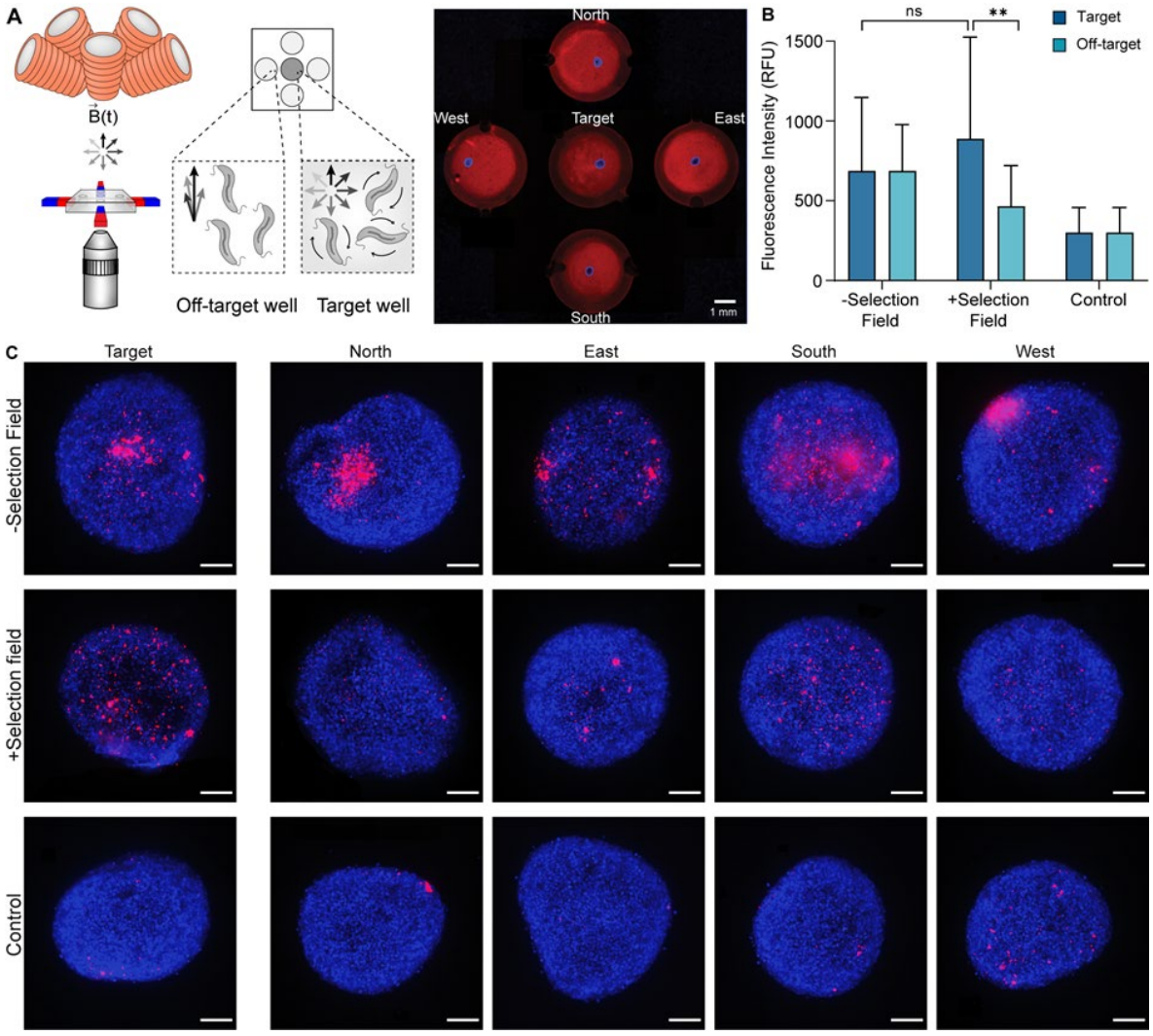

Figure 4-7: Selective accumulation of MTB in MCF-7 spheroids. **(A)** Schematic and representative confocal image of patterned PDMS wells. Spheroids stained with Hoechst 33342 (blue) and MTB were stained with a far-red dye. **(B)** Quantification of fluorescence intensity values from z-projections 24 h after actuation (20 mT and 24 Hz, 360˚ revolution) in the absence (–) or presence (+) of selection field. Control refers to unactuated samples. **(C)** Z-projections of MCF-7 spheroids following 1 hour exposure to RMF, thorough washing, and incubation for 24 h. Control refers to unactuated samples. Scale bar = 100 µm.

By analogy, it has previously been suggested that superposition of a static gating field with RMF could also be harnessed for selective actuation of MTB (*259*). The static field suppresses magnetic torque in off-target sites while bacteria near a field-free target region can still undergo full rotation when an RMF is applied. Proof-of-concept experiments were performed in patterned PDMS wells containing spheroids surrounded by suspensions of MTB and a selection field generated by four block magnets to create a centrally located field-free target well (Figure 4-7A). In these experiments, a new actuation scheme was explored in which the plane of rotation underwent a 360° revolution during the actuation period. After one hour of actuation (MFG-100-i, 20 mT and 24 Hz), spheroids were washed thoroughly and incubated for 24 hours. Confocal images of live spheroids were captured and analysed (Figure 4-7B & C). There was approximately 3-fold higher MTB accumulation in spheroids exposed to RMF compared to unactuated controls. MTB colonization in target spheroids when a selection field was applied was comparable to accumulation in spheroids actuated without a superimposed gating field. Notably, accumulation in spheroids in off-target wells was significantly lower, confirming that spatially selective actuation of MTB can be achieved using magnetostatic gating fields.

4.2.8. RMF-based control enhances intratumoural transport of MTB *in vivo*

Motivated by the pronounced effect of RMF on MTB transport *in vitro*, we next sought to test whether our RMF actuation strategy also enhanced bacterial accumulation *in vivo* with a pilot study employing a mouse model. BALB/c nude mice bearing subcutaneous MCF-7 tumours in one hind flank received intravenous injections of 1×10^9 MTB stained with a far-red proliferative dye (Figure 4-8A). While previous studies employed peritumoural administration of MTB and applied static magnetic fields to direct bacteria away from the injection site towards the tumour (*173*, *248*), we employ systemic administration where a DMF cannot be meaningfully applied at the tumour site. As such, for this experiment anaesthetized mice were placed either in the absence of magnetic actuation (control) or with tumours positioned in the workspace of an MFG-100-i applying a 20 mT RMF at 14 Hz for 1 h. For an applied field magnitude of 20 mT, uniform fields with negligible offset gradients are expected within the workspace of the field generator (Figure 4-8B, Figure S4-8), ensuring that observed effects on the accumulation of bacteria can solely be attributed to the rotational character of the applied field.

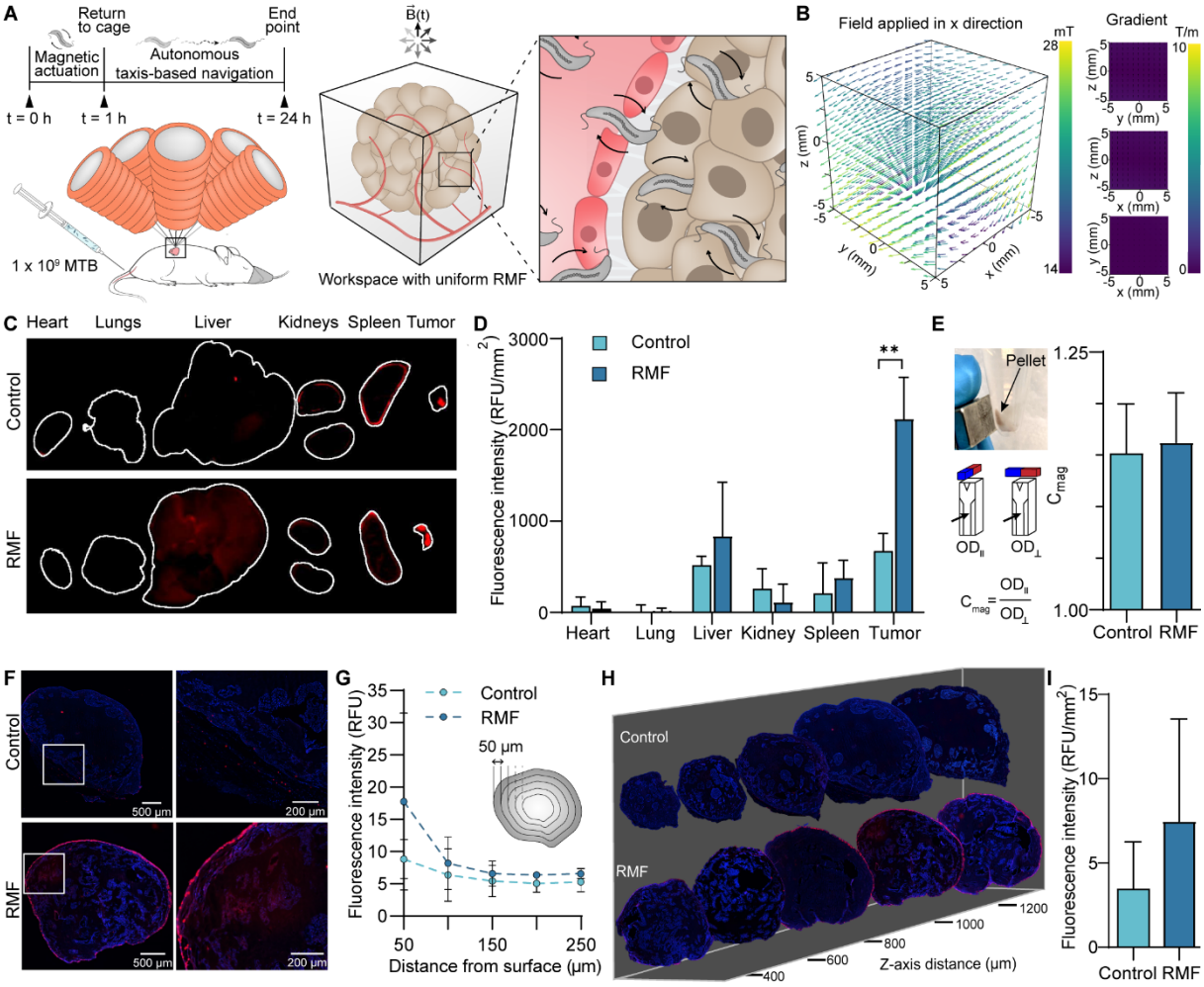

Figure 4-8: Assessment of intratumoural transport of MTB *in vivo*. **(A)** BALB/c nude mice bearing subcutaneous MCF-7 tumours in one hind flank were intravenously administered with 1×10^9 MTB stained with a far-red proliferative dye. The mice were anaesthetized for 1 h in the absence of exposure to magnetic actuation (control) or were placed on a magnetic field generator with tumours positioned in the workspace (RMF). Mice were returned to the cage for 24 h, after which the tumour and major organs were harvested for further analysis. **(B)** Plots of expected field magnitude and gradients produced in the workspace of the magnetic field generator for an applied field of 20 mT in the x dierction. **(C)** Representative fluorescence intensity images of harvested organs and tumours 24 h after injection of far-red stained MTB. **(D)** Quantitative biodistribution from harvested organs and tumours (n = 3; mean ± SD; $^{**}P < 0.01$, Student's t-test). **(E)** C_{mag} values for homogenized tumours placed in liquid culture for 8 days (n = 3 control, n = 4 RMF; mean ± SD). **(F)** Representative images of 10 µm histology sections that were sectioned at a depth of approximately 1 mm in the tumour. Cell nuclei were stained using Hoechst 33342 (blue). **(G)** Mean intensity values with increasing distance from the periphery of the tumour sections for the first 250 µm of each slice (n = 3; mean ± SD). **(H)** Representative transverse tumour sections. The z-axis denotes the approximate position of consecutive slices with respect to the surface of the tumour. Cell nuclei were stained using Hoechst 33342 (blue). **(I)** Summation of mean intensity values for consecutive traverse tumour sections (n = 3; mean ± SD).

Following treatment, mice were returned to the cage for 24 h, after which the tumour and major organs were harvested to assess the distribution of the bacteria using a whole organ fluorescence scanner (Figure 4-8C). Fluorescence signal was detected in all tumours suggesting that the bacteria innately accumulate in tumours. Notably, this signal was 3.16-fold higher in mice with tumours

exposed to RMF compared to unactuated controls (Figure 4-8D). Very low signals were detected in most of the major organs except for the liver, consistent with previous findings 24 h after intravenous administration of this bacterial strain (*275*). Bacterial accumulation in the liver is expected to decrease over time, with full clearance by day 6 (*275*).

To assess whether the bacteria detected in the fluorescence scans were still viable, harvested tumours were homogenized and placed into MTB culture media. After 8 days, large, dark pellets that were magnetically responsive were present in all tubes, indicating that the tumour homogenates contained live MTB (Figure 4-8E). C_{mag} measurements were performed to quantify the magnetic properties of the cultures and all samples had values above 1, signifying magnetic responsiveness of the bacterial suspensions.

Histological sectioning of the tumours was performed, with sections collected at a depth of approximately 1 mm in the tumour showing more pronounced accumulation at the periphery in both control and actuated samples (Figure 4-8F). Mean intensity distributions with increasing distance from the periphery for the tumour section show that bacteria can be detected throughout the first 250 μm of each slice, with higher overall signal from samples exposed to RMF compared to controls (Figure 4-8G). Transverse histology sections were also compiled and evaluated to assess the distribution of MTB with increasing distance from the surface of the tumour (Figure 4-8H). Summation of the mean fluorescence intensity for consecutive transverse tumour sections showed that the overall fluorescence intensity, and thus the amount of MTB delivered in the actuated samples, is 2.1-fold higher than in the controls (Figure 4-8J). These results, combined with the findings from our *in vitro* analysis, demonstrate the potential of magnetic torque-driven control strategies for enhanced tumour accumulation.

4.3. Discussion

The development of strategies to enhance tumour targeting and infiltration are essential for the clinical translation of bacterial cancer therapy which, to date, has been hindered by difficulties in achieving sufficient tumour colonization. Efforts to enhance the accumulation of magnetically responsive, therapeutic agents using magnetic fields have most often relied on powerful static field gradients to draw the drug carriers towards a target site (*276–278*). This approach has intrinsic limitations that narrow its potential for clinical translation. Magnetic fields decrease with the cube of the distance from a dipole and their gradients diminish even more rapidly. This

implies that the length scales associated with many tumours would require sources with impracticable field strengths. In contrast, uniform rotating magnetic fields can be generated at clinically relevant scales for actuation of magnetically responsive agents in deeply situated tumours.

The time-varying character of RMF presents the opportunity for simultaneous actuation and detection of living magnetic agents. Proof-of-concept experiments established that MTB actuated with RMF can be inductively detected and that their torque-based motion can be suppressed in off-target regions by a magnetostatic gating field. These demonstrations lay a foundation for further development of spatially confined actuation, simultaneous monitoring, and closed-loop optimization of driving parameters. *In vivo* inductive detection of magnetic tracers driven with alternating magnetic fields has already been widely investigated with magnetic particle imaging (MPI) (*279*). The possibility for concurrent imaging and actuation with MPI has also been recognized, combining particle tracking of superparamagnetic iron oxide nanoparticles with cancer hyperthermia *in vivo* (*273*). Gradient fields utilized in MPI have proven challenging to scale up to humans, but recent efforts have demonstrated MPI in deep regions in human brains with moderate resolution (*280*). One foreseeable challenge to simultaneous inductive monitoring and actuation of MTB with RMF is that frequencies of 10s of hertz are used rather than the kilohertz signals generated in MPI, resulting in correspondingly weaker inductive signals. Another is the lack of higher order harmonics contributed to the inductive signal with rotational actuation, which arise in MPI from periodic saturation of the magnetic tracers. Future work will need to identify strategies to overcome these obstacles.

Magnetic torque-driven motion, followed by autonomous taxis-based locomotion, proved to be a highly effective hybrid control strategy for enhanced transport of living therapeutics across various biological barriers. MCF-7 spheroids were used to model avascular tumour tissue while the Transwell system was used to generate a model for a robust barrier using Caco-2 cells, and HMEC-1 cells were used to mimic the vascular endothelium. In both monolayer models, translocation driven by the application of an RMF significantly outperformed the DMF and unactuated controls. Computational modelling showed that torque-driven translational motion, which led to increased cell surface exploration, was the primary mechanism responsible for increasing transport across monolayers. Although not the chief mechanism driving MTB-LP transport, shear forces exerted by rotating MTB-LP on the cell surface may still contribute in part

to higher transport across monolayers and increased accumulation in spheroids. The heterogeneity of MTB populations may allow a small subset of bacteria with especially high magnetic moments to exert sufficient forces on mechanotransducers, such as VE-cadherin and E-cadherin. This can trigger responses including transient disruptions of intercellular junctions (*281*, *282*). Combined with the translation of the bacteria on the cell surface, these relatively rare disruptions could assist in enhancing local permeability and transport of MTB-LP.

We also showed that the results from the *in vitro* characterization of our actuation strategy can be replicated in the highly complex biological environment *in vivo*. Notably, we have demonstrated that significant accumulation of systemically administer MTB can be achieved for tumours exposed to RMF. Previous studies employing magnetic actuation following peritumoural administration have shown considerable bacterial accumulation. However, this route of administration is limited to easily accessible tumours, which raises the barrier to practical clinical use. In choosing systemic delivery, we demonstrate the robustness of our strategy for improved delivery of magnetically responsive bacteria despite the added barriers posed by clearance mechanisms present in the circulatory system. Given that AMB-1 remain viable following intravenous administration, future studies will incorporate longer timepoints to facilitate the study of taxis-based accumulation in tumour cores, as well as further bacterial clearance from off-target sites.

With a demonstrated ability to overcome robust biological barriers, our actuation strategy is a potentially powerful tool for improving the targeting and efficacy of magnetically manipulable therapeutic agents. Imparting magnetic responsiveness to more commonly used bacterial species, such as *E. coli* (*283*), is of increasing interest in the field of bacterial cancer therapy aimed at potentially increasing both safety and efficacy. Strategies to achieve this include surface functionalization using magnetic nanoparticles or genetic engineering, which is supported by insights into the genes involved in the process of biomineralization in MTB for transfer into non-magnetic species (*284*). By merging the benefits of bacteria-mediated therapy with a scalable magnetic torque-driven actuation scheme, our approach enables effective, targeted delivery of living microrobots for improved cancer treatment.

4.4. Materials and methods

4.4.1. Materials

Human colorectal adenocarcinoma (Caco-2, ATCC HTB-37), human microvascular endothelium (HMEC-1, ATCC CRL-3243), human breast adenocarcinoma (MCF-7, ATCC HTB-22), human colorectal carcinoma (HCT116, ATCC CCL-247), *Magnetospirillum magneticum* (ATCC 700264), Wolfe's Vitamin Solution and Wolfe's Mineral Solution were purchased from American Type Culture Collection (Manassas, VA). 1,2-dipalmitoyl-sn-glycero-3-phosphocholine (DPPC) and 1,2-distearoyl-sn-glycero-3-phosphoethanolamine-N-[carboxy(polyethylene glycol)-2000] (sodium salt) (DSPE-PEG2000-COOH) were purchased from Avanti Polar Lipids, Inc. (Alabaster, AL). Penicillin/Streptomycin (P/S) was purchased from Corning (Corning, NY), fetal bovine serum (FBS) was purchased from BioWest (Nuaillé, France), 1-ethyl-3-[3-(dimethylamino)propyl]-carbodiimide (EDC) was purchased from TCI EUROPE (Eschborn, Germany), and Hoechst 33342 was purchased from Invitrogen (Burlington, CA). Calcein and 4% formaldehyde (HistoFix 4%) were purchased from Carl Roth (Karlsruhe, Germany). VE-cadherin rabbit monoclonal primary antibody and Alexa Fluor 488-conjugated anti-rabbit IgG secondary antibody were obtained from Cell Signalling Technology (Danvers, MA). Potassium phosphate, succinic acid, tartaric acid, sodium nitrate, ascorbic acid, sodium acetate, resazurin sodium salt, gelatin, epidermal growth factor (EGF), hydrocortisone, Hanks' Balanced Salt solution (HBSS), dimethyl sulfoxide (DMSO), Lucifer yellow CH dipotassium salt, sepharose CL-2B, bovine serum albumin (BSA), 3,3′-Dioctadecyloxacarbocyanine perchlorate (DiO), phosphate-buffered saline (PBS), Triton X-100 and N-hydroxysulfosuccinimide (sulfo-NHS) were all acquired from Sigma-Aldrich (St. Louis, MO). Dulbecco's Modified Eagle's Medium (DMEM), McCoy's 5A medium, L-glutamine, CellTrace Far-Red cell proliferation kit, agarose and MCDB131 medium were acquired from Thermo Fisher Scientific (Waltham, MA).

4.4.2. Mammalian cell culture

Caco-2 cells were cultured in high glucose DMEM supplemented with 20% FBS and 1% P/S. HMEC-1 cells were cultured in MCDB131 supplemented with 10% FBS, 1% P/S, 10 mM L-glutamine, 1 µg/mL hydrocortisone, 10 ng/mL EGF. MCF-7 cells were cultured in high glucose DMEM supplemented with 10% FBS and 1% P/S. HCT116 cells were cultured in McCoy's 5A medium supplemented with 10% FBS and 1% P/S. All cell lines were incubated at 37 °C with

5% CO_2 in a humidified atmosphere. Cells were harvested at 80% confluency and cell density was determined using a haemocytometer. The required number of cells was seeded for each experiment as specified. One day before experiments, media was replaced with antibiotic-free media.

4.4.3. Bacteria culture

Cultures of *M. magneticum* strain AMB-1 were grown in revised magnetic spirillum growth medium (MSGM, ATCC Medium 1653) which contained the following per liter of distilled water: 5.0 mL of Wolfe's Mineral Solution, 0.45 ml of 0.1 % resazurin, 0.68 g potassium phosphate, 0.37 g succinic acid, 0.37 g tartaric acid, 0.12 g sodium nitrate, 0.035 g ascorbic acid and 0.05 g sodium acetate. The final pH was adjusted to 6.75 with 1 M NaOH before autoclaving. Prior to use, Wolfe's Vitamin Solution (1000x) and 10 mM ferric quinate (200x) were added to the culture media. Incubation occurred anaerobically at 30 °C and cultures were passaged every 5 to 7 days.

4.4.4. MTB translocation across Caco-2 cell monolayers

Caco-2 cells were seeded at a density of 1×10^5 cells/cm^2 on 12-well Transwell inserts (3.0 µm pore size, Corning). Cells were cultured on the inserts for 16-21 days and media was exchanged every second day. A Lucifer yellow paracellular permeability assay was performed to determine the integrity of the established Caco-2 monolayer. Prior to and after each assay, cell monolayers were washed three times with HBSS. The basolateral compartment of a well plate was filled with 1.5 mL of 1% DMSO in HBSS and 0.5 mL of 1 mg/mL Lucifer yellow in 1% DMSO/HBSS was added to the apical compartment. After one hour incubation at 37 °C, the fluorescence intensity (FI) of the solutions from the apical and basolateral compartments were measured at 485/535 nm using a Spark multimode microplate reader (Tecan). The percent rejection of Lucifer yellow was calculated as follows:

$$\%\ \text{Lucifer Yellow Rejection} = 100 \times \left[1 - \frac{\text{FI}_{\text{basolateral}}}{\text{FI}_{\text{apical}}} \right] \quad (1)$$

Transwell inserts with a Lucifer yellow rejection value greater than 99% were used for further experiments. After each experiment, the Lucifer yellow assay was repeated to confirm that the integrity of the monolayer was maintained.

Transwell inserts with Caco-2 monolayers were placed into PDMS wells (Ø = 22 mm) containing 1.5 mL media. MTB at a concentration of 1×10^8 MTB/cm^2 was added to the apical chamber and samples were exposed to either a directional magnetic field of 12 mT or a localized rotating magnetic field of 12 mT with frequencies between 1 and 20 Hz. A magnetic force generated by the superposition of moderate gradients of 1 T/m was applied along –z. After one hour, the bacteria concentration in the basolateral chamber was determined by live counting in a haemocytometer. Bacteria concentrations for actuated samples were normalized to unactuated controls. A small-scale arbitrary magnetic field generator consisting of eight electromagnets arranged in a single hemisphere was used to apply rotating magnetic fields (MFG-100-i, Magnebotix, Zurich, Switzerland). The system was integrated with an inverted spinning disk confocal microscope (Nikon Eclipse Ti2 with Yokogawa CSU-W1 unit and Hamamatsu C13440-20CU Digital CMOS camera), which was used for all imaging. Samples were positioned between the objective lens and the hemisphere of the electromagnets.

4.4.5. Inductive detection of MTB

Inductive detection of MTB was performed using a custom-built RMF magnetometer. Two pairs of nested Helmholtz coils were wound using enamel-coated copper wire (Ø = 0.8 mm) and housed in a 3D printed frame (Figure S4-1). The inner set of coils contained 256 turns of wire and the outer coils consisted of 265 turns. Phase shifted sinusoidal signals were generated (Digilent Analog Discovery 2) and amplified (Crown D-150A Series II), resulting in a sinusoidal waveform in each set of Helmholtz coils to produce a circularly rotating magnetic field. Inductive field probes for each pair of coils were placed in the central workspace along with sense and compensation coils. Signals from the sense and compensation coils underwent differential amplification and the residual signal from the magnetized sample was acquired with an oscilloscope (Keysight DSOX2004A). All samples contained 100 µL of MTB at approximately OD_{600} = 1.5, suspended in MSGM. Measurements were collected at field amplitudes of 12 mT and 20 mT at a frequency range between 12 Hz and 80 Hz. A detailed description of the setup and the associated data processing pipeline can be found in the supplementary materials.

4.4.6. Computational model of endothelial translocation

A numerical simulation in COMSOL Multiphysics (version 5.5) was implemented to study the translocation of microstructures across an endothelial barrier under different conditions. MTB

were modelled as rigid ellipsoids possessing a magnetic dipole moment using dimensions obtained from Multisizer data collected after *in vitro* translocation experiments. Endothelial cells were modelled as hyperelastic materials and stochastic opening of cell-cell contacts was incorporated to model dynamic gap formation that occurs in endothelial cell monolayers. The effect of the surrounding fluid was modelled through linear and rotational drag coefficients assuming Stokes flow regime. A time-varying external magnetic field was applied, and this was balanced with forces and torques arising from hydrodynamic and mechanical interactions with the viscous fluid and adjacent substrate. Further details can be found in the Supporting Information.

4.4.7. Liposome characterization and covalent coupling of MTB to liposomes

Fluorescently-labeled carboxylated liposomes were prepared from a total of 14 µmol of lipids using thin-film hydration. For imaging, DPPC, DSPE-PEG2000-COOH (5 mol%) and DiO (0.5 mol%) were combined in 0.5 mL chloroform and dried to a thin film under nitrogen with further vacuum desiccation overnight at room temperature. The lipid thin film was hydrated with 1 mL PBS and placed in a water bath for 1 h at 50 °C with continuous stirring. Liposomes were downsized using sequential extrusion on a heating block (Avanti) at 50 °C. Liposomes were passed 21-times each through a 400 nm followed by a 200 nm polycarbonate membrane (Whatman). For flow cytometry, DPPC and DSPE-PEG2000-COOH (5 mol%) were combined to form a thin film as previously described. The film was rehydrated with 1 mL calcein solution (35.2 mM) and downsized as described. Unencapsulated calcein was removed by size exclusion chromatography using a Sepharose CL-2B column. The average diameter, size distribution and zeta potential of the liposomes was determined by dynamic light scattering (DLS) (Litesizer 500, Anton Paar).

MTB cells at a concentration of 1.5×10^8 cells/mL in PBS were stained using the CellTrace Far-Red cell proliferation kit. A stock solution was prepared according to the manufacturers protocol and 2 µL was added to the MTB suspension. Cells were incubated at room temperature for 20 min, protected from light with gentle agitation. After incubation, 10 µL of 1% BSA was added to the cell suspension for 5 min to remove free dye. Cells were pelleted and resuspended in PBS.

Bioconjugation was then achieved through carbodiimide coupling using an adapted protocol (247). Briefly, activation of carboxylated liposomes was accomplished by incubating 300 µL of

liposome solution with EDC and sulfo-NHS (EDC/NHS/DSPE-PEG-COOH = 30:30:3, mol/mol) for 20 min in PBS (pH 5.5) at room temperature with gentle agitation. The activated liposomes were subsequently incubated with 1.5×10^8 MTB cells for 2 hours at room temperature with gentle agitation. Unbound liposomes were separated from MTB-liposome conjugates (MTB-LP) using a two-dimensional magnetic field and the sample was redispersed in PBS (pH 7.4).

For quantitative analysis of liposome binding, MTB-LP conjugates were analysed using flow cytometry (BD LSRFortessa) with a 488 nm excitation laser and 530/30 filter. Untreated MTB cells and unbound liposomes were used as controls and the fluorescence emission of 10 000 events was recorded. Data was analysed using FlowJo (Tree Star) and appropriate gates and controls were used to generate density plots and histograms of each sample.

4.4.8. HMEC-1 monolayer culture and immunofluorescence staining

HMEC-1 cells were seeded at a density of approximately 1×10^5 cells/cm^2 on 12-well Transwell inserts (3.0 µm pore size) and cultured on the inserts for 2 days. HMEC-1 monolayers were fixed in 4% paraformaldehyde for 15 min and permeabilized in 0.1% Triton X-100 for 10 min at room temperature. Fixed cells were blocked with 1% BSA in PBS for 1 hour, followed by overnight incubation at 4 °C with a VE-cadherin rabbit monoclonal primary antibody (diluted 1:500 in blocking buffer). The monolayers were then incubated for 1 hour at room temperature in an Alexa Fluor488-conjugated anti-rabbit IgG secondary antibody (diluted 1:1000 in blocking buffer). Staining for DNA was performed with Hoechst 33342. Monolayers were incubated in Hoechst 33342 at a final concentration of 10 µg/mL in PBS for 10 min at room temperature. The membranes were then detached from the Transwell inserts, mounted on glass coverslips and imaged.

4.4.9. Translocation across HMEC-1 cell monolayers

HMEC-1 monolayers cultured on Transwell inserts were placed into PDMS wells (Ø = 22 mm) containing 1.5 mL media. MTB-LP at a concentration of 1×10^8 MTB-LP/cm^2 was added to the apical chamber and exposed to either a directional magnetic field of 12 mT or a localized rotating magnetic field of 20 mT and 24 Hz. After one hour, the concentration and size distribution of MTB-LP in the basolateral chamber was determined using a multisizer (4e Coulter Counter, Beckman Coulter). For comparison, liposomes were added to monolayers at a concentration corresponding to the liposomes on the conjugates. After 1 hour, the solutions from the apical

and basolateral compartments were collected and measured at 485/535 nm using a Spark multimode microplate reader (Tecan).

Prior to and after each assay, LY rejection (as previously described) and transendothelial electrical resistance (TEER) measurements for performed using a EVOM3 Volt/Ohmmeter (World Precision Instruments). TEER was calculated using following the equation:

$$TEER = (R_{total} - R_{blank}) \times A \quad (2)$$

where R_{total} is the measured resistance from a Transwell insert with a cultured monolayer, R_{blank} is the resistance of a Transwell insert without a monolayer, and A is the area of Transwell insert (1.12 cm^2).

4.4.10. MTB-LP accumulation in MCF-7 spheroids

MCF-7 tumour spheroids were formed and cultured in 96 well ultralow adhesion plates (Corning). Cells were seeded at a density of 10,000 cells/well in 100 µL of media. The well plates were centrifuged at 1000 × g for 10 min and incubated in a humidified atmosphere with 5% CO_2 at 37 °C. Tumour spheroids grew to approximately 500 µm in diameter after 3 days. Prior to experiments, staining for DNA was performed with Hoechst 33342. Spheroids were incubated for one hour at 37°C with Hoechst 33342 at a final concentration of 5 µg/mL in media.

MCF-7 spheroids were transferred to PDMS wells (Ø = 6 mm) containing 5×10^7 MTB-LP in 100 µL of media. Spheroids were subsequently imaged under magnetic actuation at 20 mT and 24 Hz. After one hour, spheroids were washed thoroughly with PBS and incubated in ultralow adhesion well plates for up to 6 days at 37 °C with 5% CO_2 in a humidified atmosphere.

4.4.11. Spatially selective actuation of MTB

Selection field experiments were performed in square PDMS devices featuring five patterned wells, (Ø = 3 mm). NdFeB block magnets (5 × 2.5 × 1.5 mm, Supermagnete) were placed with arbitrarily defined north poles facing inward on the east and west faces of the device, while magnets with south poles facing inwards were positioned on the remaining faces. This generated a gating field with a centrally located zero point. MCF-7 spheroids were transferred into the wells containing 25 µL of MTB at a concentration of 5×10^8 MTB/mL in media. Spheroids were exposed to RMF of 20 mT and 24 Hz where the plane of rotation underwent a 360 ° revolution

during the 1 hour actuation period. Spheroids were washed thoroughly with PBS and incubated in ultralow adhesion well plates for 24 h at 37 °C with 5% CO_2 in a humidified atmosphere.

4.4.12. Quantification of MTB-LP accumulation in MCF-7 spheroids

Analysis and processing of captured image stacks was performed in ImageJ (NIH). For each spheroid, a summation of consecutive Z-plane images in the first 100 µm was performed for each time point (Figure S4-9A). Regions of interest (ROIs) were defined using the Hoechst image stack by tracing a contour around the spheroid at 0 and 100 µm. Intermediate ROIs were defined using interpolation, with approximately 3 µm radial increments (Figure S4-9B). These ROIs were then applied to the corresponding DiO liposome image stack and fluorescence intensity measurements were performed. Fluorescence values were normalized to the fluorescence of the surrounding media (Figure S4-9C).

To generate fluorescence intensity distributions at a depth of 80 µm, rectangular regions of interest were defined at the boundaries of the spheroid. The average pixel intensity values along the x-axis were normalized to the minimum and maximum intensity across all the spheroids to allow comparison, using the following equation:

$$\text{Norm. fluorescence intensity} = \frac{\text{Ave. intensity} - \text{Min. intensity}}{\text{Max. intensity} - \text{Min. intensity}} \quad (3)$$

Normalized fluorescence intensity was plotted against normalized x-axis distance to obtain the MTB-LP distribution in the spheroids.

4.4.13. *In vivo* magnetic actuation experiments

All animal experiments were approved and performed in accordance with guidelines from Veterinamäramt Kanton Zürich under licence number ZH151/2020 and laboratory animal husbandry number 159. Female BALB/c nude mice (6-8 weeks, Charles River) were acclimatized for 3 weeks and inoculated subcutaneously in the hind flank with 5×10^6 MCF-7 cells suspended in 8 mg/mL Matrigel at a volume of 100 µl. When tumour diameters exceeded 5 mm, mice were blindly randomized into various groups with a minimum of 3 mice per group. Tail-vein (intravenous) injections of MTB stained with a far-red proliferative dye were administered at a concentration of 1×10^9 in 100 µl PBS. Mice were placed under anaesthesia in the absence of magnetic actuation (control) or with tumours positioned in the workspace of the magnetic field

generator and exposed to actuation at 20 mT and 14 Hz for 1 h (RMF). Mice were then returned to the cage for 24 h, after which the mice were euthanized and the tumour and major organs were harvested. For semiquantitative biodistribution analysis, far-red fluorescence signals were measured using an *ex vivo* fluorescence imaging system (Sapphire Biomolecular Imager, Azure Biosystems).

Harvested tumours were weighed and homogenized using a gentleMACS tissue dissociator (Miltenyi Biotec) (C-tubes) before being cultured for 8 days under the MTB culture conditions described previously. C_{mag} measurements were performed to quantify the magnetic responsiveness of the samples. Optical density (OD) at 600 nm was measured with a magnet placed parallel ($OD_{||}$) and then perpendicular ($OD_{\perp}$) to the light path. The C_{mag} value was calculated as the fraction of $OD_{||}$ and $OD_{\perp}$.

4.4.14. Histology

Spheroids and harvested tumours were fixed in 4% formaldehyde for 1 hour and washed three times with PBS. For spheroids, a 5% (w/v) agarose solution in DI water was mixed with a 5% (w/v) solution of gelatin at a 1:1 ratio, and the fixed spheroids were embedded in the resulting hydrogel. After dehydration in graded alcohol and isoparaffin (LOGOS J, Milestone Medical), spheroid-containing hydrogels or tumours were embedded in paraffin and sections of 5 – 10 µm were cut using a microtome (HM 355S, Microm AG). The sections were stained with Hoechst 33342 at a concentration of 5 µg/mL in DI water and the slides were mounted and imaged.

4.5. Supporting information

Supplementary Text

MTB propulsive force and torque-based force calculations

MTB motion is dependent on the propulsive force (F_P) generated by their flagella and the fluidic drag force (F_D). At constant velocity, this relationship is governed by:

$$F_P + F_D = 0 \tag{1}$$

When traveling at constant velocity at low Reynolds numbers the propulsive force is equal and opposite to the drag force which is defined as:

$$F_P = \gamma v \tag{2}$$

where v is the linear velocity and γ is the linear drag coefficient given by (*285*):

$$\gamma = 2\pi\eta l\left[\ln\frac{2l}{d} - 0.5\right]^{-1} \tag{3}$$

Thus, for a velocity range of 19 - 49 μm/s the propulsive force is estimated to fall between 0.14 and 0.35 pN when the dynamic viscosity of the medium (η) is approximately 1×10^{-3} Pa·s, and the length and diameter of the cell are l = 1.8 μm and d = 0.45 μm, respectively (Figure S4-2).

In contrast, when MTB are exposed to an externally rotating magnetic field, they experience a magnetic torque, $\tau_M = |m \times B| = m\,B\,sin\,\theta$, dependent on the magnetic moment (m) of the MTB and the magnetic field strength (B). The opposing hydrodynamic torque τ_H defines the steady state lag angle (θ) between the MTB and magnetic field and is governed by $\tau_H = \alpha\,\omega$, where the angular frequency (ω) is equal to the frequency of magnetic actuation under synchronous rotation. The rotational drag coefficient (α) is obtained by (*263*):

$$\alpha = \frac{\pi\eta l^3}{3}\left[\ln\frac{l}{d} - 2.4\right]^{-1} \tag{4}$$

Thus, the force (F_T) generated by this torque-based motion can be determined using the following equation:

$$F_T = \frac{\alpha\omega}{r} \tag{5}$$

For angular frequencies between 10 – 25 Hz at a field magnitude of 20 mT and distance from the axis of rotation (r) of 0.9 μm, the force generated ranges from 0.8 – 1.8 pN.

Given that force and magnetic field gradient are governed by $F = \nabla (m \cdot B)$, the estimated gradient required to produce a force on the order of 1 pN on an MTB cell with a magnetic moment of $m = 7.6 \times 10^{-16}$ A m^2 (25) was found to be approximately 1300 T/m.

RMF magnetometer for inductive detection of MTB

Inductive detection of MTB was performed using a custom-built RMF magnetometer. Two pairs of nested Helmholtz coils housed in a 3D printed frame were used to produce a circularly rotating magnetic field (Figure S4-1). Field magnitude was determined by measuring current with a shunt resistor and calibrating under constant field to a Hall probe (Metrolab THM1176), which agreed well with the expected geometric factor. Field measurements were ultimately performed with orthogonal inductive field probes (100 turns) placed in the central workspace along with sense and compensation coils (each 500 turns). Signals from the sense and compensation coils underwent differential amplification (Analog Devices EVAL-ADA4625-1) and the residual signal from the sample was acquired by an oscilloscope (Keysight DSOX2004A) under signal averaging (N = 32).

Measurements were collected at field amplitudes of 12 mT and 20 mT over a logarithmically spaced frequency range between 12 Hz and 80 Hz. Three measurements per frequency and amplitude were collected for blank samples containing MSGM and samples containing MTB. An inductive background signal at the same frequency and at 2 mT was collected both before and after every sample measurement. This approach assumes that the response of the bacteria at 2 mT and the investigated frequencies will be far smaller than their response at higher amplitudes, an assumption motivated by previous studies (*259*). Prior to conducting measurements at each condition, inductive background was minimized by minutely mechanically adjusting the angle between the sense and compensation coil to balance phase and using the potentiometer to minimize the output signal of the amplifier. After a sample or blank was loaded, care was taken not to touch the device or otherwise disturb background cancellation.

During subsequent data processing, any offset arising from amplification was subtracted and only the time-varying components of the acquired signals were considered. A linear combination of the background signals of the two field probes was fitted to the 2 mT magnetometer signals. This

uses the orthogonal signals from the field probes as references for reconstructing residual inductive signal. Estimates of the background based on the measurements at 2 mT conducted immediately prior to and after measurement at the target amplitudes were then subtracted from the blank and MTB samples, providing initial and final bounds on the sample and blank signals. Each of the bounded blank signals (six) were then subtracted from each of the bounded MTB signals (six) to form a set of 36 signals. Because background subtraction is likely dominate error in this case, this set of 36 signals can be taken to represent the variation of equally theoretically valid background-subtracted signals.

From this collection of 36 bounding signals, the mean signal generated by the MTB was found and bootstrapping was performed to provide 95% confidence intervals to quantify the uncertainty in the data presented in Figure 2A. Using a cosine function fitted to the in-phase field probe, integration was used to separate each of these 36 signals into quantities proportional to the in-phase and out-of-phase components of the magnetization. Dividing by frequency and field magnitude yielded quantities proportional to susceptibility that can be compared to each other over the range of frequencies and amplitudes. Bootstrapping was also used on these sets of values to provide a 95% confidence interval on the resulting values for real and imaginary susceptibility depicted in Figure 2B.

Predictions of the susceptibility values for MTB where made by plotting the normalized real (χ') and imaginary (χ'') components of susceptibility at 12 and 20 mT using the following equations:

$$\chi' = \frac{1}{1 + (2\pi f \tau_{eff})^2} \tag{6}$$

$$\chi'' = \frac{2\pi f \tau_{eff}}{1 + (2\pi f \tau_{eff})^2} \tag{7}$$

where f is the frequency of rotation and τ_{eff} is the effective Brownian relaxation time given by:

$$\tau_{eff} = \frac{\tau_B}{0.412\alpha + 0.143} \tag{8}$$

The Langevin parameter, α, is defined by:

$$\alpha = \frac{\mu_0 m H}{k_b T} \tag{9}$$

where, μ_0 denotes vacuum permeability, m is the magnetic moment, H is the external field magnitude, k_b is Boltzmann's constant and the temperature is T = 298 K.

The characteristic zero-field Brownian relaxation, τ_B time is given by:

$$\tau_B = \frac{3\eta V_h}{k_b T} \tag{10}$$

where η is the viscosity of the fluid and V_h is the hydrodynamic volume.

Computational modelling of MTB-LP transport across endothelial monolayers

To study the transmigration mechanism of MTB across HMEC monolayers, Finite Element Method (FEM) was employed to solve the governing equations using COMSOL Multiphysics. The cell monolayer was modelled in 2D featuring a few adjacent endothelial cells forming a sealed barrier between upper and lower compartments. Endothelial cells were modelled as hyperelastic material with shear modulus of 1 kPa (*257*, *258*). The dimensions of the cells in the monolayer were adopted from Arefi et al. (*258*). Considering the relative stiffness of gram-negative bacteria compared to endothelial cells, MTB were treated as rigid bodies. MTB were modelled as ellipsoids initially present in the upper compartment possessing a rigid dipole moment along their long axes. TEM images along with multisizer data (Figure S4-2) were used to estimate the average size of a single bacterium. Assuming 0.45 um for the short axis and using the diameter of equivalent volume from multisizer measurements, one could estimate the long axis of MTB to be approximately 1.8 um.

Motion of micron-sized objects in a fluid close to a wall is well studied as surface walkers under low Reynolds number flows (*264*, *265*, *286*). The free body diagram of single bacterium illustrates the balance of acting forces and torques in such an environment:

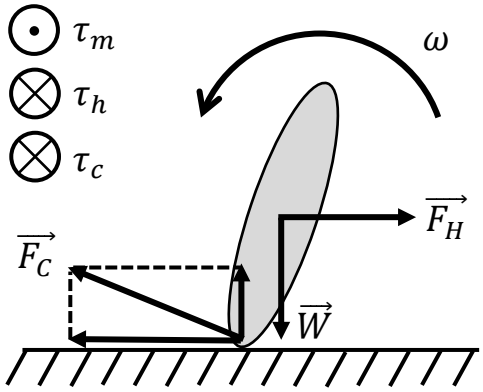

$$\sum \vec{F} = 0 \rightarrow \overrightarrow{F_H} + \overrightarrow{W} + \overrightarrow{F_C} = 0 \tag{11}$$

$$\sum \tau = 0 \rightarrow \tau_M + \tau_H + \tau_C = 0 \tag{12}$$

F_H indicates the viscous drag, W is the gravity force, and F_C is the reaction force from the substrate including both normal and frictional components. A mass density of ρ = 200 kg/m^3 was assumed for the bacteria to take the effect of buoyant force into account (*287*). In the conservation of angular momentum equation, τ_M represents magnetic torque, τ_H is hydrodynamic resistant torque, and τ_C indicates the torque coming from the interaction with the substrate and is given by:

$$\tau_C = rF_f \tag{13}$$

where the distance from the axis of rotation r = 0.9 μm and F_f is the friction force.

Magnetic torque arising from the lag between the magnetic dipole moment of MTB and external field is given by:

$$\tau_M = m\,B\,\sin\theta \tag{14}$$

where m is the magnetic dipole moment of MTB which is estimated from VSM measurements (*259*), B represents the external magnetic field, i.e. 20 mT, and θ is the phase lag between two vectors.

Stokes flow theorem correlates hydrodynamic interactions in terms of linear and rotational viscous drag with corresponding linear and angular velocities:

$$\overrightarrow{F_H} = \gamma \vec{v} \tag{15}$$

$$T_H = \alpha\omega \quad (16)$$

where γ and α are the linear drag coefficient rotational drag coefficient, respectively. Analytical expressions and empirical data were used to estimate the values of these these parameters which were set to $\gamma = 7.1 \times 10^{-9}$ N·s/m and $\alpha = 7.6 \times 10^{-20}$ N·m·s/rad in the simulations.

The velocity dependence of friction between two microscale objects has previously been reported (*288*). This feature was incorporated into the friction model in which the slip and no slip regime was determined by a critical friction force depending on normal traction and velocity difference between two objects at the point of contact. Numerically, the penalty method was employed to resolve the mechanical contact which is based on insertion of a spring between two objects, only active in the case of compression.

Rigid Body node of the Solid Mechanics interface was used to solve the above governing equations. Hydrodynamic interactions were then modeled as linear and rotational viscous damping acting on the rigid body.

In order to model the dynamic gaps forming stochastically between adjacent cells, a set of random parameters were generated for each simulation. These values determined the opening time of the junction and size of the gaps. Random gap size was within the range of 1.5 to 2.5 um (*261*) and the gap lifetime was set to 160 s (*262*). The overall simulation time was selected in a way that encompasses opening incidences of all gaps. Considering the size of the computational domain and translational motion of the bacteria, the simulation was carried out for 500 s.

Liposome characterization and bioconjugation of carboxylated liposomes to MTB

Bioconjugation of fluorescently-labelled liposomes to the MTB cell surface was achieved through carbodiimide mediated amidation. This coupling reaction relies on the terminal amine groups present in phospholipids, LPS, and various surface protein assemblies on the MTB cell membrane (*222*). In comparison to affinity-based conjugation, covalent crosslinking is a robust technique that produces a stable chemical bond for *in vitro* and *in vivo* applications (*219*, *220*).

Carboxylated liposomes fabricated using thin film hydration were found to have an average size of 184.2 ± 3.2 nm and a polydispersity index of 0.142 ± 0.055, indicating that the liposomes were monodisperse (Figure S4-5, Table S4-1). Zeta potential analysis showed that the liposomes had a

negative net surface charge of 39.8 ± 0.9 mV, confirming successful incorporation of charged carboxylic groups on the outer membrane of the liposomes.

The reactive carboxy groups on the liposomes were then covalently coupled to the primary amines on the MTB membrane using NHS chemistry. Flow cytometry was performed to confirm successful conjugation. Univariate histograms show a clear distinction between bacteria with low relative fluorescence and MTB-LP, which extend to higher relative fluorescence intensity values (Figure S4-6). The mean fluorescence intensity of the conjugates was approximately 380-fold higher than that of bacteria cells, signifying that liposomes were conjugated to the bacteria.

Supplementary Figures

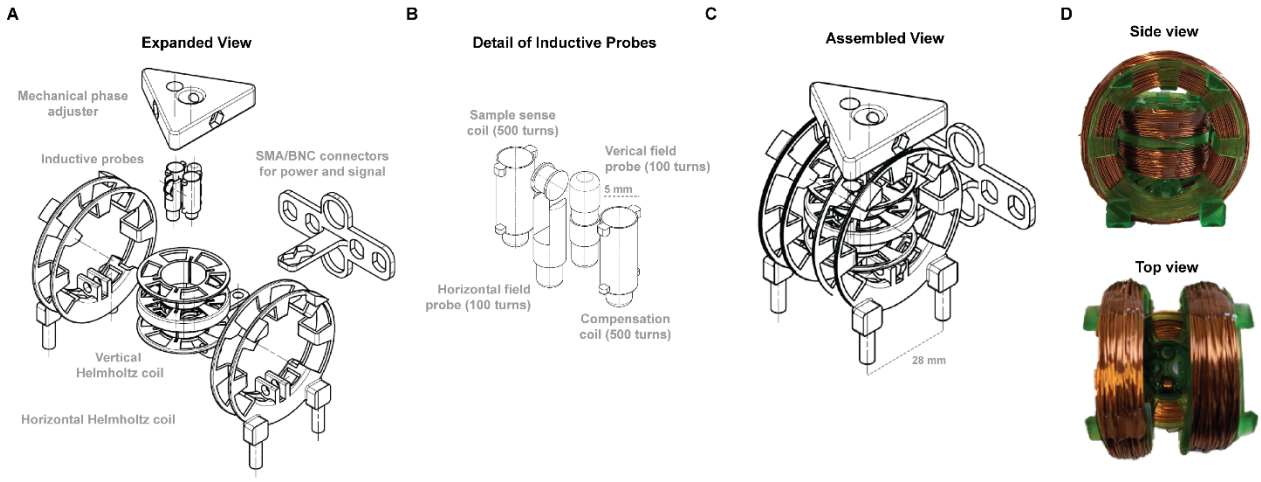

Figure S4-1: RMF magnetometer for inductive detection of MTB. (A) Technical drawing of RMF magnetometer frame and components. (B) Detailed drawing of inductive probes. (C) Technical drawing of assembled RMF magnetometer. (D) Images of side view and top view of the assembled RMF magnetometer.

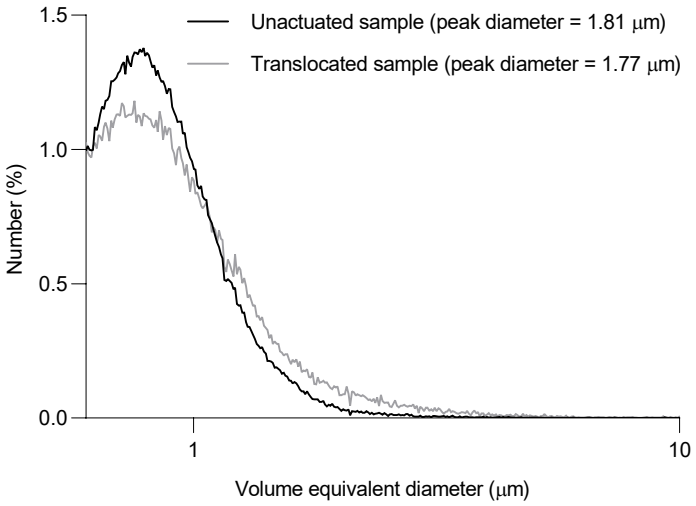

Figure S4-2: MTB size distributions before and after actuation. Average size distribution and average peak diameter values of MTB obtained by a Coulter counter. The plotted values are for the diameter of a sphere with equivalent volume and were used to estimate dimensions of the bacterial body (n = 3; mean).

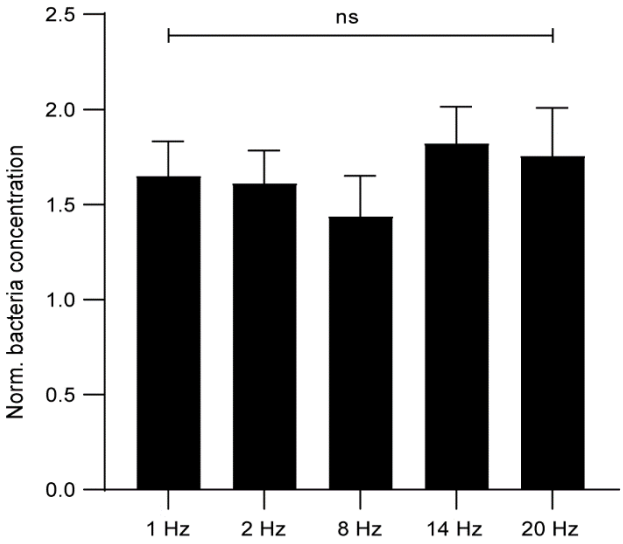

Figure S4-3: Comparison of MTB translocation across Caco-2 monolayers at varying out-of-plane rotational frequencies. Bacteria concentration was normalized to respective unactuated controls. No significance between all conditions ((*n* = 3; mean ± SD; ANOVA).

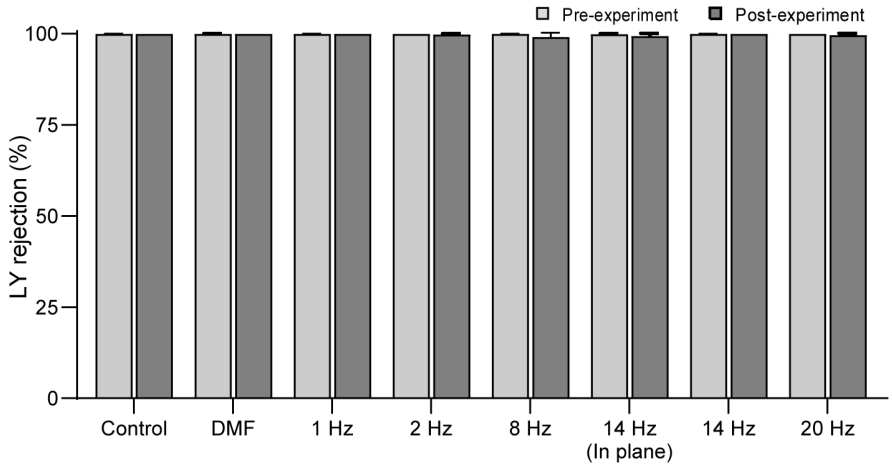

Figure S4-4: Lucifer yellow rejection values for Caco-2 monolayers. Pre- and post-experimental Lucifer yellow (LY) rejection values for all tested conditions. Experiments were performed at a magnetic field strength of 12 mT for all conditions (*n* = 3; mean ± SD).

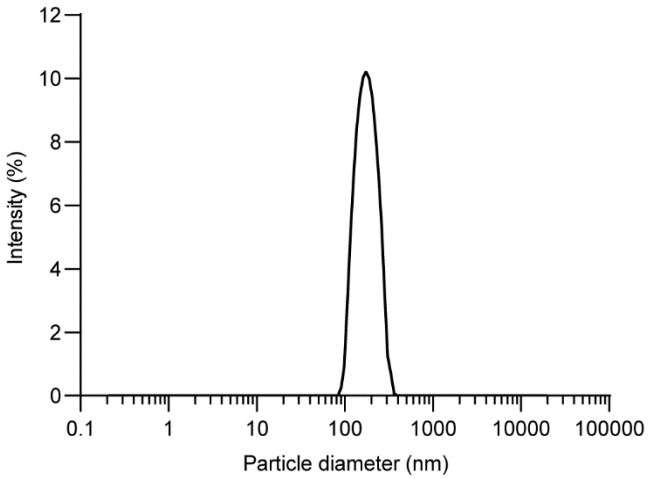

Figure S4-5: Size distribution of liposomes. Data collected using dynamic light scattering (DLS) (n = 3; mean)

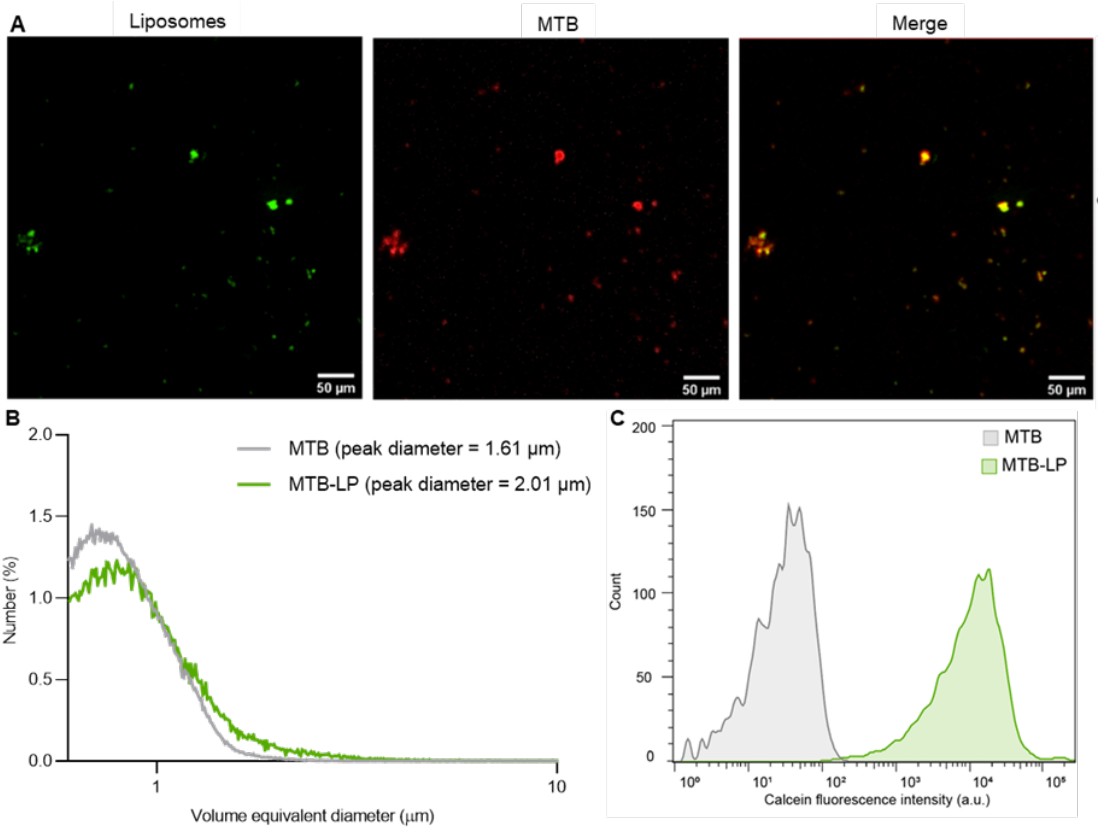

Figure S4-6: Bioconjugation of carboxylated liposomes to MTB. **(A)** Representative images of DiO-tagged liposomes conjugated to far-red stained MTB. **(B)** Size distribution and peak diameter values of MTB and MTB-LP obtained by a Coulter counter. The plotted values are for the diameter of a sphere with equivalent volume. **(C)** Representative flow cytometry histograms of unstained MTB and MTB-LP with calcein-loaded liposomes.

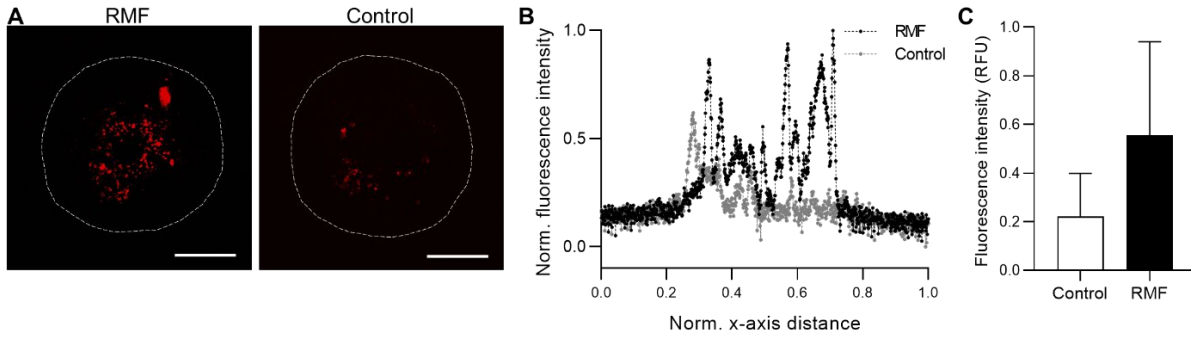

Figure S4-7: Assessment of MTB colonization in HCT116 tumour spheroids. (A) Representative *z*-projections from live HCT116 spheroids following 1 hour exposure to RMF (20 mT and 24 Hz), thorough washing, and incubation for up to 120 h without actuation. MTB were stained with a far-red proliferative stain and images were captured at 120 h. Control refers to unactuated samples. Scale bar = 200 µm. **(B)** Normalized fluorescence intensity distribution of actuated samples and controls at 120 h. Values were normalized to overall minimum and maximum fluorescence intensity values. Spheroid diameter was normalized along x-axis. **(C)** Image-based quantification of fluorescence intensity values from *z*-projections at 120 h (n = 3; mean ± SD).

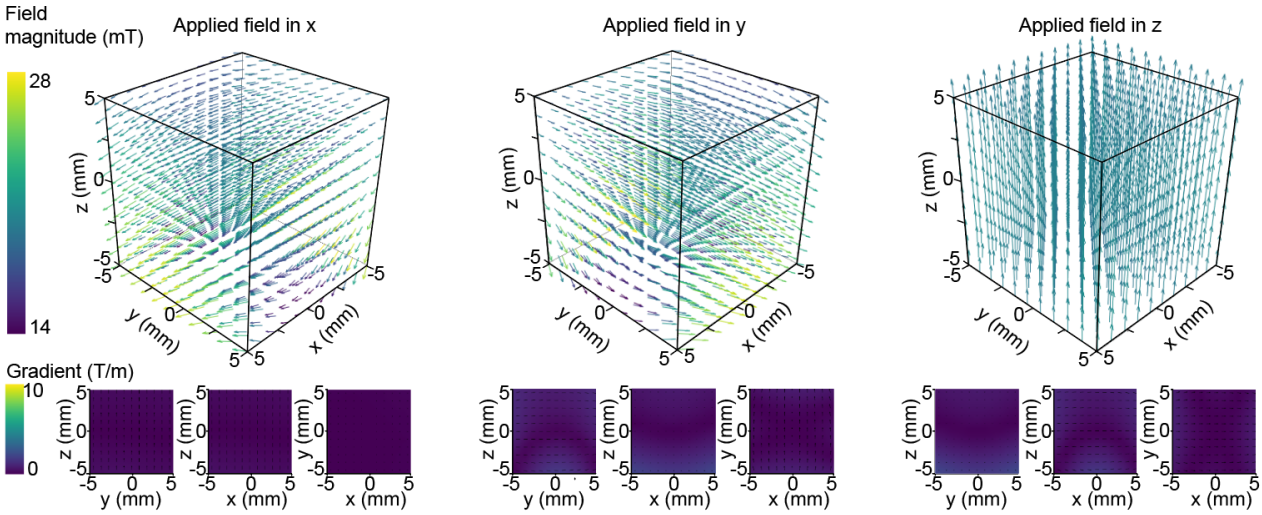

Figure S4-8: Plots of expected field magnitude and gradients. Fields and gradients produced in the workspace of the magnetic field generator for an applied field of 20 mT along the x, y, and *z*-axis.

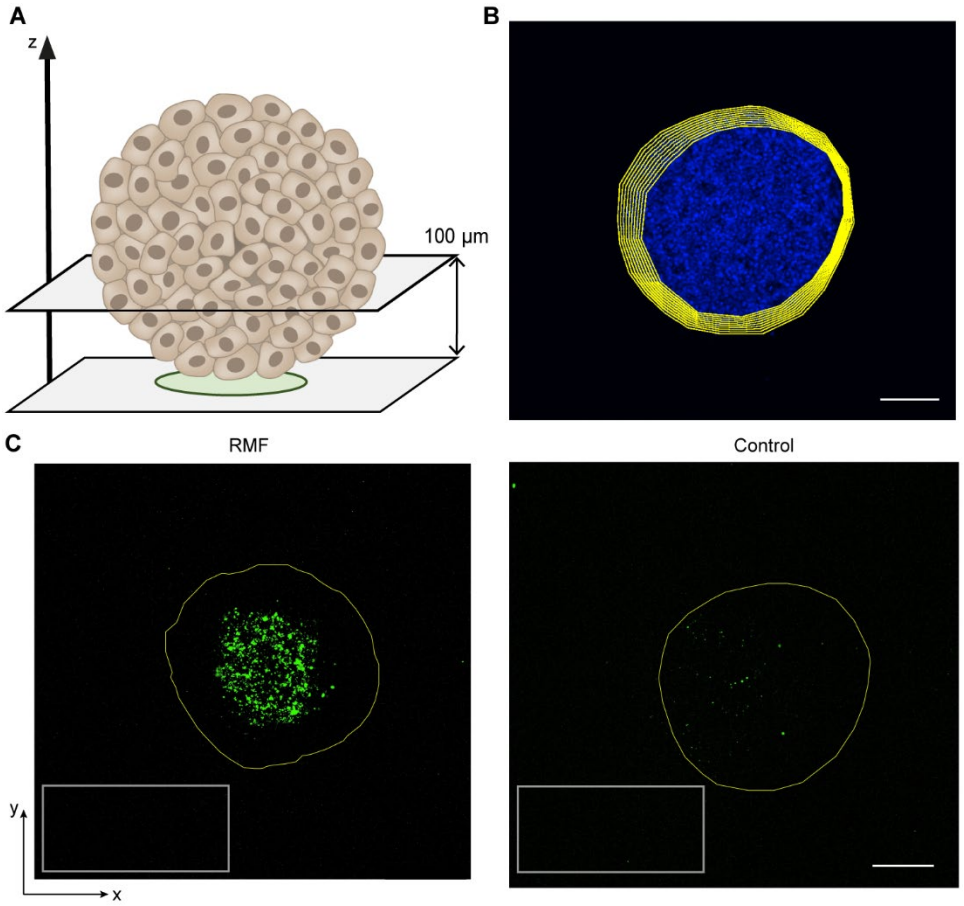

Figure S4-9: Quantification of fluorescence intensity in spheroids. (A) Schematic of MCF-7 spheroid with illustration of z-axis planes. Images were captured at 10 µm intervals from the bottom of the spheroids up to a depth of 100 µm. **(B)** Z-projection of Hoechst image stack with overlaid regions of interest (ROIs). To quantify the average fluorescence of DiO liposomes for each spheroid, ROIs were defined using the Hoechst image stack by tracing a contour around the spheroid at 0 and 100 µm. Intermediate ROIs were defined using interpolation, with approximately 3 µm radial increments. These ROIs were then applied to the corresponding DiO liposome image stack. Scale bar = 200 µm. **(C)** Representative images of sections from DiO liposome image stacks showing an interpolated ROI (yellow line). These fluorescence values were normalized to the average fluorescence of the surrounding media (ROI = gray rectangle). Scale bar = 200 µm.

Table S4-1. Physicochemical characterization of liposomes

Mean particle diamater [nm]	Mean zeta potential [mV]	Polydispersity index
184.2 ± 3.2	-39.8 ± 0.9 mV	0.142 ± 0.055

5. Conclusions and outlook

This work explored the use of MTB as a therapeutic agent for targeted cancer therapy. Although aquatic bacteria, like MTB, are an atypical choice for bacteria-mediated therapy, the innate properties of MTB present a unique opportunity to facilitate targeted delivery and colonisation of tumours. Their ability to migrate to low oxygen regions combined with their magnetic responsiveness can be leveraged for hybrid control strategies that merge magnetic manipulation with self-propulsion. Because research on the use of MTB for bacterial cancer therapy is still in its infancy, interactions between host immunity and MTB are yet to be studied. An understanding of the immunostimulatory properties of MTB will enable the safety and efficacy of this species to be established. Thus, some key properties of human innate immune cells in response to stimulation with the MTB strain *M. magneticum* AMB-1 were examined in various co-culture assays.

The ability of this living agent to effectively cross robust biological barriers when aided by magnetic actuation was also investigated. Magnetic control of conventional nanocarriers has been widely studied for decades, with most strategies relying on field gradients. The arrangement of magnetic nanoparticles within magnetosome chains in MTB enables the application of magnetic torques which can be exploited to enhance the delivery of MTB-LP. A hybrid control strategy that harnesses torque-driven motion followed by autonomous taxis-based navigation was employed to enhance MTB-LP transport *in vitro* and *in vivo* following clinically relevant systemic administration. The RMF-based strategy employed here may offer several advantages for clinical translation, including suitability for systemic deployment, scalability, inductive detection, and compatibility with selection fields. This work establishes that the MTB-LP platform combined with an RMF actuation scheme is a versatile system that could improve targeting and colonization of therapeutic bacteria in tumours.

Key findings

The main findings from this work are summarised below:

- MTB proliferate under physiological conditions and remain viable in human whole blood. MTB persisted in blood samples for 3 h and proliferation was higher at 37 °C than at 30 °C, although the magnetic responsiveness of MTB suspensions decreased over time. These findings suggested that magnetic actuation should be implemented within

the first 3 h after administration in *in vivo* applications, as viable MTB are likely to still be in circulation and the MTB population would still be magnetically responsive.

- MTB induce moDC maturation and promote the uptake of cancer cell material. Both antigen uptake and moDC maturation are crucial steps for mounting an effective antitumour response. The induction of moDC maturation by MTB was comparable to EcN and LPS after 6 h of co-culture. Furthermore, prior co-culture of cancer cells with MTB resulted in a substantial increase in the uptake of cancer cell material by moDCs, suggesting that the effect of MTB on cancer cells may be leveraged to promote active uptake by moDCs.
- MTB had a pronounced effect on arresting proliferation and inducing apoptosis in HCT116 cells. MTB compete with cancer cells for essential nutrients including iron, thus acting as a self-replicating iron chelator. This iron starvation has been found to induce cell death and dying cells release DAMPs which recruit DCs to the tumour site. This finding illustrates the ability of MTB to act as an effective living therapeutic agent that may potentially promote DC recruitment.
- Liposomes were efficiently conjugated to MTB using a copper-free click reaction. MTB-LP conjugates were used to deliver the well-established chemotherapeutic 5-FU. Following co-culture with MTB-LP, cell proliferation was significantly reduced in 4T1 cells compared to culture with MTB or liposomes alone, indicating that MTB enhanced the efficacy of 5-FU. MTB combined with 5-FU in solution was shown to substantially increase apoptosis, further suggesting a possible complementary therapeutic effect of MTB and the payload.
- Translational motion resulting from exposure to RMF enhanced the transport of MTB-LP across cell monolayers. Translocation driven by the application of out of plane RMF was significantly higher than transport following exposure to in plane RMF, DMF or in unactuated controls. Increased cell surface exploration resulting from translational motion of MTB was proposed as the primary mechanism responsible for increased transport across monolayers.
- Magnetic torque-driven motion, followed by autonomous taxis-based locomotion, proved to be highly effective in enhancing transport of MTB-LP in 3D tumour models. Actuation with RMF resulted in higher bacterial seeding in spheroids and significant accumulation in the spheroid core after 120 h. This accumulation is likely a result of taxis-based

navigation towards the hypoxic environment within the core of the spheroid. These findings demonstrate the ability of MTB-LP to form robust colonies in tumours, a prerequisite for effective bacteria-mediated cancer treatment.

- Increased accumulation of systemically administered MTB was achieved following exposure to RMF. Previous *in vivo* studies using MTB as drug delivery agents employed peritumoural administration, which is only suitable for easily accessible tumours. In contrast, this study used systemic administration which is more clinically applicable. Moreover, unlike some forms of magnetic stimulus, such as magnetic field gradients, RMF can be generated at clinically relevant scales for deeply situated tumours. Overall, this study lays the foundation for future efforts working towards the clinical translation of the MTB-LP platform for cancer therapy.

Outlook

Bacteria-based therapies are ushering in a new era of cancer treatment in which the innate tumour-targeting attributes of bacteria are leveraged to overcome current limitations of conventional therapies. There has been an exponential increase in preclinical studies that demonstrate the promise and potential of this strategy. Despite the momentum the field has experienced in recent years, there are still a few aspects that will need to be addressed for successful clinical translation of this approach.

While using tumour-targeting bacteria for cancer therapy has shown great promise, a combination of therapies may still be required, since tumour heterogeneity makes successful treatment with one agent difficult to achieve. Lessons may be taken from the treatment of bladder cancer where tumour resection is combined with treatment using BCG. Bacteria colonise the hypoxic and necrotic regions of tumours, while cytotoxic small molecules and radiation are most effective in treating highly perfused areas. As such, the synergy between bacteria and cytotoxic therapies, as demonstrated in this work, could be leveraged to more effectively eradicate tumours. Therefore, identifying suitable combinations to generate the most effective therapeutic outcomes could be a consideration in future.

Bacteria may be used to deliver a vast range of payloads to hypoxic regions, either though conjugated nanocarriers, like liposomes, or through the expression of therapeutic proteins. Expression of payloads by MTB would be advantageous as it would enable sufficiently high

quantities to be produced locally by the colonising bacteria. One limitation for such an approach is that many engineered biotherapeutics contain genes conferring antibiotic resistance and components that can facilitate horizontal gene transfer, such as plasmids. Since modified bacteria containing these elements are generally not suitable for clinical use, antibiotic-free selection and genomic integration can be explored for improved safety (*289*).

While adaptations to genetic engineering strategies for bacteria will address some safety concerns, further regulatory considerations will need to be tackled for future clinical use of live, replicating bacteria. Manufacturing living therapeutic bacteria is complex and several elements must be considered. Procedures to culture sufficient quantities of live bacteria and tests to validate that the end product is both axenic and sufficiently potent must be developed. In addition, since the final product cannot be sterilized by typical means as this would affect bacterial viability, protocols and procedures will need to be developed to comply with the standards of good manufacturing practices (GMP). This may include implementation of continuous monitoring of all steps in the manufacturing process and production of bacteria in dedicated clean rooms under strict aseptic conditions. Lastly, the final product should be tested to ensure purity and screened for causative agents.

With these considerations in mind, the combination of the unique attributes of bacteria with external guidance to facilitate robust tumour colonisation may achieve effective and enduring clinical outcomes. By complementing traditional treatment approaches with bacteria-mediated therapy, great advancements in cancer treatment may be on the horizon.

6. Bibliography

1. J. Shi, P. W. Kantoff, R. Wooster, O. C. Farokhzad, Cancer nanomedicine: progress, challenges and opportunities. *Nat. Rev. Cancer.* **17**, 20–37 (2017).
2. R. Tong, R. Langer, Nanomedicines Targeting the Tumor Microenvironment. *Cancer J.* **21**, 314–321 (2015).
3. E. Blanco, H. Shen, M. Ferrari, Principles of nanoparticle design for overcoming biological barriers to drug delivery. *Nat. Biotechnol.* **33** (2015), pp. 941–951.
4. V. P. Chauhan, T. Stylianopoulos, Y. Boucher, R. K. Jain, Delivery of Molecular and Nanoscale Medicine to Tumors: Transport Barriers and Strategies. *Annu. Rev. Chem. Biomol. Eng.* **2**, 281–298 (2011).
5. R. K. Jain, T. Stylianopoulos, Delivering nanomedicine to solid tumors. *Nat. Rev. Clin. Oncol.* **7**, 653–664 (2010).
6. S. Wilhelm, A. J. Tavares, Q. Dai, S. Ohta, J. Audet, H. F. Dvorak, W. C. W. Chan, Analysis of nanoparticle delivery to tumours. *Nat. Rev. Mater.* **1** (2016), pp. 1–12.
7. P. Koumoutsakos, I. Pivkin, F. Milde, The Fluid Mechanics of Cancer and Its Therapy. *Annu. Rev. Fluid Mech.* **45**, 325–355 (2013).
8. A. I. Minchinton, I. F. Tannock, Drug penetration in solid tumours. *Nat. Rev. Cancer.* **6** (2006), pp. 583–592.
9. M. W. Dewhirst, T. W. Secomb, Transport of drugs from blood vessels to tumour tissue. *Nat. Rev. Cancer.* **17** (2017), pp. 738–750.
10. J. K. Saggar, M. Yu, Q. Tan, I. F. Tannock, The tumor microenvironment and strategies to improve drug distribution. *Front. Oncol.* **3 JUN** (2013), , doi:10.3389/fonc.2013.00154.
11. S. Ferretti, P. R. Allegrini, M. M. Becquet, P. M. J. McSheehy, Tumor interstitial fluid pressure as an early-response marker for anticancer therapeutics. *Neoplasia.* **11**, 874–881 (2009).
12. S. Hoon Jang, M. Guillaume Wientjes, D. Lu, J. L-S Au, "Drug Delivery and Transport to Solid Tumors" (2003).
13. F. Combes, E. Meyer, N. N. Sanders, Immune cells as tumor drug delivery vehicles. *J. Control. Release.* **327**, 70–87 (2020).
14. S. Zhou, C. Gravekamp, D. Bermudes, K. Liu, Tumour-targeting bacteria engineered to fight cancer. *Nat. Rev. Cancer.* **18** (2018), pp. 727–743.
15. J. W. Yoo, D. J. Irvine, D. E. Discher, S. Mitragotri, Bio-inspired, bioengineered and biomimetic drug delivery carriers. *Nat. Rev. Drug Discov.* **10** (2011), pp. 521–535.
16. D. Akin, J. Sturgis, K. Ragheb, D. Sherman, K. Burkholder, J. P. Robinson, A. K. Bhunia, S. Mohammed, R. Bashir, Bacteria-mediated delivery of nanoparticles and cargo into cells. *Nat. Nanotechnol.* **2**, 441–449 (2007).
17. S. Chowdhury, S. Castro, C. Coker, T. E. Hinchliffe, N. Arpaia, T. Danino, Programmable bacteria induce durable tumor regression and systemic antitumor immunity. *Nat. Med.* **25**, 1057–1063 (2019).
18. F. Avogadri, C. Martinoli, L. Petrovska, C. Chiodoni, P. Transidico, V. Bronte, R. Longhi, M. P. Colombo, G. Dougan, M. Rescigno, Cancer immunotherapy based on killing of Salmonella-infected tumor cells. *Cancer Res.* **65**, 3920–3927 (2005).
19. C. H. Lee, C. L. Wu, A. L. Shiau, Toll-like receptor 4 mediates an antitumor host response induced by Salmonella choleraesuis. *Clin. Cancer Res.* **14**, 1905–1912 (2008).
20. N. S. Forbes, Engineering the perfect (bacterial) cancer therapy. *Nat. Rev. Cancer.* **10**, 785–794 (2010).
21. B. Ebbell, *The Papyrus Ebers, the greatest Egyptian medical document* (London: Oxford University Press, 1937).
22. T. A. Oelschlaeger, Bacteria as tumor therapeutics? *Bioeng. Bugs.* **1**, 146 (2010).
23. H. C. Nauts, *The beneficial effects of bacterial infections on host resistance to cancer. End results in 449 cases.* (Cancer Research Institute, New York, NY, ed. 2nd, 1980;

https://www.cancerresearch.org/CRI/media/HCN-Monographs/8_THE-BENEFICIAL-EFFECTS.pdf?ext=.pdf).

24. W. B. Coley, II. Contribution to the Knowledge of Sarcoma. *Ann. Surg.* **14**, 199–220 (1891).
25. W. B. Coley, The Treatment of Inoperable Sarcoma by Bacterial Toxins (the Mixed Toxins of the Streptococcus erysipelas and the Bacillus prodigiosus). *Proc. R. Soc. Med.* **3**, 1 (1910).
26. H. C. Nauts, J. R. McLaren, Coley toxins - The first century. *Adv. Exp. Med. Biol.* **267**, 483–500 (1990).
27. E. F. McCarthy, The Toxins of William B. Coley and the Treatment of Bone and Soft-Tissue Sarcomas. *Iowa Orthop. J.* **26**, 154 (2006).
28. C. O. Starnes, Coley's toxins in perspective. *Nature.* **357(6373):** (1992).
29. P. P. Connell, S. Hellman, Advances in Radiotherapy and Implications for the Next Century: A Historical Perspective. *Cancer Res.* **69**, 383–392 (2009).
30. N. S. Forbes, Engineering the perfect (bacterial) cancer therapy. *Nat. Rev. Cancer.* **10**, 785–94 (2010).
31. R. W. Carey, J. F. Holland, H. Y. Whang, E. Neter, B. Bryant, Clostridial oncolysis in man. *Eur. J. Cancer.* **3** (1967), doi:10.1016/0014-2964(67)90060-6.
32. F. Heppner, J. R. Möse, The liquefaction (oncolysis) of malignant gliomas by a non pathogenic Clostridium. *Acta Neurochir. (Wien).* **42**, 123–5 (1978).
33. W. Schmidt, E. M. Fabricius, U. Schneeweiss, The tumour-Clostridium phenomenon: 50 Years of developmental research (Review). *Int. J. Oncol.* **29**, 1479–1492 (2006).
34. V. Staedtke, N. J. Roberts, R. Y. Bai, S. Zhou, Clostridium novyi-NT in cancer therapy. *Genes Dis.* **3**, 144 (2016).
35. N. J. Roberts, L. Zhang, F. Janku, A. Collins, R. Y. Bai, V. Staedtke, A. W. Rusk, D. Tung, M. Miller, J. Roix, K. V. Khanna, R. Murthy, R. S. Benjamin, T. Helgason, A. D. Szvalb, J. E. Bird, S. Roy-Chowdhuri, H. H. Zhang, Y. Qiao, B. Karim, J. McDaniel, A. Elpiner, A. Sahora, J. Lachowicz, B. Phillips, A. Turner, M. K. Klein, G. Post, L. A. Diaz, G. J. Riggins, N. Papadopoulos, K. W. Kinzler, B. Vogelstein, C. Bettegowda, D. L. Huso, M. Varterasian, S. Saha, S. Zhou, Intratumoral injection of Clostridium novyi-NT spores induces antitumor responses. *Sci. Transl. Med.* **6**, 249ra111 (2014).
36. L. J. Old, D. A. Clarke, B. Benacerraf, Effect of Bacillus Calmette-Guérin Infection on Transplanted Tumours in the Mouse. *Nat. 1959 1844682*. **184**, 291–292 (1959).
37. G. Mathé, J. L. Amiel, L. Schwarzenberg, M. Schneider, A. Cattan, J. R. Schlumberger, M. Hayat, F. De Vassal, ACTIVE IMMUNOTHERAPY FOR ACUTE LYMPHOBLASTIC LEUKÆMIA. *Lancet.* **293**, 697–699 (1969).
38. D. L. Morton, F. R. Eilber, E. C. Holmes, J. S. Hunt, A. S. Ketcham, M. J. Silverstein, F. C. Sparks, BCG Immunotherapy of Malignant Melanoma: Summary of a Seven-year Experience. *Ann. Surg.* **180**, 635 (1974).
39. A. Morales, D. Eidinger, A. W. Bruce, Intracavitary Bacillus Calmette-guerin in the Treatment of Superficial Bladder Tumors. *J. Urol.* **116**, 180–182 (1976).
40. A. Morales, BCG: A throwback from the stone age of vaccines opened the path for bladder cancer immunotherapy. *Can. J. Urol.* **24** (2017).
41. N. Lobo, N. A. Brooks, A. R. Zlotta, J. D. Cirillo, S. Boorjian, P. C. Black, J. J. Meeks, T. J. Bivalacqua, P. Gontero, G. D. Steinberg, D. McConkey, M. Babjuk, J. Alfred Witjes, A. M. Kamat, 100 years of Bacillus Calmette–Guérin immunotherapy: from cattle to COVID-19. *Nat. Rev. Urol. 2021 1810.* **18**, 611–622 (2021).
42. C. Clairmont, K. C. Lee, J. Pike, M. Ittensohn, K. B. Low, J. Pawelek, D. Bermudes, S. M. Brecher, D. Margitich, J. Turnier, Z. Li, X. Luo, I. King, L. M. Zheng, Biodistribution and Genetic Stability of the Novel Antitumor Agent VNP20009, a Genetically Modified Strain of Salmonella typhimuvium. *J. Infect. Dis.* **181**, 1996–2002 (2000).
43. J. F. Toso, V. J. Gill, P. Hwu, F. M. Marincola, N. P. Restifo, D. J. Schwartzentruber, R. M. Sherry, S. L. Topalian, J. C. Yang, F. Stock, L. J. Freezer, K. E. Morton, C. Seipp, L. Haworth, S. Mavroukakis, D. White, S. MacDonald, J. Mao, M. Sznol, S. A. Rosenberg, Phase I Study of the

Intravenous Administration of Attenuated *Salmonella typhimurium* to Patients With Metastatic Melanoma. *J. Clin. Oncol.* **20**, 142–152 (2002).

44. D. M. Heimann, S. A. Rosenberg, Continuous Intravenous Administration of Live Genetically Modified Salmonella Typhimurium in Patients With Metastatic Melanoma. *J. Immunother.* **26**, 179 (2003).
45. J. Nemunaitis, C. Cunningham, N. Senzer, J. Kuhn, J. Cramm, C. Litz, R. Cavagnolo, A. Cahill, C. Clairmont, M. Sznol, Pilot trial of genetically modified, attenuated Salmonella expressing the E. coli cytosine deaminase gene in refractory cancer patients. *Cancer Gene Ther. 2003 1010*. **10**, 737–744 (2003).
46. S. Ganai, R. B. Arenas, J. P. Sauer, B. Bentley, N. S. Forbes, In tumors Salmonella migrate away from vasculature toward the transition zone and induce apoptosis. *Cancer Gene Ther.* **18**, 457–466 (2011).
47. C.-H. Lee, S.-T. Lin, J.-J. Liu, W.-W. Chang, J.-L. Hsieh, W.-K. Wang, Salmonella induce autophagy in melanoma by the downregulation of AKT/mTOR pathway. *Gene Ther.* **21**, 309–316 (2014).
48. A. Uchugonova, Y. Zhang, R. Salz, F. Liu, A. Suetsugu, L. Zhang, K. Koenig, R. M. Hoffman, M. Zhao, Imaging the different mechanisms of prostate cancer cell-killing by tumor-targeting Salmonella typhimurium A1-R. *Anticancer Res.* **35**, 5225–5230 (2015).
49. S. H. Kim, F. Castro, Y. Paterson, C. Gravekamp, High efficacy of a Listeria-based vaccine against metastatic breast cancer reveals a dual mode of action. *Cancer Res.* **69**, 5860–5866 (2009).
50. J. L. Middlebrook, R. B. Dorland, Bacterial toxins: cellular mechanisms of action. *Microbiol. Rev.* **48**, 199–221 (1984).
51. I. Cheong, X. Huang, C. Bettegowda, L. A. Diaz, K. W. Kinzler, S. Zhou, B. Vogelstein, A Bacterial Protein Enhances the Release and Efficacy of Liposomal Cancer Drugs. *Science (80-.).* **314**, 1308–1311 (2006).
52. S. Di Bella, P. Ascenzi, S. Siarakas, N. Petrosillo, A. di Masi, Clostridium difficile toxins A and B: Insights into pathogenic properties and extraintestinal effects. *Toxins (Basel).* **8**, 1–25 (2016).
53. J. E. Kim, T. X. Phan, V. H. Nguyen, H. Van Dinh-Vu, J. H. Zheng, M. Yun, S. G. Park, Y. Hong, H. E. Choy, M. Szardenings, W. Hwang, J. A. Park, S. H. Park, S. H. Im, J. J. Min, Salmonella typhimurium Suppresses Tumor Growth via the Pro-Inflammatory Cytokine Interleukin-1β. *Theranostics*. **5**, 1328 (2015).
54. M. A. Dobrovolskaia, S. N. Vogel, Toll receptors, CD14, and macrophage activation and deactivation by LPS. *Microbes Infect.* **4**, 903–914 (2002).
55. S. Leschner, K. Westphal, N. Dietrich, N. Viegas, J. Jablonska, M. Lyszkiewicz, S. Lienenklaus, W. Falk, N. Gekara, H. Loessner, S. Weiss, Tumor Invasion of Salmonella enterica Serovar Typhimurium Is Accompanied by Strong Hemorrhage Promoted by TNF-α. *PLoS One*. **4** (2009), doi:10.1371/JOURNAL.PONE.0006692.
56. F. Hayashi, K. D. Smith, A. Ozinsky, T. R. Hawn, E. C. Yi, D. R. Goodlett, J. K. Eng, S. Akira, D. M. Underhill, A. Aderem, The innate immune response to bacterial flagellin is mediated by Toll-like receptor 5. *Nat. 2001 4106832*. **410**, 1099–1103 (2001).
57. Z. Cai, A. Sanchez, Z. Shi, T. Zhang, M. Liu, D. Zhang, Activation of Toll-Like Receptor 5 on Breast Cancer Cells by Flagellin Suppresses Cell Proliferation and Tumor Growth. *Cancer Res.* **71**, 2466 (2011).
58. L. Sfondrini, A. Rossini, D. Besusso, A. Merlo, E. Tagliabue, S. Mènard, A. Balsari, Antitumor Activity of the TLR-5 Ligand Flagellin in Mouse Models of Cancer. *J. Immunol.* **176**, 6624–6630 (2006).
59. A. Kupz, R. Curtiss, S. Bedoui, R. A. Strugnell, In Vivo IFN-γ Secretion by NK Cells in Response to Salmonella Typhimurium Requires NLRC4 Inflammasomes. *PLoS One*. **9**, e97418 (2014).
60. N. D. Leigh, G. Bian, X. Ding, H. Liu, S. Aygun-Sunar, L. G. Burdelya, A. V. Gudkov, X. Cao, A Flagellin-Derived Toll-Like Receptor 5 Agonist Stimulates Cytotoxic Lymphocyte-Mediated Tumor Immunity. *PLoS One*. **9**, e85587 (2014).
61. F. Saccheri, C. Pozzi, F. Avogadri, S. Barozzi, M. Faretta, P. Fusi, M. Rescigno, Bacteria-induced gap junctions in tumors favor antigen cross-presentation and antitumor immunity. *Sci. Transl. Med.*

2 (2010), doi:10.1126/SCITRANSLMED.3000739/SUPPL_FILE/SACCHERI_SUPPL_MOVIE1.AVI.

62. H. C. Lin, C. J. Yang, Y. D. Kuan, W. K. Wang, W. W. Chang, C. H. Lee, The inhibition of indoleamine 2, 3-dioxygenase 1 by connexin 43. *Int. J. Med. Sci.* **14**, 1181 (2017).
63. A. Jahangir, D. Chandra, W. Quispe-Tintaya, M. Singh, B. C. Selvanesan, C. Gravekamp, Immunotherapy with Listeria reduces metastatic breast cancer in young and old mice through different mechanisms. *Oncoimmunology.* **6** (2017), doi:10.1080/2162402X.2017.1342025.
64. D. Chandra, A. Jahangir, W. Quispe-Tintaya, M. H. Einstein, C. Gravekamp, Myeloid-derived suppressor cells have a central role in attenuated Listeria monocytogenes-based immunotherapy against metastatic breast cancer in young and old mice. *Br. J. Cancer.* **108**, 2281–2290 (2013).
65. K. Westphal, S. Leschner, J. Jablonska, H. Loessner, S. Weiss, Containment of tumor-colonizing bacteria by host neutrophils. *Cancer Res.* **68**, 2952–2960 (2008).
66. N. Agrawal, C. Bettegowda, I. Cheong, J. F. Geschwind, C. G. Drake, E. L. Hipkiss, M. Tatsumi, L. H. Dang, L. A. Diaz, M. Pomper, M. Abusedera, R. L. Wahl, K. W. Kinzler, S. Zhou, D. L. Huso, B. Vogelstein, Bacteriolytic therapy can generate a potent immune response against experimental tumors. *Proc. Natl. Acad. Sci. U. S. A.* **101**, 15172–15177 (2004).
67. M. Shinnoh, M. Horinaka, T. Yasuda, S. Yoshikawa, M. Morita, T. Yamada, T. Miki, T. Sakai, Clostridium butyricum MIYAIRI 588 shows antitumor effects by enhancing the release of TRAIL from neutrophils through MMP-8. *Int. J. Oncol.* **42**, 903–911 (2013).
68. D. S. Leventhal, A. Sokolovska, N. Li, C. Plescia, S. A. Kolodziej, C. W. Gallant, R. Christmas, J. R. Gao, M. J. James, A. Abin-Fuentes, M. Momin, C. Bergeron, A. Fisher, P. F. Miller, K. A. West, J. M. Lora, Immunotherapy with engineered bacteria by targeting the STING pathway for anti-tumor immunity. *Nat. Commun.* **11**, 1–15 (2020).
69. J. M. Pawelek, K. B. Low, D. Bermudes, Tumor-targeted Salmonella as a novel anticancer vector. *Cancer Res.* **57**, 4537–4544 (1997).
70. D. A. Saltzman, C. P. Heise, D. E. Hasz, M. Zebede, S. M. Kelly, R. Curtiss, A. S. Leonard, P. M. Anderson, Attenuated Salmonella typhimurium containing interleukin-2 decreases MC-38 hepatic metastases: A novel anti-tumor agent. *Cancer Biother. Radiopharm.* **11**, 145–153 (1996).
71. E. M. Camacho, B. Mesa-Pereira, C. Medina, A. Flores, E. Santero, Engineering Salmonella as intracellular factory for effective killing of tumour cells. *Sci. Rep.* **6**, 1–12 (2016).
72. J. T. Panteli, N. S. Forbes, Engineered bacteria detect spatial profiles in glucose concentration within solid tumor cell masses. *Biotechnol. Bioeng.* **113**, 2474–2484 (2016).
73. R. M. Ryan, J. Green, P. J. Williams, S. Tazzyman, S. Hunt, J. H. Harmey, S. C. Kehoe, C. E. Lewis, Bacterial delivery of a novel cytolysin to hypoxic areas of solid tumors. *Gene Ther.* **16**, 329–339 (2009).
74. B. Yu, M. Yang, L. Shi, Y. Yao, Q. Jiang, X. Li, L. H. Tang, B. J. Zheng, K. Y. Yuen, D. K. Smith, E. Song, J. D. Huang, Explicit hypoxia targeting with tumor suppression by creating an "obligate" anaerobic Salmonella Typhimurium strain. *Sci. Rep.* **2**, 1–10 (2012).
75. A. Mengesha, L. Dubois, P. Lambin, W. Landuyt, R. K. Chiu, B. G. Wouters, J. Theys, Development of a flexible and potent hypoxia-inducible promoter for tumor-targeted gene expression in attenuated Salmonella. *Cancer Biol. Ther.* **5**, 1120–1128 (2006).
76. J. C. Anderson, E. J. Clarke, A. P. Arkin, C. A. Voigt, Environmentally controlled invasion of cancer cells by engineered bacteria. *J. Mol. Biol.* **355**, 619–627 (2006).
77. H. C. Wu, C. Y. Tsao, D. N. Quan, Y. Cheng, M. D. Servinsky, K. K. Carter, K. J. Jee, J. L. Terrell, A. Zargar, G. W. Rubloff, G. F. Payne, J. J. Valdes, W. E. Bentley, Autonomous bacterial localization and gene expression based on nearby cell receptor density. *Mol. Syst. Biol.* **9**, 1–8 (2013).
78. C. R. Gurbatri, I. Lia, R. Vincent, C. Coker, S. Castro, P. M. Treuting, T. E. Hinchliffe, N. Arpaia, T. Danino, Engineered probiotics for local tumor delivery of checkpoint blockade nanobodies. *Sci. Transl. Med.* **12** (2020), doi:10.1126/scitranslmed.aax0876.
79. S. Chowdhury, S. Castro, C. Coker, T. E. Hinchliffe, N. Arpaia, T. Danino, Programmable bacteria induce durable tumor regression and systemic antitumor immunity. *Nat. Med.* **25**, 1057–1063 (2019).

80. T. Harimoto, Z. S. Singer, O. S. Velazquez, J. Zhang, S. Castro, T. E. Hinchliffe, W. Mather, T. Danino, Rapid screening of engineered microbial therapies in a 3D multicellular model. *Proc. Natl. Acad. Sci. U. S. A.* **116**, 9002–9007 (2019).
81. V. Du Nguyen, J. W. Han, Y. J. Choi, S. Cho, S. Zheng, S. Y. Ko, J. O. Park, S. Park, Active tumor-therapeutic liposomal bacteriobot combining a drug (paclitaxel)-encapsulated liposome with targeting bacteria (Salmonella Typhimurium). *Sensors Actuators, B Chem.* **224**, 217–224 (2016).
82. S. J. Park, S. H. Park, S. Cho, D. M. Kim, Y. Lee, S. Y. Ko, Y. Hong, H. E. Choy, J. J. Min, J. O. Park, S. Park, New paradigm for tumor theranostic methodology using bacteria-based microrobot. *Sci. Rep.* **3**, 1–8 (2013).
83. S. B. Suh, A. Jo, M. A. Traore, Y. Zhan, S. L. Coutermarsh-Ott, V. M. Ringel-Scaia, I. C. Allen, R. M. Davis, B. Behkam, Nanoscale Bacteria-Enabled Autonomous Drug Delivery System (NanoBEADS) Enhances Intratumoral Transport of Nanomedicine. *Adv. Sci.* **6**, 1801309 (2019).
84. W. Quispe-Tintaya, D. Chandra, A. Jahangir, M. Harris, A. Casadevall, E. Dadachova, C. Gravekamp, Nontoxic radioactive Listeriaat is a highly effective therapy against metastatic pancreatic cancer. *Proc. Natl. Acad. Sci. U. S. A.* **110**, 8668–8673 (2013).
85. S. Taherkhani, M. Mohammadi, J. Daoud, S. Martel, M. Tabrizian, Covalent binding of nanoliposomes to the surface of magnetotactic bacteria for the synthesis of self-propelled therapeutic agents. *ACS Nano.* **8**, 5049–5060 (2014).
86. O. Felfoul, M. Mohammadi, S. Taherkhani, D. De Lanauze, Y. Zhong Xu, D. Loghin, S. Essa, S. Jancik, D. Houle, M. Lafleur, L. Gaboury, M. Tabrizian, N. Kaou, M. Atkin, T. Vuong, G. Batist, N. Beauchemin, D. Radzioch, S. Martel, Magneto-aerotactic bacteria deliver drug-containing nanoliposomes to tumour hypoxic regions. *Nat. Nanotechnol.* **11**, 941–947 (2016).
87. J. Xing, T. Yin, S. Li, T. Xu, A. Ma, Z. Chen, Y. Luo, Z. Lai, Y. Lv, H. Pan, R. Liang, X. Wu, M. Zheng, L. Cai, Sequential Magneto-Actuated and Optics-Triggered Biomicrorobots for Targeted Cancer Therapy. *Adv. Funct. Mater.* **31**, 1–10 (2021).
88. Z. Xiang, G. Jiang, D. Fan, J. Tian, Z. Hu, Q. Fang, Drug-internalized bacterial swimmers for magnetically manipulable tumor-targeted drug delivery. *Nanoscale*. **12**, 13513–13522 (2020).
89. J. P. Armitage, Bacterial Taxis. *Encycl. Life Sci.* (2007), doi:10.1002/9780470015902.a0000340.pub2.
90. G. H. Wadhams, J. P. Armitage, Making sense of it all: Bacterial chemotaxis. *Nat. Rev. Mol. Cell Biol.* **5**, 1024–1037 (2004).
91. T. Krell, J. Lacal, F. Muñoz-Martínez, J. A. Reyes-Darias, B. H. Cadirci, C. García-Fontana, J. L. Ramos, Diversity at its best: Bacterial taxis. *Environ. Microbiol.* **13**, 1115–1124 (2011).
92. V. Sourjik, N. S. Wingreen, Responding to chemical gradients: Bacterial chemotaxis. *Curr. Opin. Cell Biol.* **24**, 262–268 (2012).
93. H. C. Berg, The Rotary Motor of Bacterial Flagella. *Annu. Rev. Biochem.* **72**, 19–54 (2003).
94. T. Minamino, K. Imada, The bacterial flagellar motor and its structural diversity. *Trends Microbiol.* **23**, 267–274 (2015).
95. R. A. Goldstein, O. S. Soyer, Evolution of taxis responses in virtual bacteria: Non-adaptive dynamics. *PLoS Comput. Biol.* **4**, 1–7 (2008).
96. B. L. Taylor, I. B. Zhulin, M. S. Johnson, A o e -s b b (1999).
97. E. M. Purcell, Life at low Reynolds number. *Am. J. Phys.* **45**, 3–11 (1977).
98. H. C. BERG, R. A. ANDERSON, Bacteria Swim by Rotating their Flagellar Filaments. *Nature*. **245**, 380–382 (1973).
99. K. E. Peyer, L. Zhang, B. J. Nelson, Bio-inspired magnetic swimming microrobots for biomedical applications. *Nanoscale*. **5**, 1259–1272 (2013).
100. B. Rodenborn, C. H. Chen, H. L. Swinney, B. Liu, H. P. Zhang, Propulsion of microorganisms by a helical flagellum. *Proc. Natl. Acad. Sci. U. S. A.* **110** (2013).
101. Y. Sowa, R. M. Berry, Bacterial flagellar motor. *Q. Rev. Biophys.* **41**, 103–132 (2008).
102. J. Bastos-Arrieta, A. Revilla-Guarinos, W. E. Uspal, J. Simmchen, Bacterial biohybrid microswimmers. *Front. Robot. AI.* **5**, 1–16 (2018).

103. R. A. Malmgren, C. C. Flanigan, Localization of the Vegetative Form of Clostridium tetani in Mouse Tumors Following Intravenous Spore Administration. *Cancer Res.* **15**, 473–478 (1955).
104. P. Lambin, J. Theys, W. Landuyt, P. Rijken, A. Van Der Kogel, E. Van Der Schueren, R. Hodgkiss, J. Fowler, S. Nuyts, E. De Bruijn, L. Van Mellaert, J. Anné, Colonisation of Clostridium in the body is restricted to hypoxic and necrotic areas of tumours. *Anaerobe*. **4**, 183–188 (1998).
105. T. Kimura, K. Aoki, T. Baba, Selective Localizationand Growth of Bifidobacteriumbifidum in Mouse TumorsfollowingIntravenousAdministration', 2061–2068 (1980).
106. M. W. Dewhirst, T. W. Secomb, Transport of drugs from blood vessels to tumour tissue. *Nat. Rev. Cancer*. **17**, 738–750 (2017).
107. T. Stylianopoulos, L. L. Munn, R. K. Jain, Reengineering the Physical Microenvironment of Tumors to Improve Drug Delivery and Efficacy: From Mathematical Modeling to Bench to Bedside. *Trends in Cancer*. **4**, 292–319 (2018).
108. S. Taniguchi, Y. Shimatani, M. Fujimori, R. M. Hoffman, Ed. (Springer New York, New York, NY, 2016; https://doi.org/10.1007/978-1-4939-3515-4_5), pp. 49–60.
109. V. Staedtke, R. Y. Bai, W. Sun, J. Huang, K. K. Kibler, B. M. Tyler, G. L. Gallia, K. Kinzler, B. Vogelstein, S. Zhou, G. J. Riggins, Clostridium novyi-NT can cause regression of orthotopically implanted glioblastomas in rats. *Oncotarget*. **6**, 5536–5546 (2015).
110. S. Zhou, C. Gravekamp, D. Bermudes, K. Liu, Tumour-targeting bacteria engineered to fight cancer. *Nat. Rev. Cancer*. **18**, 727–743 (2018).
111. N. S. Forbes, Engineering the perfect (bacterial) cancer therapy. *Nat. Rev. Cancer*. **10**, 785–94 (2010).
112. R. W. Kasinskas, N. S. Forbes, Salmonella typhimurium lacking ribose chemoreceptors localize in tumor quiescence and induce apoptosis. *Cancer Res.* **67**, 3201–3209 (2007).
113. N. S. Forbes, L. L. Munn, D. Fukumura, R. K. Jain, Sparse initial entrapment of systemically injected Salmonella typhimurium leads to heterogeneous accumulation within tumors. *Cancer Res.* **63**, 5188–5193 (2003).
114. R. W. Kasinskas, N. S. Forbes, Salmonella typhimurium Specifically Chemotax and Proliferate in Heterogeneous Tumor Tissue In Vitro. *Biotechnol. Bioeng.* **10**, 710–721 (2006).
115. M. G. Kramer, M. Masner, F. A. Ferreira, R. M. Hoffman, Bacterial therapy of cancer: Promises, limitations, and insights for future directions. *Front. Microbiol.* **9**, 1–9 (2018).
116. S. Leschner, K. Westphal, N. Dietrich, N. Viegas, J. Jablonska, M. Lyszkiewicz, S. Lienenklaus, W. Falk, N. Gekara, H. Loessner, S. Weiss, Tumor invasion of Salmonella enterica serovar Typhimurium is accompanied by strong hemorrhage promoted by TNF-alpha. *PLoS One*. **4**, e6692 (2009).
117. M. T. Q. Duong, Y. Qin, S. H. You, J. J. Min, Bacteria-cancer interactions: bacteria-based cancer therapy. *Exp. Mol. Med.* **51** (2019), doi:10.1038/s12276-019-0297-0.
118. J. Cummins, M. Tangney, Bacteria and tumours: Causative agents or opportunistic inhabitants? *Infect. Agent. Cancer*. **8**, 1–8 (2013).
119. D. Morrissey, G. O'Sullivan, M. Tangney, Tumour Targeting with Systemically Administered Bacteria. *Curr. Gene Ther.* **10**, 3–14 (2010).
120. Y. A. Yu, S. Shabahang, T. M. Timiryasova, Q. Zhang, R. Beltz, I. Gentschev, W. Goebel, A. A. Szalay, Visualization of tumors and metastases in live animals with bacteria and vaccinia virus encoding light-emitting proteins. *Nat. Biotechnol.* **22**, 313–320 (2004).
121. N. Agrawal, C. Bettegowda, I. Cheong, J. F. Geschwind, C. G. Drake, E. L. Hipkiss, M. Tatsumi, L. H. Dang, L. A. Diaz, M. Pomper, M. Abusedera, R. L. Wahl, K. W. Kinzler, S. Zhou, D. L. Huso, B. Vogelstein, Bacteriolytic therapy can generate a potent immune response against experimental tumors. *Proc. Natl. Acad. Sci. U. S. A.* **101**, 15172–15177 (2004).
122. Y. A. Yu, Q. Zhang, A. A. Szalay, Establishment and characterization of conditions required for tumor colonization by intravenously delivered bacteria. *Biotechnol. Bioeng.* **100**, 567–578 (2008).
123. C. Piñero-Lambea, G. Bodelón, R. Fernández-Periáñez, A. M. Cuesta, L. Álvarez-Vallina, L. Á. Fernández, Programming controlled adhesion of E. coli to target surfaces, cells, and tumors with synthetic adhesins. *ACS Synth. Biol.* **4**, 463–473 (2015).

124. P. E. Massa, A. Paniccia, A. Monegal, A. De Marco, M. Rescigno, Salmonella engineered to express CD20-targeting antibodies and a drug-converting enzyme can eradicate human lymphomas. *Blood*. **122**, 705–714 (2013).
125. M. Bereta, A. Hayhurst, M. Gajda, P. Chorobik, M. Targosz, J. Marcinkiewicz, H. L. Kaufman, Improving tumor targeting and therapeutic potential of Salmonella VNP20009 by displaying cell surface CEA-specific antibodies. *Vaccine*. **25**, 4183–4192 (2007).
126. R. K. Jain, T. Stylianopoulos, Delivering nanomedicine to solid tumors. *Nat. Rev. Clin. Oncol.* **7**, 653–664 (2010).
127. N. Amreddy, A. Babu, R. Muralidharan, J. Panneerselvam, A. Srivastava, R. Ahmed, M. Mehta, A. Munshi, R. Ramesh, *Recent Advances in Nanoparticle-Based Cancer Drug and Gene Delivery* (Elsevier Inc., ed. 1, 2018), vol. 137.
128. S. Martel, Bacterial microsystems and microrobots. *Biomed. Microdevices*. **14**, 1033–1045 (2012).
129. Z. Hosseinidoust, B. Mostaghaci, O. Yasa, B. W. Park, A. V. Singh, M. Sitti, Bioengineered and biohybrid bacteria-based systems for drug delivery. *Adv. Drug Deliv. Rev.* **106**, 27–44 (2016).
130. E. Steager, C. B. Kim, J. Patel, S. Bith, C. Naik, L. Reber, M. J. Kim, Control of microfabricated structures powered by flagellated bacteria using phototaxis. *Appl. Phys. Lett.* **90**, 263901 (2007).
131. P. Zheng, M. Fan, H. Liu, Y. Zhang, X. Dai, H. Li, X. Zhou, S. Hu, X. Yang, Y. Jin, N. Yu, S. Guo, J. Zhang, X. J. Liang, K. Cheng, Z. Li, Self-Propelled and Near-Infrared-Phototaxic Photosynthetic Bacteria as Photothermal Agents for Hypoxia-Targeted Cancer Therapy. *ACS Nano*. **15**, 1100–1110 (2021).
132. Y. Alapan, O. Yasa, B. Yigit, I. C. Yasa, P. Erkoc, M. Sitti, Microrobotics and Microorganisms: Biohybrid Autonomous Cellular Robots. *Annu. Rev. Control. Robot. Auton. Syst.* **2**, 205–230 (2019).
133. B. W. Park, J. Zhuang, O. Yasa, M. Sitti, Multifunctional Bacteria-Driven Microswimmers for Targeted Active Drug Delivery. *ACS Nano*. **11**, 8910–8923 (2017).
134. M. T. Buss, P. Ramesh, M. A. English, A. Lee-Gosselin, M. G. Shapiro, Spatial Control of Probiotic Bacteria in the Gastrointestinal Tract Assisted by Magnetic Particles. *Adv. Mater.* **2007473**, 1–12 (2021).
135. R. W. Carlsen, M. R. Edwards, J. Zhuang, C. Pacoret, M. Sitti, Magnetic steering control of multi-cellular bio-hybrid microswimmers. *Lab Chip*. **14**, 3850–3859 (2014).
136. M. Aubry, W. A. Wang, Y. Guyodo, E. Delacou, J. M. Guigner, O. Espeli, A. Lebreton, F. Guyot, Z. Gueroui, Engineering E. coli for magnetic control and the spatial localization of functions. *ACS Synth. Biol.* **9**, 3030–3041 (2020).
137. A. Elfick, G. Rischitor, R. Mouras, A. Azfer, L. Lungaro, M. Uhlarz, T. Herrmannsdörfer, J. Lucocq, W. Gamal, P. Bagnaninchi, S. Semple, D. M. Salter, Biosynthesis of magnetic nanoparticles by human mesenchymal stem cells following transfection with the magnetotactic bacterial gene mms6. *Sci. Rep.* **7**, 1–8 (2017).
138. M. L. Fdez-Gubieda, J. Alonso, A. García-Prieto, A. García-Arribas, L. Fernández Barquín, A. Muela, Magnetotactic bacteria for cancer therapy. *J. Appl. Phys.* **128** (2020), doi:10.1063/5.0018036.
139. D. Kuzajewska, A. Wszołek, W. Żwierełło, L. Kirczuk, A. Maruszewska, Magnetotactic bacteria and magnetosomes as smart drug delivery systems: A new weapon on the battlefield with cancer? *Biology (Basel).* **9** (2020), doi:10.3390/biology9050102.
140. D. A. Bazylinski, D. Trubitsyn, Magnetotactic bacteria and magnetosomes. *Magn. Nanoparticles Biosensing Med.*, 251–284 (2019).
141. D. Faivre, D. Schüler, Magnetotactic bacteria and magnetosomes. *Chem. Rev.* **108**, 4875–4898 (2008).
142. L. Yan, S. Zhang, P. Chen, H. Liu, H. Yin, H. Li, Magnetotactic bacteria, magnetosomes and their application. *Microbiol. Res.* **167**, 507–519 (2012).
143. S. Martel, M. Mohammadi, O. Felfoul, Zhao Lu, P. Pouponneau, Flagellated magnetotactic bacteria as controlled MRI-trackable propulsion and steering systems for medical nanorobots operating in the human microvasculature. *Int. J. Rob. Res.* **28**, 571–582 (2009).

144. S. Martel, O. Felfoul, J. B. Mathieu, A. Chanu, S. Tamaz, M. Mohammadi, M. Mankiewicz, N. Tabatabaei, MRI-based medical nanorobotic platform for the control of magnetic nanoparticles and flagellated bacteria for target interventions in human capillaries. *Int. J. Rob. Res.* **28**, 1169–1182 (2009).
145. N. Mokrani, O. Felfoul, F. A. Zarreh, M. Mohammadi, R. Aloyz, G. Batist, S. Martel, Magnetotactic bacteria penetration into multicellular tumor spheroids for targeted therapy. *2010 Annu. Int. Conf. IEEE Eng. Med. Biol. Soc. EMBC'10*, 4371–4374 (2010).
146. O. Felfoul, S. Martel, Assessment of navigation control strategy for magnetotactic bacteria in microchannel: Toward targeting solid tumors. *Biomed. Microdevices.* **15**, 1015–1024 (2013).
147. B. Shapiro, Towards dynamic control of magnetic fields to focus magnetic carriers to targets deep inside the body. *J. Magn. Magn. Mater.* **321**, 1594–1599 (2009).
148. I. S. M. Khalil, M. P. Pichel, L. Abelmann, S. Misra, Closed-loop control of magnetotactic bacteria. *Int. J. Rob. Res.* **32**, 637–649 (2013).
149. I. S. M. Khalil, S. Misra, Control characteristics of magnetotactic bacteria: Magnetospirillum magnetotacticum strain MS-1 and magnetospirillum magneticum strain AMB-1. *IEEE Trans. Magn.* **50** (2014), doi:10.1109/TMAG.2013.2287495.
150. D. Loghin, C. Tremblay, M. Mohammadi, S. Martel, Exploiting the responses of magnetotactic bacteria robotic agents to enhance displacement control and swarm formation for drug delivery platforms. *Int. J. Rob. Res.* **36**, 1195–1210 (2017).
151. D. Loghin, C. Tremblay, S. Martel, Improved three-dimensional remote aggregations of magnetotactic bacteria for tumor targeting. *2016 Int. Conf. Manip. Autom. Robot. Small Scales, MARSS*, 1–6 (2016).
152. N. Mirkhani, M. G. Christiansen, S. Schuerle, Living, Self-Replicating Ferrofluids for Fluidic Transport. *Adv. Funct. Mater.* **30**, 1–11 (2020).
153. S. Schuerle, A. P. Soleimany, T. Yeh, G. M. Anand, M. Häberli, H. E. Fleming, N. Mirkhani, F. Qiu, S. Hauert, X. Wang, B. J. Nelson, S. N. Bhatia, Synthetic and living micropropellers for convection-enhanced nanoparticle transport. *Sci. Adv.* **5** (2019), doi:10.1126/sciadv.aav4803.
154. B. Amulic, C. Cazalet, G. L. Hayes, K. D. Metzler, A. Zychlinsky, Neutrophil function: From mechanisms to disease. *Annu. Rev. Immunol.* **30** (2012), pp. 459–489.
155. C. Tecchio, A. Micheletti, M. A. Cassatella, Neutrophil-derived cytokines: Facts beyond expression. *Front. Immunol.* **5** (2014), p. 508.
156. C. Silvestre-Roig, A. Hidalgo, O. Soehnlein, Neutrophil heterogeneity: implications for homeostasis and pathogenesis. *Blood.* **127**, 2173–2181 (2016).
157. K. Westphal, S. Leschner, J. Jablonska, H. Loessner, S. Weiss, Containment of Tumor-Colonizing Bacteria by Host Neutrophils. *Cancer Res.* **68**, 2952–2960 (2008).
158. M. Shinnoh, M. Horinaka, T. Yasuda, S. Yoshikawa, M. Morita, T. Yamada, T. Miki, T. Sakai, Clostridium butyricum MIYAIRI 588 shows antitumor effects by enhancing the release of TRAIL from neutrophils through MMP-8. *Int. J. Oncol.* **42**, 903–911 (2013).
159. D. Abraham, K. Zins, M. Sioud, T. Lucas, R. Schäfer, E. R. Stanley, S. Aharinejad, Stromal cell-derived CSF-1 blockade prolongs xenograft survival of CSF-1-negative neuroblastoma. *Int. J. Cancer.* **126**, 1339–1352 (2010).
160. N. Halama, I. Zoernig, A. Berthel, C. Kahlert, F. Klupp, M. Suarez-Carmona, T. Suetterlin, K. Brand, J. Krauss, F. Lasitschka, T. Lerchl, C. Luckner-Minden, A. Ulrich, M. Koch, J. Weitz, M. Schneider, M. W. Buechler, L. Zitvogel, T. Herrmann, A. Benner, C. Kunz, S. Luecke, C. Springfeld, N. Grabe, C. S. Falk, D. Jaeger, Tumoral Immune Cell Exploitation in Colorectal Cancer Metastases Can Be Targeted Effectively by Anti-CCR5 Therapy in Cancer Patients. *Cancer Cell.* **29**, 587–601 (2016).
161. L. Bonapace, M. M. Coissieux, J. Wyckoff, K. D. Mertz, Z. Varga, T. Junt, M. Bentires-Alj, Cessation of CCL2 inhibition accelerates breast cancer metastasis by promoting angiogenesis. *Nature.* **515**, 130–133 (2014).
162. K. B. Long, W. L. Gladney, G. M. Tooker, K. Graham, J. A. Fraietta, G. L. Beatty, IFNγ and CCL2 cooperate to redirect tumor-infiltrating monocytes to degrade fibrosis and enhance chemotherapy

efficacy in pancreatic carcinoma. *Cancer Discov.* **6**, 400–413 (2016).
163. B. Z. Qian, J. Li, H. Zhang, T. Kitamura, J. Zhang, L. R. Campion, E. A. Kaiser, L. A. Snyder, J. W. Pollard, CCL2 recruits inflammatory monocytes to facilitate breast-tumour metastasis. *Nature*. **475**, 222–225 (2011).
164. A. Mantovani, S. Sozzani, M. Locati, P. Allavena, A. Sica, Macrophage polarization: Tumor-associated macrophages as a paradigm for polarized M2 mononuclear phagocytes. *Trends Immunol.* **23** (2002), pp. 549–555.
165. A. Mantovani, F. Marchesi, A. Malesci, L. Laghi, P. Allavena, Tumour-associated macrophages as treatment targets in oncology. *Nat. Rev. Clin. Oncol.* **14** (2017), pp. 399–416.
166. J. Xue, S. V. Schmidt, J. Sander, A. Draffehn, W. Krebs, I. Quester, D. DeNardo, T. D. Gohel, M. Emde, L. Schmidleithner, H. Ganesan, A. Nino-Castro, M. R. Mallmann, L. Labzin, H. Theis, M. Kraut, M. Beyer, E. Latz, T. C. Freeman, T. Ulas, J. L. Schultze, Transcriptome-Based Network Analysis Reveals a Spectrum Model of Human Macrophage Activation. *Immunity*. **40**, 274–288 (2014).
167. A. Mildner, S. Jung, Development and function of dendritic cell subsets. *Immunity*. **40** (2014), pp. 642–656.
168. H. L. Hanson, D. L. Donermeyer, H. Ikeda, J. M. White, V. Shankaran, L. J. Old, H. Shiku, R. D. Schreiber, P. M. Allen, Eradication of established tumors by CD8+ T cell adoptive immunotherapy. *Immunity*. **13**, 265–276 (2000).
169. H. Matsushita, M. D. Vesely, D. C. Koboldt, C. G. Rickert, R. Uppaluri, V. J. Magrini, C. D. Arthur, J. M. White, Y. S. Chen, L. K. Shea, J. Hundal, M. C. Wendl, R. Demeter, T. Wylie, J. P. Allison, M. J. Smyth, L. J. Old, E. R. Mardis, R. D. Schreiber, Cancer exome analysis reveals a T-cell-dependent mechanism of cancer immunoediting. *Nature*. **482**, 400–404 (2012).
170. V. Shankaran, H. Ikeda, A. T. Bruce, J. M. White, P. E. Swanson, L. J. Old, R. D. Schreiber, IFNγ, and lymphocytes prevent primary tumour development and shape tumour immunogenicity. *Nature*. **410**, 1107–1111 (2001).
171. C. H. June, J. T. Warshauer, J. A. Bluestone, Is autoimmunity the Achilles' heel of cancer immunotherapy? *Nat. Med. 2017 235*. **23**, 540–547 (2017).
172. J. Y. Fan, Y. Huang, Y. Li, T. A. Muluh, S. Z. Fu, J. B. Wu, Bacteria in cancer therapy: A new generation of weapons. *Cancer Med.* (2022), doi:10.1002/CAM4.4799.
173. O. Felfoul, M. Mohammadi, S. Taherkhani, D. de Lanauze, Y. Zhong Xu, D. Loghin, S. Essa, S. Jancik, D. Houle, M. Lafleur, L. Gaboury, M. Tabrizian, N. Kaou, M. Atkin, T. Vuong, G. Batist, N. Beauchemin, D. Radzioch, S. Martel, Magneto-aerotactic bacteria deliver drug-containing nanoliposomes to tumour hypoxic regions. *Nat. Nanotechnol.* **11**, 941–947 (2016).
174. X. Yu, C. Lin, J. Yu, Q. Qi, Q. Wang, Bioengineered Escherichia coli Nissle 1917 for tumour-targeting therapy. *Microb. Biotechnol.* **13**, 629 (2020).
175. W. Zhao, H. Zhao, M. Li, C. Huang, Microfluidic devices for neutrophil chemotaxis studies. *J. Transl. Med.* **18**, 1–19 (2020).
176. K. E. Veldkamp, H. C. J. M. Heezius, J. Verhoef, J. A. G. Van Strijp, K. P. M. Van Kessel, Modulation of Neutrophil Chemokine Receptors by Staphylococcus aureus Supernate. *Infect. Immun.* **68**, 5908 (2000).
177. W. Chanput, J. J. Mes, H. J. Wichers, THP-1 cell line: An in vitro cell model for immune modulation approach. *Int. Immunopharmacol.* **23**, 37–45 (2014).
178. K. Meijer, D. Weening, M. P. de Vries, M. G. Priebe, R. J. Vonk, H. Roelofsen, Quantitative proteomics analyses of activation states of human THP-1 macrophages. *J. Proteomics*. **128**, 164–172 (2015).
179. T. Starr, T. J. Bauler, P. Malik-Kale, O. Steele-Mortimer, The phorbol 12-myristate-13-acetate differentiation protocol is critical to the interaction of THP-1 macrophages with Salmonella Typhimurium. *PLoS One*. **13**, e0193601 (2018).
180. C. A. Dinarello, Overview of the IL-1 family in innate inflammation and acquired immunity. *Immunol. Rev.* **281**, 8–27 (2018).
181. P. Menten, A. Wuyts, J. Van Damme, Macrophage inflammatory protein-1. *Cytokine Growth Factor*

Rev. **13**, 455–481 (2002).
182. B. M, The role of interleukin-8 in inflammation and mechanisms of regulation. *J. Periodontol.* **64**, 456–460 (1993).
183. G. Cavalli, S. Colafrancesco, G. Emmi, M. Imazio, G. Lopalco, M. C. Maggio, J. Sota, C. A. Dinarello, Interleukin 1α: a comprehensive review on the role of IL-1α in the pathogenesis and treatment of autoimmune and inflammatory diseases. *Autoimmun. Rev.* **20**, 102763 (2021).
184. T. Tanaka, M. Narazaki, T. Kishimoto, IL-6 in Inflammation, Immunity, and Disease. *Cold Spring Harb. Perspect. Biol.* **6**, 16295–16296 (2014).
185. H. T. Idriss, J. H. Naismith, TNFα and the TNF receptor superfamily: Structure-function relationship(s). *Microsc. Res. Tech.* **50** (2000), doi:10.1002/1097-0029(20000801)50:3<184::AID-JEMT2>3.0.CO;2-H.
186. L. J. Bendall, K. F. Bradstock, G-CSF: From granulopoietic stimulant to bone marrow stem cell mobilizing agent. *Cytokine Growth Factor Rev.* **25**, 355–367 (2014).
187. J. A. Hamilton, Cytokines Focus: GM-CSF in inflammation. *J. Exp. Med.* **217** (2020), doi:10.1084/JEM.20190945.
188. K. V. Sawant, K. M. Poluri, A. K. Dutta, K. M. Sepuru, A. Troshkina, R. P. Garofalo, K. Rajarathnam, Chemokine CXCL1 mediated neutrophil recruitment: Role of glycosaminoglycan interactions. *Sci. Reports 2016 61.* **6**, 1–8 (2016).
189. I. Ushach, A. Zlotnik, Biological role of granulocyte macrophage colony-stimulating factor (GM-CSF) and macrophage colony-stimulating factor (M-CSF) on cells of the myeloid lineage. *J. Leukoc. Biol.* **100**, 481 (2016).
190. M. Liu, S. Guo, J. K. Stiles, The emerging role of CXCL10 in cancer. *Oncol. Lett.* **2**, 583–589 (2011).
191. M. A. Crawford, K. R. Margulieux, A. Singh, R. K. Nakamoto, M. A. Hughes, Mechanistic insights and therapeutic opportunities of antimicrobial chemokines. *Semin. Cell Dev. Biol.* **88**, 119–128 (2019).
192. G. A. Duque, A. Descoteaux, Macrophage cytokines: Involvement in immunity and infectious diseases. *Front. Immunol.* **5**, 491 (2014).
193. L. Ulloa, K. J. Tracey, The 'cytokine profile': a code for sepsis. *Trends Mol. Med.* **11**, 56–63 (2005).
194. P. Jin, T. H. Han, J. Ren, S. Saunders, E. Wang, F. M. Marincola, D. F. Stroncek, Molecular signatures of maturing dendritic cells: implications for testing the quality of dendritic cell therapies. *J. Transl. Med.* **8**, 4 (2010).
195. Y. Waeckerle-Men, E. Scandella, E. Uetz-Von Allmen, B. Ludewig, S. Gillessen, H. P. Merkle, B. Gander, M. Groettrup, Phenotype and functional analysis of human monocyte-derived dendritic cells loaded with biodegradable poly(lactide-co-glycolide) microspheres for immunotherapy. *J. Immunol. Methods.* **287**, 109–124 (2004).
196. H. Zuo, M. J. C. van Lierop, J. Kaspers, R. Bos, A. Reurs, S. Sarkar, T. Konry, A. Kamermans, G. Kooij, H. E. de Vries, T. D. de Gruijl, A. Karlsson-Parra, E. H. Manting, A. M. Kruisbeek, S. K. Singh, Transfer of cellular content from the allogeneic cell-based cancer vaccine DCP-001 to host dendritic cells hinges on phosphatidylserine and is enhanced by CD47 blockade. *Cells.* **10** (2021), doi:10.3390/CELLS10113233/S1.
197. K. Tarte, G. Fiol, J. F. Rossi, B. Klein, Extensive characterization of dendritic cells generated in serum-free conditions: regulation of soluble antigen uptake, apoptotic tumor cell phagocytosis, chemotaxis and T cell activation during maturation in vitro. *Leuk. 2000 1412.* **14**, 2182–2192 (2000).
198. A. Nyga, U. Cheema, M. Loizidou, 3D tumour models: Novel in vitro approaches to cancer studies. *J. Cell Commun. Signal.* **5**, 239–248 (2011).
199. A. Sontheimer-Phelps, B. A. Hassell, D. E. Ingber, Modelling cancer in microfluidic human organs-on-chips. *Nat. Rev. Cancer.* **19**, 65–81 (2019).
200. L. Le Nagard, V. Morillo-López, C. Fradin, D. A. Bazylinski, Growing Magnetotactic Bacteria of the Genus Magnetospirillum: Strains MSR-1, AMB-1 and MS-1. *J. Vis. Exp.*, 58536 (2018).

201. R. J. Calugay, H. Miyashita, Y. Okamura, T. Matsunaga, Siderophore production by the magnetic bacterium Magnetospirillum magneticum AMB-1. *FEMS Microbiol. Lett.* **218**, 371–375 (2003).
202. C. Moisescu, S. Bonneville, S. Staniland, I. Ardelean, L. G. Benning, Iron Uptake Kinetics and Magnetosome Formation by Magnetospirillum gryphiswaldense as a Function of pH, Temperature and Dissolved Iron Availability. *https://doi.org/10.1080/01490451.2011.594146*. **28**, 590–600 (2011).
203. F. Sônego, F. V. e. S. Castanheira, R. G. Ferreira, A. Kanashiro, C. A. V. G. Leite, D. C. Nascimento, D. F. Colón, V. de F. Borges, J. C. Alves-Filho, F. Q. Cunha, Paradoxical Roles of the Neutrophil in Sepsis: Protective and Deleterious. *Front. Immunol.* **7**, 155 (2016).
204. J. E. Norton, S. Kommineni, P. Akrivoulis, D. A. Gutierrez, D. J. Hazuda, G. Swaminathan, Primary Human Dendritic Cells and Whole-Blood Based Assays to Evaluate Immuno-Modulatory Properties of Heat-Killed Commensal Bacteria. *Vaccines*. **9**, 1–17 (2021).
205. W. Li, Eat-me signals: Keys to molecular phagocyte biology and "appetite" control. *J. Cell. Physiol.* **227**, 1291 (2012).
206. Z. Chen, T. Moyana, A. Saxena, R. Warrington, Z. Jia, J. Xiang, Efficient antitumor immunity derived from maturation of dendritic cells that had phagocytosed apoptotic/necrotic tumor cells. *Int. J. Cancer*. **93**, 539–548 (2001).
207. X. Wu, M. A. Newbold, C. L. Haynes, Recapitulation of in vivo-like neutrophil transendothelial migration using a microfluidic platform. *Analyst*. **140**, 5055–5064 (2015).
208. U. Haessler, Y. Kalinin, M. A. Swartz, M. Wu, An agarose-based microfluidic platform with a gradient buffer for 3D chemotaxis studies. *Biomed. Microdevices*. **11**, 827–835 (2009).
209. N. Gjorevski, B. Avignon, R. Gérard, L. Cabon, A. B. Roth, M. Bscheider, A. Moisan, Neutrophilic infiltration in organ-on-a-chip model of tissue inflammation. *Lab Chip*. **20**, 3365–3374 (2020).
210. B. Smolkova, M. Dusinska, A. Gabelova, Nanomedicine and epigenome. Possible health risks. *Food Chem. Toxicol.* **109**, 780–796 (2017).
211. A. Gao, X. li Hu, M. Saeed, B. fan Chen, Y. ping Li, H. jun Yu, Overview of recent advances in liposomal nanoparticle-based cancer immunotherapy. *Acta Pharmacol. Sin.* **40**, 1129–1137 (2019).
212. Y. Barenholz, Doxil® - The first FDA-approved nano-drug: Lessons learned. *J. Control. Release*. **160**, 117–134 (2012).
213. M. K. Rasmussen, J. N. Pedersen, R. Marie, Size and surface charge characterization of nanoparticles with a salt gradient. *Nat. Commun.* **11**, 1–8 (2020).
214. E. Chibowski, A. Szcześ, Zeta potential and surface charge of DPPC and DOPC liposomes in the presence of PLC enzyme. *Adsorption*. **22**, 755–765 (2016).
215. B. Heurtault, P. Saulnier, B. Pech, J. E. Proust, J. P. Benoit, Physico-chemical stability of colloidal lipid particles. *Biomaterials*. **24**, 4283–4300 (2003).
216. M. Danaei, M. Kalantari, M. Raji, H. Samareh Fekri, R. Saber, G. P. Asnani, S. M. Mortazavi, M. R. Mozafari, B. Rasti, A. Taheriazam, Probing nanoliposomes using single particle analytical techniques: effect of excipients, solvents, phase transition and zeta potential. *Heliyon*. **4**, e01088 (2018).
217. D. Needham, R. S. Nunn, Elastic deformation and failure of lipid bilayer membranes. *Biophys. J.* **58**, 997–1009 (1990).
218. M. L. Briuglia, C. Rotella, A. McFarlane, D. A. Lamprou, Influence of cholesterol on liposome stability and on in vitro drug release. *Drug Deliv. Transl. Res.* **5**, 231–242 (2015).
219. K. Dutta, D. Hu, B. Zhao, A. E. Ribbe, J. Zhuang, S. Thayumanavan, Templated Self-Assembly of a Covalent Polymer Network for Intracellular Protein Delivery and Traceless Release. *J. Am. Chem. Soc.* **139**, 5676–5679 (2017).
220. Y. Anraku, A. Kishimura, M. Kamiya, S. Tanaka, T. Nomoto, K. Toh, Y. Matsumoto, S. Fukushima, D. Sueyoshi, M. R. Kano, Y. Urano, N. Nishiyama, K. Kataoka, Systemically Injectable Enzyme-Loaded Polyion Complex Vesicles as in Vivo Nanoreactors Functioning in Tumors. *Angew. Chemie - Int. Ed.* **55**, 560–565 (2016).
221. D. H. Ess, G. O. Jones, K. N. Houk, Transition states of strain-promoted metal-free click chemistry: 1,3-dipolar cycloadditions of phenyl azide and cyclooctynes. *Org. Lett.* **10**, 1633–1636 (2008).

222. T. J. Silhavy, D. Kahne, S. Walker, The bacterial cell envelope. *Cold Spring Harb. Perspect. Biol.* **2** (2010), , doi:10.1101/cshperspect.a000414.
223. S. Udenfriend, S. Stein, P. Böhlen, W. Dairman, W. Leimgruber, M. Weigele, Fluorescamine: A Reagent for Assay of Amino Acids, Peptides, Proteins, and Primary Amines in the Picomole Range. *Science (80-.).* **178**, 871–872 (1972).
224. R. Rutman, A. Cantarow, A. E. Paschkis, Studies in 2-Acetylaminofluorene Carcinogenesis III. The Utilization of Uracil-2-C14 by Preneoplastic Rat Liver and Rat Hepatoma* (available at http://aacrjournals.org/cancerres/article-pdf/14/2/119/2371098/cr0140020119.pdf).
225. D. B. Longley, D. P. Harkin, P. G. Johnston, 5-Fluorouracil: mechanisms of action and clinical strategies. *Nat. Rev. Cancer 2003 35.* **3**, 330–338 (2003).
226. S. Vodenkova, T. Buchler, K. Cervena, V. Veskrnova, P. Vodicka, V. Vymetalkova, 5-fluorouracil and other fluoropyrimidines in colorectal cancer: Past, present and future. *Pharmacol. Ther.* **206**, 107447 (2020).
227. L. Zhang, X. Xing, F. Meng, Y. Wang, D. Zhong, Oral fluoropyrimidine versus intravenous 5-fluorouracil for the treatment of advanced gastric and colorectal cancer: Meta-analysis. *J. Gastroenterol. Hepatol.* **33**, 209–225 (2018).
228. R. Thakare, G. Kaul, M. Shukla, P. Kesharwani, N. Srinivas, A. Dasgupta, S. Chopra, Repurposing nonantibiotic drugs as antibacterials. *Drug Discov. Target. Drug-Resistant Bact.*, 105–138 (2020).
229. J. R. McLeod, P. A. Harvey, C. S. Detweiler, An Oral Fluorouracil Prodrug, Capecitabine, Mitigates a Gram-Positive Systemic Infection in Mice. *Microbiol. Spectr.* **9** (2021), doi:10.1128/SPECTRUM.00275-21/SUPPL_FILE/REVIEWER-COMMENTS.PDF.
230. S. Giacchetti, B. Perpoint, R. Zidani, N. Le Bail, R. Faggiuolo, C. Focan, P. Chollet, J. F. Llory, Y. Letourneau, B. Coudert, F. Bertheaut-Cvitkovic, D. Larregain-Fournier, A. Le Rol, S. Walter, R. Adam, J. L. Misset, F. Lévi, Phase III multicenter randomized trial of oxaliplatin added to chronomodulated fluorouracil-leucovorin as first-line treatment of metastatic colorectal cancer. *J. Clin. Oncol.* **18**, 136–147 (2000).
231. J. Y. Douillard, D. Cunningham, A. D. Roth, M. Navarro, R. D. James, P. Karasek, P. Jandik, T. Iveson, J. Carmichael, M. Alakl, G. Gruia, L. Awad, P. Rougier, Irinotecan combined with fluorouracil compared with fluorouracil alone as first-line treatment for metastatic colorectal cancer: a multicentre randomised trial. *Lancet.* **355**, 1041–1047 (2000).
232. S. Yano, Y. Zhang, M. Zhao, Y. Hiroshima, S. Miwa, F. Uehara, H. Kishimoto, H. Tazawa, M. Bouvet, T. Fujiwara, R. Hoffman, Tumor-targeting Salmonella typhimurium A1-R decoys quiescent cancer cells to cycle as visualized by FUCCI imaging and become sensitive to chemotherapy. *Cell Cycle.* **13**, 3958 (2014).
233. K. Igarashi, K. Kawaguchi, T. Kiyuna, K. Miyake, M. Miyake, S. Li, Q. Han, Y. Tan, M. Zhao, Y. Li, S. D. Nelson, S. M. Dry, A. S. Singh, I. A. Elliott, T. A. Russell, M. A. Eckardt, N. Yamamoto, K. Hayashi, H. Kimura, S. Miwa, H. Tsuchiya, F. C. Eilber, R. M. Hoffman, Tumor-targeting Salmonella typhimurium A1-R combined with recombinant methioninase and cisplatinum eradicates an osteosarcoma cisplatinum-resistant lung metastasis in a patient-derived orthotopic xenograft (PDOX) mouse model: decoy, trap and kill chemotherapy moves toward the clinic. *Cell Cycle.* **17**, 801 (2018).
234. J. M. Carethers, Systemic Treatment of Advanced Colorectal Cancer: Tailoring Therapy to the Tumor. *Therap. Adv. Gastroenterol.* **1**, 33 (2008).
235. M. D. Kaeser, S. Pebernard, R. D. Iggo, Regulation of p53 Stability and Function in HCT116 Colon Cancer Cells. *J. Biol. Chem.* **279**, 7598–7605 (2004).
236. P. Parajuli, V. Pisarev, J. Sublet, A. Steffel, M. Varney, R. Singh, D. Laface, J. E. Talmadge, Immunization with wild-type p53 gene sequences coadministered with Flt3 ligand induces an antigen-specific type 1 T-cell response. *Cancer Res.* **61**, 8227–8234 (2001).
237. S. Menghini, P. S. Ho, T. Gwisai, S. Schuerle, Magnetospirillum magneticum as a Living Iron Chelator Induces TfR1 Upregulation and Decreases Cell Viability in Cancer Cells. *Int. J. Mol. Sci. 2021, Vol. 22, Page 498.* **22**, 498 (2021).
238. L. L. Cao, H. Liu, Z. Yue, L. Liu, L. Pei, J. Gu, H. Wang, M. Jia, Iron chelation inhibits cancer cell

growth and modulates global histone methylation status in colorectal cancer. *BioMetals*. **31**, 797–805 (2018).
239. T. Ohara, Y. Tomono, X. Boyi, S. Yingfu, K. Omori, A. Matsukawa, T. Ohara, Y. Tomono, X. Boyi, S. Yingfu, K. Omori, A. Matsukawa, A novel, nontoxic iron chelator, super-polyphenol, effectively induces apoptosis in human cancer cell lines. *Oncotarget*. **9**, 32751–32760 (2018).
240. S. Felgner, D. Kocijancic, M. Frahm, S. Weiss, Bacteria in Cancer Therapy: Renaissance of an Old Concept. *Int. J. Microbiol.* **2016** (2016), doi:10.1155/2016/8451728.
241. D. L. Lamm, BCG immunotherapy for transitional-cell carcinoma in situ of the bladder. *Oncology*. **9** (1995), pp. 947-952+955.
242. A. Sahari, M. A. Traore, B. E. Scharf, B. Behkam, Directed transport of bacteria-based drug delivery vehicles: bacterial chemotaxis dominates particle shape. *Biomed. Microdevices*. **16**, 717–725 (2014).
243. E. Steager, C. B. Kim, J. Patel, S. Bith, C. Naik, L. Reber, M. J. Kim, Control of microfabricated structures powered by flagellated bacteria using phototaxis. *Appl. Phys. Lett.* **90**, 263901 (2007).
244. E. B. Steager, M. S. Sakar, D. H. Kim, V. Kumar, G. J. Pappas, M. J. Kim, Electrokinetic and optical control of bacterial microrobots. *J. Micromechanics Microengineering*. **21**, 035001 (2011).
245. S. Martel, C. C. Tremblay, S. Ngakeng, G. Langlois, Controlled manipulation and actuation of micro-objects with magnetotactic bacteria. *Appl. Phys. Lett.* **89**, 8–11 (2006).
246. A. Farzin, S. A. Etesami, J. Quint, A. Memic, A. Tamayol, Magnetic Nanoparticles in Cancer Therapy and Diagnosis. *Adv. Healthc. Mater.* **9**, 1901058 (2020).
247. S. Taherkhani, M. Mohammadi, J. Daoud, S. Martel, M. Tabrizian, Covalent binding of nanoliposomes to the surface of magnetotactic bacteria for the synthesis of self-propelled therapeutic agents. *ACS Nano*. **8**, 5049–5060 (2014).
248. J. Xing, T. Yin, S. Li, T. Xu, A. Ma, Z. Chen, Y. Luo, Z. Lai, Y. Lv, H. Pan, R. Liang, X. Wu, M. Zheng, L. Cai, Sequential Magneto-Actuated and Optics-Triggered Biomicrorobots for Targeted Cancer Therapy. *Adv. Funct. Mater.*, 2008262 (2020).
249. N. Mokrani, O. Felfoul, F. A. Zarreh, M. Mohammadi, R. Aloyz, G. Batist, S. Martel, in *2010 Annual International Conference of the IEEE Engineering in Medicine and Biology Society, EMBC'10* (2010), pp. 4371–4374.
250. B. Shapiro, S. Kulkarni, A. Nacev, S. Muro, P. Y. Stepanov, I. N. Weinberg, Open challenges in magnetic drug targeting. *Wiley Interdiscip. Rev. Nanomedicine Nanobiotechnology*. **7**, 446–457 (2015).
251. S. ichi Takeda, F. Mishima, S. Fujimoto, Y. Izumi, S. Nishijima, Development of magnetically targeted drug delivery system using superconducting magnet. *J. Magn. Magn. Mater.* **311**, 367–371 (2007).
252. A. S. Bahaj, P. A. B. James, F. D. Moeschler, An alternative method for the estimation of the magnetic moment of non-spherical magnetotactic bacteria. *IEEE Trans. Magn.* **32**, 5133–5135 (1996).
253. S. Seong, T. H. Park, Swimming characteristics of magnetic bacterium,Magnetospirillum sp. AMB-1, and implications as toxicity measurement. *Biotechnol. Bioeng.* **76**, 11–16 (2001).
254. P. Artursson, K. Palm, K. Luthman, Caco-2 monolayers in experimental and theoretical predictions of drug transport. *Adv. Drug Deliv. Rev.* **46**, 27–43 (2001).
255. N. Cruz, L. Qi, X. Alvarez, R. D. Berg, E. A. Deitch, The Caco-2 Cell Monolayer System as an In Vitro Model for Studying Bacterial-Enterocyte Interactions and Bacterial Translocation. *J. Burn Care Rehabil.* **15**, 207–212 (1994).
256. M. Yasuda, S. Nagata, S. Yamane, C. Kunikata, Y. Kida, K. Kuwano, C. Suezawa, J. Okuda, Pseudomonas aeruginosa serA Gene Is Required for Bacterial Translocation through Caco-2 Cell Monolayers. *PLoS One*. **12**, e0169367 (2017).
257. X. Cao, E. Moeendarbary, P. Isermann, P. M. Davidson, X. Wang, M. B. Chen, A. K. Burkart, J. Lammerding, R. D. Kamm, V. B. Shenoy, A Chemomechanical Model for Nuclear Morphology and Stresses during Cell Transendothelial Migration. *Biophys. J.* **111**, 1541–1552 (2016).
258. S. M. A. Arefi, D. Tsvirkun, C. Verdier, J. J. Feng, A biomechanical model for the transendothelial migration of cancer cells. *Phys. Biol.* **17** (2020), doi:10.1088/1478-3975/ab725c.
259. N. Mirkhani, M. G. Christiansen, S. Schuerle, Living, Self-Replicating Ferrofluids for Fluidic

Transport. *Adv. Funct. Mater.* **30**, 2003912 (2020).
260. P. Panorchan, J. P. George, D. Wirtz, Probing Intercellular Interactions between Vascular Endothelial Cadherin Pairs at Single-molecule Resolution and in Living Cells. *J. Mol. Biol.* **358**, 665–674 (2006).
261. J. Escribano, M. B. Chen, E. Moeendarbary, X. Cao, V. Shenoy, J. M. Garcia-Aznar, R. D. Kamm, F. Spill, Balance of mechanical forces drives endothelial gap formation and may facilitate cancer and immune-cell extravasation. *PLoS Comput. Biol.* **15**, e1006395 (2019).
262. R. Szulcek, C. M. L. Beckers, J. Hodzic, J. DeWit, Z. Chen, T. Grob, R. J. P. Musters, R. D. Minshall, V. W. M. Van Hinsbergh, G. P. Van Nieuw Amerongen, Localized RhoA GTPase activity regulates dynamics of endothelial monolayer integrity. *Cardiovasc. Res.* **99**, 471–482 (2013).
263. K. G. Kornev, Y. Gu, P. Aprelev, A. Tokarev, in *Magnetic Characterization Techniques for Nanomaterials* (Springer Berlin Heidelberg, 2017; https://link.springer.com/chapter/10.1007/978-3-662-52780-1_2), pp. 51–83.
264. R. M. Erb, J. J. Martin, R. Soheilian, C. Pan, J. R. Barber, Actuating Soft Matter with Magnetic Torque. *Adv. Funct. Mater.* **26**, 3859–3880 (2016).
265. W. Huang, F. Yang, L. Zhu, R. Qiao, Y. Zhao, Manipulation of magnetic nanorod clusters in liquid by non-uniform alternating magnetic fields. *Soft Matter.* **13**, 3750–3759 (2017).
266. F. Hirschhaeuser, H. Menne, C. Dittfeld, J. West, W. Mueller-Klieser, L. A. Kunz-Schughart, Multicellular tumor spheroids: An underestimated tool is catching up again. *J. Biotechnol.* **148**, 3–15 (2010).
267. S. B. Suh, A. Jo, M. A. Traore, Y. Zhan, S. L. Coutermarsh-Ott, V. M. Ringel-Scaia, I. C. Allen, R. M. Davis, B. Behkam, Nanoscale Bacteria-Enabled Autonomous Drug Delivery System (NanoBEADS) Enhances Intratumoral Transport of Nanomedicine. *Adv. Sci.* **6**, 1801309 (2019).
268. S. W. Byers, C. L. Sommers, B. Hoxter, A. M. Mercurio, A. Tozeren, Role of E-cadherin in the response of tumor cell aggregates to lymphatic, venous and arterial flow: measurement of cell-cell adhesion strength. *J. Cell Sci.* **108 (Pt 5)**, 2053–64 (1995).
269. D. S. Richardson, J. W. Lichtman, Clarifying Tissue Clearing. *Cell.* **162** (2015), pp. 246–257.
270. C. T. Lefèvre, M. Bennet, L. Landau, P. Vach, D. Pignol, D. A. Bazylinski, R. B. Frankel, S. Klumpp, D. Faivre, Diversity of magneto-aerotactic behaviors and oxygen sensing mechanisms in cultured magnetotactic bacteria. *Biophys. J.* **107**, 527–538 (2014).
271. S. Riffle, R. S. Hegde, Modeling tumor cell adaptations to hypoxia in multicellular tumor spheroids. *J. Exp. Clin. Cancer Res.* **36** (2017), , doi:10.1186/s13046-017-0570-9.
272. N. Mirkhani, T. Gwisai, S. Schuerle, Engineering Cell-Based Systems for Smart Cancer Therapy. *Adv. Intell. Syst.*, 2100134 (2021).
273. Z. W. Tay, P. Chandrasekharan, A. Chiu-Lam, D. W. Hensley, R. Dhavalikar, X. Y. Zhou, E. Y. Yu, P. W. Goodwill, B. Zheng, C. Rinaldi, S. M. Conolly, Magnetic Particle Imaging-Guided Heating in Vivo Using Gradient Fields for Arbitrary Localization of Magnetic Hyperthermia Therapy. *ACS Nano.* **12**, 3699–3713 (2018).
274. J. F. Liu, N. Neel, P. Dang, M. Lamb, J. McKenna, L. Rodgers, B. Litt, Z. Cheng, A. Tsourkas, D. Issadore, J. F. Liu, N. Neel, P. Dang, M. Lamb, J. McKenna, L. Rodgers, B. Litt, Z. Cheng, A. Tsourkas, D. Issadore, Radiofrequency-Triggered Drug Release from Nanoliposomes with Millimeter-Scale Resolution Using a Superimposed Static Gating Field. *Small.* **14**, 1802563 (2018).
275. M. R. Benoit, D. Mayer, Y. Barak, I. Y. Chen, W. Hu, Z. Cheng, S. X. Wang, D. M. Spielman, S. S. Gambhir, A. Matin, Visualizing implanted tumors in mice with magnetic resonance imaging using magnetotactic bacteria. *Clin. Cancer Res.* **15**, 5170–5177 (2009).
276. A. E. David, A. J. Cole, B. Chertok, Y. S. Park, V. C. Yang, A combined theoretical and in vitro modeling approach for predicting the magnetic capture and retention of magnetic nanoparticles in vivo. *J. Control. Release.* **152**, 67–75 (2011).
277. A. K. A. Silva, N. Luciani, F. Gazeau, K. Aubertin, S. Bonneau, C. Chauvierre, D. Letourneur, C. Wilhelm, Combining magnetic nanoparticles with cell derived microvesicles for drug loading and targeting. *Nanomedicine Nanotechnology, Biol. Med.* **11**, 645–655 (2015).
278. B. Polyak, I. Fishbein, M. Chorny, I. Alferiev, D. Williams, B. Yellen, G. Friedman, R. J. Levy,

High field gradient targeting of magnetic nanoparticle-loaded endothelial cells to the surfaces of steel stents. *Proc. Natl. Acad. Sci. U. S. A.* **105**, 698–703 (2008).
279. B. Gleich, J. Weizenecker, Tomographic imaging using the nonlinear response of magnetic particles. *Nature*. **435**, 1214–1217 (2005).
280. M. Graeser, F. Thieben, P. Szwargulski, F. Werner, N. Gdaniec, M. Boberg, F. Griese, M. Möddel, P. Ludewig, D. van de Ven, O. M. Weber, O. Woywode, B. Gleich, T. Knopp, Human-sized magnetic particle imaging for brain applications. *Nat. Commun.* **10**, 1–9 (2019).
281. Y. Qiu, S. Tong, L. Zhang, Y. Sakurai, D. R. Myers, L. Hong, W. A. Lam, G. Bao, Magnetic forces enable controlled drug delivery by disrupting endothelial cell-cell junctions. *Nat. Commun.* **8**, 1–10 (2017).
282. G. R. Kale, X. Yang, J. M. Philippe, M. Mani, P. F. Lenne, T. Lecuit, Distinct contributions of tensile and shear stress on E-cadherin levels during morphogenesis. *Nat. Commun.* **9**, 1–16 (2018).
283. M. Aubry, W. A. Wang, Y. Guyodo, E. Delacou, J. M. Guigner, O. Espeli, A. Lebreton, F. Guyot, Z. Gueroui, Engineering E. coli for magnetic control and the spatial localization of functions. *ACS Synth. Biol.* **9**, 3030–3041 (2020).
284. C. R. Grant, M. Amor, H. A. Trujillo, S. Krishnapura, A. T. Iavarone, A. Komeili, Distinct gene clusters drive formation of ferrosome organelles in bacteria. *Nat. 2022*, 1–5 (2022).
285. H. C. Berg, *Random Walks in Biology: New and Expanded Edition* (Princeton University Press, Princeton, NJ, 1993).
286. Y. Yang, Y. Zhao, Discretized Motion of Surface Walker under a Nonuniform AC Magnetic Field. *Langmuir*. **36**, 11125–11137 (2020).
287. J. Fan, Z. Sun, J. Zhang, Q. Huang, S. Yao, Y. Zong, Y. Kohmura, T. Ishikawa, H. Liu, H. Jiang, Quantitative Imaging of Single Unstained Magnetotactic Bacteria by Coherent X-ray Diffraction Microscopy. *Anal. Chem.* **87**, 5849–5853 (2015).
288. Y. Gongyang, W. Ouyang, C. Qu, M. Urbakh, B. Quan, M. Ma, Q. Zheng, Temperature and velocity dependent friction of a microscale graphite-DLC heterostructure. *Friction*. **8**, 462–470 (2020).
289. C. Mignon, R. Sodoyer, B. Werle, Antibiotic-Free Selection in Biotherapeutics: Now and Forever. *Pathogens*. **4**, 157 (2015).
290. A. Plan Sangnier, S. Preveral, A. Curcio, A. K. A. Silva, C. T. Lefèvre, D. Pignol, Y. Lalatonne, C. Wilhelm, Targeted thermal therapy with genetically engineered magnetite magnetosomes@RGD: Photothermia is far more efficient than magnetic hyperthermia. *J. Control. Release*. **279**, 271–281 (2018).
291. Z. Xiang, X. Yang, J. Xu, W. Lai, Z. Wang, Z. Hu, J. Tian, L. Geng, Q. Fang, Tumor detection using magnetosome nanoparticles functionalized with a newly screened EGFR/HER2 targeting peptide. *Biomaterials*. **115**, 53–64 (2017).
292. J. W. Bartholomew, T. Mittwer, THE GRAM STAIN. *Bacteriol. Rev.* **16**, 1 (1952).
293. R. Meguro, Y. Asano, S. Odagiri, C. Li, H. Iwatsuki, K. Shoumura, Nonheme-iron histochemistry for light and electron microscopy: a historical, theoretical and technical review. *Arch. Histol. Cytol.* **70**, 1–19 (2007).
294. G. E. Myers, Staining Iron Bacteria. *Stain Technol.* **33**, 283–285 (1958).

Appendix A: Peptide-Fused Magnetosomes as Functional Binding Agents

Portions of this text are adapted from 'Genetic Encoding of Targeted Magnetic Resonance Imaging Contrast Agents for Tumour Imaging' by Simone Schuerle, Maiko Furubayashi, Ava P. Soleimany, Tinotenda Gwisai, Wei Huang, Christopher Voigt, and Sangeeta N. Bhatia published in ACS Synthetic Biology (2020).

Imaging of tumours for diagnosis and treatment monitoring has the potential to improve healthcare outcomes. Wide recognition of this principle, combined with established screening practices based on non-invasive imaging modalities, has spurred investigation into contrast agents that aid in distinguishing tumours from surrounding tissue. Among possible imaging modalities, magnetic resonance imaging (MRI) is especially appealing because magnetic fields are relatively innocuous compared to ionizing radiation and targets throughout the body can be readily resolved. Contrast agents designed to identify tumours do so by exploiting their unique physical and biochemical characteristics. An effective tumour-selective imaging agent must therefore combine the properties that make it robustly detectable via the imaging modality with features that lead to preferential accumulation or enhanced contrast effects in tumours. Because targeting strategies often rely upon biomarkers specific to particular types of tumours, tumour-selective contrast agents based on generalized characteristics of tumours are especially desirable.

MRI contrast agents typically function by detectably altering the longitudinal (T1) or transverse (T2) relaxation times of nearby hydrogen nuclei. Synthetic magnetic nanomaterials have been deployed as MRI contrast agents due to their magnetic properties and biocompatibility. Nanomaterial synthesis and synthetic biology intersect with the intriguing concept of harnessing magnetotactic bacteria (MTB), a group of prokaryotes known for their ability to biomineralize pristine intracellular nanocrystals of magnetite (Fe_3O_4), as a biogenic source of high quality T2 contrast agents. These particles occur in chains and are surrounded by a phospholipid bilayer membrane, forming a structure called a magnetosome. Research demonstrated the display of targeting peptides on the surfaces of these magnetosomes, such as Arg-Gly-Asp (RGD) and recently the GFR/HER2-targeting peptide P75 (*290*, *291*). As targeting moieties, peptides offer several advantages, including their small size, high affinity, ease of modification, and low immunogenicity. Despite their promise, some peptides are challenging to attach to the surface of synthetic iron oxide nanoparticles while maintaining their structural conformation, making

transgenic expression on the surface of magnetosomes the most direct means to produce contrast agents in such cases.

This work provides the first report of magnetic nanoparticles displaying genetically encoded pH low insertion peptide (pHLIP), a long peptide that is ill suited for chemical conjugation (Figure A-1). The targeting mechanisms based on pH responsiveness hold particular promise as broadly tumour-selective MRI contrast agents, since they exploit the extracellular acidity associated with the tumour microenvironment for a contrast enhancement. In separate genetically engineered magnetosomes, we incorporated the αv integrin-binding cyclic peptide iRGD, which is known to specifically target tumours by binding integrin-expressing cells in a neuropilin-1-dependent manner (Figure A-1). Upon binding to α_v integrins on the endothelium of tumour vessels, it is proteolytically cleaved within the tumour microenvironment, increasing the affinity for neuropilin-1 and facilitating the tissue penetration of co-administered, conjugated drugs, or imaging agents. In addition to verifying the applicability of this technique for the functionalization of magnetosomes with widely different peptide ligands, this approach provided a means to compare the performance of pHLIP against a peptide with known tumour targeting and penetration capabilities.

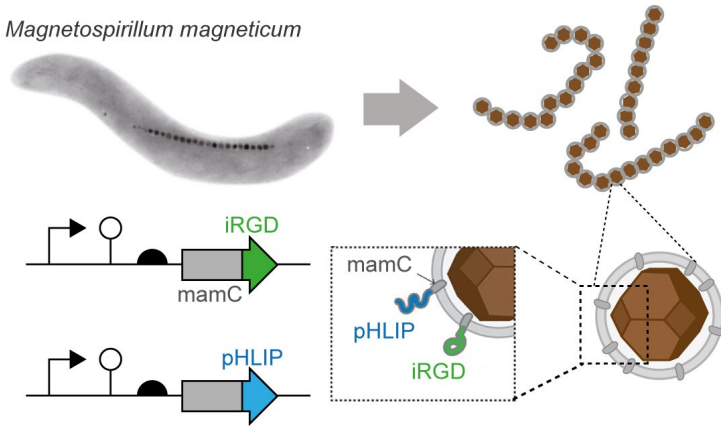

Figure A-1: Schematic of peptide-functionalised magnetosomes. Magnetotosomes displayed genetically encoded pHLIP and iRGD peptides for improved tumour targeting.

The unique characteristic of pHLIP is its ability to associate with lipid bilayers as an unstructured monomer at a neutral pH, while inserting across a bilayer or membrane as an α helix in acidic conditions. Consequently, magnetosomes displaying pHLIP are expected to show a pH-dependent fusion to cell membranes compared to results for unmodified magnetosomes. Thus, we cultured cells of the human breast cancer cell line MDA-MB-231, both at a standard pH of 7.5 and at a low, slightly acidic pH of 6.5, which is representative of average tumour acidity. We fluorescently labeled magnetosomes with and without the expression of pHLIP using a lipophilic membrane dye (DiI) inserted into the membrane of the magnetosome. We incubated both wild-

type and pHLIP-functionalized magnetosomes with MDA-MB-231 cells at a low pH and a standard pH and analyzed the binding efficiency by flow cytometry. Our data revealed a significant increase in bound magnetosomes to cells for pHLIP-functionalized magnetosomes at a low pH compared to those at a neutral pH, as well as compared to pure magnetosomes at a low pH, demonstrating pH-activated binding to cancer cells *in vitro* (Figure A-2A). As expected, there was no observable difference in the binding efficiency of pure magnetosomes with cancer cells between these two different pH levels.

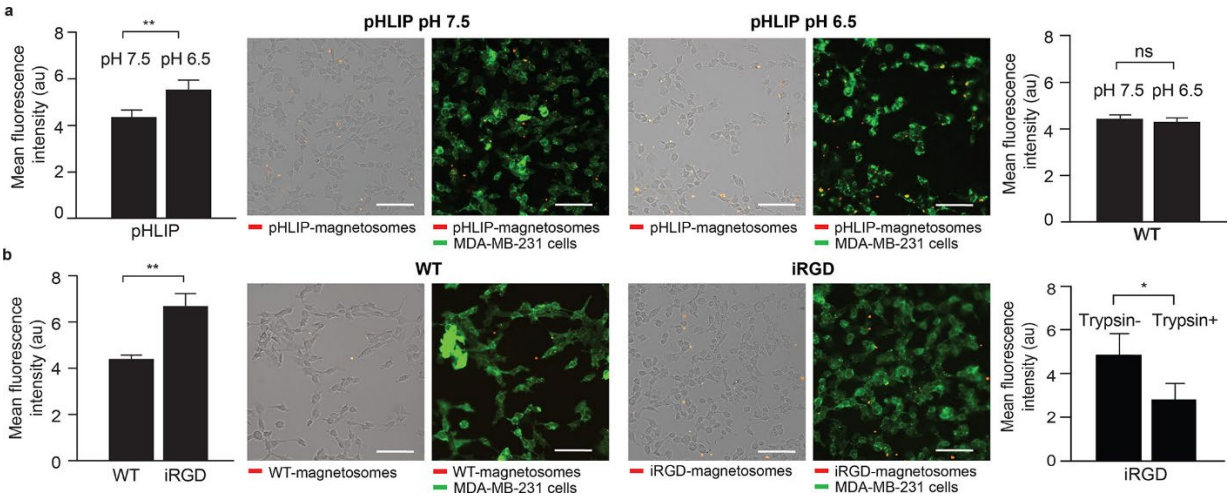

Figure A-2. Magnetosomes functionalized with tumour-targeting peptides pHLIP and iRGD show increased binding affinity to cancer cells. **(A)** pHLIP and wild-type magnetosomes were fluorescently labeled with a membrane dye (red) and incubated with MDA-MB-231 breast cancer cells at a standard (pH 7.5) and a low pH (pH 6.5). The increased binding for pHLIP magnetosomes at a low pH was measured by flow cytometry, compared to their binding at a standard pH (left, $p = 0.0078$, unpaired, two sample *t* tests). This can be also seen in bright field and fluorescence images of cells (blank/green) with magnetosomes (red), shown on the right (scale bars = 100 µm). No such pH dependency was observed for wild-type magnetosomes (right, $p = 0.6420$, unpaired, two sample *t* tests). **(B)** In another experiment, iRGD magnetosomes were incubated with the same cell line, known to express αv integrins. A significantly increased selectivity to these cells was observed for iRGD magnetosomes than for wild-type magnetosomes (left, $p = 0.0033$, unpaired, two sample *t* tests), which is also reflected in the bright field and fluorescent microscopy images on the right (scale bars = 100 µm). The binding efficiency significantly dropped when iRGD-functionalized magnetosomes were incubated with trypsinized cells (trypsin +), and thus bearing cleaved integrins, compared to untrypsinized cells (trypsin −) with preserved integrin expression (right, $p = 0.0411$, unpaired, two sample *t* tests).

Analogously, we assessed the functionality of iRGD displayed on magnetosomes by testing the specificity of binding to $\alpha v\beta 3$ expressing cells, such as the MDA-MB-231 cells used in the previous experiments. A 1.53-fold increase in the binding efficiency was measured by flow cytometry for iRGD-functionalized magnetosomes compared to that for wild-type magnetosomes (Figure A-2B). The analysis of fixed samples by confocal imaging also revealed the localization of the

magnetosomes at the cell surface. Further, trypsin treatment, which has been shown to cleave cell-surface integrins nonspecifically, resulted in a 42% decrease in the fluorescent intensity of iRGD-functionalized magnetosome binding, further supporting our hypothesis of integrin-selective targeting of iRGD-functionalized magnetosomes (Figure A-2B).

Appendix B: Establishing detection methods for MTB in tissue samples

Portions of this text are adapted from the semester project report written by Mira Jacobs and supervised by Tinotenda Gwisai.

To use MTB for new treatment strategies for cancer, the ability to detect the bacteria within different tissues may aid in assessing the efficacy of the delivery approach and the overall therapeutic effect. Some unanswered questions specifically for MTB are the detection limits of established histology methods and how the distribution and localization of MTB within the tissues can best be detected.

Two possible methods of detection include classical histological staining and fluorescent labelling of MTB prior to use. Among the classical histology stains, Gram staining (*292*) and Prussian blue staining (*293*) were investigated. The Gram stain makes use of a crystal violet solution, which results in uniform purple colourisation of the sample. Subsequently, mordant iodine is added which forms a complex with crystal violet. The next step involves decolourisation of the sample, which is typically performed with ethanol, acetone, or a mixture of both. This step removes dye from Gram-negative bacteria while dye within Gram-positive bacteria is retained. Dye is removed from Gram-negative bacteria because the thin cell wall and outer membrane are disrupted, while Gram-positive bacteria possess a thick, relatively impermeable cell wall that remains and retains the dye. In the last step, a counterstain is added resulting in purple-stained Gram-positive bacteria and pink-stained Gram-negative bacteria.

The Prussian blue stain is used to detect iron in tissues. The technique makes use of an acid and, most frequently, potassium ferrocyanide solution, which are mixed and applied to the sample. The optimal concentrations and ratios vary according to sample and tissue types, but the result is a deep blue staining of tissue regions that contain iron. Hydrochloric acid is used to dissolve iron, resulting in the release of ferrous (Fe^{2+}) as well as ferric iron (Fe^{3+}). The ferric iron ions react with the ferrocyanide ions to form the Prussian blue complex:

$$\underset{\text{(ferric iron)}}{4Fe^{3+}} + \underset{\text{(ferrocyanide)}}{3\,[Fe^{II}(CN)_6]^{4-}} \rightarrow \underset{\text{(Prussian blue)}}{Fe^{III}_4\,[Fe^{II}(CN)_6]_3} \qquad (1)$$

A very similar stain called Turnbull blue makes use of ferricyanide ions that form a complex with ferrous iron ions. The result is nevertheless a blue complex:

$$3Fe^{2+} + 2\,[Fe^{III}(CN)_6]^{3-} \rightarrow Fe^{II}_3\,[Fe^{III}(CN)_6]_2 \quad (2)$$

(ferrous iron) (ferricyanide) (Turnbull blue)

The magnetite found in MTB consists of both ferrous and ferric iron. Thus, Prussian blue was considered a promising approach for staining magnetosomes in MTB, thus enabling detection of the bacteria. In addition to the histology stains, the use of GFP-expressing MTB and MTB stained with fluorescent CellTrace dyes were investigated. CellTrace dyes enter the cell in a non-fluorescent form and are converted to a fluorescent derivative by intracellular esterases which binds covalently to amine groups inside the cell.

To investigate the efficacy of the selected staining approaches in different tissues, sections were prepared from chicken hearts and livers. The tissue was cut into slices of approximately 1 × 0.75 × 0.75 cm and placed on ice. Fluorescently labelled MTB suspended in agar was injected into the tissue pieces in multiple sites and the lower temperature of the tissue facilitated gelation of the agar. Next, the tissue sections were fixed in 4% formaldehyde for 1 hour at room temperature. Successful injections were confirmed by imaging the tissue sections using a fluorescence scanner (Sapphire Biomolecular Imager, Azure Biosystems), after which the slices were transferred into 15% sucrose and incubated over night at 4°C in the dark. Slices were then transferred to 30% sucrose and incubated over night at 4°C in the dark. The tissue slices were then cryoembedded in MCC (Milestone Cryoembedding Compound, Milestone Medical) and sectioned with the PrestoCHILL system to 8 µm thick slices. The tissue sections prepared with bacteria are referred to as “positive tissues”, while those prepared without bacteria are termed “negative tissues”.

Gram staining produced inconclusive results (Figure B-1). Both positive and the negative tissues contained clusters of deeply stained purple spots. Given the form and size of these spots, it was concluded that this was likely unspecific staining of cell nuclei. Future studies could use a different counterstain, such as fuchsin, which may stain the Gram-negative MTB more intensely.

Having observed inconclusive results with the Gram stain, detection of MTB using Prussian blue staining of magnetosomes was explored. The Prussian blue stain was first performed on bacterial smears to establish whether iron within the magnetosomes of MTB would be stained (Figure B-2). MTB were counterstained pink/purple and a slightly blue stained structure inside of some MTB was observed.

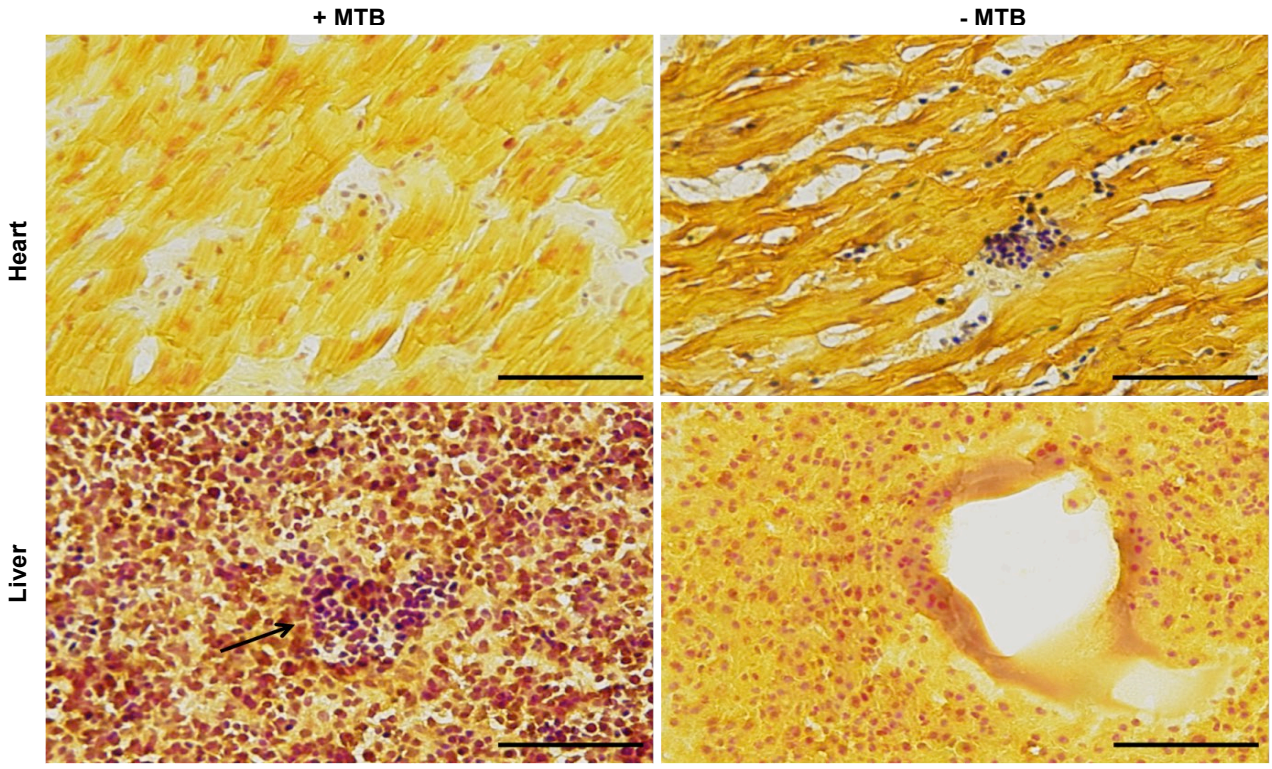

Figure B-1: Gram-stained heart and liver tissue with and without injected bacteria. The arrow highlights a cluster of pink stained cells. Scale bar = 50 µm.

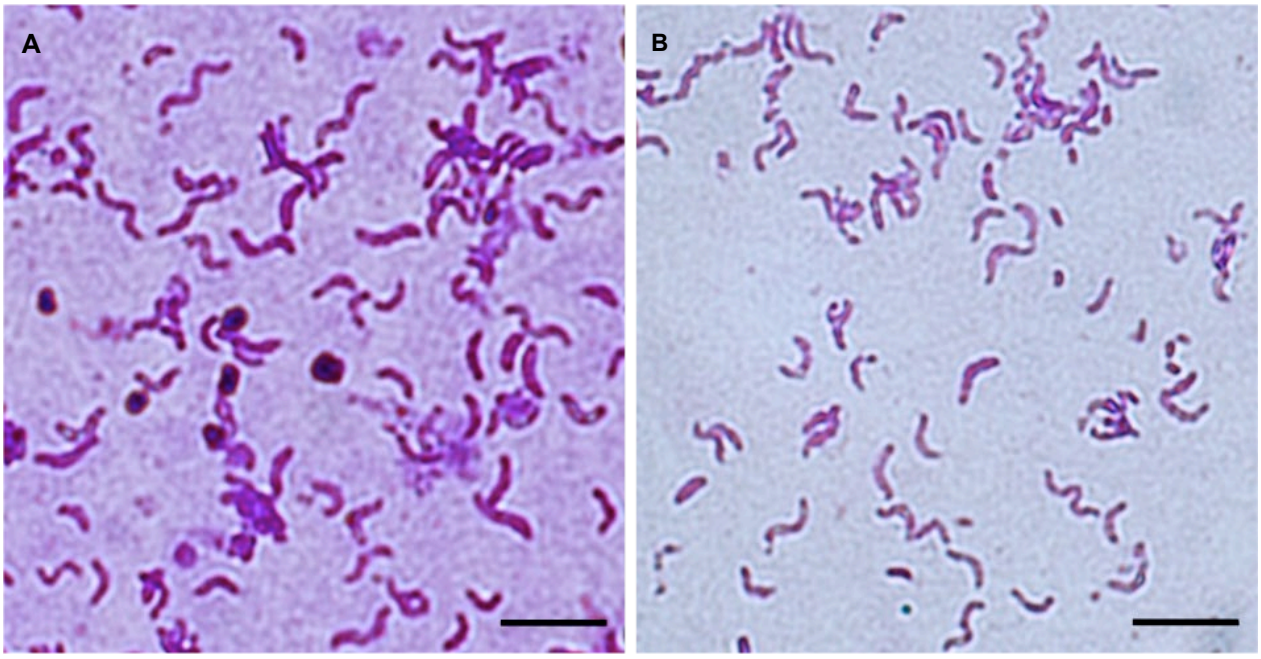

Figure B-2: Prussian blue-stained bacterial smears. (A) Bacterial smear with high density of MTB. **(B)** Smear with a lower density of bacteria. The bacteria were visible as purple helical structures about 2-3 µm in length. Scale bar = 5 µm.

Next, to assess whether the results produced with the smears could be reproduced in different tissue samples, Prussian blue staining was performed using the tissue slides according to the details in the table below:

Experiment	Working stain solution			Incubation time			
	Potassium ferrocyanide (% w/v)	HCl (mmol/L)	Ratio	Stain solution (min)	Counterstain solution (min)	Alcohol (s)	Xylene (s)
Smear	4	1.2	1:1	10	5	~~~	~~~
A	4	1.2	1:1	10	5	2	10
B	4	324.32	1:1	30	3	5	10
C	4	648.65	1:2	30	3	5	10

The positive and negative tissues displayed no differences, which would indicate the presence of stained bacteria (Figure B-3). It was hypothesised that the amount of hydrogen ions present in the stain solution may not have been sufficient to release enough iron ions from the magnetosomes to form detectable Prussian blue complexes. To improve the results of the Prussian blue staining, the accessibility of the ferrocyanide could be increased using Triton-X prior to

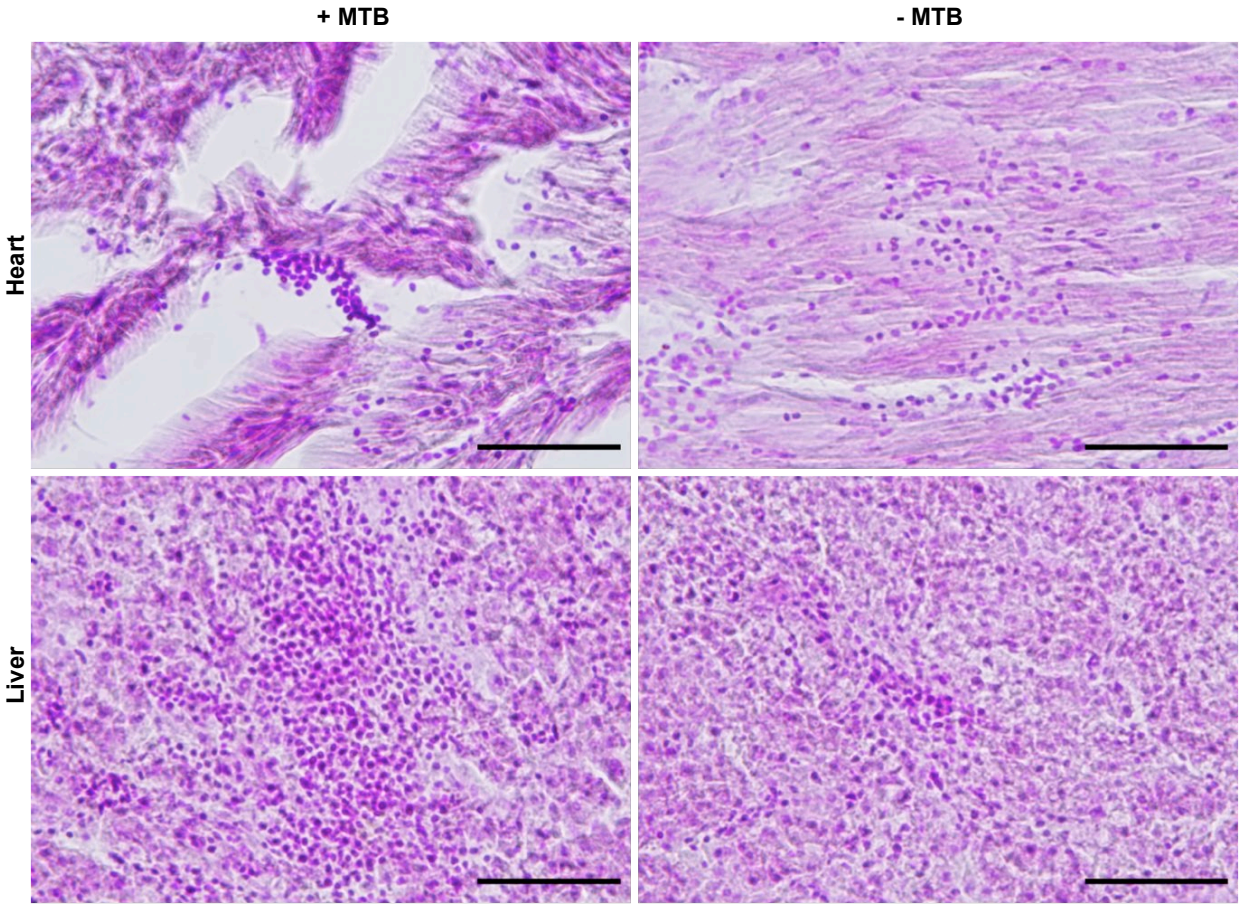

Figure B-3: Prussian blue stained heart and liver tissue prepared with and without bacteria. Scale bar = 50 µm.

staining to make the cell wall and lipid bilayer surrounding the magnetosomes more permeable. This would facilitate the reaction of ferrocyanide with the iron ions to enable formation of the Prussian blue complex.

Another possible explanation for the inconclusive results of the staining may be suboptimal ratios of HCl and potassium ferrocyanide. On one hand, excess potassium ions could lead to a delay in complex formation due to the formation of soluble Prussian blue, and on the other hand, highly concentrated HCl leads to the dissolution of Prussian blue. It can, therefore, be difficult to determine the optimal concentrations and ratios of the two solutions. This is also supported by the high variation of ratios and concentrations found in the literature, illustrating that protocols which work successfully for certain cell types do not guarantee successful staining of others (*294*).

After attempts to stain MTB using classical histology stains produced inconclusive results, the use of GFP-expressing MTB and MTB stained with fluorescent CellTrace dyes were investigated. In a preliminary experiment the fixation of GFP-expressing MTB and CFSE-stained MTB with 4% formaldehyde was performed to investigate whether chemical fixation would affect the fluorescence signal of the bacteria.

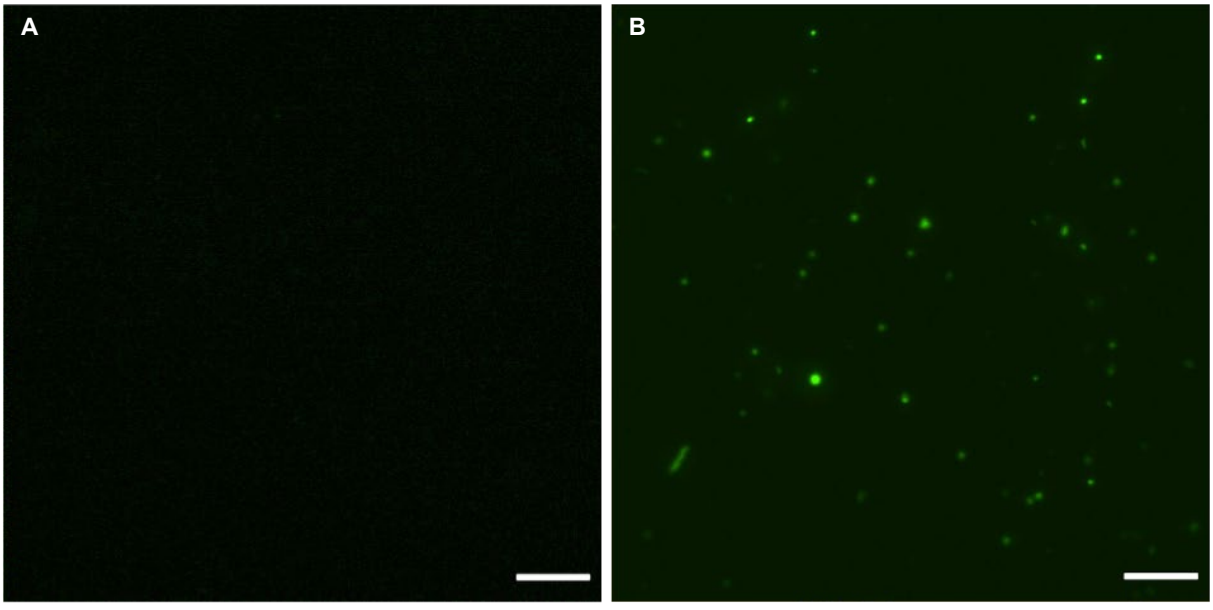

Figure B-4: Fluorescence of bacteria after fixation in 4% PFA. (A) GFP-expressing bacteria. **(B)** CFSE stained wildtype. Scale bar = 20 µm.

After incubation in 4% formaldehyde, fluorescence signal was not visible for GFP-expressing MTB (Figure B-4A). Chemical crosslinking of the GFP protein with formaldehyde may have resulted in interactions that extinguished the fluorophore. The experiment was repeated using

CFSE stained wildtype MTB. Here, the fluorescence was still present after the incubation time (Figure B-4B). Thus, stained wildtype bacteria were subsequently used for further characterisation.

CellTrace CFSE and far-red were used to stain the bacteria prior to injection into different tissue samples and the two stains were then compared. After the preparation of the tissues, imaging using a fluorescence scanner was performed to confirm successful injection of the MTB. Both tissue types exhibited autofluorescence, however, bright clusters were observed in injected samples, confirming the presence of MTB (Figure B-5).

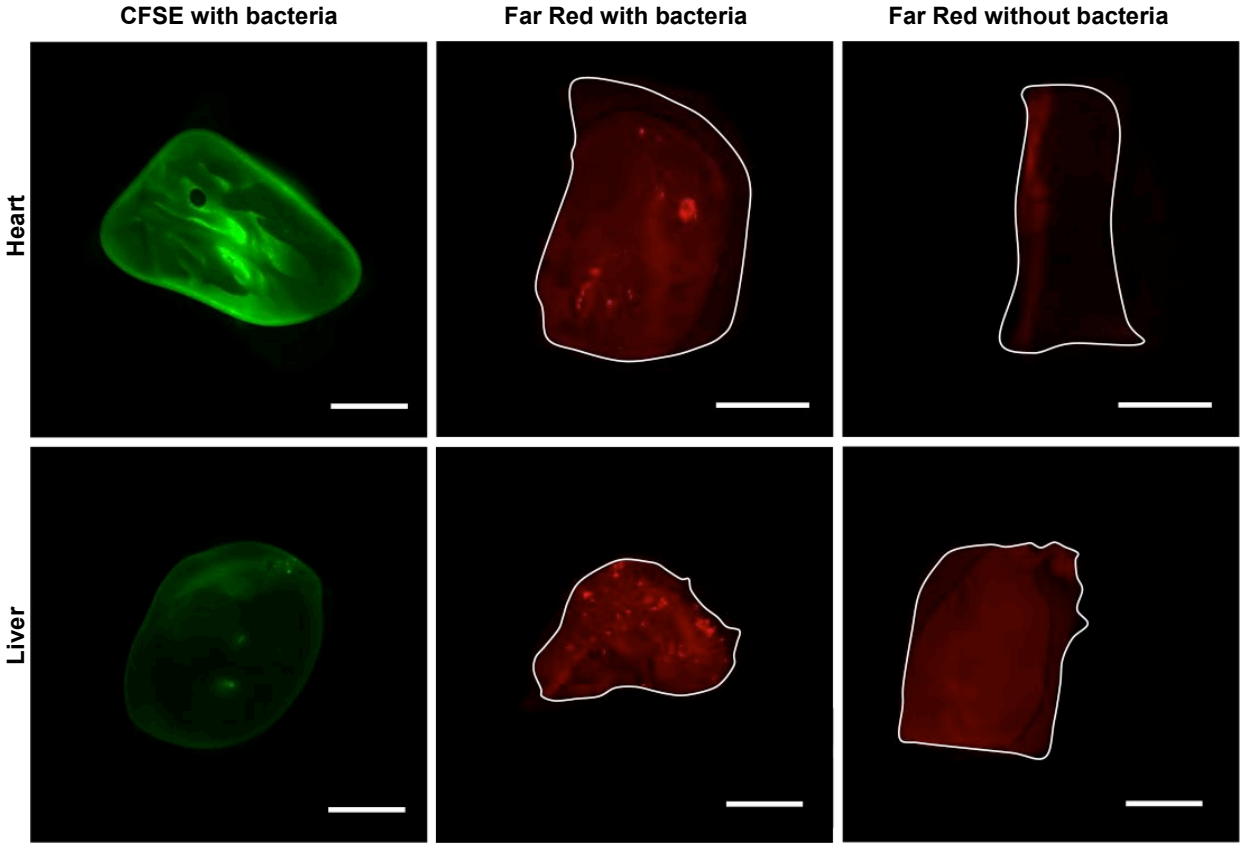

Figure B-5: Laser scanner images of tissue slices after injection of CFSE or far-red stained bacteria. The samples were fixed in 4% PFA prior to imaging. The tissues showed a uniform green or red autofluorescence, but there were brighter clusters visible in the positive slices. Scale bar = 5 mm.

The tissue samples were cryo-sectioned and slides were imaged. As with the scanner images, autofluorescence observed in the tissue sections, however, substantially brighter spots of stained bacteria could be observed (Figure B-6 and B-7). Both the CFSE and far-red stain were found to be easily applicable methods to reliably stain bacteria and enable detection in different tissue samples. The far-red stain produced the best results due to lower tissue autofluorescence.

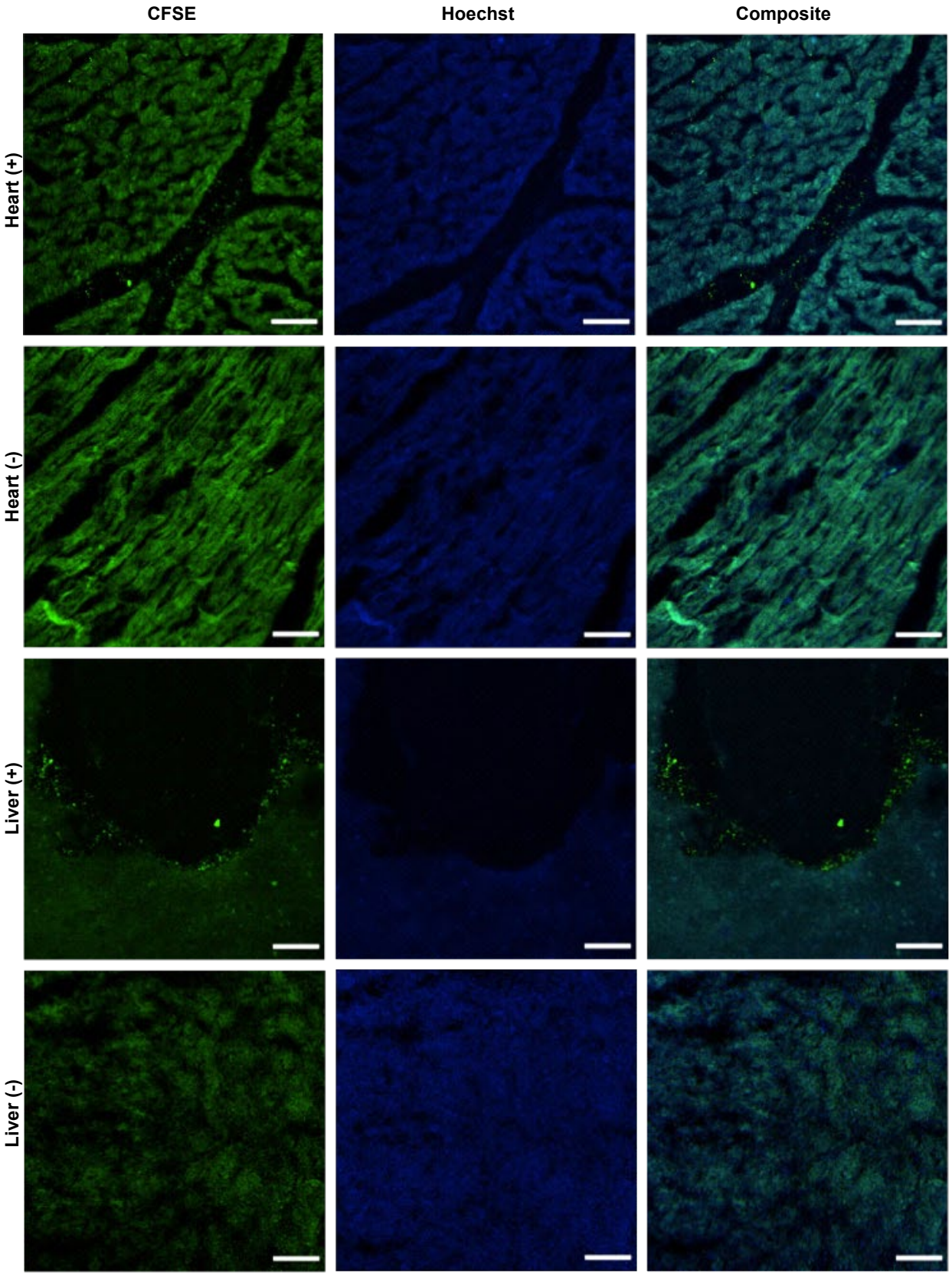

Figure B-6: Heart and liver tissue containing CFSE stained MTB. Samples prepared with bacteria are labelled with '+' while the samples prepared without bacteria are labelled with '-'. Scale bar = 50 µm.

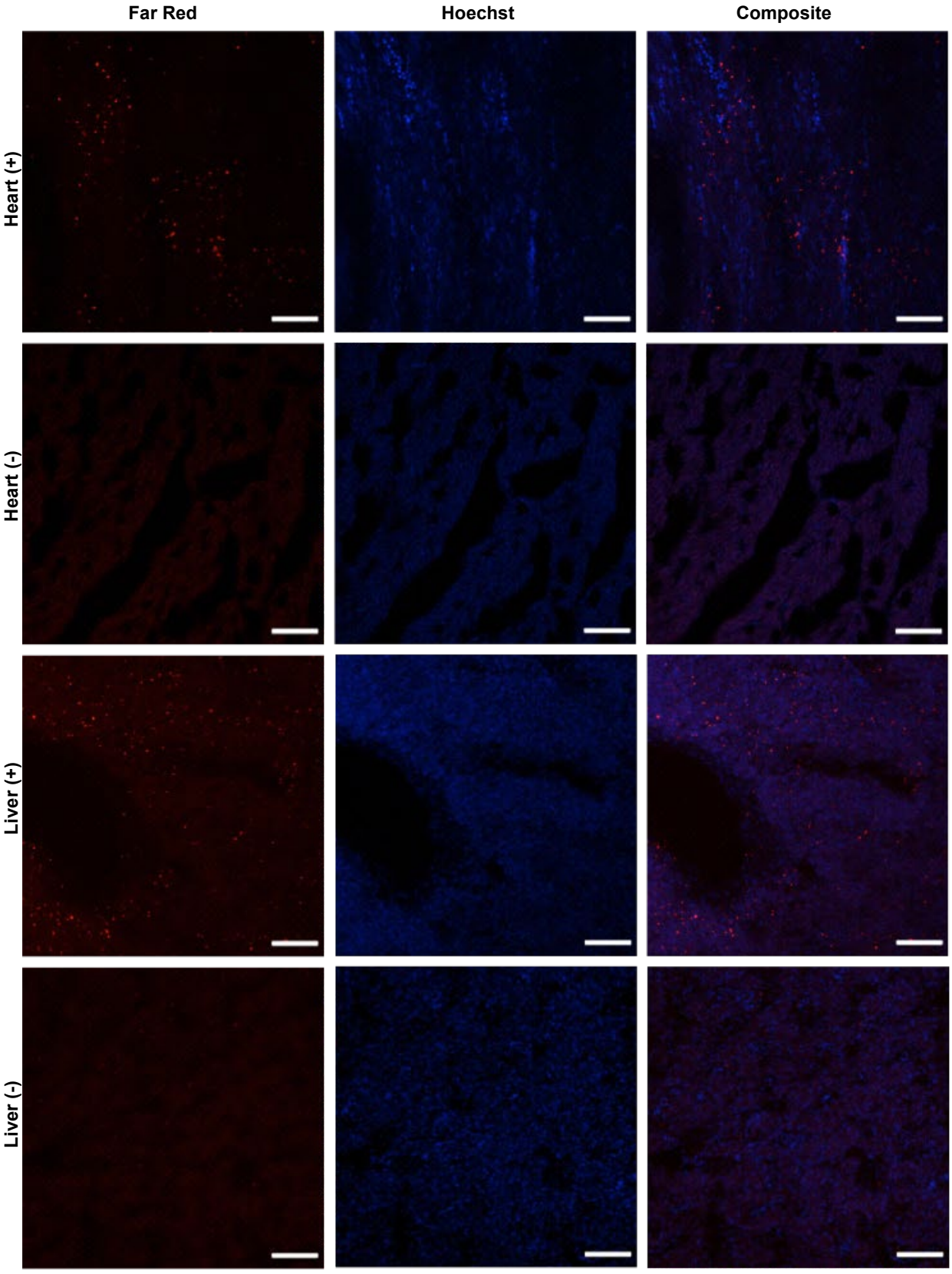

Figure B-7: Heart and liver tissue containing far-red stained MTB. Samples prepared with bacteria are labelled with '+' while the samples prepared without bacteria are labelled with '-'. Scale bar = 50 µm.

Appendix C: Characterisation of cancer spheroid growth and development

Portions of this text are adapted from the master's thesis submitted by Mira Jacobs and supervised by Tinotenda Gwisai.

Tumour spheroids provide a 3D system that can recapitulate the complex architecture of avascular tumour tissue and can facilitate the study of bacteria-based cancer therapies. To develop protocols to reproducibly generate spheroids, the growth and development of MCF-7 spheroids seeded at different densities was analysed over 7 days. Images captured over the culture period were used to derive the mean area and diameter for each seeding density and timepoint.

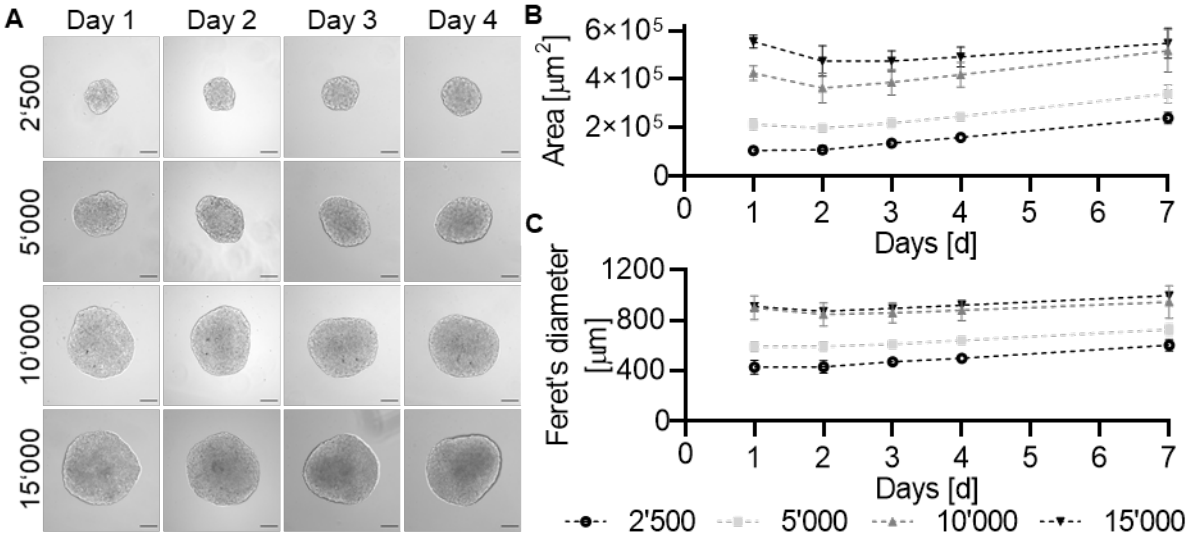

Figure C1: Cancer spheroid growth. **(A)** Representative images of spheroids for four seeding densities after 1 – 4 days of incubation. Scale bar = 200 µm. **(B)** Development of spheroid area for four seeding densities over 7 days. Data is presented as mean ± sd of five replicates. **(C)** Development of spheroid diameter for four seeding densities over 7 days. Data is presented as mean ± SD of five replicates.

At day 1, the cells had accumulated in a round cluster within the well (Figure C1-A). By day 4, the cells formed round aggregates, or spheroids, for all seeding densities. Both the analysis of the spheroid area and diameter show that spheroid size decreased from day 1 to day 2 before starting to increase again (Figure C1-B, C). Spheroids seeded at 2'500 cells/well were for all timepoints the smallest, with a maximum diameter of 603.0 ± 45.4 µm after 10 days of incubation. Spheroids seeded with 10 000 cells and 15 000 cells/well had approximately the same area and diameter from day 2 to day 7. The maximum diameter for 15 000 cells/well was measured at day 7 with 996.8 ± 28.2 µm.

Next, the formation of a hypoxic core within the spheroids at four seeding densities was assessed. Hypoxia is a key feature of tumours and provides a niche for preferential accumulation and colonisation of bacteria. Spheroids were incubated for 3 or 7 days before staining with the Image-iT Green Hypoxia Reagent for 2 h. They were then incubated in media for at least 3 h before imaging. In some spheroids, the centre appeared bright green (15 000 cells, day 3; 2'500 cells, day 7), while in some spheroids the outer cells of the spheroids were stained the brightest (10 000 cells, day 3). In other spheroids, all cells appeared only very faint green (2 500 cells, day 3).

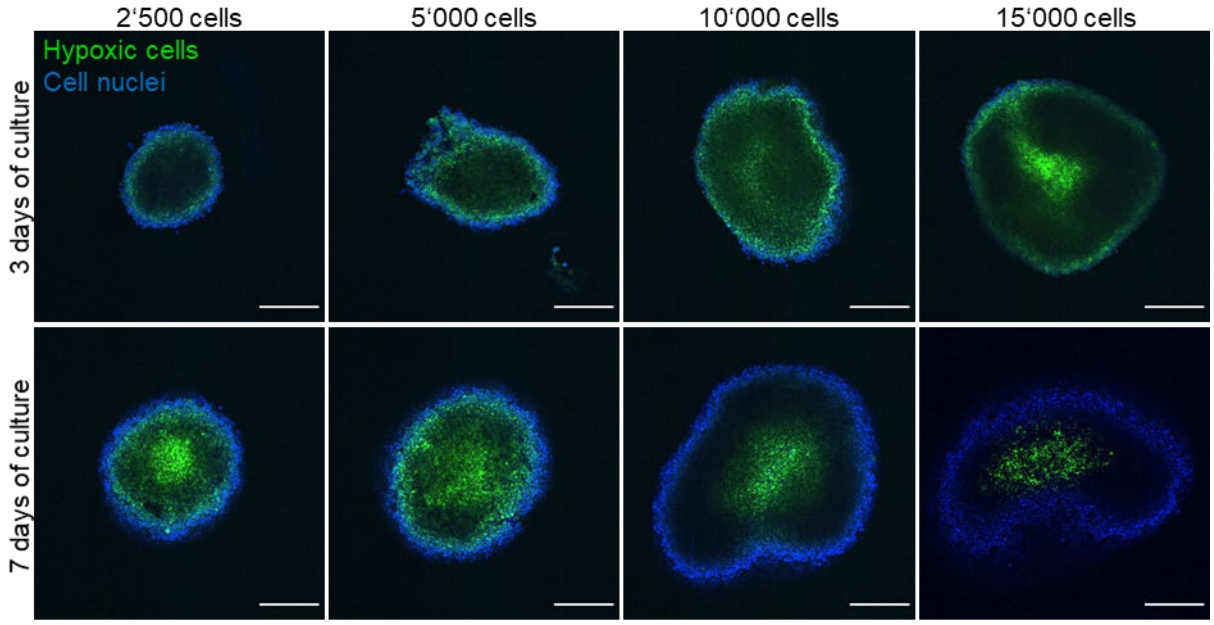

Figure C-2: Hypoxic core formation in breast cancer spheroids. MCF-7 spheroids of four different seeding densities were incubated for 3 and 7 days before being stained. Hypoxic cells were stained with hypoxia stain (green) and cell nuclei were stained with Hoechst (blue). Scale bar = 200 µm.

After closer inspection, it was observed that differences in spheroid morphology were responsible for the observed distribution of the stain. Spheroids that were 'biconcave' had a brightly stained centre, while the surrounding areas were unstained (Figure C3-A). In contrast, 'compact' spheroids had a more uniform fluorescence intensity distribution and overall higher fluorescence intensity signal particularly in the centre of the spheroid (Figure C3-B). Given these findings, only compact spheroids were selected for subsequent experiments.

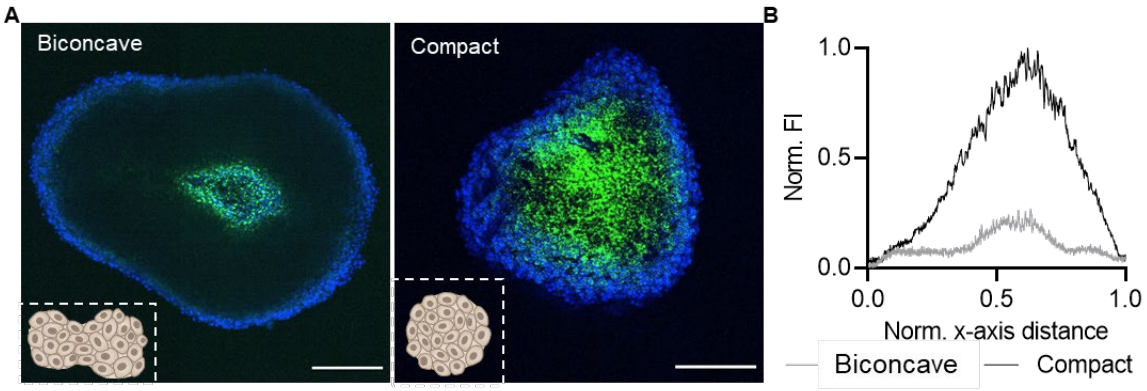

Figure C3: Effect of spheroid shape on hypoxia staining results. (A) Comparison of staining results for not compact and compact spheroids. Z-projections of the spheroids are shown. In the bottom left corner of each Z-projection the corresponding scheme of the cross section of the spheroid is shown. Hypoxic cells were stained with hypoxia stain (green) and cell nuclei were stained with Hoechst (blue). Scale bar = 200 µm. **(B)** Plot of the normalized fluorescence intensities of the spheroids are shown.

Appendix D: MTB transport in 3D tissue models

Portions of this text are adapted from the master's thesis submitted by Thuy Trinh Nguyen and supervised by Tinotenda Gwisai. Nima Mirkhani provided support for the design and execution of the experiments in Figure D-1.

MTB were shown to successfully cross cellular barriers when aided by RMF (Chapter 4). Here, additional 3D systems were explored to study MTB transport. MDA-MB-231 breast cancer cells were seeded in a collagen matrix in a Kamm design microfluidic device to mimic a tumour-like environment. The cancer cells were stained with Hoechst 33342 prior to seeding in a collagen hydrogel at a final concentration of 2.5 mg/mL. GFP-expressing MTB were injected into the collagen-adjacent channel and actuated for 30 min. Based on previous results, MTB were actuated out of plane at 14 Hz and 12 mT. Fluorescence images were taken before and after actuation to assess the distribution of MTB within the 3D collagen matrix and establish whether MTB would propel into deeper regions of the collagen.

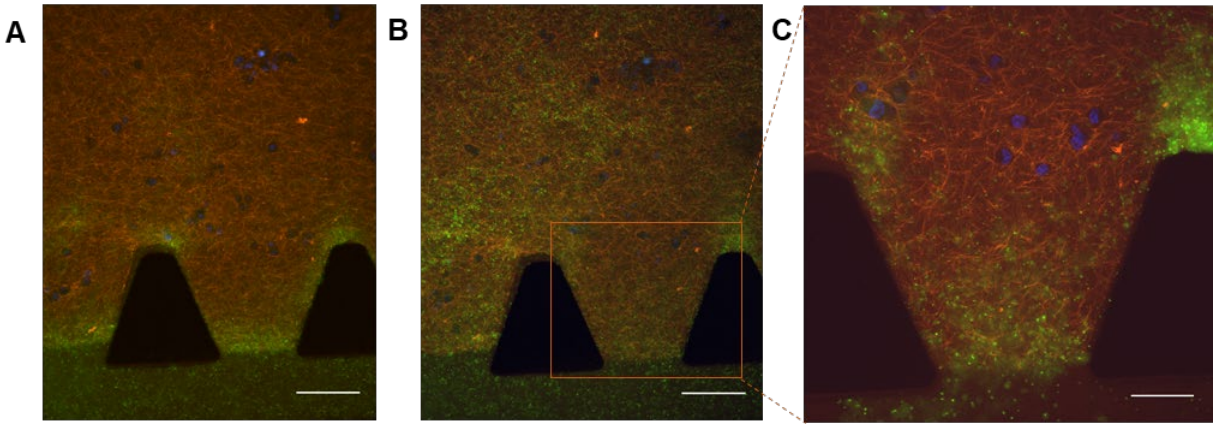

Figure D-1: Distribution of GFP expressing MTB (green) in TAMRA-stained collagen (red) with embedded MDA-MB-231 cells stained with Hoechst 33342 (blue). **(A)** Before actuation (t = 0 min). Scale bar marks 100 µm. **(B)** After actuation (t = 30 min). Scale bar marks 100 µm. **(C)** Distribution of MTB in 3D collagen at higher magnification. Scale bar = 50 µm.

Immediately after injection into the centre channel, MTB was observed mainly at the interface of the collagen-filled chamber. Most of the MTB was detected at the periphery of the collagen and highly concentrated around the PDMS posts, with a low number of MTB observed further within the collagen (Figure D-1A). After 30 min of actuation, an increased number of MTB were found in deeper collagen regions, while less MTB were observed in the centre channel of the microfluidic device, indicating that MTB successfully propelled into the collagen upon actuation

(Figure D-1B). Additionally, MTB were distributed throughout the collagen matrix following actuation, as shown in Figure D-1C.

Next magnetically-enhanced infiltration of MTB was studied in a microfluidic chip containing spheroids embedded in a collagen matrix (Figure D2). MTB was injected into an adjacent channel and actuation was performed (1 h; 24 Hz, 20 mT). After actuation, the channels were flushed to remove any unseeded bacteria and devices were incubated for 24 h, after which the devices were imaged and MTB infiltration was assessed. MTB accumulation was substantially higher with RMF exposure and these results were consistent with the findings in Chapter 4.

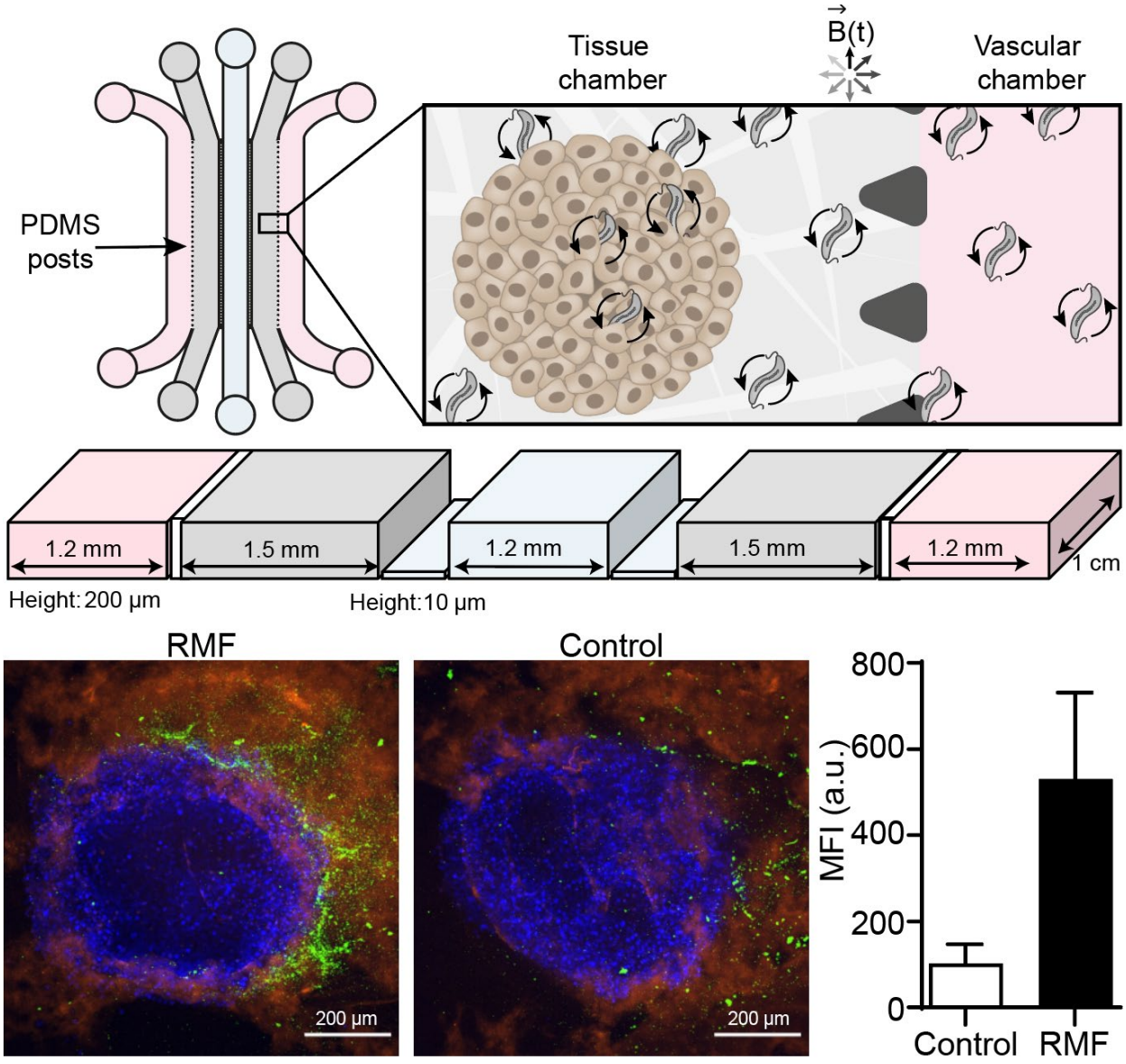

Figure D-2: Microfluidic chip with spheroid embedded in collagen. Chip design (top) and Z-projection of spheroid in collagen with corresponding summed mean fluorescence intensity 24 h after RMF exposure (bottom). MTB = green, collagen = red, nuclei =blue

Overall, these findings support the use of such assays for further investigation and characterisation of MTB transport. Future studies may be performed with additional cell lines to establish the applied actuation is effective for a range of cancer types. Furthermore, additional complexity may be added to the devices to more closely recapitulate *in vivo* conditions and insights gained from such studies may be used to inform the actuation strategy employed. For instance, devices with endothelialised channels may be used to gain an understanding of how magnetic actuation can aid MTB to cross this barrier and effectively propel through collagen towards tumours. Lastly, establishing continuous fluid flow in the microfluidic channel would allow studies of how MTB is transported from circulation to be performed. This can be achieved by creating a hydrostatic pressure gradient by having a higher fluid level in the inlet compared to the outlet.

Appendix E: Development of a microfluidic platform to study immune cell migration

Portions of this text are adapted from the master's thesis submitted by Simone Hersberger and supervised by Tinotenda Gwisai.

The goal of the following experiments was to achieve reproducible preparation of microfluidic devices and establishing an image acquisition and analysis pipeline. The microfluidic devices contain a central immune cell channel that is connected to the two adjacent MTB-collagen channels by microchannels. It is of particular importance that the bacteria remain in the chamber in order to stimulate immune cell migration into the MTB chamber. In initial experiments, bacteria were visible in the central immune chamber. Therefore, a strategy was developed to reproducibly immobilize the bacteria and prevent them from entering into the central immune chamber.

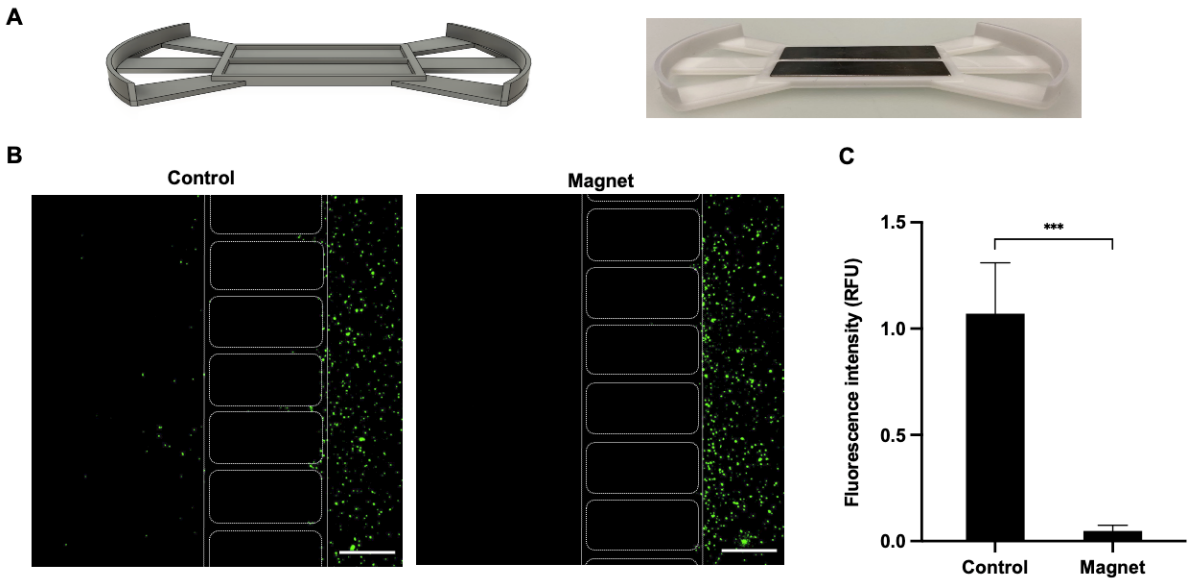

Figure E-1: Magnetic immobilisation of MTB in microfluidic chips. (A) CAD model for magnet holder (left) and 3D printed magnet holder with permanent magnets placed in indentations. **(B)** Representative images of a device placed on a magnet holder and a control device without magnet holder. MTB were stained with CFSE (green). The microchannels are indicated by dotted lines. Maximum intensity z projections. 20x magnification. Scale bar = 100 µm. **(C)** Fluorescence intensity (RFU) in central chamber for n = 4 images of devices on a magnet holder and n = 4 control images. Bars are indicated as mean ± SD. A significant difference was observed with a p-value of 0.0001.

A CAD model of a magnet holder for the petri dish containing the microfluidic chips was designed and 3D printed (Figure E-1A). Microfluidic devices were prepared by injecting MTB seeded in collagen into 2 channels and the devices were imaged after 30h. To assess the successful

immobilisation of MTB, devices placed on a magnet holder were compared to control devices without a magnet holder (Figure E-1B). The mean fluorescence intensity of bacteria in the central chamber was measured. A significantly higher mean fluorescence intensity of 1.07 ± 0.24 RFU was observed in devices without magnetic MTB immobilisation compared to 0.05 ± 0.03 RFU measured for the devices placed on magnets ((Figure E-1C). With the 3D printed magnet holder, a convenient assistive device for alignment of the microfluidic chips on the magnets was developed and successful immobilisation of MTB in the collagen matrix was achieved. Using this magnetic holder, a clear border for the bacteria was established allowing the maintenance of a strong chemotactic gradient over time.

Next, three different MTB seeding densities in microfluidic chips were compared. To ensure consistent experimental conditions, it is important to uniformly seed the bacteria into the chips. Devices were prepared with collagen gels containing bacterial concentrations of 10^7, 10^8 and 10^9 MTB/mL and both sides of the devices were imaged at 24 h. The central chambers were flushed with media prior to imaging. For quantification, the mean fluorescence intensity of the MTB chamber was measured. The bacteria were uniformly distributed in the collagen gel for seeding densities of 10^7 and 10^8 MTB/mL in all devices (Figure E-2A). For the highest concentration of 10^9 MTB/mL, the bacteria was evenly distributed in the collagen in most regions, but aggregates of MTB were observed in some regions (Figure A7). For devices seeded at the lowest density of 10^7 MTB/mL, a mean fluorescence intensity of 1.39 ± 0.89 RFU was measured (Figure E-2B). For the intermediate MTB seeding density of 10^8 MTB/mL, a mean fluorescence intensity of 12.39 ± 5.62 RFU was obtained and for the highest seeding density of 10^9 MTB/mL, a mean fluorescence intensity of 19.15 ± 6.22 RFU was measured.

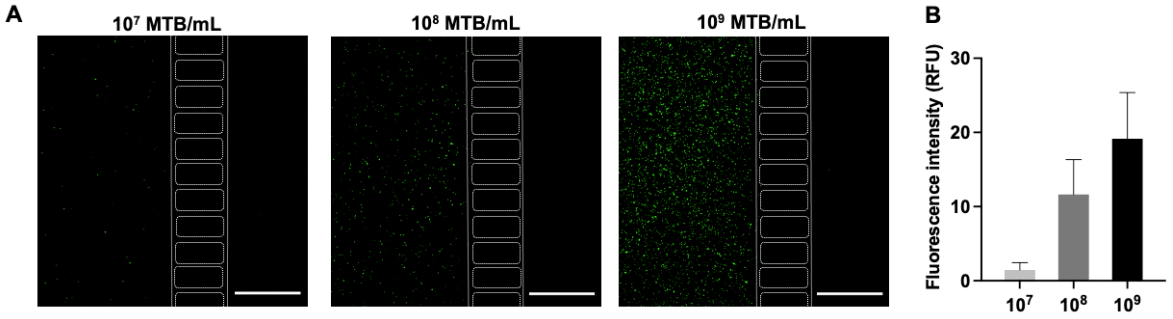

Figure E-2: Comparison of varying MTB seeding densities in microfluidic chips. (A) Representative images of a device at MTB seeding concentrations of 10^7, 10^8 and 10^9 MTB/mL. MTB were stained with CFSE (green). The microchannels are indicated by dotted lines. Maximum intensity z projections. 10x magnification. Scale bar = 250 µm. **(B)** Fluorescence intensity (RFU) in MTB chamber for n = 4 images of each MTB concentration. Bars are indicated as mean ± SD.

As expected, the mean increase in fluorescence intensity from the 10^7 MTB/mL seeding density to the intermediate 10^8 MTB/mL seeding density was approximately 10-fold. However, for the highest seeding concentration of 10^9 MTB/mL, only a 1.5-fold mean increase was measured compared with the intermediate concentration. This attenuated increase could be explained by different phenomena. One hypothesis is that a high MTB seeding density could lead to a higher number of bacteria leaving the MTB chamber and entering the central channel or the media chamber. The bacteria that entered the central chamber will then be flushed out of the device prior to imaging. Bacteria overlay could have an additional influence on the attenuated fluorescence intensity of the highest concentration. If we compare a total of 50 bacteria to a total of 5000 bacteria in a given volume (z stack), the probability that some of the 5000 bacteria are at the same x and y position, and will therefore be overlaid in a maximum intensity z stack projection, is much higher compared to the probability of overlays in a volume with only 50 bacteria. Furthermore, when applying a cell counting algorithm, the difference of the number of counted particles between the different concentrations is closer to the 1:10:100 ratio that we would expect from the seeding concentrations.

The overall migration of macrophages towards magnetotactic bacteria was investigated over 30 h in the microfluidic devices. Devices with a seeding density of 10^8 MTB/mL were compared to control devices without bacteria. To prevent the MTB from entering the central chamber, the bacteria were immobilized using the 3D-printed magnet holder. Images were acquired at 0, 6, 24 and 30 h after macrophage injection and both sides of each device were imaged. Between the imaging time points, the devices were kept in an incubator at 37 °C and 5% CO_2. The MTB chamber and the microchannels were defined as the ROI for quantification of cell migration.

In devices with bacteria, directed cell migration into the microchannels towards the adjacent MTB chamber was observed, while no directed migration was observed in controls without MTB (Figure E-3A). The extent and distance of directed cell migration over time was assessed by fluorescence intensity shifts and cell counting in the ROI. The measured fluorescence intensities along the x-axis were normalized for each device and plotted against a normalized x-axis indicating the migrated distance. The zero point of the x-axis was set on the lower left corner of the region of interest, which is at the onset of the microchannels. The shift of the fluorescence intensity to the right in the devices with bacteria indicates the directed migration of macrophages into the microchannels (Figure E-3B). For the control devices, no fluorescence intensity shifts were visible.

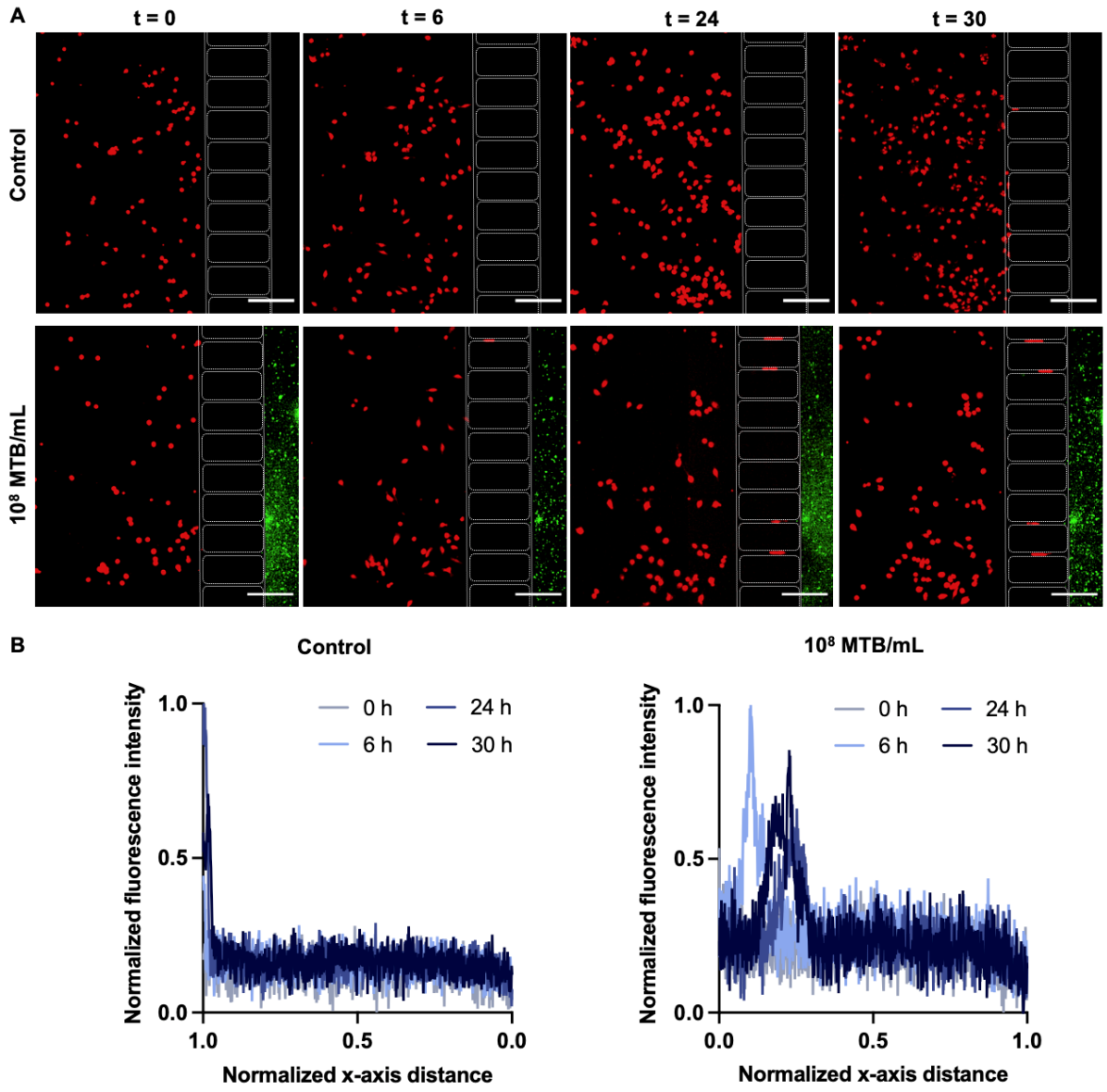

Figure E-3: Representative time-lapse images from long-term cell migration experiment. **(A)** Maximum intensity z projections of macrophages and MTB in a microfluidic chip were acquired at 0, 6, 24 and 30h. Macrophages were stained with Far Red (red) and MTB were stained with CFSE (green). The microchannels are indicated by dotted lines.. Scale bar = 150 µm. **(B)** Representative fluorescence intensity shift plots for control devices and devices with 10^8 MTB/mL. The fluorescence intensity was normalized for each device and plotted against a normalized x-axis distance.

Cell counting was performed to determine the number of cells that migrated into the ROI. In the maximum intensity Z-projection image, the ROI was cropped, and a median filter was applied (Figure E-4). Then, the RGB image was converted into a binary image and a suitable automatic threshold was defined. A watershed algorithm and a dilution operation were applied alternately to achieve an optimal trade-off between separating cells with direct contact and filling gaps of a single cell.

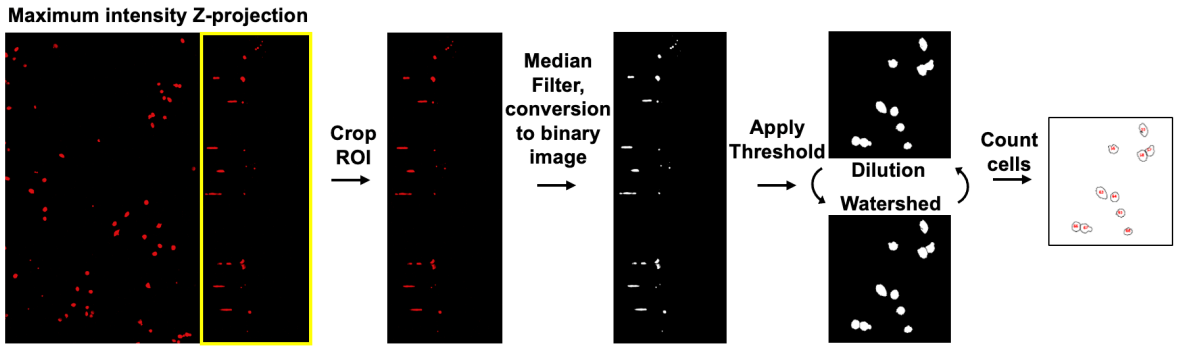

Figure E-4: Image processing pipeline for cell counting. The ROI of the maximum intensity Z-projection image was cropped, and a median filter was applied, the RGB image was converted into a binary image, a suitable automatic threshold was defined, and a watershed algorithm and a dilution operation were finally applied alternately to achieve an optimal trade-off between separating cells with direct contact and filling gaps of a single cell.

At 30 h, the number of cells that migrated into the ROI was significantly higher in the devices with bacteria compared to the control devices (Figure E-5). The initial number of cells in the ROI was subtracted from the detected number of cells for all time points. At time point 6 h and 24 h, there were no significant differences between the number of migrated cells into the ROI between the two groups. At 30 h, the number of migrated cells increased to 7.75 ± 2.17 in the devices with bacteria, compared to 2.00 ± 1.00 migrated cells in the control devices. The standard deviation was especially high in the devices with bacteria at 24 h, indicating high variation among the devices. These substantial differences between microfluidic devices could be explained by a delayed onset of cell migration in some devices due to slightly different conditions in each device. Several factors could have an effect on the survival, spreading and migratory behaviour of cells in a microfluidic chip, including the macrophage seeding density, the humidity in the petri dish, the hydrophobicity of the chip and the collagen gelation. After 30 h, this high variation between devices was reduced, indicating cell migration in all devices.

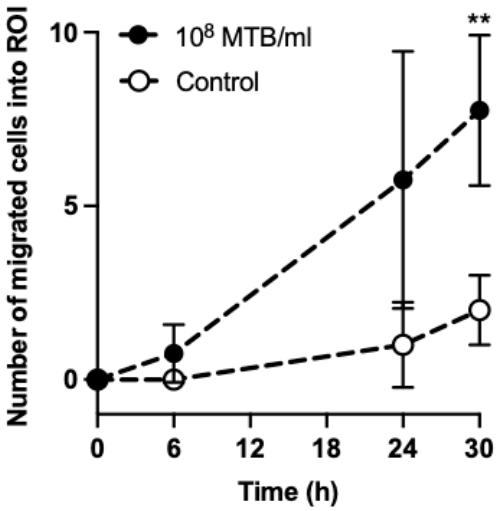

Figure E-5: Number of migrated cells into ROI. Numbers of migrated cells into the ROI were counted at 0, 6, 24 and 30 h. A significant difference in the number of migrated cells in devices with 10^8 MTB/mL and control devices without bacteria was observed at 30 h with a p-value of 0.0029. Four devices were analysed per group. Values are indicated as mean ± SD.

Future experiments could be performed with primary immune cells using the protocols established for device preparation, imaging consistency and image analysis. Two interesting immune cells to study would be dendritic cells (DCs) and natural killer (NK) cells. DCs are mediator cells, which can link the innate and adaptive immune system and induce a coordinated immune response against cancer. NK cells are considered the main effector cells of the innate immune system as they show inherent cytotoxicity against tumour cells. Investigating the migration of primary DC and NK cells to magnetotactic bacteria and the MTB-liposome conjugates will provide important insights that can aid on evaluating the use of MTB for cancer immunotherapy